KU Leuven

Biomedical Sciences Group

Faculty of Medicine

Department of Cardiovascular Sciences



MECHANISMS OF TRIGGERS AND SUBSTRATE OF VENTRICULAR ARRHYTHMIAS IN THE MYOCARDIAL INFARCTION BORDER ZONE

Matthew AMONI

Jury: Prof. Peter SINNAEVE

Prof. Rudi VENNEKENS

Supervisor: Prof. Karin SIPIDO

Co-supervisor: Prof. Rik WILLEMS

Chair examining committee:

Dissertation presented in partial fulfilment of the requirements for the degree of Doctor in Medical Sciences

Date: 29 september 2022 - submitted by Profs. Sipido and Willems on March 13th, 2023

Contents

CHAPTER 1: General introduction 3
Part 1: Cardiac physiology and pathophysiology 4
Part 2: Arrhythmias in Ischemic Heart Disease 6
CHAPTER 2: Rationale and aims 25
CHAPTER 3: The peri-infarct region – A source of arrhythmia susceptibility 28
CHAPTER 4: Initiation of Arrhythmias – Role of delayed afterdepolarisations and premature ventricular complexes 58
CHAPTER 5: Heterogeneous repolarization within the myocardial infarction border zone – A functional substrate for arrhythmias 92
CHAPTER 6: Electrocardiogram beat-to-beat variability of repolarization (BVR) during acute ischemia. 151
CHAPTER 7: Temporal changes in BVR can predict imminent arrhythmias in high risk patients 177
CHAPTER 8: General discussion and future perspectives 206
SUMMARY 214
ACKNOWLEDGEMENTS 215
CURRICULUM VITAE MATTHEW AMONI 217
PUBLICATIONS 219
POSTSCRIPTUM 224

CHAPTER 1: General introduction

Part 1: Cardiac physiology and pathophysiology

The heart is a muscular organ made up of 4 chambers (2 atria and 2 ventricles) that pump and circulate blood around the body delivering oxygen and nutrients that sustain life. The mechanical contractions of the heart are triggered and synchronized by electrical signals spreading through an electrical system embedded in the cardiac muscle (Figure 1). The normal sequence of each heartbeat, starts in the sinoatrial node (SA) a spontaneously firing group of cells. This signal is rapidly disseminated to the atria leading to their contraction which transfers blood to the ventricles. Concurrently, the electrical signal is propagated to the atrioventricular node, then down the His and purkinje fibres terminating on ventricular cells. This produces a coordinated contraction of the large ventricles necessary to generate sufficient force to circulate blood.

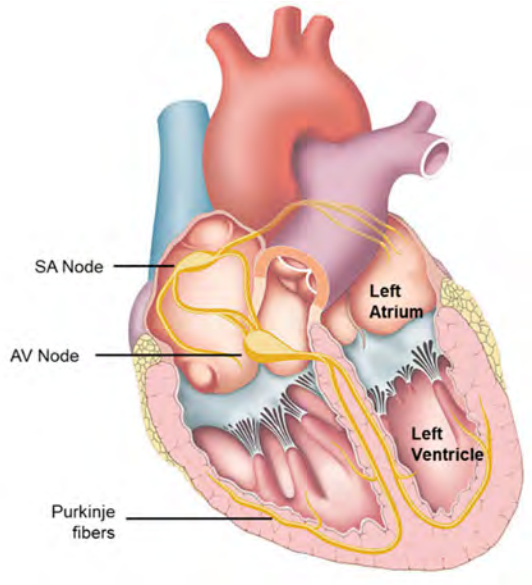

Figure 1. Anatomy of the heart and electrical conducting system. Adapted with permission from [1].

The muscle contractions of the heart that pump blood in the vascular circulation are the result of a co-ordinated symphony of cellular electrical events, collectively called the action potential; which is coupled to mechanical contraction. The heart muscle consists of cardiac cells, that are excitable with membranes containing ion channels coupled to a contractile protein apparatus. The cardiac cycle is initiated by an influx of sodium that depolarizes the cell, activating calcium channels. This influx of calcium activates calcium release from internal stores via the ryanodine receptor channels. The large amount of calcium in the cytosol binds to the contractile apparatus facilitating contraction. The depolarized state and prevailing calcium activate potassium channels that repolarize the cell by refluxing potassium. Concurrently, sodium calcium, sodium-potassium and sarco-endoplasmic reticulum calcium exchange pump restores these major ions to their resting balance (Figure 2).

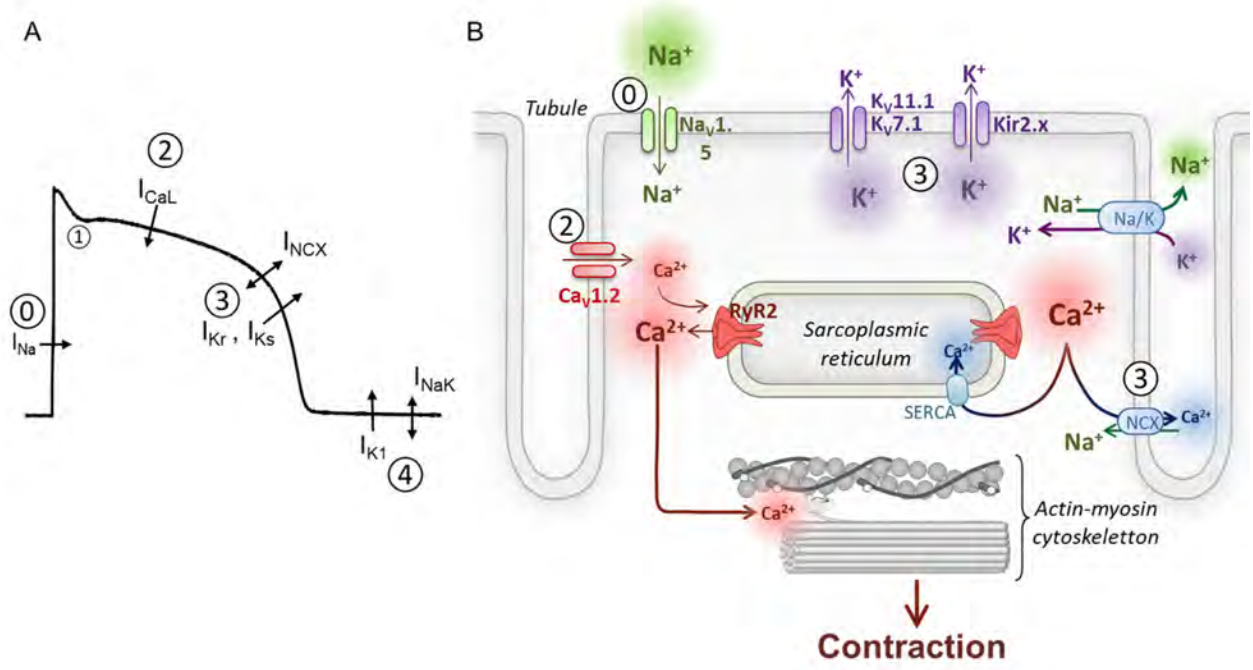

Figure 2. Illustration of normal cardiac cellular electrophysiology.
A, Normal ventricular action potential. Stimulation leads to Phase 0 – activation and Na^+ influx, followed by a brief repolarization, Phase 1, then a plateau due to Ca^{2+} influx, Phase 2. Finally, K^+ efflux leads to repolarization (Phase 3) and maintained resting membrane potential, Phase 4.
B, Illustration of the excitation-contraction coupling. After Ca^{2+} influx (Phase 2), activating the Ryanodine receptor releasing Ca^{2+} from the sarcoplasmic reticulum store that then facilitates contraction by actin-myosin contractile apparatus. Ca^{2+} is returned to stores and pumped out of the cell. Adapted from [2].

In addition to the intrinsic electrical signalling governing cardiac activity, there are external regulators of cardiac function, in particular the autonomic nervous system and circulating hormones contribute to external control of the heart including what is referred to as the 'flight-or-fight response'.

Disruption of the electrical activity of the heart can interfere with efficiency of the pump, manifesting as heart failure; and can also lead to a lethal arrhythmia.

1.1. SUDDEN CARDIAC DEATH

Sudden cardiac death (SCD) is defined as an unexpected natural death from a cardiac cause within a short time period (generally ≤1 hour from the onset of symptoms) [3]. The rapid deterioration is predominantly attributable to abnormal cardiac electrical activity generating arrhythmias that disrupt cardiac function. These life threathening arrhythmias include ventricular

tachycardia (VT) and ventricular fibrillation (VF) that produce ineffective contractions degenerating to asystole and cessation of corporal perfusion [4]. SCD is a leading cause of death accounting for approximately 7 million deaths annually worldwide (~20% of deaths). The overwhelming majority of SCD cases (~80%) have underlying ischemic heart disease that is central to the mechanisms initiating and driving arrhythmias that lead to SCD [5,6].

1.2. ISCHEMIC HEART DISEASE (IHD)

Ischemic heart disease (IHD) describes conditions where the blood supply to the heart is compromised leading to deprivation of oxygen and nutrients to the cardiac cells. The primary pathology here is coronary artery disease due to atherosclerosis [7]. Atherosclerosis is a build-up of plaque in the artery wall leading to narrowing of coronary arteries and ischaemia; complete coronary artery occlusion occurs when thrombosis superimposes on a vulnerable plaque lesion leading to critical deprivation of perfusion and death of the cardiac muscle called myocardial infarction (MI).

The process of injury and healing during MI are complex and eventually result in a scar that replaces the dead muscle [5]. This scar can be a source of abnormal electrical signalling that can interfered with and cause the heart to fail in its electrical signalling and pumping ultimately death.

With this background, the following section is a more detailed overview of the interplay between IHD and SCD as state-of-the art background of the mechanisms of ventricular arrhythmias in IHD.

Part 2: Arrhythmias in Ischemic Heart Disease

The following is part of a review published as Amoni M, Dries E, Ingelaere S, Vermoortele D, Roderick HL, Claus P, Willems R, Sipido KR. Ventricular Arrhythmias in Ischemic Cardiomyopathy – New Avenues for Mechanism-Guided Treatment. Cells. 2021; 10(10):2629. DOI: https://doi.org/10.3390/cells10102629

The Unique Nature and Central Role of the Border Zone

After MI, three structurally distinct ventricular regions can be distinguished (Figure 1A): the infarct region, the border zone (BZ) and the remote region. The infarct region is subjected to ischaemia, and reperfusion in most cases, where necrotic tissue is replaced by fibrosis, with scar formation preserving the wall integrity. Surrounding the infarct is a transition BZ which was subject to relative ischaemia and collateral perfusion. Here the fraction of myocytes that survived this insult is intermixed with fibrosis. Third is the remote region that was unaffected by the ischemic insult, but which will eventually have to compensate for the loss of muscle mass.

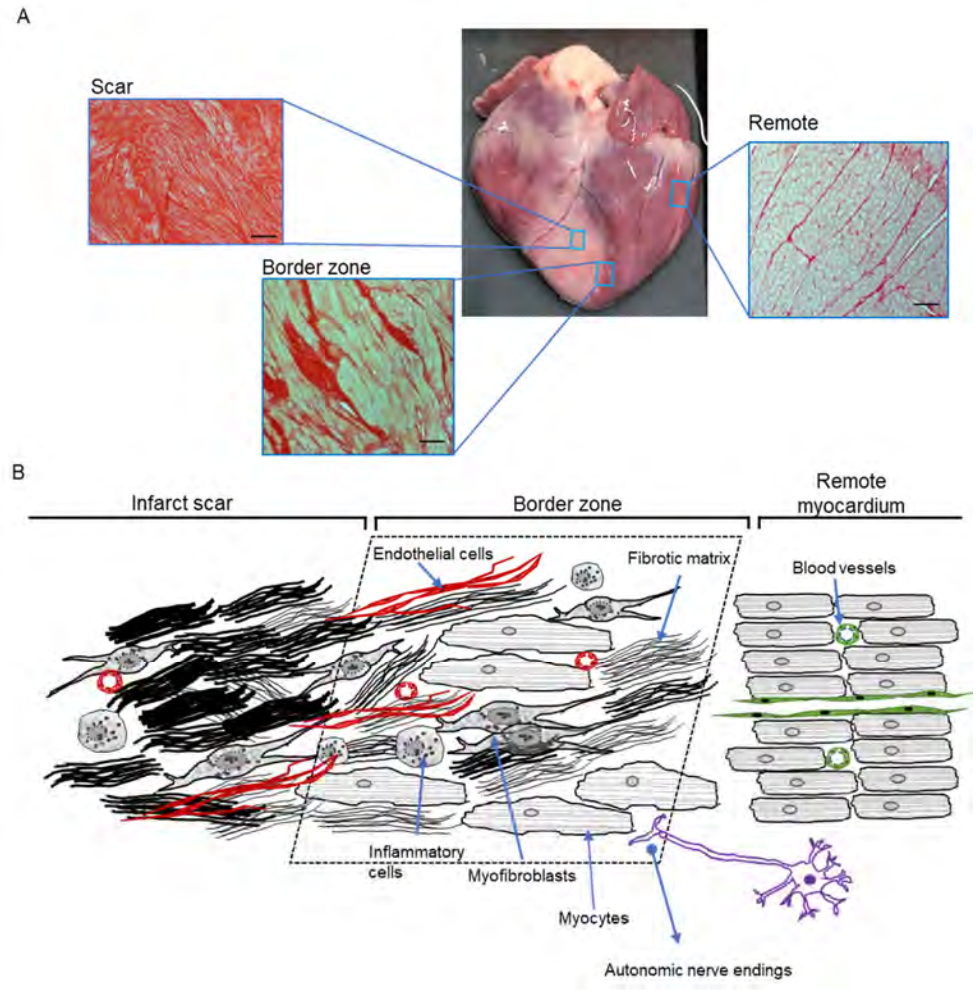

Figure 1. The unique nature of the myocardial infarction border zone. (**A**) Picture of a pig heart from with ischaemia/reperfusion injury-induced myocardial infarction after 1 month, illustrating the histological fibrotic structure of the scar (left insert) the mixed fibrosis and myocytes in the border zone (middle insert) and the healthy/non-infarcted remote myocardium (right insert) by Picosirius red staining (Adapted from [7]). (**B**) Schematic diagram illustrating the multicellular milieu of the border zone as transition between scar and myocardium without ischemic damage (remote myocardium).

Our understanding of the pathology and time-course of post-MI repair and remodelling has deepened through experimental studies [6]. The initial phase of MI (day 1–5) is characterised by cell death and inflammation. During this phase rapid myocyte loss occurs by necrosis and apoptosis, with infiltration and activation of immune cells and fibroblasts. The intermediate phase (Day 7–30) is characterised by resolution of the inflammation and replacement of myocyte loss by fibrosis leading to a myocardial infarct or scar. The chronic phase (Day 30 onwards) is the remodelling phase during which the remaining myocytes remodel to adapt to the changes due to the loss of a part of the ventricle.

The BZ formation involves a complex symphony of immune cells, including neutrophils, infiltrating monocytes, regulatory T cells and resident macrophages, as well as pericytes, endothelial cells and fibroblasts interacting directly and indirectly with myocytes in the BZ [6,8,9].

The myocytes in the BZ undergo substantial remodelling in response to different signals. The transient ischaemia leads to activation of survival pathways such as the RISK and SAFE pathways [10,11]. The acute loss of a significant percentage of myocardium in MI results in abrupt and progressive changes of ventricular loading and local wall stress leading to abnormal strain in the surviving border zone and non-infarcted remote region, that contribute to remodelling and altered regional strain [12,13]. The wall stress in the scar and BZ is higher than to that of the remote myocardium primarily due to the difference in thickness [14-16], affecting fibroblast properties as well [17]. In addition, the BZ is under unique load during systole, due to the non-compliant scar tissue on one side leading to uneven mechanical forces and contraction [55,56]. This contributes to a BZ-specific myocyte phenotype, different from the remodelling in the remote myocardium [7,13,15,18].

Another important feature of the BZ is the altered nature of the local autonomic innervation. Cardiac sympathetic nerves also suffer ischemic injury and death in the infarct region resulting in denervation [19,20]. Similar processes are observed to a lesser extent in the BZ. Here surviving neurons attempt to regenerate and sprout, leading to a heterogeneous innervation [21,22]. Various nerve growth factors including NGF, GAP43, and protein tyrosine phosphatase sigma (PTP) have been described to regulate neuronal re-innervation and targeting such factors can improve innervation and abate arrhythmias [23,24]. Following MI, the innervation of the heart undergoes remodelling in the form of denervation-re-innervation with aberrant nerve sprouting particularly in the BZ [23,25]. These processes modulate myocyte function and remodelling, influencing ion channel expression and the BZ phenotype [26]. Neurons in the non-infarcted region also undergo neuronal remodelling [27]. Moreover, extra-cardiac neuronal remodelling occurs with observed enlargement and dendritic sprouting of stellate ganglia in MI-models that further influences myocyte remodelling [23,28,29].

Lastly, not only the myocardium and innervating network, but also the perfusing vasculature and microcirculation in the ischemic area are damaged with subsequent remodelling in the reperfused BZ [30,31]. The observations of a rest-stress perfusion defect mismatch in high risk patients confirms that perfusion of the BZ is dysfunctional [32,33]. In the BZ, local vascular damage, stenosis, and angiogenesis occur during infarct healing [34]. These new vessels have abnormalities of smooth muscle and organisation, leading to dysfunction particularly under stress where nitric-oxide and bradykinin-mediated vasodilatation is impaired [35-37]. This contributes to the vulnerability to ischaemia of the BZ and consequent arrhythmias.

Taken together, as illustrated in Figure 1B, the BZ microarchitecture, resulting from a complex local remodelling process, forms a unique substrate for arrhythmias in IHD as supported by in vivo studies.

Origin and Maintenance of VT – Mechanistic Insights Obtained In Vivo

The Conceptual Framework

Clinical and experimental mapping and ablation studies have greatly advanced our understanding of the *in vivo* arrhythmogenesis in ICM. The current mechanistic framework is that underlying and pre-existing vulnerability is created through structural and functional abnormalities. In the post-MI heart, this is classically due to the scar formation and LV remodelling with creation of the unique BZ. On this substrate, initiating events, e.g., adrenergic activation, ischaemia, mechanical loading and electrolyte abnormalities, create the trigger for arrhythmias, typically a PVC (Figure 2). Progression to VT and maintenance are mostly the result of the properties of the underlying substrate.

Triggers and Arrhythmia Initiation

Monitoring studies have highlighted that the majority of arrhythmias in ICM are initiated by a triggering-PVC [38,39]. Such PVCs can be due to automaticity, triggered activity or micro-reentry (Figure 2B).

Automaticity is implicated particularly in acute ischaemia where injury current flows between ischemic depolarised tissue and unaffected myocardium [40]. This could depolarise injured Purkinje fibres, which develop enhanced firing and trigger PVCs [41,42].

Triggered activity from afterdepolarisations is another important mechanism of PVCs and often the consequence of increased adrenergic drive, which increases intracellular calcium [43,44]. Clinical observations that frequent PVCs can be reproduced during an EP study by infusion of isoproterenol and by high rate pacing support the link between cellular events and PVCs [44,45]. Delayed afterdepolarisations (DAD) occur during phase 4 or resting membrane potential due to spontaneous calcium release leading to calcium extrusion via sodium-calcium exchanger. The resulting transient inward current induces membrane depolarisation. If these depolarisations are large enough to reach threshold for activation of Na^+ channels, an action potential (AP) is triggered, resulting in a PVC. Afterdepolarisations have been documented in Purkinje fibres and myocytes in ischaemia and at different stages after MI [44,46]. Myocytes within the BZ are particularly prone to DADs under adrenergic drive [47,48], and during in vivo studies in the pig with MI, we recently could demonstrate co-localisation of DADs and PVC sites within the BZ (see chapter 4).

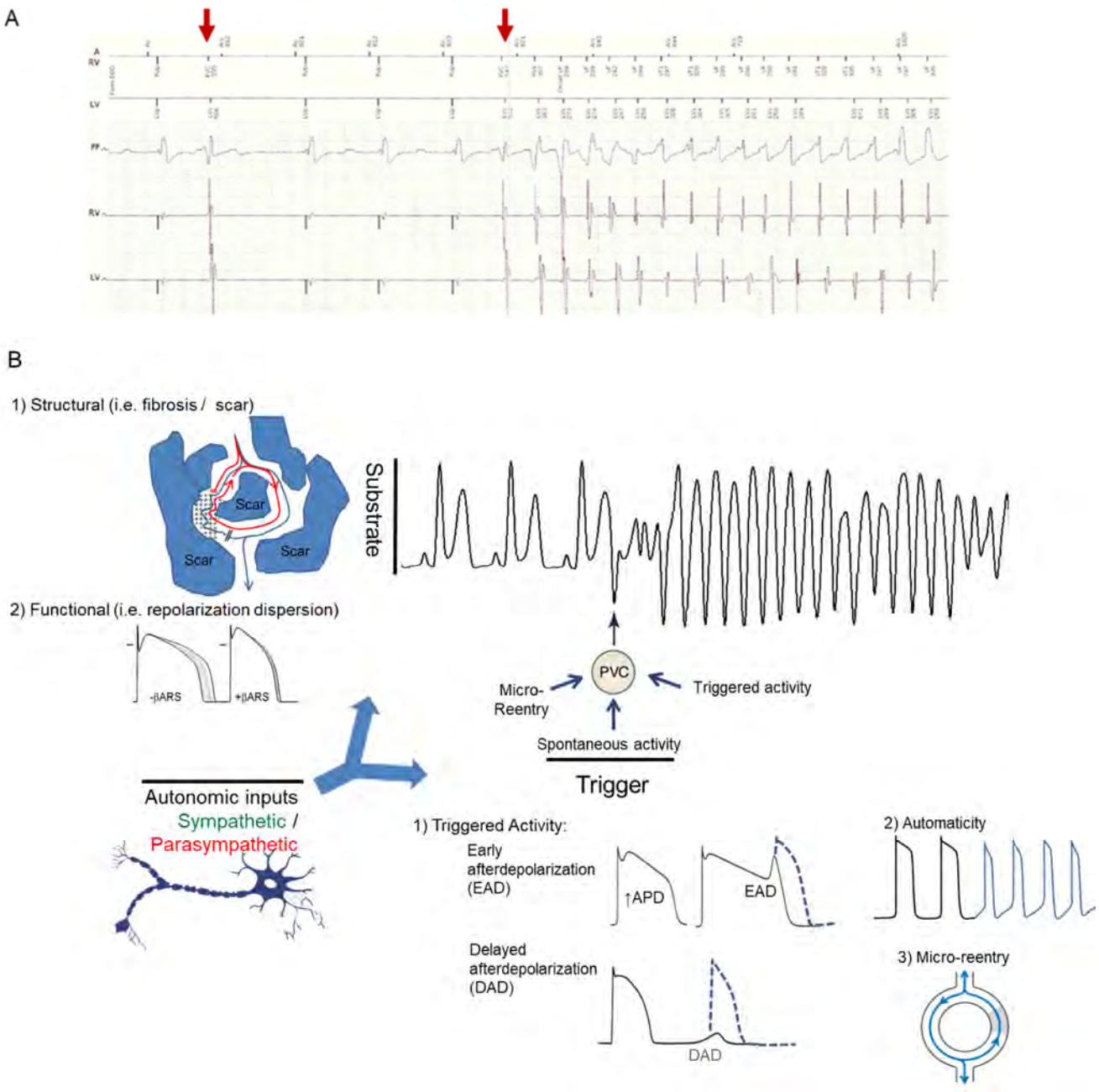

Figure 2. Arrhythmia mechanisms in vivo. (**A**) Example of ventricular arrhythmia initiation by a premature ventricular complex (PVC) from ICD recording of a patient (Courtesy Prof. Dr. Rik Willems, University Hospitals Leuven). (**B**) Framework of arrhythmia mechanisms.

Another possibility is micro-reentry, e.g., within the BZ. This has not been demonstrated experimentally in ICM, but it is postulated to occur where fibrosis intersperses myocytes with variable action potential duration (APD). This would allow conduction block and re-activation in a small area <5mm creating a PVC [49,50]. In this scenario, early afterdepolarisations (EADs)

associated with AP prolongation, as well as dispersion of repolarisation, in space and time, are important contributing factors.

Finally, mechano-electrical feedback in vivo, e.g., during sudden increase of afterload can be part of the initiating event or PVC [51]. At cellular level, acute stretch produces membrane depolarisations that affect the AP and membrane repolarisation or resting phase interrupting it with afterdepolarisations that can trigger APs and PVCs via calcium-mediated modulation of ion channel and ryanodine receptor function [52,53]. Classical in vivo studies utilizing monophasic action potential (MAP) recordings in human surgery and altering loading conditions by transient aortic constriction demonstrated the effects of mechanical feedback on the AP and the generation of afterdepolarisations that triggered PVCs [54].

Arrhythmia Substrate for Progression and Sustenance/Maintenance

The BZ has a central role for arrhythmia sustenance. The structural obstacles are classically understood to induce conduction slowing as electrical activation needs to zig-zag through the BZ maze around the scar, thereby allowing re-entry circuits to form [55]. In addition, it is increasingly recognised that functional abnormalities facilitate and are often essential to the re-entry circuit. Myocyte electrophysiology in the BZ is considered critical to the functional unidirectional block in the re-entry circuit [56,57]. Specifically, depolarisation and repolarisation differences contribute to the conduction block and allow re-activation of refractory regions allowing a re-entry loop [56,57]. In early experiments on post-MI VT mechanisms, El-Sherif and collaborators demonstrated by in vivo mapping the importance of the functional substrate and specifically dispersion of refractoriness, as well as the underlying myocyte-driven changes in ionic currents and APD [58,59]. In our recent work, we also recorded time-dependent variation in repolarisation in the BZ that likewise would facilitate re-entry (see chapter 3). Mechano-electrical coupling and regional differences in wall stress mechanics may also impact on the functional substrate and sustenance of arrhythmias. Orini et al. demonstrated using a multielectrode myocardial sock the induction of spatial inhomogeneity of repolarisation due to alterations in loading conditions that may contribute to the arrhythmia substrate and in a case report elegantly mapped the transition to arrhythmia during ischaemia in an ICM patient [60,61]. The understanding of impact of mechano-electrical feedback on electrical and mechanical activity has also advanced greatly by the studies of mechanical dyssynchrony. Here mechanical inhomogeneity linked to ECG parameters of abnormal repolarisation is greater in ICM patients with documented arrhythmias and improves SCD prediction [62].

Recent advanced imaging combined with computational studies in experimental MI large-animal models has allowed description of the heterogeneous fibrosis and myofibre disorganisation that is characteristic of reentry circuit areas [63,64]. This data has led to novel clinical ablation strategies based on detailed imaging analysis to predict arrhythmia ablation sites with initial reassuring success [65]. The prescribed approach to ablation of post-MI VT typically depends upon the induction of stable arrhythmia pacing manoeuvres, like pace-mapping and entrainment, to determine the ablation target [45,66]. The advances in detailed 3D electro-anatomical mapping have had a profound influence on the approach for VT ablation [67,68]. A first improvement is the possibility to tackle critical features of the substrate identified with mapping during sinus rhythm, like isthmuses or channels in the border zone of the infarct, determined by heterogeneous scar and late or isolated potentials or fragmented signals [69]. Another approach is homogenisation of the substrate, independent of critical features. By ablation of the entire BZ with relatively preserved voltages on mapping (0.5–1.5 mV), the culprit region is rendered

electrically inert and almost all potentials rendered <0.5 mV [66,70]. Finally, in some cases of hemodynamically unstable VT or VF storm, the triggering PVCs are located and targeted for ablation [71,72]. Of these strategies, critical substrate targeting has substantially benefited from incorporation of advanced imaging into the procedure, making future changes in standard clinical practice likely. Pre-procedural magnetic resonance imaging visualises the location and extent of the infarct and fibrosis, feeding into computational modelling to create a substrate map on which critical vulnerable sites can be identified. This information is then used to personalise the ablation strategy [54,73,74]. Novel strategies including stereotactic non-invasive ablation, rely on preprocedural imagining for procedural planning and execution [75]. Initial success and encouraging results of accurate critical isthmus prediction from MRI reconstructions promises much to be expected from these strategies.

Despite these mechanistic insights in the role of post-MI substrate and triggers gained from in vivo studies, effective and safe anti-arrhythmic pharmacological therapy is lacking. A possible hindrance to pharmacology has been neglect of the heterogeneity of remodelling in the LV. Also, the multicellular environment of the BZ affects local myocyte remodelling and in vivo electrical function, factors that also need to be taken into account when designing molecular therapy.

In summary, electrical remodelling of myocytes and the heterocellular interactions in the BZ create a unique environment for arrhythmogenesis, both as a substrate promoting re-entry and as a setting facilitating triggered events. The latter mostly result from an extra stimulus, with a prominent role for altered autonomic drive as initiating event.

Role of Autonomic Inputs in the BZ for Arrhythmogenesis

Inputs from the autonomic nervous system superimpose on the myocyte remodelling to enhance and initiate arrhythmias in several ways [22,76-78].

As mentioned above, innervation within the BZ is heterogeneous resulting from the denervation-re-innervation sprouting during ischaemia, reperfusion, and recovery. Early experimental studies demonstrated sympathetic innervation to be pro-arrhythmic by enhancement of the substrate by increasing dispersion of repolarisation and triggered activity that is counteracted by the anti-arrhythmic action of the parasympathetic system [79,80].

More recent studies showed that sympathetic stimulation leads to variable AP profiles in subareas of this region, reflecting the variable innervation and related modulatory actions on underlying ion channels and calcium handling [23,28,81]. Altered innervation was observed to be linked to increased transmural dispersion of repolarisation due to alterations in transient outward and inward rectifier K^+ currents [82,83].

Cardiac myocytes have a predominance of beta-adrenergic receptors and circulating catecholamines may also contribute to or superimpose on the vulnerable substrate to promote arrhythmias. Infusion of isoproterenol has been demonstrated to increase dispersion of repolarisation in ICM patients [84]. We recently demonstrated in a pig MI model that adrenergic stimulation increased temporal dispersion, i.e., beat-to-beat variation of repolarisation, which also contributes to the functional substrate (see chapter 3) [48].

Importantly, increased sympathetic tone is a major factor for initiation of arrhythmias, by generating PVCs. The link between adrenergic-enhanced spontaneous calcium release in myocytes, concurrent depolarisations through the Na/Ca exchange currents, and eventually triggered APs is well known [85]. In the BZ, the conditions to translate into a PVC are met

including reduced cell-cell coupling, interspersing fibrosis, reduced repolarisation reserve and AP electrical remodelling [86]. Our recent work demonstrated this link, and we could identify preferred sites of PVCs (see chapter 4).

At cellular level, the adrenergic response also reflects changes in the myocyte signalling pathway. Spontaneous calcium release is mediated by Ca^{2+}-calmodulin kinase (CaMK) acting on the RYRs which are differently distributed within the myocytes after MI [48,87]. Moreover, our recent data (chapter 4) supports altered response to adrenergic signalling with increased sensitivity in the MI BZ as an underlying mechanism leading to triggered activity in the BZ [7]. Whether this relates to a reduction in receptor density or intracellular signalling is not yet established, but work from Gorelik and her group underscore the changes in receptor localisation and subtypes [88].

The knowledge about autonomic modulation of arrhythmogenesis has been translated to clinical practice with the established role of first-line beta blockers in the prevention of arrhythmias in patients post-MI [89,90]. Neuromodulation is also gaining traction as studies have demonstrated its effectiveness, particularly in treating refractory ventricular tachycardia and arrhythmia storms [91,92].

In summary, the knowledge on cellular mechanisms of arrhythmogenesis in the BZ invites further translational and mechanistic research to improve specific targeting of remodelling in this region. The management of VT/VF to prevent SCD after myocardial infarction remains challenging and calls for novel mechanistic-based non-invasive treatment. Identification of the arrhythmia critical sites and characterisation of the molecular signature unique to these sites can open avenues to targeted therapy and reduce off-target effects that have hampered systemic pharmacotherapy. Such advances are in line with precision medicine and a patient-tailored therapy.

Animal Models for Post-MI Remodelling

When considering the time-dependent remodelling in vivo, the confounders of therapy, concomitant disease and the limited access to human tissue, it is clear that animal models remain a cornerstone for the study of post-MI changes in cardiac myocyte properties. Myocyte remodelling after MI has been studied for decades, leading to progressive insights, but also confounding the field and potential translation because of the wide variety of models that have been used [93]. Variety has been in species, type of intervention to create MI and timing of the observations at myocyte level and the lack of large data sets that are inherent to patch clamp studies. Studies of the 1980s and 90s mostly used rats in a surgical coronary ligation model, whereas the dog was the typical large-animal model for MI, created during surgery. Rat studies allowed more time points to be investigated and ligation typically induces large infarcts with extensive remodelling, eventually leading to heart failure. Nowadays, creation of MI in rats and mice after ligation, is often used as a model for heart failure. An important limitation of these small-animal models for the study of BZ and remote regions, is the difficulty of regional sampling for functional single myocyte studies and consequently, mostly data come from an aggregate of cells isolated from surviving myocardium. Some of the early data on cell morphology, nevertheless already indicated the presence of regional differences in hypertrophy between near-MI and remote regions [94,95] as also recently seen for the loss of T-tubules in the rat model [15]. The dog model allowed more precise regional sampling but typically had a short

observation window, linked on the one hand to logistics and on the other hand to the limitation of the extensive collaterals and smaller infarcts. For these and other reasons, since the 2000s, the pig is becoming a leading animal model [96]. Pig cardiac anatomy and physiology is closer to humans, and infarcts can be created through ischaemia-reperfusion without surgery [93,96]. As well, surgical, and non-surgical, interventions have been developed to study chronic coronary stenosis and hibernation [97,98]. The breeding of transgenic animals with human histocompatibility genes for xenotransplantation [99,100] further increases interest in this animal model, which can be studied in vivo using clinical tools for EP studies, imaging, etc. Limitations are the logistics of handling adult pigs during long-term experiments. Logistically, sheep are easier to handle but like the dog, have coronary circulatory differences compared to man, and typically more than one coronary branch needs to be occluded to obtain large infarcts. The rabbit has been used as an intermediate size animal model, in terms of advantages and limitations [101,102].

In the dog and pig, different modes of MI induction have been used. In the dog, rich collateral circulation requires more extensive interventions to reduce blood flow and typically requires surgery to occlude or reduce flow in multiple coronary branches. In the pig, collaterals are sparser and a temporary single-vessel occlusion suffices to induce infarction. Permanent occlusive or stenosis methods to induce MI including ligation, embolisation and flow-limitation, in contrast to occlusion-reperfusion techniques such as balloon-occlusion create different phenotypes of MI. The former is likely more relevant to the pre-reperfusion/PCI era where coronary lesions remained in the chronic phase. In the current era of primary revascularisation, the ischaemia-reperfusion (I/R) models are likely more representative of the clinical phenotype, though the absence of pre-existing coronary and cardiac pathology remains a major distinction. Key differences are likely to be in the infarct and BZ, which are the principle source of arrhythmias and underlying SCD in ICM. In permanent occlusion models, the lack of blood-flow to the infarct and limited flow to the BZ limits infiltration and myocyte recovery. As such, larger infarcts are more observed in permanent occlusion compared to reperfusion [103]. Post-MI time-course in small-animal models, pre-clinical large-animal models and human MI are different as well [104]. In particular small-animal models exhibit a more rapid time-course and different qualitative features of cellular infiltration and signalling involved in infarct healing than large-animal models and human MI. Recent work suggests that the fibroblasts differentiation and invasion of the scar and BZ exhibit a unique phenotype and temporal profile as well [105,106].

In the last 20 years, mice have taken centre stage as animal model, mostly due to the power of genetic manipulation [103]. MI has mostly been induced by coronary artery ligation and mice are able to survive large infarcts of up to 40% of the LV. However, this often quickly progresses to heart failure and thus the ligation model is more suitable to study HF than early post-MI remodelling without overt HF [107]. More recently, I/R methods were introduced that are more relevant to study post-MI remodelling as well as being more relevant to the optimal clinical management of patients [108]. However, the small size of the mouse heart makes it difficult to isolate sub-regions.

Finally, in the choice of animal models to study arrhythmic mechanisms post-MI, the electrophysiology of the myocytes is also important as species differences in ion currents shape the AP morphology with implications on repolarisation and the functional substrate for arrhythmias [109]. For small-animal models, there is a large disparity with the human AP, though this is less of a limitation for the rabbit compared to rat and mouse [110]. The dog, sheep and

pig have an AP morphology and rate response that is close to human, but none has the exact same make-up in ion channels [111].

In the experimental models of this thesis, we make use of large animal (pig) models for their similarity to human anatomy and physiology as well as similar cardiomyocyte structure and electrophysiology [1]. We also employ two models of MI: a non-reperfused, chronic stenosis model of MI and an ischemia-reperfusion model of MI. These models are described in their relevant chapters and reflect the different advantages of remodelling and pathophysiology reviewed by Lindsey *et al*., [111]

References

1. GettyImages. Conductions system(3). **2015**, Av Node, Heart Shape, 2015, Human Body Part, Human Heart, doi:https://www.istockphoto.com/vector/conducao3-gm464420812-59020482.

2. Gilbert, G.; Demydenko, K.; Dries, E.; Puertas, R.D.; Jin, X.; Sipido, K.; Roderick, H.L. Calcium Signaling in Cardiomyocyte Function. *Cold Spring Harb Perspect Biol* **2020**, *12*, a035428, doi:10.1101/cshperspect.a035428.

3. Zipes, D.P.; Wellens, H.J.J. Sudden Cardiac Death. *Circulation* **1998**, *98*, 2334-2351, doi: 10.1161/01.cir.98.21.2334.

4. Huikuri, H.V.; Castellanos, A.; Myerburg, R.J. Sudden Death Due to Cardiac Arrhythmias. *N Engl J Med* **2001**, *345*, 1473-1482, doi:10.1056/nejmra000650.

5. Adabag, A.S.; Luepker, R.V.; Roger, V.L.; Gersh, B.J. Sudden cardiac death: epidemiology and risk factors. *Nat Rev Cardiol.* **2010**, *7*, 216-225, doi:10.1038/nrcardio.2010.3.

6. Hayashi, M.; Shimizu, W.; Albert, C.M. The Spectrum of Epidemiology Underlying Sudden Cardiac Death. *Circ Res* **2015**, *116*, 1887-1906, doi:10.1161/circresaha.116.304521.

7. Bergmark, B.A.; Mathenge, N.; Merlini, P.A.; Lawrence-Wright, M.B.; Giugliano, R.P. Acute coronary syndromes. *Lancet* **2022**, *399*, 1347-1358, doi:10.1016/s0140-6736(21)02391-6.

8. Frangogiannis, N.G. The inflammatory response in myocardial injury, repair, and remodelling. *Nat Rev Cardiol* **2014**, *11*, 255-265, doi:10.1038/nrcardio.2014.28.

9. Frangogiannis, N.G. Regulation of the Inflammatory Response in Cardiac Repair. *Circ Res* **2012**, *110*, 159-173, doi:10.1161/circresaha.111.243162.

10. Amoni, M.; Claus, P.; Dries, E.; Nagaraju, C.; De Buck, S.; Vandenberk, B.; Ingelaere, S.; Vermoortele, D.; Roderick, H.L.; Sipido, K.R.; et al. Discrete sites of frequent premature ventricular complexes cluster within the infarct border zone and coincide with high frequency of delayed afterdepolarizations under adrenergic stimulation. *Heart Rhythm* **2021**, *18*, 1976-1987, doi:10.1016/j.hrthm.2021.07.067.

11. Daseke, M.J.; Chalise, U.; Becirovic-Agic, M.; Salomon, J.D.; Cook, L.M.; Case, A.J.; Lindsey, M.L. Neutrophil signaling during myocardial infarction wound repair. *Cellular Signalling* **2021**, *77*, 109816, doi:10.1016/j.cellsig.2020.109816.

12. Ma, Y.; Mouton, A.J.; Lindsey, M.L. Cardiac macrophage biology in the steady-state heart, the aging heart, and following myocardial infarction. *Translational Research* **2018**, *191*, 15-28, doi:10.1016/j.trsl.2017.10.001.

13. Rossello, X.; Yellon, D.M. The RISK pathway and beyond. *Basic Res Cardio.* **2018**, *113*, doi:10.1007/s00395-017-0662-x.

14. Hadebe, N.; Cour, M.; Lecour, S. The SAFE pathway for cardioprotection: is this a promising target? *Basic Res Cardiol* **2018**, *113*, doi:10.1007/s00395-018-0670-5.

15. Opie, L.H.; Commerford, P.J.; Gersh, B.J.; Pfeffer, M.A. Controversies in ventricular remodelling. *Lancet* **2006**, *367*, 356-367, doi:10.1016/s0140-6736(06)68074-4.

16. Ashikaga, H.; Mickelsen, S.R.; Ennis, D.B.; Rodriguez, I.; Kellman, P.; Wen, H.; McVeigh, E.R. Electromechanical analysis of infarct border zone in chronic myocardial infarction. *Am J Physiol Heart Circ Physiol* **2005**, *289*, H1099-1105, doi:10.1152/ajpheart.00423.2005.

17. Jackson, B.M.; 3rd, J.H.G.; Salgo, I.S.; Moainie, S.L.; Plappert, T.; John-Sutton, M.S.; Jr, L.H.E.; Gorman, R.C. Border zone geometry increases wall stress after myocardial infarction: contrast echocardiographic assessment. *Am J Physiol Heart Circ Physiol* **2003**, *284*, H475-479, doi:10.1152/ajpheart.00360.2002.

18. Frisk, M.; Ruud, M.; Espe, E.K.S.; Aronsen, J.M.; Røe, Å.T.; Zhang, L.; Norseng, P.A.; Sejersted, O.M.; Christensen, G.A.; Sjaastad, I.; et al. Elevated ventricular wall stress disrupts cardiomyocyte t-tubule structure and calcium homeostasis. *Cardiovasc Res* **2016**, *112*, 443-451, doi:10.1093/cvr/cvw111.

19. Galan, D.T.; Bito, V.; Claus, P.; Holemans, P.; Abi-Char, J.; Nagaraju, C.K.; Dries, E.; Vermeulen, K.; Ventura-Clapier, R.; Sipido, K.R.; et al. Reduced mitochondrial respiration in the ischemic as well as in the remote nonischemic region in postmyocardial infarction remodeling. *Am J Physiol Heart Circ Physiol y* **2016**, *311*, H1075-H1090, doi:10.1152/ajpheart.00945.2015.

20. Nagaraju, C.K.; Dries, E.; Popovic, N.; Singh, A.A.; Haemers, P.; Roderick, H.L.; Claus, P.; Sipido, K.R.; Driesen, R.B. Global fibroblast activation throughout the left ventricle but localized fibrosis after myocardial infarction. *Sci Rep* **2017**, *7*, doi:10.1038/s41598-017-09790-1.

21. Cox, M. Morphometric mapping of regional myocyte diameters after healing of myocardial infarction in cats. *J Mol Cell Cardiol* **1991**, *23*, 127-135, doi:10.1016/0022-2828(91)90100-z.

22. Yokoyama, T.; Lee, J.-K.; Miwa, K.; Opthof, T.; Tomoyama, S.; Nakanishi, H.; Yoshida, A.; Yasui, H.; Iida, T.; Miyagawa, S.; et al. Quantification of sympathetic hyperinnervation and denervation after myocardial infarction by three-dimensional assessment of the cardiac sympathetic network in cleared transparent murine hearts. *PLoS One* **2017**, *12*, e0182072, doi:10.1371/journal.pone.0182072.

23. Matsunari, I.; Schricke, U.; Bengel, F.M.; Haase, H.-U.; Barthel, P.; Schmidt, G.; Nekolla, S.G.; Schoemig, A.; Schwaiger, M. Extent of Cardiac Sympathetic Neuronal Damage Is

Determined by the Area of Ischemia in Patients With Acute Coronary Syndromes. *Circulation* **2000**, *101*, 2579-2585, doi:10.1161/01.cir.101.22.2579.

24. Cao, J.-M.; Fishbein, M.C.; Han, J.B.; Lai, W.W.; Lai, A.C.; Wu, T.-J.; Czer, L.; Wolf, P.L.; Denton, T.A.; Shintaku, I.P.; et al. Relationship Between Regional Cardiac Hyperinnervation and Ventricular Arrhythmia. *Circulation* **2000**, *101*, 1960-1969, doi:10.1161/01.cir.101.16.1960.

25. Rajendran, P.S.; Nakamura, K.; Ajijola, O.A.; Vaseghi, M.; Armour, J.A.; Ardell, J.L.; Shivkumar, K. Myocardial infarction induces structural and functional remodelling of the intrinsic cardiac nervous system. *J Physiol* **2016**, *594*, 321-341, doi:10.1113/jp271165.

26. Gardner, R.T.; Wang, L.; Lang, B.T.; Cregg, J.M.; Dunbar, C.L.; Woodward, W.R.; Silver, J.; Ripplinger, C.M.; Habecker, B.A. Targeting protein tyrosine phosphatase σ after myocardial infarction restores cardiac sympathetic innervation and prevents arrhythmias. *Nat Comm* **2015**, *6*, 6235, doi:10.1038/ncomms7235.

27. Zhou, S.; Chen, L.S.; Miyauchi, Y.; Miyauchi, M.; Kar, S.; Kangavari, S.; Fishbein, M.C.; Sharifi, B.; Chen, P.-S. Mechanisms of Cardiac Nerve Sprouting After Myocardial Infarction in Dogs. *Circ Re* **2004**, *95*, 76-83, doi:10.1161/01.res.0000133678.22968.e3.

28. Habecker, B.A.; Anderson, M.E.; Birren, S.J.; Fukuda, K.; Herring, N.; Hoover, D.B.; Kanazawa, H.; Paterson, D.J.; Ripplinger, C.M. Molecular and cellular neurocardiology: development, and cellular and molecular adaptations to heart disease. *J Physiol* **2016**, *594*, 3853-3875, doi:10.1113/jp271840.

29. Wang, K.; Lee, P.; Mirams, G.R.; Sarathchandra, P.; Borg, T.K.; Gavaghan, D.J.; Kohl, P.; Bollensdorff, C. Cardiac tissue slices: preparation, handling, and successful optical mapping. *Am J Physiol Heart Circ Physiol* **2015**, *308*, H1112-1125, doi:10.1152/ajpheart.00556.2014.

30. Ajijola, O.A.; Yagishita, D.; Patel, K.J.; Vaseghi, M.; Zhou, W.; Yamakawa, K.; So, E.; Lux, R.L.; Mahajan, A.; Shivkumar, K. Focal myocardial infarction induces global remodeling of cardiac sympathetic innervation: neural remodeling in a spatial context. *Am J Physiol Heart Circ Physiol* **2013**, *305*, H1031-1040, doi:10.1152/ajpheart.00434.2013.

31. Ajijola, O.A.; Yagishita, D.; Reddy, N.K.; Yamakawa, K.; Vaseghi, M.; Downs, A.M.; Hoover, D.B.; Ardell, J.L.; Shivkumar, K. Remodeling of stellate ganglion neurons after spatially targeted myocardial infarction: Neuropeptide and morphologic changes. *Heart Rhythm* **2015**, *12*, 1027-1035, doi:10.1016/j.hrthm.2015.01.045.

32. Han, S.; Kobayashi, K.; Joung, B.; Piccirillo, G.; Maruyama, M.; Vinters, H.V.; March, K.; Lin, S.-F.; Shen, C.; Fishbein, M.C.; et al. Electroanatomic Remodeling of the Left Stellate Ganglion After Myocardial Infarction. *J Am Coll Cardiol* **2012**, *59*, 954-961, doi:10.1016/j.jacc.2011.11.030.

33. Padro, T.; Manfrini, O.; Bugiardini, R.; Canty, J.; Cenko, E.; De Luca, G.; Duncker, D.J.; Eringa, E.C.; Koller, A.; Tousoulis, D.; et al. ESC Working Group on Coronary Pathophysiology and Microcirculation position paper on 'coronary microvascular dysfunction in cardiovascular disease'. *Cardiovasc Res* **2020**, *116*, 741-755, doi:10.1093/cvr/cvaa003.

34. Robbers, L.F.; Eerenberg, E.S.; Teunissen, P.F.; Jansen, M.F.; Hollander, M.R.; Horrevoets, A.J.; Knaapen, P.; Nijveldt, R.; Heymans, M.W.; Levi, M.M.; et al. Magnetic resonance imaging-defined areas of microvascular obstruction after acute myocardial infarction

represent microvascular destruction and haemorrhage. *Eur Heart J* **2013**, *34*, 2346-2353, doi:10.1093/eurheartj/eht100.

35. Van Der Burg, A.E.B.; Bax, J.J.; Boersma, E.; Pauwels, E.K.J.; Van Der Wall, E.E.; Schalij, M.J. Impact of Viability, Ischemia, Scar Tissue, and Revascularization on Outcome After Aborted Sudden Death. *Circulation* **2003**, *108*, 1954-1959, doi:10.1161/01.cir.0000091410.19963.9a.

36. Travin, M.I.; Dessouki, A.; Cameron, T.; Heller, G.V. Use of exercise technetiumtium-99m sestamibi SPECT imagina to detect residual ischemia and for risk stratification after acute myocardial infarction. *Am J Cardiol* **1995**, *75*, 665-669, doi:10.1016/s0002-9149(99)80650-x.

37. Wu, X.; Reboll, M.R.; Korf-Klingebiel, M.; Wollert, K.C. Angiogenesis after acute myocardial infarction. *Cardiovasc Res* **2021**, *117*, 1257-1273, doi:10.1093/cvr/cvaa287.

38. Merkus, D.; Muller-Delp, J.; Heaps, C.L. Coronary microvascular adaptations distal to epicardial artery stenosis. *Am J Physiol Heart Circ Physiol* **2021**, *320*, H2351-H2370, doi:10.1152/ajpheart.00992.2020.

39. A.J.Kalkman, E.; Haren, P.v.; R.Saxena, P.; G.Schoemaker, R. Regionally Different Vascular Response to Vasoactive Substances in the Remodelled Infarcted Rat Heart; Aberrant Vasculature in the Infarct Scar. *J Mol Cell Cardiol* **1997**, *29*, 1487-1497, doi:10.1006/jmcc.1997.0388.

40. Sellke, F.W.; Kagaya, Y.; Johnson, R.G.; Shafique, T.; Schoen, F.J.; Grossman, W.; Weintraub, R.M. Endothelial modulation of porcine coronary microcirculation perfused via immature collaterals. *Am J Physiol.* **1992**, *262*, H1669-1675, doi:10.1152/ajpheart.1992.262.6.H1669.

41. Gorenek, B.; Cengiz, O.; Kudaiberdieva, G.; Durak, I.; Dogan, V.; Yasar, B.; Birdane, A.; Cavusoglu, Y.; Ata, N. Mode of onset of polymorphic ventricular tachycardia in acute myocardial infarction. *Can J Cardiol* **2010**, *26*, e254-e257, doi:10.1016/s0828-282x(10)70421-9.

42. Lerma, C.; Gorelick, A.; Ghanem, R.N.; Glass, L.; Huikuri, H.V. Patterns of ectopy leading to increased risk of fatal or near-fatal cardiac arrhythmia in patients with depressed left ventricular function after an acute myocardial infarction. *Europace* **2013**, *15*, 1304-1312, doi:10.1093/europace/eus415.

43. Janse, M.J.; Van Capelle, F.J.; Morsink, H.; Kléber, A.G.; Wilms-Schopman, F.; Cardinal, R.; D'Alnoncourt, C.N.; Durrer, D. Flow of "injury" current and patterns of excitation during early ventricular arrhythmias in acute regional myocardial ischemia in isolated porcine and canine hearts. Evidence for two different arrhythmogenic mechanisms. *Circ Res* **1980**, *47*, 151-165, doi:10.1161/01.res.47.2.151.

44. Szumowski, L.; Sanders, P.; Walczak, F.; Hocini, M.; Jaïs, P.; Kepski, R.; Szufladowicz, E.; Urbanek, P.; Derejko, P.; Bodalski, R.; et al. Mapping and ablation of polymorphic ventricular tachycardia after myocardial infarction. *J Am Coll Cardiol* **2004**, *44*, 1700-1706, doi:10.1016/j.jacc.2004.08.034.

45. Xing, D.; Martins, J.B. Triggered activity due to delayed afterdepolarizations in sites of focal origin of ischemic ventricular tachycardia. *Am J Physiol Heart Circ Physiol* **2004**, *287*, H2078-2084, doi:10.1152/ajpheart.00027.2004.

46. Volders, P.G.; Vos, M.A.; Szabo, B; Sipido, K.R.; de Groot, S.H.; Gorgels, A.P.; Wellens, H.J.; Lazzara r. Progress in the understanding of cardiac early afterdepolarizations and torsades de pointes: time to revise current concepts. *Cardiovasc Res* **2000**, *46*, 376-392, doi:10.1016/s0008-6363(00)00022-5.

47. Wit, A.L. Afterdepolarizations and triggered activity as a mechanism for clinical arrhythmias. *Pacing Clin Electrophysiol* **2018**, *41*, 883-896, doi:10.1111/pace.13419.

48. Cronin, E.M.; Bogun, F.M.; Maury, P.; Peichl, P.; Chen, M.; Namboodiri, N.; Aguinaga, L.; Leite, L.R.; Al-Khatib, S.M.; Anter, E.; et al. 2019 HRS/EHRA/APHRS/LAHRS expert consensus statement on catheter ablation of ventricular arrhythmias: executive summary. *Europace* **2020**, *22*, 450-495, doi:10.1093/europace/euz332.

49. Janse, M.J.; Wit, A. Electrophysiological mechanisms of ventricular arrhythmias resulting from myocardial ischemia and infarction. *Physiol Rev.* **1989**, *69*, 1049-1169, doi:10.1152/physrev.1989.69.4.1049.

50. Hegyi, B.; Bossuyt, J.; Griffiths, L.G.; Shimkunas, R.; Coulibaly, Z.; Jian, Z.; Grimsrud, K.N.; Sondergaard, C.S.; Ginsburg, K.S.; Chiamvimonvat, N.; et al. Complex electrophysiological remodeling in postinfarction ischemic heart failure. *Proc Nat Acad Sci* **2018**, *115*, E3036-E3044, doi:10.1073/pnas.1718211115.

51. Dries, E.; Amoni, M.; Vandenberk, B.; Johnson, D.M.; Gilbert, G.; Nagaraju, C.K.; Puertas, R.D.; Abdesselem, M.; Santiago, D.J.; Roderick, H.L.; et al. Altered adrenergic response in myocytes bordering a chronic myocardial infarction underlies in vivo triggered activity and repolarization instability. *J Physiol* **2020**, *598*, 2875-2895, doi:10.1113/jp278839.

52. Gouvêa De Barros, B.; Weber Dos Santos, R.; Lobosco, M.; Alonso, S. Simulation of Ectopic Pacemakers in the Heart: Multiple Ectopic Beats Generated by Reentry inside Fibrotic Regions. *Biomed Res Int* **2015**, *2015*, 1-18, doi:10.1155/2015/713058.

53. Oliveira, R.S.; Alonso, S.; Campos, F.O.; Rocha, B.M.; Fernandes, J.F.; Kuehne, T.; Dos Santos, R.W. Ectopic beats arise from micro-reentries near infarct regions in simulations of a patient-specific heart model. *Sci Rep* **2018**, *8*, doi:10.1038/s41598-018-34304-y.

54. Haemers, P.; Sutherland, G.; Cikes, M.; Jakus, N.; Holemans, P.; Sipido, K.R.; Willems, R.; Claus, P. Further insights into blood pressure induced premature beats: Transient depolarizations are associated with fast myocardial deformation upon pressure decline. *Heart Rhythm* **2015**, *12*, 2305-2315, doi:10.1016/j.hrthm.2015.06.037.

55. Johnson, D.M.; Antoons, G. Arrhythmogenic Mechanisms in Heart Failure: Linking beta-Adrenergic Stimulation, Stretch, and Calcium. *Front Physiol* **2018**, *9*, 1453, doi:10.3389/fphys.2018.01453.

56. Ravens, U. Mechano-electric feedback and arrhythmias. *Prog Biophys Mol Biol* **2003**, *82*, 255-266, doi:10.1016/s0079-6107(03)00026-9.

57. Taggart, P.; Sutton, P.M. Cardiac mechano-electric feedback in man: clinical relevance. *Prog Biophys Mol Biol.* **1999**, *71*, 139-154, doi:10.1016/s0079-6107(98)00039-x.

58. De Bakker, J.M.; Van Capelle, F.J.; Janse, M.J.; Tasseron, S.; Vermeulen, J.T.; De Jonge, N.; Lahpor, J.R. Slow conduction in the infarcted human heart. 'Zigzag' course of activation. *Circulation* **1993**, *88*, 915-926, doi:10.1161/01.cir.88.3.915.

59. Ciaccio, E.J.; Coromilas, J.; Wit, A.L.; Peters, N.S.; Garan, H. Formation of Functional Conduction Block During the Onset of Reentrant Ventricular Tachycardia. *Circ Arrhythm Electrophysiol* **2016**, *9*, e004462, doi:10.1161/circep.116.004462.

60. Baba, S.; Dun, W.; Cabo, C.; Boyden, P.A. Remodeling in Cells From Different Regions of the Reentrant Circuit During Ventricular Tachycardia. *Circulation* **2005**, *112*, 2386-2396, doi:10.1161/circulationaha.105.534784.

61. Restivo, M.; Gough, W.B.; El-Sherif, N. Ventricular arrhythmias in the subacute myocardial infarction period. High-resolution activation and refractory patterns of reentrant rhythms. *Circ Res* **1990**, *66*, 1310-1327, doi:10.1161/01.res.66.5.1310.

62. Qin, D.; Zhang, Z.-H.; Caref, E.B.; Boutjdir, M.; Jain, P.; El-Sherif, N. Cellular and Ionic Basis of Arrhythmias in Postinfarction Remodeled Ventricular Myocardium. *Circ Res* **1996**, *79*, 461-473, doi:10.1161/01.res.79.3.461.

63. Orini, M.; Taggart, P.; Bhuva, A.; Roberts, N.; Di Salvo, C.; Yates, M.; Badiani, S.; Van Duijvenboden, S.; Lloyd, G.; Smith, A.; et al. Direct in vivo assessment of global and regional mechanoelectric feedback in the intact human heart. *Heart Rhythm* **2021**, *18*, 1406-1413, doi:10.1016/j.hrthm.2021.04.026.

64. Orini, M.; Taggart, P.; Hayward, M.; Lambiase, P.D. Spatiotemporal characterization of the transition from sinus rhythm to ventricular fibrillation during an acute ischemic event in the intact human heart by whole-heart sock-mapping. *HeartRhythm Case Rep* **2017**, *3*, 259-263, doi:10.1016/j.hrcr.2017.01.002.

65. Haugaa, K.H.; Edvardsen, T.; Amlie, J.P. Prediction of Life-Threatening Arrhythmias – Still an Unresolved Problem. *Cardiology* **2011**, *118*, 129-137, doi:10.1159/000327093.

66. León, D.G.; López-Yunta, M.; Alfonso-Almazán, J.M.; Marina-Breysse, M.; Quintanilla, J.G.; Sánchez-González, J.; Galán-Arriola, C.; Castro-Núñez, F.; González-Ferrer, J.J.; Ibáñez, B.; et al. Three-dimensional cardiac fibre disorganization as a novel parameter for ventricular arrhythmia stratification after myocardial infarction. *Europace* **2019**, *21*, 822-832, doi:10.1093/europace/euy306.

67. Pashakhanloo, F.; Herzka, D.A.; Halperin, H.; McVeigh, E.R.; Trayanova, N.A. Role of 3-Dimensional Architecture of Scar and Surviving Tissue in Ventricular Tachycardia. *Circ Arrhythm Electrophysiol* **2018**, *11*, e006131, doi:10.1161/circep.117.006131.

68. Trayanova, N.A.; Doshi, A.N.; Prakosa, A. How personalized heart modeling can help treatment of lethal arrhythmias: A focus on ventricular tachycardia ablation strategies in post-infarction patients. *Wiley Interdiscip Rev Syst Biol Med* **2020**, *12*, e1477, doi:10.1002/wsbm.1477.

69. Sadek, M.M.; Schaller, R.D.; Supple, G.E.; Frankel, D.S.; Riley, M.P.; Hutchinson, M.D.; Garcia, F.C.; Lin, D.; Dixit, S.; Zado, E.S.; et al. Ventricular Tachycardia Ablation – The Right Approach for the Right Patient. *Arrhythm Electrophysiol Rev* **2014**, *3*, 161, doi:10.15420/aer.2014.3.3.161.

70. Kim, Y.H.; Chen, S.A.; Ernst, S.; Guzman, C.E.; Han, S.; Kalarus, Z.; Labadet, C.; Lin, Y.J.; Lo, L.W.; Nogami, A.; et al. 2019 APHRS expert consensus statement on three-dimensional mapping systems for tachycardia developed in collaboration with HRS, EHRA, and LAHRS. *J Arrhythm* **2020**, *36*, 215-270, doi:10.1002/joa3.12308.

71. Gepstein, L.; Hayam, G.; Ben-Haim, S.A. A novel method for nonfluoroscopic catheter-based electroanatomical mapping of the heart. In vitro and in vivo accuracy results. *Circulation* **1997**, *95*, 1611-1622, doi:10.1161/01.cir.95.6.1611.

72. Wolf, M.; Sacher, F.; Cochet, H.; Kitamura, T.; Takigawa, M.; Yamashita, S.; Vlachos, K.; Cheniti, G.; Frontera, A.; Martin, R.; et al. Long-Term Outcome of Substrate Modification in Ablation of Post–Myocardial Infarction Ventricular Tachycardia. *Circ Arrhythm Electrophysiol* **2018**, *11*, e005635, doi:10.1161/circep.117.005635.

73. Briceño, D.F.; Romero, J.; Villablanca, P.A.; Londoño, A.; Diaz, J.C.; Maraj, I.; Batul, S.A.; Madan, N.; Patel, J.; Jagannath, A.; et al. Long-term outcomes of different ablation strategies for ventricular tachycardia in patients with structural heart disease: systematic review and meta-analysis. *Europace* **2018**, *20*, 104-115, doi:10.1093/europace/eux109.

74. Bogun, F.; Crawford, T.; Chalfoun, N.; Kuhne, M.; Sarrazin, J.F.; Wells, D.; Good, E.; Jongnarangsin, K.; Oral, H.; Chugh, A.; et al. Relationship of frequent postinfarction premature ventricular complexes to the reentry circuit of scar-related ventricular tachycardia. *Heart Rhythm* **2008**, *5*, 367-374, doi:10.1016/j.hrthm.2007.11.026.

75. Marrouche, N.F.; Verma, A.; Wazni, O.; Schweikert, R.; Martin, D.O.; Saliba, W.; Kilicaslan, F.; Cummings, J.; Burkhardt, J.D.; Bhargava, M.; et al. Mode of initiation and ablation of ventricular fibrillation storms in patients with ischemic cardiomyopathy. *J Am Coll Cardiol* **2004**, *43*, 1715-1720, doi:10.1016/j.jacc.2004.03.004.

76. Okada, D.R.; Miller, J.; Chrispin, J.; Prakosa, A.; Trayanova, N.; Jones, S.; Maggioni, M.; Wu, K.C. Substrate Spatial Complexity Analysis for the Prediction of Ventricular Arrhythmias in Patients With Ischemic Cardiomyopathy. *Circ Arrhythm Electrophysiol* **2020**, *13*, doi:10.1161/circep.119.007975.

77. Prakosa, A.; Arevalo, H.J.; Deng, D.; Boyle, P.M.; Nikolov, P.P.; Ashikaga, H.; Blauer, J.J.E.; Ghafoori, E.; Park, C.J.; Blake, R.C.; et al. Personalized virtual-heart technology for guiding the ablation of infarct-related ventricular tachycardia. *Nat Biomed Eng* **2018**, *2*, 732-740, doi:10.1038/s41551-018-0282-2.

78. Sharma, A.; Wong, D.; Weidlich, G.; Fogarty, T.; Jack, A.; Sumanaweera, T.; Maguire, P. Noninvasive stereotactic radiosurgery (CyberHeart) for creation of ablation lesions in the atrium. *Heart Rhythm* **2010**, *7*, 802-810, doi:10.1016/j.hrthm.2010.02.010.

79. Shen, M.J.; Zipes, D.P. Role of the Autonomic Nervous System in Modulating Cardiac Arrhythmias. *Circ Res* **2014**, *114*, 1004-1021, doi:10.1161/circresaha.113.302549.

80. Vaseghi, M.; Shivkumar, K. The Role of the Autonomic Nervous System in Sudden Cardiac Death. *Progr Cardiovasc Dis* **2008**, *50*, 404-419, doi:10.1016/j.pcad.2008.01.003.

81. Gardner, R.T.; Ripplinger, C.M.; Myles, R.C.; Habecker, B.A. Molecular Mechanisms of Sympathetic Remodeling and Arrhythmias. *Circ Arrhythm Electrophysiol* **2016**, *9*, e001359, doi:10.1161/CIRCEP.115.001359.

82. Schwartz, P.J.; Vanoli, E.; Stramba-Badiale, M.; De Ferrari, G.M.; Billman, G.E.; Foreman, R.D. Autonomic mechanisms and sudden death. New insights from analysis of baroreceptor reflexes in conscious dogs with and without a myocardial infarction. *Circulation* **1988**, *78*, 969-979, doi:10.1161/01.cir.78.4.969.

83. Vanoli, E.; De Ferrari, G.M.; Stramba-Badiale, M.; Hull, S.S.; Foreman, R.D.; Schwartz, P.J. Vagal stimulation and prevention of sudden death in conscious dogs with a healed myocardial infarction. *Circ Res* **1991**, *68*, 1471-1481, doi:10.1161/01.res.68.5.1471.

84. Wang, L.; Olivas, A.; Francis Stuart, S.D.; Tapa, S.; Blake, M.R.; Woodward, W.R.; Habecker, B.A.; Ripplinger, C.M. Cardiac sympathetic nerve transdifferentiation reduces action potential heterogeneity after myocardial infarction. *Am J Physiol Heart Circ Physiol* **2020**, *318*, H558-H565, doi:10.1152/ajpheart.00412.2019.

85. Jiang, H.; Lu, Z.; Yu, Y.; Zhao, D.; Yang, B.; Huang, C. Relationship between sympathetic nerve sprouting and repolarization dispersion at peri-infarct zone after myocardial infarction. *Auton Neurosci* **2007**, *134*, 18-25, doi:10.1016/j.autneu.2007.01.014.

86. Yoshioka, K.; Gao, D.-W.; Chin, M.; Stillson, C.; Penades, E.; Lesh, M.; O'Connell, W.; Dae, M. Heterogeneous Sympathetic Innervation Influences Local Myocardial Repolarization in Normally Perfused Rabbit Hearts. *Circulation* **2000**, *101*, 1060-1066, doi:10.1161/01.cir.101.9.1060.

87. Vaseghi, M.; Lux, R.L.; Mahajan, A.; Shivkumar, K. Sympathetic stimulation increases dispersion of repolarization in humans with myocardial infarction. *Am J Physiol Heart Circ Physiol* **2012**, *302*, H1838-1846, doi:10.1152/ajpheart.01106.2011.

88. Priori, S.G.; Mantica, M.; Schwartz, P.J. Delayed afterdepolarizations elicited in vivo by left stellate ganglion stimulation. *Circulation* **1988**, *78*, 178-185, doi:10.1161/01.cir.78.1.178.

89. Xie, Y.; Sato, D.; Garfinkel, A.; Qu, Z.; Weiss, J.N. So Little Source, So Much Sink: Requirements for Afterdepolarizations to Propagate in Tissue. *Biophys J* **2010**, *99*, 1408-1415, doi:10.1016/j.bpj.2010.06.042.

90. Dries, E.; Santiago, D.J.; Gilbert, G.; Lenaerts, I.; Vandenberk, B.; Nagaraju, C.K.; Johnson, D.M.; Holemans, P.; Roderick, H.L.; Macquaide, N.; et al. Hyperactive ryanodine receptors in human heart failure and ischaemic cardiomyopathy reside outside of couplons. *Cardiovasc Res* **2018**, *114*, 1512-1524, doi:10.1093/cvr/cvy088.

91. Schobesberger, S.; Wright, P.; Tokar, S.; Bhargava, A.; Mansfield, C.; Glukhov, A.V.; Poulet, C.; Buzuk, A.; Monszpart, A.; Sikkel, M.; et al. T-tubule remodelling disturbs localized beta2-adrenergic signalling in rat ventricular myocytes during the progression of heart failure. *Cardiovasc Res* **2017**, *113*, 770-782, doi:10.1093/cvr/cvx074.

92. Al-Khatib, S.M.; Stevenson, W.G.; Ackerman, M.J.; Bryant, W.J.; Callans, D.J.; Curtis, A.B.; Deal, B.J.; Dickfeld, T.; Field, M.E.; Fonarow, G.C.; et al. 2017 AHA/ACC/HRS guideline for management of patients with ventricular arrhythmias and the prevention of sudden cardiac death: Executive summary. *Heart Rhythm* **2018**, *15*, e190-e252, doi:10.1016/j.hrthm.2017.10.035.

93. Al-Gobari, M.; Khatib, C.E.; Pillon, F.; Gueyffier, F. Beta-blockers for the prevention of sudden cardiac death in heart failure patients: a meta-analysis of randomized controlled trials. *BMC Cardiovasc Disord* **2013**, *13*, 52, doi:10.1186/1471-2261-13-52.

94. Meng, L.; Tseng, C.H.; Shivkumar, K.; Ajijola, O. Efficacy of Stellate Ganglion Blockade in Managing Electrical Storm: A Systematic Review. *JACC Clin Electrophysiol* **2017**, *3*, 942-949, doi:10.1016/j.jacep.2017.06.006.

95. Vaseghi, M.; Gima, J.; Kanaan, C.; Ajijola, O.A.; Marmureanu, A.; Mahajan, A.; Shivkumar, K. Cardiac sympathetic denervation in patients with refractory ventricular arrhythmias or electrical storm: Intermediate and long-term follow-up. *Heart Rhythm* **2014**, *11*, 360-366, doi:10.1016/j.hrthm.2013.11.028.

96. Lindsey, M.L.; Bolli, R.; Canty, J.M., Jr.; Du, X.J.; Frangogiannis, N.G.; Frantz, S.; Gourdie, R.G.; Holmes, J.W.; Jones, S.P.; Kloner, R.A.; et al. Guidelines for experimental models of myocardial ischemia and infarction. *Am J Physiol Heart Circ Physiol* **2018**, *314*, H812-H838, doi:10.1152/ajpheart.00335.2017.

97. Anversa, P.; Beghi, C.; Kikkawa, Y.; Olivetti, G. Myocardial response to infarction in the rat. Morphometric measurement of infarct size and myocyte cellular hypertrophy. *Am J Pathol* **1985**, *118*, 484-492.

98. Anversa, P.; Olivetti, G.; Capasso, J.M. Cellular basis of ventricular remodeling after myocardial infarction. *Am J Cardiol* **1991**, *68*, 7-16, doi:10.1016/0002-9149(91)90256-k.

99. Heusch, G.; Skyschally, A.; Schulz, R. The in-situ pig heart with regional ischemia/reperfusion — Ready for translation. *J Mol Cell Cardiol* **2011**, *50*, 951-963, doi:10.1016/j.yjmcc.2011.02.016.

100. Canty, J.M.; Suzuki, G.; Banas, M.D.; Verheyen, F.; Borgers, M.; Fallavollita, J.A. Hibernating Myocardium. *Circ Res* **2004**, *94*, 1142-1149, doi:10.1161/01.res.0000125628.57672.cf.

101. Wu, M.; D'Hooge, J.; Ganame, J.; Ferferieva, V.; Sipido, K.R.; Maes, F.; Dymarkowski, S.; Bogaert, J.; Rademakers, F.E.; Claus, P. Non-invasive characterization of the area-at-risk using magnetic resonance imaging in chronic ischaemia. *Cardiovasc Res* **2011**, *89*, 166-174, doi:10.1093/cvr/cvq257.

102. Wolf, E.; Kemter, E.; Klymiuk, N.; Reichart, B. Genetically modified pigs as donors of cells, tissues, and organs for xenotransplantation. *Anim Front* **2019**, *9*, 13-20, doi:10.1093/af/vfz014.

103. Längin, M.; Mayr, T.; Reichart, B.; Michel, S.; Buchholz, S.; Guethoff, S.; Dashkevich, A.; Baehr, A.; Egerer, S.; Bauer, A.; et al. Consistent success in life-supporting porcine cardiac xenotransplantation. *Nature* **2018**, *564*, 430-433, doi:10.1038/s41586-018-0765-z.

104. Desantiago, J.; Ai, X.; Islam, M.; Acuna, G.; Ziolo, M.T.; Bers, D.M.; Pogwizd, S.M. Arrhythmogenic Effects of β 2 -Adrenergic Stimulation in the Failing Heart Are Attributable to Enhanced Sarcoplasmic Reticulum Ca Load. *Circ Res* **2008**, *102*, 1389-1397, doi:10.1161/circresaha.107.169011.

105. Currie, S.; Quinn, F.R.; Sayeed, R.A.; Duncan, A.M.; Kettlewell, S.; Smith, G.L. Selective down-regulation of sub-endocardial ryanodine receptor expression in a rabbit model of left ventricular dysfunction. *J Mol Cell Cardiol* **2005**, *39*, 309-317, doi:10.1016/j.yjmcc.2005.04.005.

106. De Villiers, C.; Riley, P.R. Mouse models of myocardial infarction: comparing permanent ligation and ischaemia-reperfusion. *Dis Models Mech* **2020**, *13*, dmm046565, doi:10.1242/dmm.046565.

107. Dewald, O.; Ren, G.; Duerr, G.D.; Zoerlein, M.; Klemm, C.; Gersch, C.; Tincey, S.; Michael, L.H.; Entman, M.L.; Frangogiannis, N.G. Of Mice and Dogs: Species-Specific Differences in the Inflammatory Response Following Myocardial Infarction. *Am J Pathol* **2004**, *164*, 665-677, doi:10.1016/s0002-9440(10)63154-9.

108. Fu, X.; Khalil, H.; Kanisicak, O.; Boyer, J.G.; Vagnozzi, R.J.; Maliken, B.D.; Sargent, M.A.; Prasad, V.; Valiente-Alandi, I.; Blaxall, B.C.; et al. Specialized fibroblast differentiated states underlie scar formation in the infarcted mouse heart. *J Clin Invest* **2018**, *128*, 2127-2143, doi:10.1172/jci98215.

109. Humeres, C.; Frangogiannis, N.G. Fibroblasts in the Infarcted, Remodeling, and Failing Heart. *JACC: Basic Transl Sci* **2019**, *4*, 449-467, doi:10.1016/j.jacbts.2019.02.006.

110. Houser, S.R.; Margulies, K.B.; Murphy, A.M.; Spinale, F.G.; Francis, G.S.; Prabhu, S.D.; Rockman, H.A.; Kass, D.A.; Molkentin, J.D.; Sussman, M.A.; et al. Animal Models of Heart Failure. *Circ Res* **2012**, *111*, 131-150, doi:10.1161/res.0b013e3182582523.

111. Lindsey, M.L.; De Castro Brás, L.E.; Deleon-Pennell, K.Y.; Frangogiannis, N.G.; Halade, G.V.; O'Meara, C.C.; Spinale, F.G.; Kassiri, Z.; Kirk, J.A.; Kleinbongard, P.; et al. Reperfused vs. nonreperfused myocardial infarction: when to use which model. *Am J Physiol Heart Circ Physiol* **2021**, *321*, H208-H213, doi:10.1152/ajpheart.00234.2021.

112. Sala, L.; Hegyi, B.; Bartolucci, C.; Altomare, C.; Rocchetti, M.; Váczi, K.; Mostacciuolo, G.; Szentandrássy, N.; Severi, S.; Pál Nánási, P.; et al. Action potential contour contributes to species differences in repolarization response to β-adrenergic stimulation. *Europace* **2018**, *20*, 1543-1552, doi:10.1093/europace/eux236.

113. De Boer, T.P.; Stengl, M. Action potential contour and inter-species differences. *Europace* **2018**, *20*, 1395-1396, doi:10.1093/europace/eux308.

114. O'Hara, T.; Rudy, Y. Quantitative comparison of cardiac ventricular myocyte electrophysiology and response to drugs in human and nonhuman species. *Am J Physiol Heart Circ Physiol* **2012**, *302*, H1023-1030, doi:10.1152/ajpheart.00785.2011.

CHAPTER 2: Rationale and aims

The overall aim of this doctoral study was to gain insight into mechanisms underlying the triggers and substrate of ventricular arrhythmias in ischemic heart disease (IHD), that could form the basis for novel and translateable therapeutic strategies targetting the prevention or treatment ventricular arrhythmias in IHD.

We formulated five research questions. Three research questions were fundermental and sought insight into mechanisms of arrhythmias, and two were translational evaluating repolarization lability as a metric for arrhythmia prediction. These research questions formed the basis of the individual chapters of the thesis.

1. **Is myocyte remodelling in the peri-infarct border zone (BZ), the source of arrhythmia susceptibility after myocardial infarction (MI)?**

Identifying the region arrhythmia suseptibility after MI is key to further investigation and identification of appropriate therapeutic targets. Early experimental studies and clinical observations implicated the peri-infarce border zone (BZ) as the dominant site of arrhythmias. However, the mechanism of arrhythmia susceptibility in terms of triggers and substrate remain poorly characterized and described, thus limiting effective pharmacological development.

Utilising a well-established coronary-stenosis pig model of myocardial infarction (MI), in chapter 3 we study the regional source of arrhythmia triggers and substrate after MI, correlating *in vivo* observations of delayed after depolarizations (DADs) and repolarization lability, with cellular abnormalities of Ca^{2+} handling in the BZ. These results are presented in **chapter 3**.

2. **What are the unique spatial and cellular characteristics of the BZ contributing to *in vivo* arrhythmia initiation after MI?**

Ventricular arrythmias are frequently initiated by premature ventricular complexes (PVCs). Some clinical reports have suggested that these PVCs initiating lethal arrhythmias originate from the BZ. Moreover, arrhythmia-maintenance is dependent on critical sites where unique electrophysiological properties such as late potentials facilitate arrythmias. Whether PVCs localize to discrete sites has not been systematically evaluated, moreover, the mechanisms underlying PVCs after MI have not been determined.

Having identified the peri-infarct BZ as the source of arrhythmia susceptibility in, in chapter 4 we narrow in on this BZ to further describe arrhythmia properties with interest in spatial properties and intraregion vulnerability. Using electroanatomical mapping and advanced imaging *in vivo* combined with correlative cellular experiments we investigate the role of BZ myocyte adrenergic signalling in afterdepolarizations that trigger premature ventricular complexes (PVC) and may initiate arrhythmias. These results are presented in **chapter 4**.

3. **Is there heterogeneous myocyte remodelling in the BZ that contributes to the in vivo arrhythmia substrate?**

In the arrhythmia framework, the substrate for arrhythmia maintainance is the ying to the yang of the trigger/initiating event. It is well established that the substrate for arrhythmia maintenance after MI is reentry. Both fibrosis creating propagation obstacles and repolarization properties of myocytes are critical to the re-entrant mechanism. Heterogeneity of repolarization may underlie the functional arm and conduction block essential to the re-entry mechanism. Understanding of myocyte electrophysiological variability after MI is limited by the lack of large samples.

We develop a high-density mapping and analysis approach to assess *in* vivo local repolarization variability of the left ventricular regions after MI. In addition, we develop complementary high-throughput approachs to assess cellular electrophysiological and molecular expression profiles of large populations of myocytes *in vitro* to evaluate underlying myocyte heterogeneity in the BZ. These results are presented in **chapter 5**.

4. **Is beat-to-beat variability of repolarization (BVR) increased during acute myocardial ischemia (AMI) and does it predict imminent arrhythmia?**

Arrhythmia risk assessment is a cornerstone of sudden cardiac death (SCD) prevention including the prophylactic implantation of implantable cardioverter defibrillators (ICDs). Currently, left ventricular ejection fraction (LVEF) remains the key stratifier for high-risk patients after MI. However, it is a poor predictor of arrhythmia occurrence that would be essential to arrhythmia deterrent rather than treatment. As such, monitorable metrices such as electrocardiogram repolarization are sought for impending arrhythmia prediction.

In the experimental setting, we investigate whether we can improve on arrhythmia prediction in a preclinical model. IHD is the strongest underlying clinical factor in SCD (present in ~80% of cases), and SCD frequently complicates acute myocardial ischemia (AMI). BVR is a metric of repolarization lability and is also observed before arrhythmia initiation during pharmacological provocation in animal studies. However, whether it can predict arrhythmias in the clinically relevant context of acute ischemia has not been demonstrated. In **chapter 6**, we therefore investigate changes in BVR preceding ventricular fibrillation during AMI in the pig model.

5. **Can the assessment of changes in beat-to-beat variability of repolarization (BVR) predict imminent ventricular arrhythmia in high-risk patients?**

We also investigate the potential for clinical application as BVR has shown excellent results in predicting arrhythmias in animal models. However, the predictive value of BVR in identifying imminent arrhythmias has not been evaluated in the clinical setting. We use 24h Holter recordings from high-risk patients with dilated or ischemic cardiomyopathy that received an ICD for the prevention of SCD to test the hypothesis that BVR increases prior to the occurrence of non-sustained arrhythmias. This study is presented in **chapter 7**.

CHAPTER 3: The peri-infarct region – A source of arrhythmia susceptibility

Published as:

Eef Dries*, Matthew Amoni*, Bert Vandenberk, Daniel M Johnson, Guillaume Gilbert, Chandan K Nagaraju, Rosa Doñate Puertas, Mouna Abdesselem, Demetrio J Santiago, H Llewelyn Roderick, Piet Claus, Rik Willems, Karin R Sipido. “Altered adrenergic response in myocytes bordering a chronic myocardial infarction underlies in vivo triggered activity and repolarization instability,” J. Physiol., vol. 598, no. 14, pp. 2875–2895, 2020, doi: 10.1113/JP278839. (* Shared first authorship)

Abstract

Ventricular arrhythmias are a major complication early after myocardial infarction (MI). The heterogeneous peri-infarct zone forms a substrate for re-entry while arrhythmia initiation is often associated with sympathetic activation. We studied the mechanisms triggering these post-MI arrhythmias *in vivo* and their relation to regional myocyte remodelling.

In pigs with chronic MI (6 weeks), *in vivo* monophasic action potentials were simultaneously recorded in the peri-infarct and remote regions during adrenergic stimulation with isoproterenol (ISO). Sham animals served as controls. During infusion of ISO *in vivo*, the incidence of delayed afterdepolarizations (DADs) and beat-to-beat variability of repolarization (BVR) was higher in the peri-infarct than in the remote region. Myocytes isolated from the peri-infarct region, in comparison to myocytes from the remote region, had more DADs, associated with spontaneous Ca^{2+} release, and a higher incidence of spontaneous action potentials when exposed to ISO (10.0±4.2 *vs.* 0.5±0.3 APs/min, p=0.027); these were suppressed by CaMKII inhibition. Peri-infarct myocytes also had reduced repolarization reserve and increased BVR (26±10ms *vs.* 9±7ms, p<0.001), correlating with DAD activity. In contrast to these regional distinctions under ISO, alterations in Ca^{2+} handling at baseline and myocyte hypertrophy were present throughout the LV. Expression of some of the related genes was however different between the regions.

In conclusion, altered myocyte adrenergic responses in the peri-infarct, but not in the remote region, provide a source of triggered activity *in vivo* and of repolarization instability amplifying the substrate for re-entry. These findings stimulate further exploration of region-specific therapies targeting myocytes and autonomic modulation.

Key points

- Ventricular arrhythmias are a major complication after myocardial infarction (MI), associated with sympathetic activation. The structurally heterogeneous peri-infarct zone is a known substrate but the functional role of the myocytes is less well known.
- Using monophasic action potentials in vivo one can observe that the peri-infarct zone is a source of delayed afterdepolarizations (DADs) and has a high beat-to-beat variability of repolarization (BVR) during adrenergic stimulation (isoproterenol, ISO).
- Myocytes isolated from the peri-infarct region have more DADs and spontaneous action potentials, with spontaneous Ca^{2+} release, under ISO. These myocytes also have reduced repolarization reserve and increased BVR. Other properties of post-MI remodelling are present in both peri-infarct and remote myocytes.
- These data highlight the importance of altered myocyte adrenergic responses in the peri-infarct region as source and substrate of post-MI arrhythmias.

Introduction

Sudden cardiac death, attributable to ventricular arrhythmia (ventricular fibrillation and tachycardia), is a leading cause of death worldwide, and a common complication after myocardial infarction (MI) (Hayashi et al. 2015). The infarct and adjacent border zone, consisting of strands of surviving myocytes interspersed with fibrous tissue, create a structural substrate for re-entry circuits, that are central to post-MI arrhythmias (De Bakker et al. 1993; Ashikaga et al. 2007).

In addition to the structural substrate of the peri-infarct region, inhomogeneity of repolarization in the surviving myocardium could facilitate re-entry (Ciaccio et al. 2018). Experimental studies in small animal models have identified action potential (AP) changes and reduced repolarization reserve in myocytes isolated from the non-infarcted tissue of the left ventricle (LV) (Wong et al. 1982; Aimond et al. 1999). In mouse models, information regarding differential remodelling in different regions is scarce, though a recent study identified specific transcriptional profiles (van Duijvenboden et al. 2019). Data from large animal models support a role for abnormal myocyte repolarization in the peri-infarct region contributing to the functional re-entry substrate (Lue & Boyden, 1992; Baba et al. 2005; Sasano et al. 2006; Hegyi et al. 2018). However, direct evidence, in particular in vivo, for a distinct arrhythmogenic repolarization profile in this region, different from the overall post-MI remodelling in the first weeks after MI, is limited.

In clinical practice, the vulnerable substrate is identified through programmed stimulation using premature stimuli as the simulated arrhythmia triggers. With this approach, the MI border zone is often found to be the culprit site and is a common target for ablation post-MI to prevent lethal arrhythmias (Verma et al. 2005; Ashikaga et al. 2007; Cronin et al. 2019). More recently, computational modelling using structural information and simulated triggers could reproduce in vivo studies and identify the vulnerable substrate for ablation (Prakosa et al. 2018).

Compared to the body of knowledge on the substrate for re-entry, much less is known about the cellular mechanisms triggering in vivo post-MI arrhythmias. Premature ventricular complexes (PVC) are most commonly the initiating event, as observed in recordings from intracardiac devices and monitoring studies (Saeed et al. 2000; Lerma et al. 2013). In vivo studies have localized PVCs to the border zone (Marrouche et al. 2004), and or correlated their site of origin to the critical exit site of the re-entry circuit, marking these sites for ablation (Bogun et al. 2008). A number of studies using isolated tissues have implicated spontaneous depolarizations and automaticity from Purkinje fibres with abnormal potentials (Xing & Martins, 2004; Bogun et al. 2006; Hirose et al. 2008). Using isolated myocytes, other studies have implicated triggered activity due to delayed afterdepolarizations (DADs) and Ca^{2+} handling abnormalities in the border zone (Baba et al. 2005; Belevych et al. 2012; Hegyi et al. 2018). However, the contribution of such DADs to triggered activity in vivo is poorly documented as it requires sophisticated experimentation using monophasic action potential recordings (Priori et al. 1988; De Groot et al. 1995). In addition, there is paucity of evidence of correlation between myocyte spontaneous activity and the in vivo situation after MI.

In vivo, sympathetic imbalance and increased adrenergic drive are thought to underlie the PVCs that initiate post-MI arrhythmias, and adrenergic stimulation increases PVC incidence after MI (Rivas et al. 2009). After MI, cardiac innervation undergoes extensive remodelling with denervation in the scar and partial denervation and nerve re-growth or sprouting in the peri-infarct region (Cao et al. 2000; Rajendran et al. 2016). Restoring sympathetic innervation

reduced post-MI arrhythmias in a recent experimental study (Gardner et al. 2015). Sympathetic nerve stimulation or hyperinnervation increases dispersion of repolarization resulting in arrhythmias and sudden death (Cao et al. 2000; Ajijola et al. 2017). We have previously shown that myocytes isolated from the area adjacent to MI have Ca^{2+}-driven DADs during adrenergic stimulation (Dries et al. 2018).

Therefore, it can be hypothesized that adrenergic stimulation leads to triggering of arrhythmias in vivo and, through increasing repolarization instability, contributes to the functional substrate after MI (Liu et al. 2015). This could remain confined to the peri-infarct region where chronic changes in local innervation may contribute to differential myocyte remodelling (Habecker et al. 2016; Pianca et al. 2019). In the present study, we have set out to investigate the above hypotheses. We study mechanisms underlying arrhythmia after MI, using adrenergic stimulation as the initiating event rather than programmed stimulation. We focus on triggers for arrhythmias and the potential for a dynamic interplay between triggers and functional substrate. Using monophasic action potential recordings, we first explore in vivo the regional sources of afterdepolarizations and repolarization instability and subsequently correlate these findings with intrinsic myocyte remodelling in different regions by studying the properties of isolated myocytes. Rather than noradrenaline, we use isoproterenol both for myocytes and in vivo experiments, to exclude α-receptor-mediated vascular effects with secondary confounding reflex activity.

Methods

Ethical approval

The animal experimental protocols used in this study were approved by the in-house ethical committee (Ethische Commissie Dierproeven, KU Leuven), with permit numbers P10139, P14176 and P16110. Animals were housed and treated according to the Guide for the Care and Use of Laboratory Animals (National Institute of Health, USA), and the European Directive 2010/63/EU; and complies with The Journal of Physiology ethical checklist (Grundy, 2015). A standard 14 h light, 10 h dark cycle, 22 ± 2°C temperature and 45–70% humidity was maintained. Standard chow (Optivo Pro 9041, AVEVE, Belgium) and water were provided ad libitum except in the days prior to and after experimental procedures when animals were either fasted or fed twice a day with welfare monitoring. All interventions were performed under full anaesthesia.

Pig model of chronic myocardial infarction

The pig model of MI was as previously described (Galan et al. 2016). In this model, a copper-coated stent is implanted during a percutaneous procedure. This leads to intima proliferation, severe stenosis and MI within 1 week. Twenty-seven young-adult domestic pigs (Sus scrofa domesticus, breed: Piétrain) of both sexes (20–25 kg) were included in the study, after a 6-week protocol. Animals were randomized to either MI (N = 14) or Sham (N = 13) groups before the stent implantation procedure on day 0.

Before coronary catherization and stent implantation, animals received amiodarone (300 mg; 3 days loading before intervention), aspirin (100 mg) and clopidogrel (300 mg; 1 day before intervention), to protect against arrhythmias and thromboembolisms during the percutaneous intracoronary intervention. Anaesthesia was induced by intramuscular injection of tiletamine/zolazepam (4 mg kg−1) together with xylazine (2.5 mg kg−1). Intravenous infusion of propofol (10 mg kg−1 h−1) and remifentanil (0.018–0.03 µg−1 kg h−1) was used for maintenance of the anaesthesia. After oral tracheal intubation, animals were mechanically ventilated with 1:1 oxygen/air. During the intervention, animals received an intravenous bolus of heparin (10000 IU) to prevent thromboembolism and were continuously monitored for heart rate and rhythm using 6-lead electrocardiogram (ECG).

For coronary catheterization and stent implantation, the right carotid artery was dissected and cannulated with an 8 Fr introducer sheath. An 8 Fr Judkins-left coronary guiding catheter was positioned in the left main coronary ostium under fluoroscopic guidance. Using a 2.5–2.75 mm angioplasty balloon, the copper-coated stent was implanted in the left anterior descending coronary artery immediately after the first diagonal branch. Sham animals underwent the same surgical procedure, without stent implantation.

After the intervention, additional analgesia and antibiotics to prevent wound infection were administered intramuscularly using buprenorphine (0.01–0.05 mg kg−1) as necessary and enrofloxacin (2.5 mg kg−1). Furthermore, antiplatelet medication and analgesia were orally administered on a daily basis for 6 weeks (clopidogrel (75 mg) and aspirin (100 mg) daily). Animals were monitored daily for general activity and behaviour, food intake and possible wound infections.

As this model of MI has been previously characterized (Galan et al. 2016), here subsets of MI (11 out of 14) and Sham (9 out of 13) animals were used to demonstrate consistency with the established model in a structural and functional assessment using magnetic resonance imaging (MRI) 6 weeks after stent implantation (3 tesla, Magnetom PRISMA; Siemens, Erlangen, Germany). Before and during MRI, anaesthesia was induced and maintained, and animals were mechanically ventilated as described above. During imaging, heart rate and rhythm were continuously monitored using 3-lead ECG. Images were acquired using a phased-array body coil wrapped over the thorax to increase signal to noise ratio, with ECG gating. Respiration of the animal was manually stopped to reduce motion artefacts during imaging. Mechanical ventilation was again continued as soon as the collection of images was completed. All images were analysed with custom software (RightVol; KU Leuven). Infarct size was determined by late gadolinium enhancement, 12 min following a bolus of Gd (gadoterate meglumine, 0.2 mmol kg−1). Table 1 summarizes the findings, confirming a mean infarct size of 10% of LV mass, with dilatation of the LV and reduced ejection fraction.

Thereafter, in the same sixth week, an in vivo electrophysiology study was performed.

Table 1. Left ventricular function and remodeling after MI

	MI (N_{pigs} = 11)	Sham (N_{pigs} = 9)	p-value
Infarct size (%)	9.5±3.53	0	<0.0001
End-diastolic volume (mL)	172±31.49	132±24.99	0.0059
End-systolic volume (mL)	101±22.87	54±11.01	<0.0001
Ejection fraction (%)	41.5±5.31	58.7±3.34	<0.0001
Left ventricular mass (g)	107±21.96	114±21.3	0.459
Left ventricular systolic pressure (mmHg)	114±25.04	110±15.29	0.636

In vivo electrophysiology study and MAP recordings

Prior to in vivo electrophysiological studies, anaesthesia was induced using intramuscular injection of tiletamine/zolazepam (4–8 mg kg−1) only, to prevent anti-arrhythmic effects induced by xylazine (Gonca, 2015). Maintenance of anaesthesia and mechanical ventilation were performed as described above. The right and left carotid arteries, femoral artery and the femoral or jugular vein were cannulated. A bolus of heparin (5 000–10 000 IU) was periodically administered for anticoagulation. Under fluoroscopic guidance, monophasic action potential (MAP) catheters (MedFact GmbH, Germany) were inserted into the LV and positioned in the peri-infarct and non-infarcted remote region, guided by fluoroscopy and coronary angiography and the absence of a MAP signal in the infarct area (Fig. 1A). A 7 Fr diagnostic electrophysiology catheter (Biosense Webster, Belgium) was positioned in the right atrium for pacing. Continuous 12-lead ECG and simultaneous MAPs in both peri-infarct and remote regions were recorded at 4 kHz using a Labsystem Pro EP recording system (Boston Scientific, USA). To eliminate effects of heart rate variations, animals were atrially paced at 120 beats min−1, and recordings were performed at baseline pacing and during pacing with infusion with isoproterenol (ISO; 1–2 µg min−1; Isuprel). This dose was chosen based on its use clinically to facilitate arrhythmia testing (Heidbüchel et al. 2003) and to provoke afterdepolarizations in at-risk patients (Shimizu et al. 1991). Following the experiments, animals received the same care as described above.

At baseline, the following acceptance criteria for MAP recordings was applied: amplitude of at least 10 mV, with an identifiable plateau, and a stable baseline (Franz, 1999). DADs were defined as an increase in baseline potential exceeding 1 mV in amplitude. DAD incidence and amplitude were analysed; DAD amplitude was normalized to the amplitude of the precedent AP. Beat-to-beat variability of repolarization (BVR), a marker of repolarization instability, was calculated as short-term variability of 90% of MAP duration (MAPD90) from 30 consecutive APs by: $\Sigma(|QT_{n+1} - QT_n|) / [nbeats \times \sqrt{2}]$ (Thomsen et al. 2004);

Only paced beats were taken into account. During a 5-min period after stabilization and ISO infusion, ventricular extrasystoles or arrhythmias were quantified and reported as events per minute. Arrhythmic events were also translated into a score, accumulating all events over the 5-min recording.

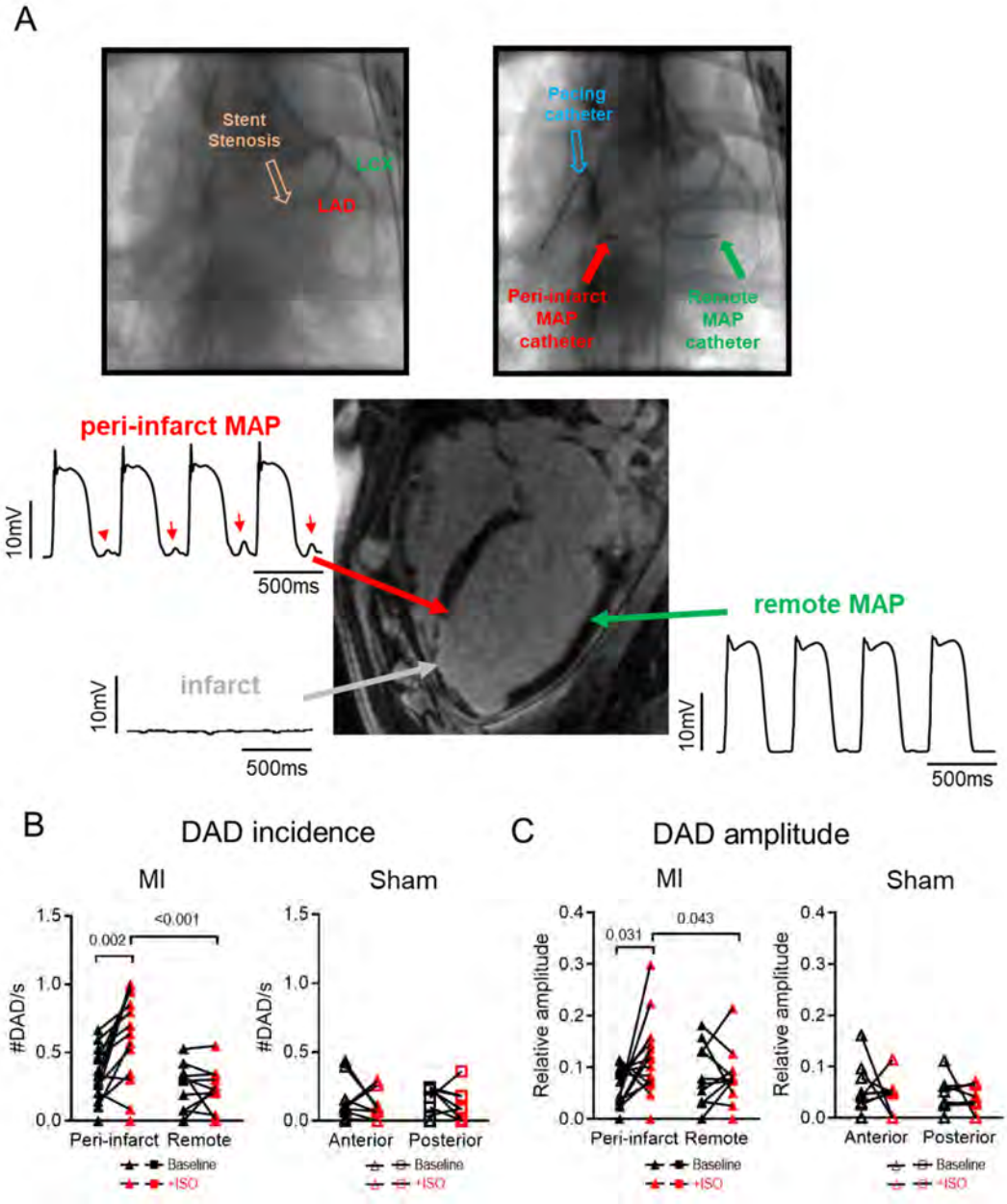

Figure 1. *In vivo* adrenergic stimulation induces more and higher amplitude delayed afterdepolarizations (DADs) in the peri-infarct region (A) Example of data acquisition in an MI pig with regional catheter positioning guided by coronary angiography and absence of monophasic action potential (MAP) in the infarct. Top left: coronary angiography with stenosis indicated by a green arrow (LAD = left anterior descending coronary artery, LCX = left circumflex coronary artery). Top right: Overlay of the coronary angiography and positioning of the MAP catheters in the peri-infarct and remote regions, and pacing catheter in the right atrium. Bottom: Pre-procedural MRI illustrating the infarct, peri-infarct and remote regions with corresponding examples of *in vivo* regional MAP recordings during ISO infusion (red arrows illustrate DADs in the peri-infarct region). (B) Mean data for DAD incidence and (C) amplitude in MI (N_{pigs} = 14) and Sham (N_{pigs} = 10) animals. (Repeated measures 2-way Anova with Bonferroni post-hoc testing).

Cell isolation

After 3–5 days recovery from the in vivo studies, animals were euthanized. Anaesthesia was induced as described above and maintained using intravenous administration of pentobarbital (2.5 mg kg−1), while mechanically ventilating the animals. Thereafter, the thorax was quickly opened, an overdose of pentobarbital (20 mg kg−1) was given and the heart was taken out. Biopsies were taken for molecular studies and hearts processed for cellular studies. Single cardiomyocytes from the LV were enzymatically isolated from the peri-infarct region and non-infarcted remote region in MI pigs, and from matching regions in Sham pigs (Nagaraju et al. 2017). The coronary artery perfusing these regions was cannulated and a wedge of tissue excised and enzymatically digested on a constant flow perfusion system at 37°C. The digested tissue was minced and filtered, and the isolated myocytes resuspended in HEPES-buffered Tyrode solution (in mmol l−1: NaCl 137, KCl 5.4, MgCl2 0.5, CaCl2 1.8, Na-HEPES 11.8, and glucose 10; pH 7.4). After isolation, the cells were allowed to recover for 1 h before experiments were commenced.

Cell structure measurements

Cell size (length and width) was measured in randomly selected cells from both regions of Sham and MI. Sarcolemma, transverse and axial tubular structures (TATS) were stained by incubating cells with Alexa Fluor 594 conjugated to wheat germ agglutinin (WGA, 10 µg ml−1; ThermoFischer, W11262). Images were collected in a Z-stack using a 40× objective, 1.3 NA oil immersion, on a Zeiss LSM 510 confocal microscope and quantified using Image J software (NIH, USA, v1.5, RRID: SCR_003070). TATS signals within the cell margins were identified against the background by thresholding. The sarcolemmal membrane was subtracted from thresholded images. Thresholded images were further processed to skeletonize TATS signals. TATS density was quantified as the number of signal-positive pixels over all pixels within the cell margins.

Cellular electrophysiological and calcium recordings

Cells were studied in whole-cell patch clamp mode, using either voltage- or current-clamp configuration (Axon 200B amplifier, Axon Instruments). Cells were constantly superfused with HEPES-buffered Tyrode solution at 37°C and patch pipettes (2–3 MΩ) (GB 200-8P, Science Products) were filled with (in mmol l−1): potassium aspartate 120, NaCl 10, KCl 20, K-HEPES 10, MgATP 5, and K5Fluo-4 0.05; pH 7.2. In voltage-clamp mode, cells were stimulated for 2 min using 200 ms depolarizing steps from −70 mV to +10 mV at 2 Hz stimulation frequency and with recording for 15 s at −70 mV after stopping stimulation. In current-clamp mode, cells were stimulated with a suprathreshold depolarizing pulse of 2–5 nA, at 2 Hz and 1 Hz for 3–5 min in steady states. In both modes, Ca^{2+} was simultaneously recorded. Ca^{2+} transients were recorded on a photometry epifluorescence set-up, with $[Ca^{2+}]i$ reported as the fluorescence normalized to baseline values, after background subtraction as F/F 0. In other experiments, local Ca^{2+} events (Ca^{2+} waves, Ca^{2+} sparks) and Ca^{2+} transients (used for kinetic measurements) were recorded using confocal line-scanning along the long axis of the cell in a central plane and avoiding the nucleus (Zeiss LSM 510, 40× oil immersion objective; scanning at 650 Hz with a pixel size of 0.2–0.3 µm). Ca^{2+} waves were recorded as previously described and quantified using a custom-made analysis program (Dries et al. 2018). Ca^{2+} wave incidence was normalized to cell length

and time as number of waves 100 µm−1 s−1. We defined coupled (dyadic) and non-coupled (non-dyadic) release sites as previously described (Dries et al. 2018). SR Ca^{2+} content was measured by integrating the inward NCX current (I NCX) during rapid caffeine superfusion (10 mmol l−1 for 8 s) after a conditioning train of 2 Hz stimulation. AP duration was calculated at APD90 and BVR was calculated as described above. All protocols were performed at baseline and presence of 10 nm ISO, a low concentration chosen to detect increased sensitivity.

Quantitative real time PCR experiments

After harvesting the heart, peri-infarct and remote tissue samples from MI and matched anterior and posterior regions in Sham were snap-frozen in liquid nitrogen and immediately stored at −80°C. Total RNA was extracted from all frozen biopsies with an miRNeasy mini kit according to the manufacturer's instructions (Qiagen, Hilden, Germany). A 500 ng sample of total RNA was used for cDNA synthesis with SuperScript II Reverse Transcriptase (Thermo Fisher Scientific, Carlsbad, USA). The final cDNA concentration was 1.25 ng µl−1.

mRNA levels of genes encoding calcium handling proteins, ion channels and adrenergic signalling components were measured by real-time qRT-PCR using gene specific primers (Table 2) and GoTaq qPCR Master Mix (Promega, Madison, USA). Amplification was performed using a CFX384 Real-Time PCR Detection System. Results are presented as relative mRNA abundance, with each sample normalized to the geometric mean of RPL32 and TBP, which were used as reference genes. The stability of these reference genes was first established using geNORM (Vandesompele et al. 2002).

Table 2. PCR Primers

Gene product	Gene name	Forward primers (5'-3')	Reverse primers (5'-3')
Inward rectifier potassium channel	KCNJ2	CCGCTACAGCATTGTCTCTT	TGGACCTTACTCTTCCCGTT
Delayed rectifier (rapid) potassium channel	KCNH2	TGGGCTTTGGCAATGTCTC	AAGATGCTGGCGTACATGAG
Delayed rectifier (slow) potassium channel	KCNQ1	CTGGAAGTGCTTCGTCTACC	GCGACATACTGCTCAATGGT
Natriuretic peptide A	NPPA	CTTCGGGGGTAGGATGGACA	TCTTCAGTACCGGAAGCTGTTA
Beta-1 Adrenergic receptor	β_1AR	CCAACCTCTTCATCATGTCC	GCAGAAGAAGGAGCCGTACT
Beta-2 Adrenergic receptor	β_2AR	CCAGACGGTCACCAACTACT	CCGAAAGTCCACATTTTCAT
G Protein-Coupled Receptor Kinase 2	GRK2	ATGCAGAAGTACCTGGAGGA	ACAGAAGTCTCGGAAAAGCA

Western blot for protein expression

Snap frozen samples of regional myocardial tissue were homogenized in a buffer containing (in mM): imidazole 10, sucrose 300, dithiotreitol 1, sodium metabisulfite 1, sodium fluoride 25, sodium ethylene diaminetetraacetic acid (EDTA) 5, sodium pyrophosphate 5, phenylmethylsulfonyl fluoride 0.3, and a protease inhibitor cocktail ('Complete-Mini' Roche Molecular Biochemicals). Equal amounts of proteins were then separated on a 4–12% Bis-Tri gradient gel (Invitrogen) and transferred onto polyvinylidene difluoride membrane (Millipore). The membrane was blocked with Odyssey TBS blocking buffer. Blocked membranes were then incubated with antibodies for CaMKII (1:1000 dilution, SC-5392, Santa Cruz) and GAPDH (1:10,000 dilution, G8795, Sigma) overnight at 4°C. Detection was performed using IRDye secondary antibodies (1/15,000 dilution, LI-COR) and blots were scanned using an infrared imaging system (Odyssey CLx, LI-COR); in Fig. 10 the full-length blots are shown. Band intensity was quantitated using Image Studio software. The membrane was stripped with antibody stripping solution (2504, Millipore) and re-probed with the Phospho-CaM Kinase II pThr286 antibody (PA1-14076, Invitrogen). The detection was performed again using IRDye secondary antibody. The band intensity was analysed using Image Studio software.

Experimental design and statistics

Data acquisition was performed by multiple investigators. Investigators were blinded when doing analysis off-line by creating coded data files. For quality control and to check on consistency, sets of experiments were analysed by two independent and blinded investigators.

All individual data points are shown in dot plots, with each dot representing the data of an animal. In the case of cellular studies with multiple cells per animal, the dot plot is the mean value for this animal. Statistically, data were compared using a nested design taking into account the number of cells (n) and animals (N), with Student's t test or a two-way ANOVA with Bonferroni post hoc testing; repeated measures was used when the same samples were measured before and after ISO treatment. A chi-squared test was used to compare proportions. In one data set we examined correlations using regression analysis, linear fitting and two-tailed t test. Data were considered significantly different when the P value was < 0.05, while the exact values have been inserted in the graphs. Additional information on statistical testing may be found online in the Statistical Summary Document.

Results

Increased incidence and amplitude of DADs in the peri-infarct region in vivo

Figure 1A illustrates MAPs simultaneously recorded in the MI peri-infarct and remote region during atrial pacing at 2 Hz. At baseline, there was no difference in DAD incidence or amplitude between regions in either Sham or MI. However, during ISO infusion, there was both an increased incidence and amplitude of DADs in the MI peri-infarct region compared to baseline and to the MI remote region (Fig. 1B and C). Infusion of ISO did not alter the DAD incidence or amplitude in the corresponding regions in Sham animals.

BVR is larger in the peri-infarct than remote region in vivo

We also examined repolarization properties that could facilitate arrhythmia by analysing AP duration and BVR (Fig. 2A). During 2 Hz atrial pacing, the mean MAP duration (MAPD) was not different between the MI peri-infarct and remote regions and was also not different compared to matched Sham regions at baseline and during ISO (data not shown). There were no apparent regional differences in BVR of MAPD in either MI or Sham animals at baseline. During ISO infusion, BVR increased significantly in both the peri-infarct and remote regions but eventual BVR was significantly larger in the peri-infarct region than in the remote region (Fig. 2B).

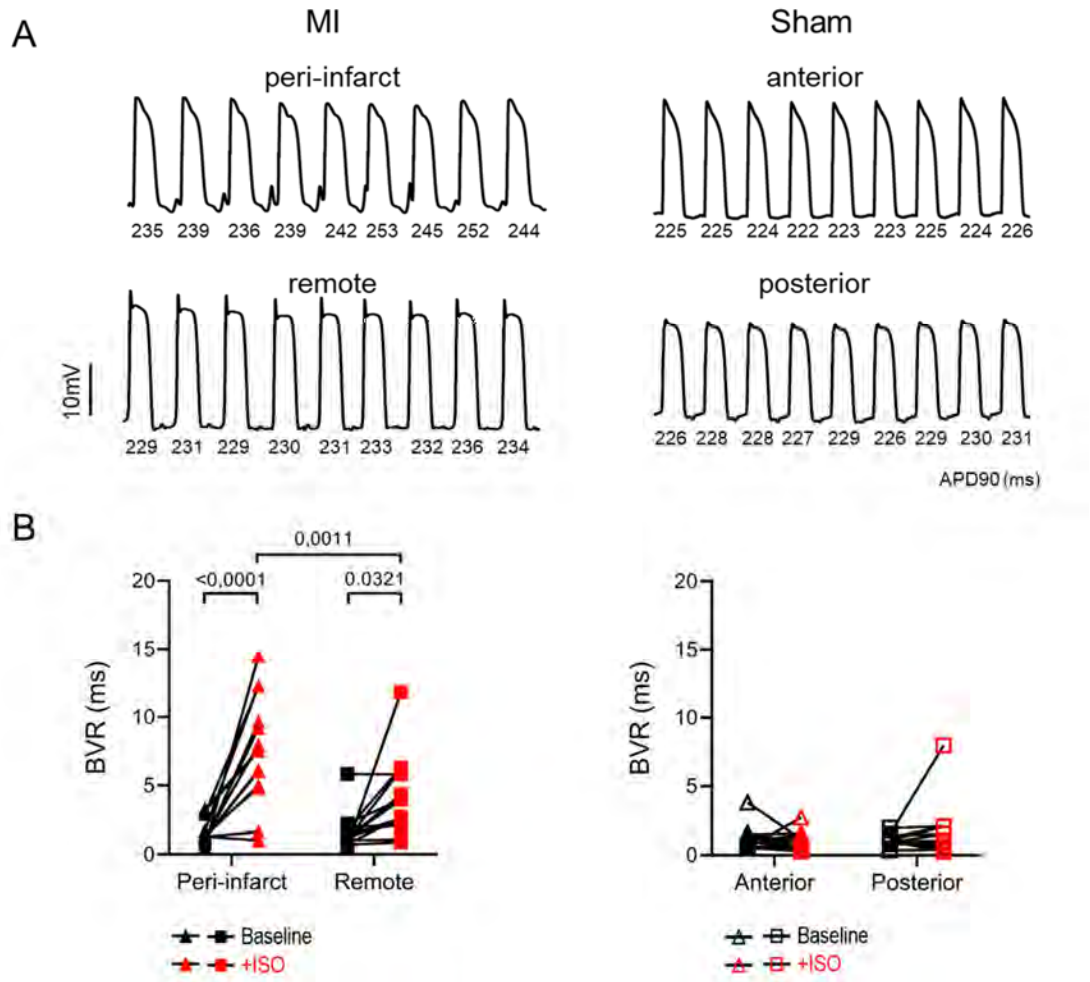

Figure 2. Adrenergic stimulation induces higher beat-to-beat variability of repolarization (BVR) in the peri-infarct region *in vivo*. (A) Examples of BVR during ISO infusion *in vivo*: MAP recordings in MI peri-infarct and remote, as well as matched Sham anterior and posterior regions. (B) Mean data for regional BVR in MI (N_{pigs} = 14) and Sham (N_{pigs} = 13) animals. (Repeated measures 2-way Anova with Bonferroni post-hoc testing).

More PVCs and complex extrasystoles during ISO in vivo

The peri-infarct increase in DADs and BVR during ISO resulted in a higher arrhythmia potential in MI pigs, as recorded in the ECG. Occasionally a local peri-infarct DAD appeared to precede a PVC on the ECG (Fig. 3A), though a causal relation could not be ascertained. MI pigs had a

higher incidence of PVCs per minute compared to Sham animals (Fig. 3B). Additionally, more couplets (two consecutive beats; p = 0.095), triplet PVCs (three consecutive beats; p = 0.014) and non-sustained ventricular tachycardia (VT) (p = 0.028) were observed in MI pigs during ISO, compared to Sham animals, translating into a higher arrhythmia score after MI (Fig. 3C).

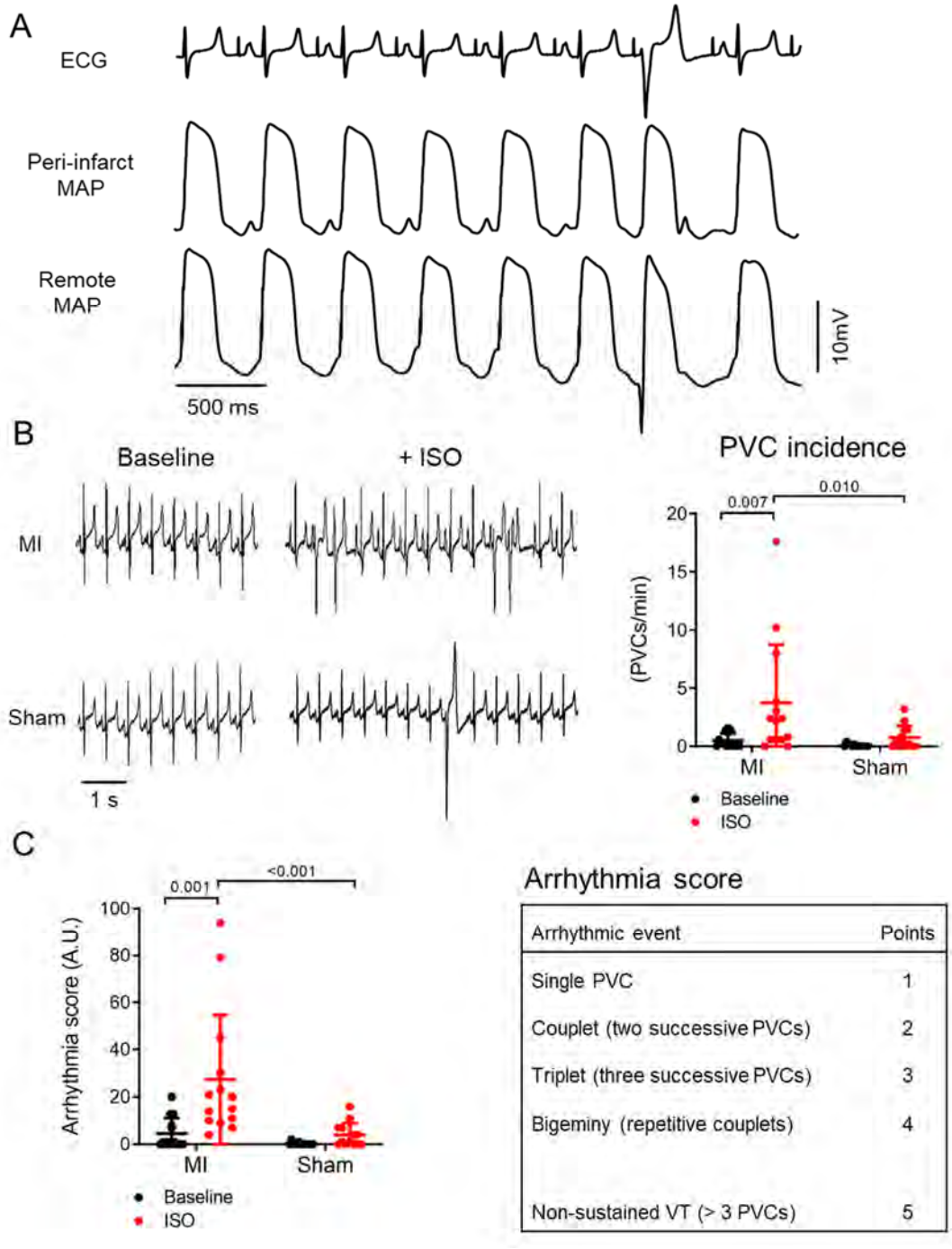

Arrhythmia score

Arrhythmic event	Points
Single PVC	1
Couplet (two successive PVCs)	2
Triplet (three successive PVCs)	3
Bigeminy (repetitive couplets)	4
Non-sustained VT (> 3 PVCs)	5

Figure 3. PVCs and arrhythmias in MI pigs during ISO infusion (A) Example of DADs in the peri-infarct region with a PVC on ECG. (B) Examples of ECG in MI and Sham pigs before and after infusion of ISO with mean data for PVC incidence. (C) Arrhythmia scoring using criteria of the inset. Data from MI (N_{pigs} = 14) and Sham (N_{pigs} = 13) animals before and after ISO infusion. DAD - delayed afterdepolarization; PVC - premature ventricular complex. (Repeated measures 2-way Anova with Bonferroni post-hoc testing).

Cellular hypertrophy and altered Ca^{2+} handling in peri-infarct and remote myocytes

We postulated that the regional arrhythmic potential in the peri-infarct region was related to a more pronounced cellular remodelling. To investigate this possibility, we isolated and compared the phenotypes and physiology of cardiomyocytes from the different study regions (Fig. 4A). In both MI peri-infarct and remote myocytes, cell width and length were significantly increased and density of the transverse and axial tubular structures (TATS) was reduced compared to Sham myocytes (Fig. 4B). Baseline Ca^{2+} transients from both MI peri-infarct and remote myocytes were reduced in amplitude and rate of upstroke compared to Sham myocytes (Fig. 4C), without differences in the SR Ca^{2+} content (data not shown). Concurrent with reduced TATS density, the distribution of the time to half-maximal Ca^{2+} release was shifted to the right, with more delayed sites in MI myocytes (Fig. 5A). Sites defined as non-coupled were more numerous in MI (Fig. 5B).

These data indicate that after MI, structural and functional myocyte remodelling occurs throughout the whole LV.

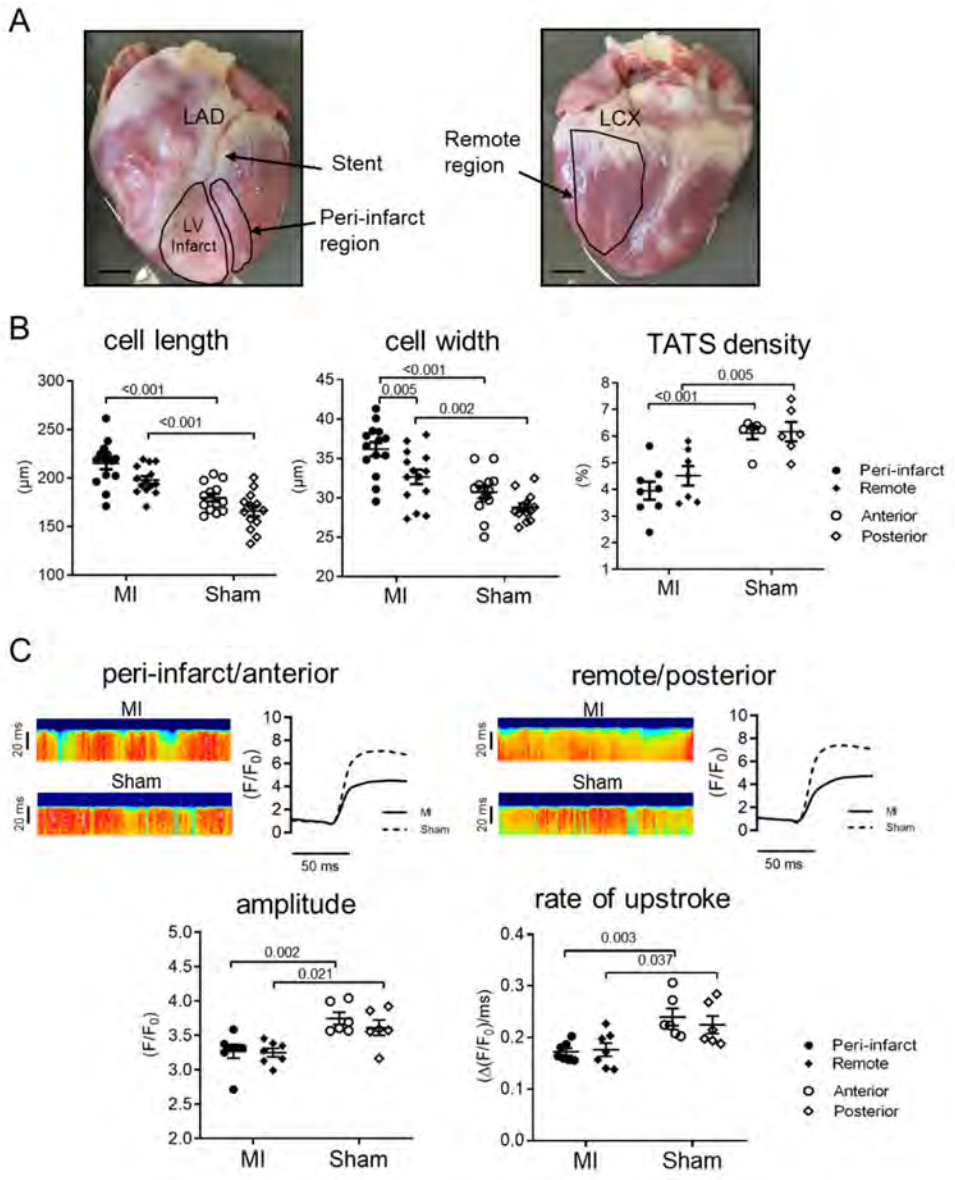

Figure 4. Regional myocyte remodeling and Ca^{2+} handling after MI

(A) Photograph of an infarcted heart showing the peri-infarct and remote regions used for cell isolation, scale bar – 1cm (LV = Left ventricle, LAD = left anterior descending coronary artery, LCX = left circumflex coronary artery). (B) Mean data for cell size (MI: n_{cells} = 178-192; N_{pigs} = 14 and Sham: n_{cells}= 164-218; N_{pigs} = 13) and TATS density (MI: n_{cells} = 24-27; N_{pigs} = 6 and Sham: n_{cells} = 18-21; N_{pigs} = 4) in different regions of MI and Sham myocytes. (C) Top: Example of confocal line scan recording of Ca^{2+} transient and corresponding plots in different regions for MI and Sham myocytes. Bottom: Mean data for Ca^{2+} transient amplitude and rate of upstroke in different regions for MI (n_{cells} = 24-27; N_{pigs} = 7) and Sham (n_{cells} = 17-18; N_{pigs} = 6) myocytes. (2-way Anova with Bonferroni post-hoc testing).

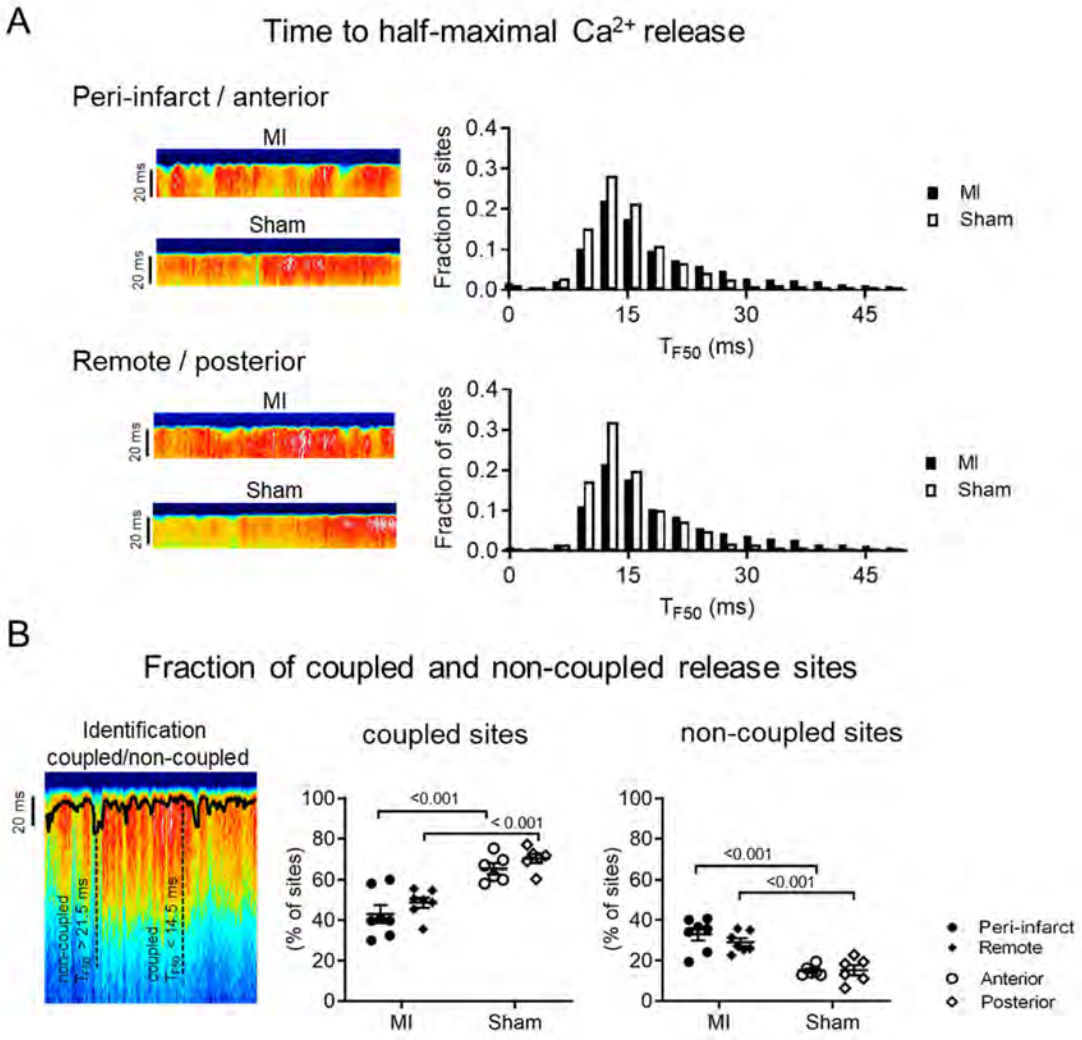

Figure 5. Delayed Ca^{2+} release in myocytes from both peri-infarct and remote regions. (A) Examples of confocal line scan images and distribution plots of the time to half-maximal Ca^{2+} release of the Ca^{2+} transient (TF50) of Ca^{2+} release along line scans in MI (n_{cells} = 26-27; N_{pigs} = 7) and Sham (n_{cells} = 17-18; N_{pigs} = 6) myocytes from peri-infarct/anterior and remote/posterior regions. (B) Left: Example of a confocal line scan image with the use of cut-off criteria for time to half-maximal Ca^{2+} release of the Ca^{2+} transient (TF50) to identify coupled and non-coupled Ca^{2+} release sites. Right: Mean data of coupled and non-coupled sites in MI (n_{cells} = 26-27; N_{pigs} = 7) and Sham (n_{cells} = 17-18; N_{pigs} = 6) myocytes in different regions of the heart. (2-way Anova with Bonferroni post-hoc testing).

Higher prevalence of Ca^{2+} waves, DADs and spontaneous APs in peri-infarct myocytes in the presence of ISO

To relate myocyte function to the in vivo observations, we assessed the arrhythmic potential of cells under ISO. To this end, we applied a conditioning train of square depolarizing pulses at 2 Hz and subsequently measured spontaneous Ca^{2+} releases and corresponding membrane

currents. Spontaneous releases were seen in all groups, but MI peri-infarct myocytes had a significantly higher frequency of Ca^{2+} waves and depolarizing currents compared to MI remote and Sham myocytes (Fig. 6A). This translated into more DADs as well as spontaneous APs in current clamp mode (Fig. 6B).

Inhibition of CaMKII signalling using autocamtide-2 related inhibitory peptide (AIP, 10 µm), a highly specific CaMKII inhibitor, was able to lower the incidence of DADs in MI peri-infarct myocytes (Fig. 6C).

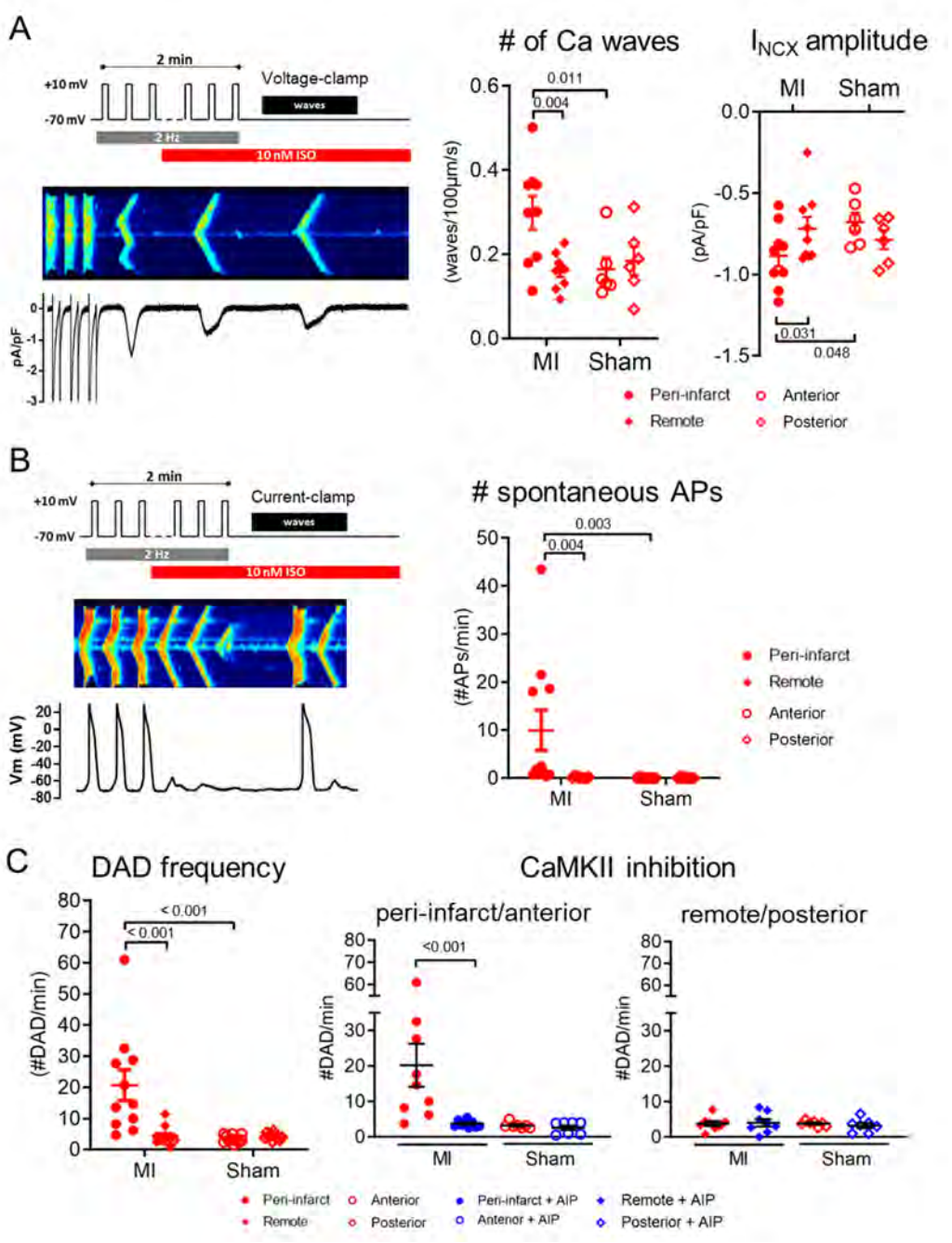

Figure 6. More Ca^{2+} waves and DADs in peri-infarct myocytes under ISO. (A) Left: Example and protocol under voltage clamp. Right: mean data for Ca^{2+} waves in different regions in MI (n_{cells} = 44-46; N_{pigs} = 9) and Sham (n_{cells} = 24-27; N_{pigs} = 6) myocytes. (B) Left: Example and protocol with switch to current clamp. Right: mean data for DAD frequency and spontaneous APs in different regions in MI (n_{cells} = 36-57; N_{pigs} = 11) and sham (n_{cells} = 48-52; N_{pigs} = 11) myocytes. (C) Mean data for DAD frequency in the presence and absence of the specific CaMKII inhibitor (AIP) in MI (-AIP: n_{cells} = 20-46; N_{pigs} = 9 and +AIP: n_{cells} = 22-31; N_{pigs} =9) and Sham (-AIP: n_{cells} = 16-18; N_{pigs} = 7 and +AIP: n_{cells} = 22-30; N_{pigs} = 7) myocytes from different regions of the heart. (2-way Anova with Bonferroni post-hoc testing).

Increased BVR in MI peri-infarct myocytes in the presence of ISO

We further investigated cellular AP repolarization and BVR under current-clamp conditions, to compare with the in vivo observations during 2 Hz atrial pacing. However, 48% of MI peri-infarct myocytes had impaired frequency-dependent acceleration of repolarization and did not follow 2 Hz pacing because of incomplete repolarization within 500 ms, compared to 20% in MI remote myocytes ($p = 0.002$) and to 13% in the corresponding Sham region ($p < 0.0001$). In order not to exclude a large fraction of cells, the effects of ISO on AP repolarization were studied during 1 Hz stimulation. Under ISO, APD shortened to a greater extent in Sham myocytes when compared to MI myocytes, resulting in peri-infarct myocytes displaying a significantly longer APD90 than Sham in the presence of ISO (351 ± 12 ms vs. Sham: 223 ± 10 ms, $p = 0.002$).

Under ISO, BVR was increased significantly in the MI peri-infarct myocytes compared to MI remote myocytes and occasionally early afterdepolarizations (EAD) were observed (Fig. 7A). In Sham myocytes, BVR did not increase significantly with ISO (Fig. 7B).

Taken together, these data indicate that the peri-infarct myocytes have reduced repolarization reserve and a higher degree of instability, further exacerbated under ISO, than myocytes from the remote region, or from Sham.

Spontaneous Ca^{2+} waves and DADs contribute to BVR

We further examined the interplay between the occurrence of spontaneous Ca^{2+} release, DADs and BVR. After a Ca^{2+} wave and accompanying DAD, the Ca^{2+} transient during the stimulated AP merged with the wave and was generally smaller. As illustrated in Fig. 8A, this stimulated AP following a DAD with a Ca wave (marked with an arrow) was longer than the preceding AP. Analysis of the grouped data confirmed that in MI, higher DAD incidence, associated with Ca^{2+} waves, correlated with higher BVR, with the incidence of both DADs and BVR highest in peri-infarct myocytes (Fig. 8B).

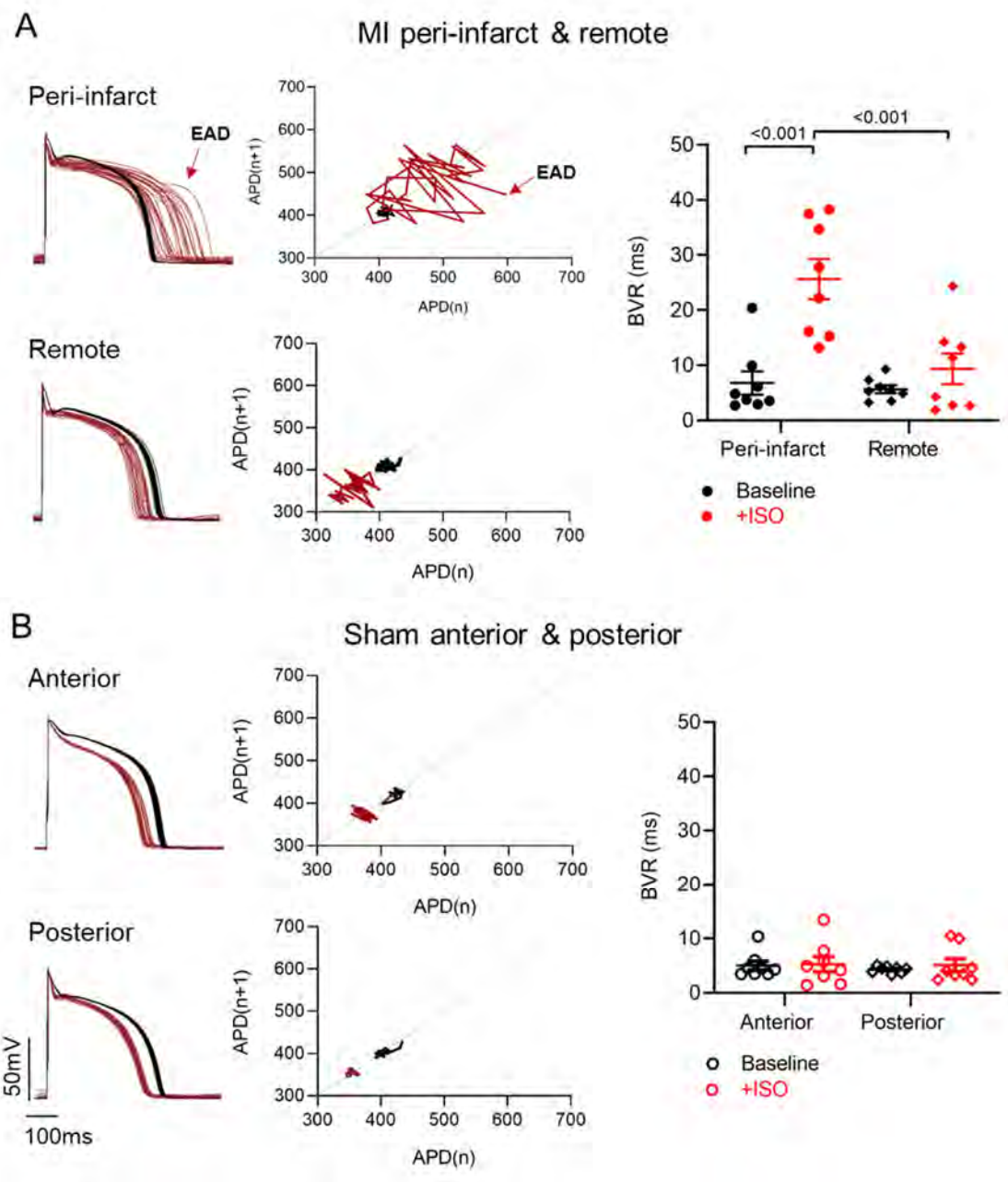

Figure 7. Higher BVR in peri-infarct myocytes under ISO. Left: Examples of 30 steady state action potentials at baseline (black) and under ISO (red); middle: their corresponding Poincaré plots of myocytes from the different regions for (A) MI and (B) Sham myocytes. Right: Mean data for cellular BVR in different regions for MI (n_{cells} = 39-46; N_{pigs} = 8) and Sham (n_{cells} = 40-42; N_{pigs} = 8) myocytes. (Repeated measures 2-way Anova with Bonferroni post-hoc testing).

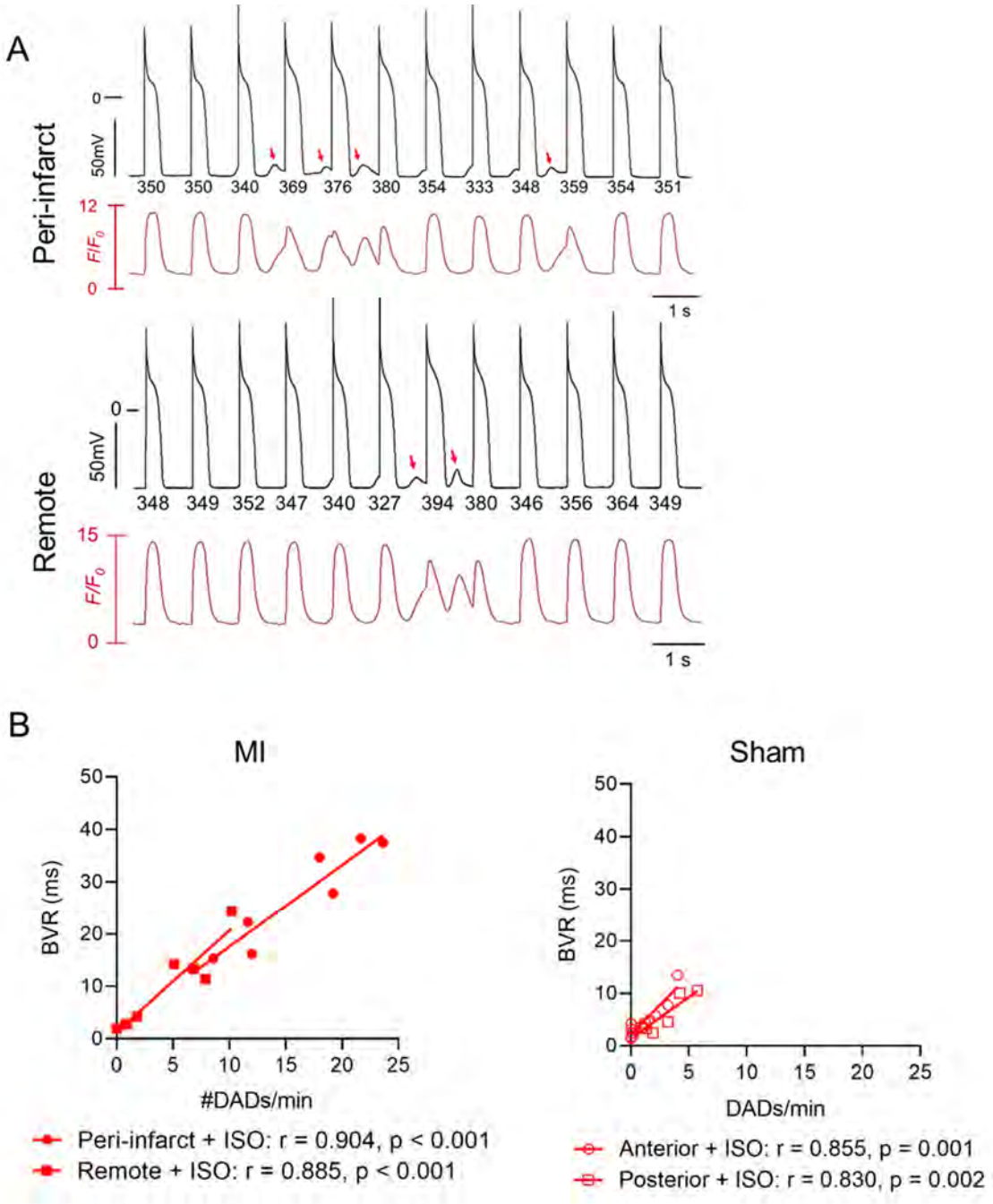

Figure 8. Spontaneous Ca^{2+} release and DADs are associated with increased BVR in peri-infarct myocytes. (A) Examples illustrating spontaneous Ca^{2+} release DAD contributing to subsequent Ca^{2+} transient and action potential duration (APD) changes - red arrows indicate stimulated AP with merger Ca events and longer APD. (B) Correlation between DADs and BVR in myocytes from the different regions of MI (n_{cells} = 14-23; N_{pigs} = 8) and Sham (n_{cells} = 6-8; N_{pigs} = 6). (Linear regression fitting and correlation analysis with two-tailed t-test).

Molecular actors in adrenergic signalling show regional differences in their expression

In tissue samples, we examined regional expression levels of a panel of genes selected based on their relation to the functional observations. Of the genes encoding major K+ channels in pig heart (which lacks transient outward K+ channels), only KCNJ2, encoding the channel for the inward rectifier current I K1, was reduced significantly in the peri-infarct region (Fig. 9A). The expression of ADRB1, coding for β1-adrenergic receptor was significantly reduced in the MI peri-infarct region compared to MI remote region (Fig. 9B). Expression of NPPA, as a marker for hypertrophy, was larger in the peri-infarct region than in the remote region (Fig. 9C).

We expanded the study of cellular adrenergic signalling examining the expression of CaMKII and constitutive phosphorylation in tissue biopsies but could not find any differences (Fig. 10A). In a pilot experiment, we compared the effect of β1 and of β2 block on Ca^{2+} transients and sparks recorded in the presence of ISO, in isolated myocytes from the peri-infarct region and matching Sham region (Fig. 10B). MI myocytes had a response to β2 block and less to β1 block.

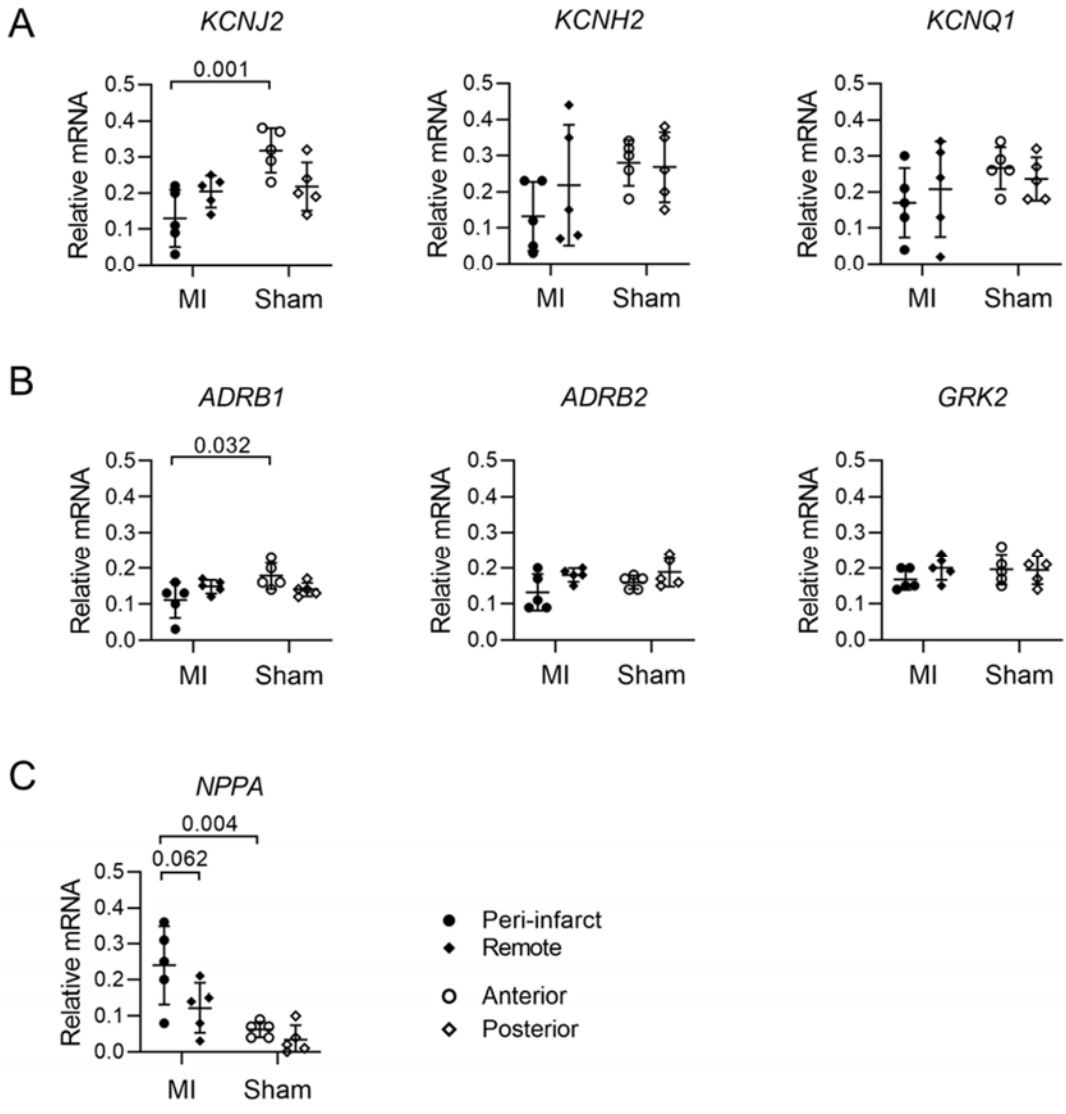

Figure 9. Post-MI differences in gene expression. (A) Reduced expression of *KCNJ2* coding for the inward rectifier current, I_{K1}, in the MI peri-infarct region. (B) β-Adrenergic receptor 1:2 stoichiometry shifted with reduced β1 receptor transcription. (C) Increased transcription of a hypertrophic marker gene, natriuretic peptide A (*NPPA*). MI (N_{pigs} = 5) and Sham (N_{pigs} = 5). (2-way Anova with Bonferroni post-hoc testing)

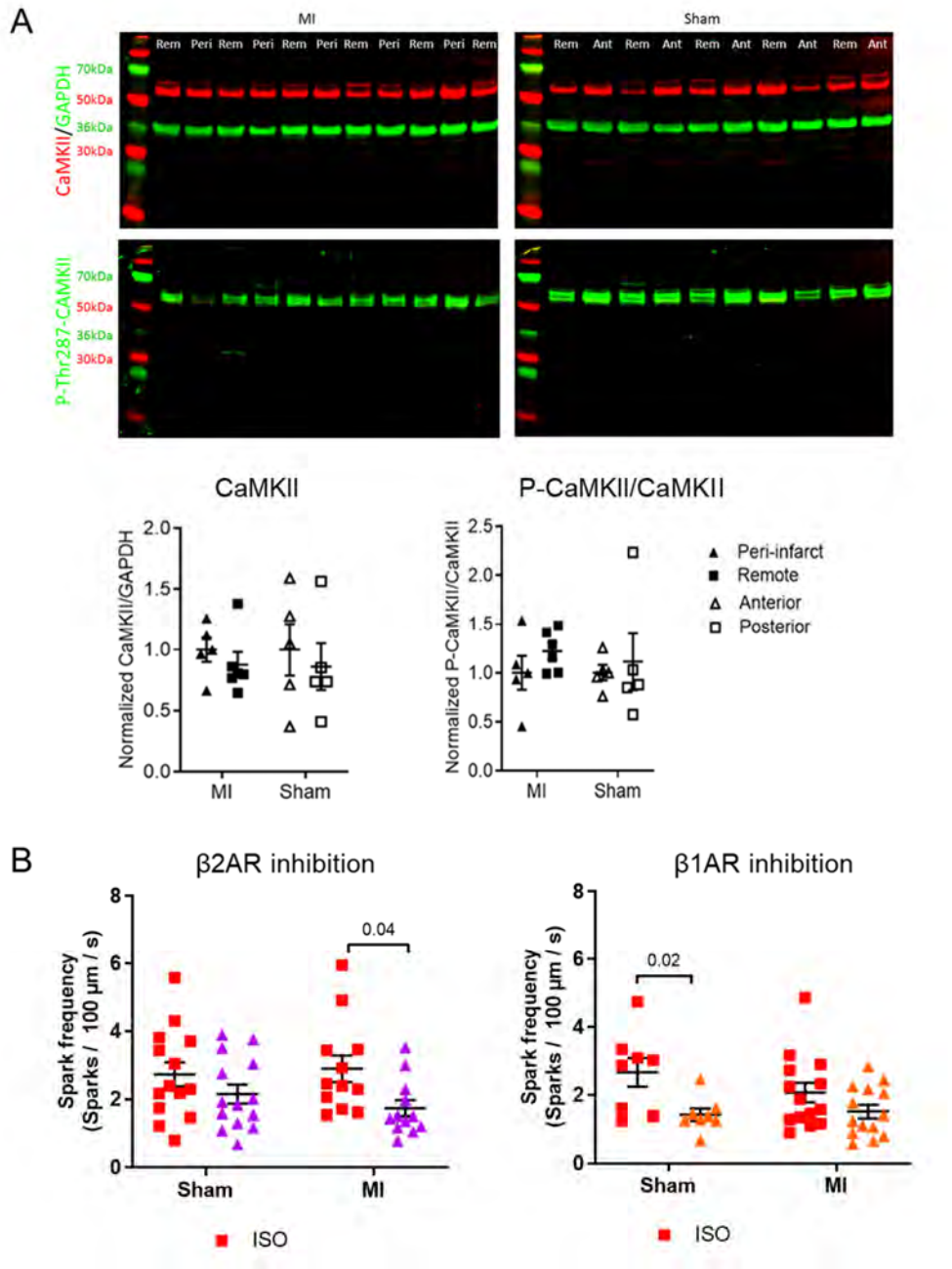

Figure 10. Adrenergic signaling. (A) Western blot for CaMKII (55kDa) and GAPDH (37kDa) expression and phosphorylated CaMKII (top); total CaMKII was normalized to GAPDH and the

level of phosphorylation determined by the ratio of phosphorylated and total CaMKII (bottom). MI (N_{pigs} = 6) and Sham (N_{pigs} = 5). (B) Reduced spark frequency in response to β1 block (CPG-20712 dihydrochloride, 100 nM) vs. β2 block (ICI-118.551 hydrochloride, 50 nM), in the presence of 10 nM ISO with preconditioning at 0.5 Hz. MI peri-infarct (n_{cells} = 12-14; N_{pigs} = 4-5) and matched Sham (n_{cells} = 8-14; N_{pigs} = 4-5). (2-way Anova with Bonferroni post-hoc testing).

Discussion

The main findings of this study are that in vivo, under adrenergic stimulation with ISO, the peri-infarct, but not the remote, region is a source of triggered activity and of repolarization instability creating a functional substrate for re-entry. This is related to intrinsic myocyte properties. While myocytes from both peri-infarct and remote regions share features of remodelling, other properties are unique to the peri-infarct region, in particular the adrenergic response.

The peri-infarct region as source of triggered activity and repolarization instability in vivo

Studies of ventricular arrhythmia using programmed electrical stimulation identify vulnerable substrates and sources of PVCs, but cannot distinguish whether the latter result from triggered activity or (micro) re-entry. Here we used MAP catheters to study local events and thereby regional differences in repolarization and afterdepolarizations, and this in the absence of programmed electrical stimulation. The MAP recording reflects the myocyte transmembrane action potential, even if reporting from groups of cells rather than a single cell. Thereby it provides a view of myocyte behaviour in vivo, and is a highly valuable tool to demonstrate the presence of early and delayed afterdepolarizations in vivo, including in clinical studies (Moore & Franz, 2007). In the pig post-MI, DADs were mostly observed in the peri-infarct region, and this observation correlated with unique properties of the myocytes isolated from this region.

These data extend findings from previous studies by Boyden and colleagues that identified Purkinje fibres as a potential source of PVCs in the first days after MI. Isolated Purkinje cells and tissues have abnormal calcium handling and DADs (Hirose et al. 2008). Electrical remodelling of Na+ channels can further facilitate arrhythmias in vivo through altered conduction, with a potential role for oxidized CaMKII (Christensen et al. 2009; Dun et al. 2013, 2018). Recently, Hegyi et al. (2018) studied isolated myocytes from the post-MI pig heart, but without prior matched in vivo recordings. They reported more DADs and spontaneous APs in myocytes isolated from the MI border zone compared to the remote zone without adrenergic stimulation. We did not see such differences at baseline in our model at 6 weeks post-MI. These authors studied an end-stage heart failure model (6 months post-MI), where potentially more extensive remodelling will shape regional differences.

In vivo repolarization instability can provide a functional re-entry substrate that adds to the well-known MI structural substrate (De Bakker et al. 1993; Ashikaga et al. 2007; Ciaccio et al. 2015). Computational studies consider generalized myocyte remodelling with AP prolongation and repolarization instability but do not include a region-specific myocyte profile (Pashakhanloo et al. 2018).

Here, using MAP recordings we find evidence that post-MI adrenergic stimulation in vivo enhances repolarization instability and facilitates arrhythmias specifically in the peri-infarct region. These in vivo findings correlate to increased BVR in isolated myocytes from the peri-infarct region, only observed during adrenergic stimulation. The co-incidence of both afterdepolarizations and BVR allows for dual mechanisms of triggered activity, focal as well as micro-reentry, as also proposed for torsade de pointes (Dunnink et al. 2017) and suggested by modelling studies (Liu et al. 2015).

Cellular mechanisms of repolarization instability and afterdepolarizations

The vulnerability of the peri-infarct zone superimposes on general myocyte remodelling. Hypertrophy and loss of T-tubules are present throughout the surviving LV. These findings are in line with the specific peri-infarct changes in fibrosis, superimposed on general fibroblast activation (Nagaraju et al. 2017) and consistent with the recent study in the post-MI mouse heart, identifying specific peri-infarct signalling (van Duijvenboden et al. 2019). Reduced Ca^{2+} transient amplitude and rise time at baseline are seen in all regions, and could be due to the loss of T-tubules as well as changes in protein expression and regulation. The gene expression of the hypertrophy marker NPPA was nevertheless higher in the peri-infarct region, suggesting there may a different gene expression programme.

The present study did not compile a functional catalogue of individual currents in the myocytes but agrees with Hegyi et al. (2018) that multiple currents are likely to be involved in facilitating re-entry as well as triggered activity, e.g. the reduction in KCNJ2 will affect repolarization as well as facilitate delayed afterdepolarizations. The data further suggest interaction between spontaneous release events, repolarization and BVR, as previously proposed (Johnson et al. 2013). Firstly, we noted a high correlation between cellular DAD incidence and increased BVR. Secondly, after a spontaneous Ca^{2+} release and DAD, the subsequent global Ca^{2+} transient was reduced, often accompanied by APD prolongation. These findings are in line with Ca^{2+}-dependent modulation of the L-type Ca^{2+} current as a factor driving adrenergic-stimulated BVR (Johnson et al. 2013; Antoons et al. 2015). Reduced inactivation of the L-type Ca^{2+} current would in turn contribute to cellular Ca^{2+} load. Whilst requiring further corroboration, such a mechanism supports the notion that impaired Ca^{2+} handling during adrenergic signalling acts as a central event contributing to both the trigger and the functional substrate for arrhythmias after MI.

Convergence of trigger and substrate in the peri-infarct region through altered adrenergic response

Our data indicate that an altered adrenergic response is likely to define the pro-arrhythmic nature of the peri-infarct myocytes, with a convergence of triggered activity and facilitation of re-entry. We used a low dose of ISO to detect subtle differences in response that could relate to changes in the signalling pathways. At the molecular level, differences in the adrenergic signalling cascade and/or structure could explain the unique vulnerability of the peri-infarct myocytes. Data on their expression at mRNA level suggest a local shift in β1-AR: β2-AR stoichiometry and signalling. The different response to β1-AR block compared to β2AR is consistent with this notion. Reduced expression of β1-AR and preserved β2-AR expression has been observed in heart failure (DeSantiago et al. 2008; Lang et al. 2015). This altered expression results in different sensitivity and signalling, where β2-AR signalling becomes dominant in heart failure (Pogwizd et al. 2001) and leads to arrhythmias mediated by

spontaneous Ca^{2+} release (DeSantiago et al. 2008). Recent studies indicate a significant crosstalk between β-AR signalling and CaMKII activation (Curran et al. 2007; Dries et al. 2016; Shugg et al. 2018), presenting CaMKII as a possible downstream mediator of detrimental β-AR signalling after MI. In support of this, CaMKII inhibition reduced DAD incidence and amplitude in peri-infarct myocytes.

Differences in cellular β-AR signalling could also be the result of local re-organization of receptors at the surface and T-tubular membranes (Nikolaev et al. 2010). The changes in adrenergic signalling and responses can themselves be consequent on the altered regional innervation and its trophic influence on the myocytes (Habecker et al. 2016; Pianca et al. 2019).

In vivo, differential nerve sprouting post MI contributes to the arrhythmogenic nature of the border zone (Gardner et al. 2015). Neuromodulation and reduction of sympathetic inputs suppress arrhythmias after MI in the pig model (Chui et al. 2017) and patients with intractable VT can benefit from bilateral stellectomy (Vaseghi et al. 2017). Ischaemia, evoked by adrenergic stimulation, may superimpose on the vulnerable peri-infarct myocytes and enhance arrhythmic potential. The interactions of the local heterogeneous peri-infarct innervation with varying amounts of circulating catecholamines and other hormones may contribute to additional regional heterogeneity and should be the subject of further investigation.

Implications for arrhythmogenesis and therapy

The findings of the present study underscore the potential benefit for targeting neuro-hormonal, and in particular adrenergic, signalling to prevent arrhythmia and sudden cardiac death after MI, as included in current guidelines (Al-Khatib et al. 2018). Our findings additionally support the caution against drugs that challenge an already limited repolarization reserve. Given the residual high risk for arrhythmia post MI, within the time window studied here, novel pharmacological approaches are needed. Our study identifies altered Ca^{2+} handling that can be prevented by CaMKII inhibition, which has also been shown to be beneficial in human cellular and tissue studies (Sossalla et al. 2010; Dries et al. 2018), and advocates for its potential in post-MI therapy.

Ablative strategies targeting the peri-infarct substrate are effective at treating post-MI arrhythmia but also have limitations (Baldinger et al. 2016). Our study highlights the role of myocyte remodelling for both the triggers and functional substrate of the arrhythmia. Therefore, targeting the myocytes through local approaches such as targeted gene therapy (Sasano et al. 2006) and exosome targeting (Antes et al. 2018) may offer alternative, non-destructive strategies to treat post-MI arrhythmia.

Limitations

The neurotransmitter of adrenergic activation in vivo is noradrenaline, activating both α- and β-receptors in heart and vasculature, with a contribution of circulating adrenaline. Here we chose to use isoproterenol to focus on the myocyte responses and to be able to use a similar agent in vivo and in vitro. Although we could use noradrenaline in isolated myocytes, when applied in vivo, peripheral vascular effects and secondary adaptations would confound the cardiac response to noradrenaline. In myocytes, the β-receptor-mediated response has a major role in the calcium changes, hence the choice for ISO as a single agent in vivo and in vitro.

The current study aimed to record DADs using MAP catheters and this approach did not allow us to definitively correlate the ECG recorded PVC with its site of origin. More comprehensive mapping needs to be included in future studies.

Post-MI remodelling may affect transmural regions differentially and was not investigated in the present study. Cellular studies used the mid-myocardial layers, which constitutes the bulk of the cardiac mass but we did not examine the transmural spectrum.

In the translation of single cell observations to whole heart arrhythmias, factors such as cell coupling and the source-sink mismatch play an important role and could not be resolved in the present study. Additionally, we did not address how multiple cell types contribute to the electrophysiological phenotype, nor individual ionic current remodelling; this needs to be explored in future studies.

Conclusions

Altered myocyte adrenergic responses define the peri-infarct zone as a prominent source of triggered activity and of concomitant repolarization instability, amplifying the potential for re-entry and contributing to the substrate for arrhythmia. This is the result of the unique properties of the peri-infarct myocytes. These findings stimulate further exploration of local therapies targeting myocytes and autonomic modulation.

Additional Information

Competing interests

R.W. has received research funding from Biotronik, Boston Scientific and Medtronic and speakers and consultancy fees from Biotronik, Boston Scientific, Medtronic, St Jude Medical and Sorin. This has no influence on the exploratory study reported here and is therefore not a competing interest.

Author contributions

K.R.S., R.W., P.C., H.L.R., E.D., M.A. contributed to conception and design of the work; K.R.S., R.W., P.C., H.L.R., E.D., M.A., B.V., D.M.J., G.G., C.K.N., R.D.P., M.Ab., D.J.S. were involved in acquiring, analysing or interpreting the data of this work; K.R.S., R.W., P.C., H.L.R., E.D., M.A., B.V., D.M.J., G.G., C.K.N., R.D.P., M.Ab., D.J.S. were involved in drafting the work or revising it. All authors revised and approved the final version of the manuscript. All persons designated as author, qualify for authorship and are listed.

Funding

This work was supported by the Fund for Scientific Research-Flanders (FWO projects G.0617.09 and G.0918.15 to K.R.S., FWO Project grant G08861N and FWO Odysseus Project 90 663 to H.L.R.; FWO Senior Clinical Investigator to R.W.; FWO postdoctoral fellowships to E.D., D.M.J. and G.G.; FWO PhD fellowship to M.A.), and by Horizon 2020 MSCA-IF-2016-752824 to M.Ab.

Acknowledgements

We thank Patricia Holemans, Roxane Menten and Sofie van Soest for technical assistance.

References

Aimond F, Alvarez JL, Rauzier JM, Lorente P & Vassort G (1999). Ionic basis of ventricular arrhythmias in remodeled rat heart during long-term myocardial infarction. *Cardiovasc Res* **42,** 402–415.

Ajijola OA, Lux RL, Khahera A, Kwon O, Aliotta E, Ennis DB, Fishbein MC, Ardell JL & Shivkumar K (2017). Sympathetic modulation of electrical activation in normal and infarcted myocardium: implications for arrhythmogenesis. *Am J Physiol Heart Circ Physiol* **312,** H608–H621.

Al-Khatib SM, Stevenson WG, Ackerman MJ, Bryant WJ, Callans DJ, Curtis AB, Deal BJ, Dickfeld T, Field ME, Fonarow GC, Gillis AM, Granger CB, Hammill SC, Hlatky MA, Joglar JA, Kay GN, Matlock DD, Myerburg RJ & Page RL (2018). 2017 AHA/ACC/HRS guideline for management of patients with ventricular arrhythmias and the prevention of sudden cardiac death: Executive summary: A Report of the American College of Cardiology/American Heart Association Task Force on Clinical Practice Gui. *Heart Rhythm* **15,** e190–e252.

Antes TJ, Middleton RC, Luther KM, Ijichi T, Peck KA, Liu WJ, Valle J, Echavez AK & Marbán E (2018). Targeting extracellular vesicles to injured tissue using membrane cloaking and surface display. *J Nanobiotechnology* **16,** 1–15.

Antoons G, Johnson DM, Dries E, Santiago DJ, Ozdemir S, Lenaerts I, Beekman JDM, Houtman MJC, Sipido KR & Vos MA (2015). Calcium release near l-type calcium channels promotes beat-to-beat variability in ventricular myocytes from the chronic AV block dog. *J Mol Cell Cardiol* **89,** 326–334.

Ashikaga H, Sasano T, Dong J, Zviman MM, Evers R, Hopenfeld B, Castro V, Helm RH, Dickfeld T, Nazarian S, Donahue JK, Berger RD, Calkins H, Abraham MR, Marbán E, Lardo AC, McVeigh ER & Halperin HR (2007). Magnetic resonance-based anatomical analysis of scar-related ventricular tachycardia: Implications for catheter ablation. *Circ Res* **101,** 939–947.

Baba S, Dun W, Cabo C & Boyden PA (2005). Remodeling in cells from different regions of the reentrant circuit during ventricular tachycardia. *Circulation* **112,** 2386–2396.

De Bakker JMT, Van Capelle FJL, Janse MJ, Tasseron S, Vermeulen JT, De Jonge N & Lahpor JR (1993). Slow conduction in the infarcted human heart: “Zigzag” course of activation. *Circulation* **88,** 915–926.

Baldinger SH, Stevenson WG & John RM (2016). Ablation of ischemic ventricular tachycardia: Evidence, techniques, results, and future directions. *Curr Opin Cardiol* **31,** 29–36.

Belevych AE, Terentyev D, Terentyeva R, Ho HT, Gyorke I, Bonilla IM, Carnes CA, Billman GE & Györke S (2012). Shortened Ca 2+ signaling refractoriness underlies cellular arrhythmogenesis in a postinfarction model of sudden cardiac death. *Circ Res* **110,** 569–577.

Bogun F, Good E, Reich S, Elmouchi D, Igic P, Tschopp D, Dey S, Wimmer A, Jongnarangsin K, Oral H, Chugh A, Pelosi F & Morady F (2006). Role of Purkinje Fibers in Post-Infarction Ventricular Tachycardia. *J Am Coll Cardiol* **48,** 2500–2507.

Cao JM, Chen LS, KenKnight BH, Ohara T, Lee MH, Tsai J, Lai WW, Karagueuzian HS, Wolf PL, Fishbein MC & Chen PS (2000). Nerve sprouting and sudden cardiac death. *Circ Res* **86,** 816–821.

Christensen MD, Dun W, Boyden PA, Anderson ME, Mohler PJ & Hund TJ (2009). Oxidized calmodulin kinase II regulates conduction following myocardial infarction: A computational analysis. *PLoS Comput Biol*.

Chui RW, Buckley U, Rajendran PS, Vrabec T, Shivkumar K & Ardell JL (2017). Bioelectronic block of paravertebral sympathetic nerves mitigates post–myocardial infarction ventricular arrhythmias. *Heart Rhythm* **14,** 1665–1672.

Ciaccio EJ, Coromilas J, Ashikaga H, Cervantes DO, Wit AL, Peters NS, McVeigh ER & Garan H (2015). Model of unidirectional block formation leading to reentrant ventricular tachycardia in the infarct border zone of postinfarction canine hearts. *Comput Biol Med* **62,** 254–263.

Ciaccio EJ, Coromilas J, Wit AL, Peters NS & Garan H (2018). Source-Sink Mismatch Causing Functional Conduction Block in Re-Entrant Ventricular Tachycardia. *JACC Clin Electrophysiol* **4,** 1–16.

Cronin EM et al. (2019). 2019 HRS/EHRA/APHRS/LAHRS expert consensus statement on catheter ablation of ventricular arrhythmias. *Europace* **21,** 1143–1144.

Curran J, Hinton MJ, Ríos E, Bers DM & Shannon TR (2007). B-Adrenergic Enhancement of Sarcoplasmic Reticulum Calcium Leak in Cardiac Myocytes Is Mediated By Calcium/Calmodulin-Dependent Protein Kinase. *Circ Res* **100,** 391–398.

DeSantiago J, Ai X, Islam M, Acuna G, Ziolo MT, Donald M & Pogwizd SM (2008). Arrhythmogenic effects of β2 -adrenergic stimulation in the failing heart are due to enhanced SR Ca load. *Circ Res* **102,** 1389–1397.

Dries E, Santiago D, Johnson DM, Gilbert G, Holemans P, Korte SM, Roderick L, Sipido KR & Experimental (2016). Calcium/calmodulin-dependent kinase II and nitric oxide synthase 1-dependent modulation of ryanodine receptors during β-adrenergic stimulation is restricted to the dyadic cleft. *Physiol Res* **65,** 461–468.

Dries E, Santiago DJ, Gilbert G, Lenaerts I, Vandenberk B, Nagaraju CK, Daniel M, Holemans P, Roderick HL, Macquaide N, Claus P, Sipido KR, Sciences M, Kingdom U & Sipido KR (2018). Hyperactive ryanodine receptors in human heart failure and ischemic cardiomyopathy reside outside of couplons. *Cardiovasc Res* **114,** 1512–1524.

van Duijvenboden K, de Bakker DEM, Man JCK, Janssen R, Günthel M, Hill MC, Hooijkaas IB, van der Made I, van der Kraak PH, Vink A, Creemers EE, Martin JF, Barnett P, Bakkers J & Christoffels VM (2019). Conserved NPPB+ Border Zone Switches from MEF2 to AP-1 Driven Gene Program. *Circulation* **31,** [Epub ahead of print].

Dun W, Danilo P, Mohler PJ & Boyden PA (2018). Microtubular remodeling and decreased expression of Nav1.5 with enhanced EHD4 in cells from the infarcted heart. *Life Sci* **201,** 72–80.

Dun W, Lowe JS, Wright P, Hund TJ, Mohler PJ & Boyden PA (2013). Ankyrin-G Participates in

INa Remodeling in Myocytes from the Border Zones of Infarcted Canine Heart. *PLoS One* **8,** 1–13.

Dunnink A, Stams TRG, Bossu A, Meijborg VMF, Beekman JDM, Wijers SC, De Bakker JMT & Vos MA (2017). Torsade de pointes arrhythmias arise at the site of maximal heterogeneity of repolarization in the chronic complete atrioventricular block dog. *Europace* **19,** 858–865.

Franz MR (1999). Current status of monophasic action potential recording: Theories, measurements and interpretations. *Cardiovasc Res* **41,** 25–40.

Galan DT, Bito V, Claus P, Holemans P, Abi-Char J, Nagaraju CK, Dries E, Vermeulen K, Ventura-Clapier R, Sipido KR & Driesen RB (2016). Reduced mitochondrial respiration in the ischemic as well as in the remote nonischemic region in postmyocardial infarction remodeling. *Am J Physiol Heart Circ Physiol* **311,** H1075–H1090.

Gardner R, Wang L, Lang B, Cregg J, Dunbar C, Woodward W, Silver J, Ripplinger C & Habecker B (2015). Targeting protein tyrosine phosphatase σ after myocardial infarction restores cardiac sympathetic innervation and prevents arrhythmias. *Nat Commun* **6,** 1–9.

Gonca E (2015). Comparison of thiopental and ketamine+xylazine anesthesia in ischemia/reperfusion-induced arrhythmias in rats. *Turkish J Med Sci* **45,** 1413–1420.

De Groot SHM, Vos MA, Gorgels APM, Leunissen JDM, Van Der Steld BJ & Wellens HJJ (1995). Combining monophasic action potential recordings with pacing to demonstrate delayed afterdepolarizations and triggered arrhythmias in the intact heart: Value of diastolic slope. *Circulation* **92,** 2697–2704.

Grundy D (2015). Principles and standards for reporting animal experiments in The Journal of Physiology and Experimental Physiology. *J Physiol* **593,** 2547–2549.

Habecker BA, Anderson ME, Birren SJ, Fukuda K, Herring N, Hoover DB, Kanazawa H, Paterson DJ & Ripplinger CM (2016). Molecular and cellular neurocardiology: development, and cellular and molecular adaptations to heart disease. *J Physiol* **594,** 3853–3875.

Hayashi M, Shimizu W & Albert CM (2015). The Spectrum of Epidemiology Underlying Sudden Cardiac Death. *Circulation* **116,** 1887–1906.

Hegyi B et al. (2018). Complex electrophysiological remodeling in postinfarction ischemic heart failure. *Proc Natl Acad Sci U S A* **115,** E3036–E3044.

Heidbüchel H, Hoogsteen J, Fagard R, Vanhees L, Ector H, Willems R & Van Lierde J (2003). High prevalence of right ventricular involvement in endurance athletes with ventricular arrhythmias: Role of an electrophysiologic study in risk stratification. *Eur Heart J* **24,** 1473–1480.

Hirose M, Stuyvers BD, Dun W, ter Keurs HEDJ & Boyden PA (2008). Function of Ca(2+) release channels in Purkinje cells that survive in the infarcted canine heart: a mechanism for triggered Purkinje ectopy. *Circ Arrhythm Electrophysiol* **1,** 387–395.

Johnson DM, Heijman J, Bode EF, Greensmith DJ, Van Der Linde H, Abi-Gerges N, Eisner DA, Trafford AW & Volders PGA (2013). Diastolic spontaneous calcium release from the sarcoplasmic reticulum increases beat-to-beat variability of repolarization in canine ventricular myocytes after β-adrenergic stimulation. *Circ Res* **112,** 246–256.

Lang D, Holzem K, Kang C, Xiao M, Hwang HJ, Ewald GA, Yamada KA & Efimov IR (2015). Arrhythmogenic remodeling of β2 versus β1 adrenergic signaling in the human failing heart.

Circ Arrhythm Electrophysiol **8,** 409–419.

Lerma C, Gorelick A, Ghanem RN, Glass L & Huikuri H V. (2013). Patterns of ectopy leading to increased risk of fatal or near-fatal cardiac arrhythmia in patients with depressed left ventricular function after an acute myocardial infarction. *Europace* **15,** 1304–1312.

Liu MB, De Lange E, Garfinkel A, Weiss JN & Qu Z (2015). Delayed afterdepolarizations generate both triggers and a vulnerable substrate promoting reentry in cardiac tissue. *Heart Rhythm* **12,** 2115–2124.

Lue W & Boyden P (1992). Abnormal electrical properties of myocytes from chronically infarted canine heart. *Circulation* **85,** 1175–1188.

Marrouche NF, Verma A, Wazni O, Schweikert R, Martin DO, Saliba W, Kilicaslan F, Cummings J, Burkhardt JD, Bhargava M, Bash D, Brachmann J, Guenther J, Hao S, Beheiry S, Rossillo A, Raviele A, Themistoclakis S & Natale A (2004). Mode of initiation and ablation of ventricular fibrillation storms in patients with ischemic cardiomyopathy. *J Am Coll Cardiol* **43,** 1715–1720.

Moore HJ & Franz MR (2007). Monophasic action potential recordings in humans. *J Cardiovasc Electrophysiol* **18,** 787–790.

Nagaraju CK, Dries E, Popovic N, Singh AA, Haemers P, Roderick HL, Claus P, Sipido KR & Driesen RB (2017). Global fibroblast activation throughout the left ventricle but localized fibrosis after myocardial infarction. *Sci Rep* **7,** 1–14.

Nikolaev VO, Moshkov A, Lyon AR, Miragoli M, Novak P, Paur H, Lohse MJ, Korchev YE, Harding SE & Gorelik J (2010). β2-Adrenergic Receptor Redistribution in Heart Failure Changes cAMP Compartmentation. *Science (80-)* **327,** 1653–1658.

Pashakhanloo F, Herzka DA, Halperin H, McVeigh ER & Trayanova NA (2018). Role of 3-Dimensional Architecture of Scar and Surviving Tissue in Ventricular Tachycardia: Insights from High-Resolution Ex Vivo Porcine Models. *Circ Arrhythmia Electrophysiol* **11,** 1–12.

Pianca N, Di Bona A, Lazzeri E, Costantini I, Franzoso M, Prando V, Armani A, Rizzo S, Fedrigo M, Angelini A, Basso C, Pavone FS, Rubart M, Sacconi L, Zaglia T & Mongillo M (2019). Cardiac sympathetic innervation network shapes the myocardium by locally controlling cardiomyocyte size through the cellular proteolytic machinery. *J Physiol* **597,** 3639–3656.

Pogwizd SM, Schlotthauer K, Li L, Yuan W & Bers DM (2001). Arrhythmogenesis and Contractile Dysfunction in Heart Failure: Roles of Sodium-Calcium Exchange, Inward Rectifier Potassium Current, and Residual Beta-Adrenergic Responsiveness. *Circ Res* **88,** 1159–1167.

Prakosa A, Arevalo HJ, Deng D, Boyle PM, Nikolov PP, Ashikaga H, Blauer JJE, Ghafoori E, Park CJ, Blake RC, Han FT, MacLeod RS, Halperin HR, Callans DJ, Ranjan R, Chrispin J, Nazarian S & Trayanova NA (2018). Personalized virtual-heart technology for guiding the ablation of infarct-related ventricular tachycardia. *Nat Biomed Eng* **2,** 732–740.

Priori SG, Mantica M & Schwartz PJ (1988). Delayed afterdepolarizations elicited in vivo by left stellate ganglion stimulation. *Circulation* **78,** 178–185.

Rajendran PS, Nakamura K, Ajijola OA, Vaseghi M, Armour JA, Ardell JL & Shivkumar K (2016). Myocardial infarction induces structural and functional remodelling of the intrinsic cardiac nervous system. *J Physiol* **594,** 321–341.

Rivas N, Dhruvakumar S, Mainigi SK, Smith T, Gerstenfeld EP & Marchlinski FE (2009). Ventricular premature depolarizations triggered by incremental dose isoproterenol infusion: common electrocardiographic features. *J Interv Card Electrophysiol* **25,** 43–51.

Saeed M, Link MS, Mahapatra S, Mouded M, Tzeng D, Jung V, Contreras R, Swygman C, Homoud M, Mark Estes NA & Wang PJ (2000). Analysis of intracardiac electrograms showing monomorphic ventricular tachycardia in patients with implantable cardioverter-defibrillators. *Am J Cardiol* **85,** 580–587.

Sasano T, McDonald AD, Kikuchi K & Donahue JK (2006). Molecular ablation of ventricular tachycardia after myocardial infarction. *Nat Med* **12,** 1256–1258.

Shimizu W, Ohe T, Kurita T, Takaki H, Aihara N, Kamakura S, Matsuhisa M & Shimomura K (1991). Early afterdepolarizations induced by isoproterenol in patients with congenital long QT syndrome. *Circulation* **84,** 1915–1923.

Shugg T, Johnson DE, Shao M, Lai X, Witzmann F, Cummins TR, Rubart-Von-der Lohe M, Hudmon A & Overholser BR (2018). Calcium/calmodulin-dependent protein kinase II regulation of IKs during sustained β-adrenergic receptor stimulation. *Heart Rhythm* **15,** 895–904.

Sossalla S, Fluschnik N, Schotola H, Ort KR, Neef S, Schulte T, Wittköpper K, Renner A, Schmitto JD, Gummert J, El-Armouche A, Hasenfuss G & Maier LS (2010). Inhibition of elevated Ca2+/calmodulin-dependent protein kinase II improves contractility in human failing myocardium. *Circ Res* **107,** 1150–1161.

Thomsen MB, Verduyn SC, Stengl M, Beekman JDM, de Pater G, van Opstal J, Volders PGA & Vos MA (2004). Increased short-term variability of repolarization predicts d-sotalol-induced torsades de pointes in dogs. *Circulation* **110,** 2453–2459.

Vandesompele J, De Preter K, Pattyn F, Poppe B, Van Roy N, Speleman, De Paepe A & Speleman F (2002). Accurate normalization of real-time quantitative RT-PCR data by geometric averaging of multiple internal control genes. *Genome Biol* **3,** research0034.1–0034.11.

Vaseghi M, Barwad P, Malavassi Corrales FJ, Tandri H, Mathuria N, Shah R, Sorg JM, Gima J, Mandal K, Sàenz Morales LC, Lokhandwala Y & Shivkumar K (2017). Cardiac Sympathetic Denervation for Refractory Ventricular Arrhythmias. *J Am Coll Cardiol* **69,** 3070–3080.

Verma A, Marrouche NF, Schweikert RA, Saliba W, Wazni O, Cummings J, Abdul-Karim A, Bhargava M, Burkhardt JD, Kilicaslan F, Martin DO & Natale A (2005). Relationship between successful ablation sites and the scar border zone defined by substrate mapping for ventricular tachycardia post-myocardial infarction. *J Cardiovasc Electrophysiol* **16,** 465–471.

Wong SS, Bassett AL, Cameron JS, Epstein K, Kozlovskis P & Myerburg RJ (1982). Dissimilarities in the electrophysiological abnormalities of lateral border and central infarct zone cells after healing of myocardial infarction in cats. *Circ Res* **51,** 486–493.

Xing D & Martins JB (2004). Triggered activity due to delayed afterdepolarizations in sites of focal origin of ischemic ventricular tachycardia. *Am J Physiol Heart Circ Physiol* **287,** H2078-84.

CHAPTER 4: Initiation of Arrhythmias – Role of delayed afterdepolarisations and premature ventricular complexes

Published as:

Matthew Amoni, Piet Claus, Eef Dries, Chandan Nagaraju, Stijn De Buck, Bert Vandenberk, Sebastian Ingelaere, Dylan Vermoortele, H. Llewelyn Roderick, Karin R. Sipido, Rik Willems. Discrete sites of frequent premature ventricular complexes cluster within the infarct border zone and coincide with high frequency of delayed afterdepolarizations under adrenergic stimulation. Heart Rhythm, Volume 18, Issue 11, November 2021, Pages 1976-1987

Editorial in:

Takeshi Aiba. Ischemia-induced premature ventricular complexes: Is it still complex? Heart Rhythm, Volume 18, Issue 11, November 2021, Pages 1988-1989

ABSTRACT

Background: Sympathetic activation in ischemic heart disease can cause lethal arrhythmias. These are often preceded by premature ventricular complexes (PVCs), which could at cellular level, result from delayed afterdepolarizations.

Objective: To identify and map vulnerable areas for arrhythmia initiation after myocardial infarction (MI) and to explore the link between PVCs and cellular events.

Methods: Anterior-septal wall MI was induced by 120 minutes of coronary occlusion followed by reperfusion (27 MI and 16 Sham pigs). After 4 weeks, EnSite™ electroanatomical mapping combined with imaging was performed to precisely locate PVC sites of origin and subsequently record monophasic action potentials. Cardiomyocytes were isolated from different regions to study regional cellular remodeling. Isoproterenol was used as surrogate for adrenergic stimulation both *in vivo* and in cardiomyocytes.

Results: PVCs originated from the MI border zone (BZ) and occurred at discrete areas with clusters of PVCs within the BZ. At these sites, frequent delayed afterdepolarizations and occasional associated spontaneous action potentials translating to a PVC were present. Cardiomyocytes isolated from the MI BZ exhibited more spontaneous action potentials than cardiomyocytes from remote region. Sensitivity to adrenergic stimulation was increased in MI, *in vivo* and in cardiomyocytes. In awake, freely moving MI animals, frequent PVCs, ventricular arrhythmia and sudden cardiac death occurred spontaneously at moderately elevated heart rates.

Conclusion: Post-MI, arrhythmias initiate from discrete vulnerable areas within the BZ, where delayed afterdepolarizations, related to increased adrenergic response of BZ cardiomyocytes, can generate PVCs.

Keywords: myocardial infarction, premature ventricular complex, action potential, delayed afterdepolarization; non-contact electroanatomical mapping.

INTRODUCTION

Ischemic heart disease is a common cause of sudden cardiac death (SCD) due to lethal ventricular tachycardia (VT) or fibrillation (VF) [1]. An established risk factor for SCD in ischemic heart disease is autonomic dysfunction and increased sympathetic drive [2]. A contributive factor is the abnormalities of autonomic innervation, as seen in experimental models [3,4] and corroborated by clinical data [5]. Causality is inferred by the observations that sympathetic activation precedes arrhythmias [6] and premature ventricular complexes (PVCs) can initiate VT/VF [7].

However, there is limited *in vivo* evidence on the mechanism for spontaneous adrenergic-driven PVCs and arrhythmias; whether PVCs result from cellular triggered events, and whether these arise at preferential locations. Studies of isolated cardiomyocytes indicate that remodeling post-MI promotes spontaneous calcium release and delayed afterdepolarizations (DADs) [8,9], which could trigger PVCs *in vivo*. Direct evidence for the correlation between cellular events and PVCs *in vivo* is however limited.

Using monophasic action potential (MAP) recordings *in vivo*, Priori and colleagues [10] first demonstrated a link between sympathetic stimulation, DADs and triggered PVCs in structurally normal hearts. We recently reported an increased incidence of DADs in MAPs recorded at random sites in the region adjacent to an MI during adrenergic stimulation, correlating with enhanced propensity of DADs in cardiomyocytes [11]. Whether these DADs form the missing link to the emergence of spontaneous PVCs is still open. Clinical observations suggest that PVCs are restricted to locations within the BZ [7,12]. Therefore, if DADs are indeed mechanistically related to spontaneous PVCs during increased adrenergic drive, it would imply that DADs are also restricted and correlate with PVC sites within the BZ.

In the present study, we address the question whether adrenergic stimulation leads to identifiable vulnerable areas within the BZ where both DADs and PVCs arise. We combine comprehensive electro-anatomical mapping of the LV with site-directed recording of MAPs *in vivo* at PVC and non-PVC sites within the BZ and in remote regions. We use incremental isoproterenol (ISO) doses to simulate myocyte β-adrenergic activation and investigate altered sensitivity after MI. We also isolate cardiomyocytes from two BZ sites and from the remote region to evaluate arrhythmogenic cardiomyocyte properties outside of their local environment.

METHODS

Detailed methods are provided in the Online Supplement, appended below.

Pig model of myocardial infarction

Forty-three domestic pigs (Strain TN70, Topigs, Norsvin) of both sexes were used. Treatment was in accordance with ARRIVE guidelines and the Guide for the Care and Use of Laboratory Animals. Protocols were approved by the KU Leuven ethical committee. All *in vivo* interventions were performed under general anesthesia.

MI was induced by balloon occlusion in the left anterior descending coronary artery immediately after the first diagonal branch for 120 minutes. Sham animals underwent the same procedure without occlusion. In a subset of 7 MI and 6 Sham animals, a loop recorder (REVEAL XT™ or LINQ™, Medtronic, Belgium) was implanted to sample cardiac rhythm. The timeline of interventions and experimental protocols are illustrated in Supplemental figure 1A.

Cardiac magnetic resonance imaging

After 1 month, heart structure and function were assessed by cardiac magnetic resonance imaging (cMRI), including delineation of the MI (Fig.1A). Functional data are summarized in Supplemental table 1. cMRI was used to create a 3D left ventricle model for use in the *in vivo* study performed 2-4 days later (Suppl. fig. 1B).

Cardiac electrophysiology study

An EnSite Precision 2.0 mapping system (Abbott Medical, New Jersey, USA) paired with a BARD Electrophysiology Labsystem Pro EP (Boston Scientific, USA) was used for electroanatomical mapping. The EnSite multi-electrode array (MEA), was positioned centrally in the LV. ISO was infused in incremental doses of 0.01 µg/kg until 0.04 µg/kg (4 steps of 5 minutes each) with continuous non-contact electroanatomical mapping. In a subset of animals, simultaneous contact mapping defined the BZ: the peri-infarct area with bipolar voltage > 0.5 mV and < 1.5 mV.

Following appropriate recovery, MAPs were recorded from different sites. The most common PVC sites were tagged on the MRI-derived anatomical LV model using the biplane augmented reality tool (LARCA, Leuven Augmented Reality Catheter Ablation) [13], which was used to position the MAP catheters at PVC sites and at selected non-PVC sites (or matched regions in Sham). MAP recordings were performed at baseline and in the presence of ISO, at the dose with maximal PVC occurrence during mapping studies.

After 1-3 days recovery, animals were sacrificed for tissue sampling and cell isolation.

Isolated tissue and cardiomyocyte studies

Protocols for tissue processing and staining for fibrosis were described previously [14]. Cardiomyocytes were isolated from the anterior and septal BZ and the non-infarcted remote region (MI remote), and matched regions in Sham [11]. Freshly isolated cardiomyocytes were imaged on an inverted microscope, and studied in whole-cell patch clamp mode with measurement of cytosolic calcium using a photometry epifluorescence setup [11].

Data analysis and statistics

Off-line data analysis was performed with the operator blinded. All data are presented as mean ± SD. Data were compared with 1- or 2-way ANOVA with Bonferroni or Dunn's post-hoc testing, and Fisher's exact test, as indicated in the figure legends. For cellular data, we used a nested design.

RESULTS

Frequent premature ventricular complexes (PVCs) predominantly originate from the infarct border zone (BZ)

The electrically defined scar area (< 0.5 mV) had an excellent correlation to cMRI infarct size (Fig. 1A). MI pigs had more frequent and complex PVCs than Sham translating to a higher arrhythmia score (Suppl. fig. 2B, 2C). The location of PVCs origin during incremental doses of ISO was determined by non-contact mapping of the LV activation (Fig. 1B, PVC site marked by *). In MI, these PVCs predominantly originated from the BZ, (Fig. 1B, right). The QRS duration in sinus rhythm was 38±7 ms in sham and 42±9 ms in MI, while for PVCs it was 89±18 ms in Sham and 102±15 ms in MI. This more than doubling indicates a myocardial origin of these complexes is more likely than a fascicular ($P < 0.001$).

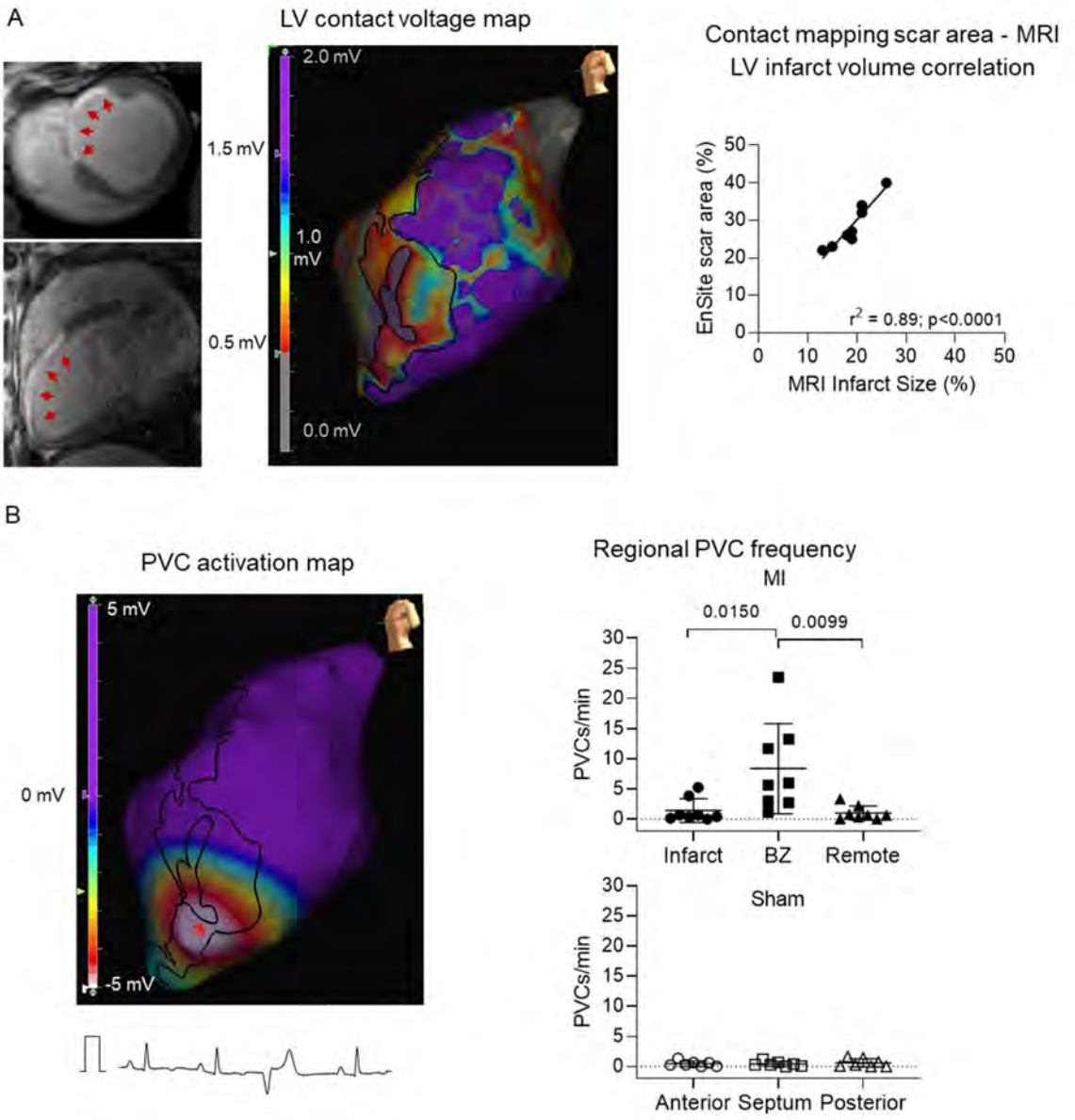

Figure 1. Origin of premature ventricular complexes (PVCs) during adrenergic stimulation *in vivo*.

A: Left, cMRI short axis (top) and long axis (bottom) slice with the infarct showing during late enhancement with Gd (red arrows). Middle, corresponding left anterior oblique (LAO) projection of bipolar voltage mapping illustrating the infarct (grey area, voltage < 0.5 mV), BZ, i.e. the region of voltage 0.5 mV (red) to 1.5 mV (blue), and remote myocardium (purple, voltage > 1.5 mV). Right, correlation between EnSite-defined scar area to cMRI-defined infarct volume (N = 8).

B: Left, LAO projection of the non-contact activation mapping of a PVC illustrating its origin from the anterior BZ. Right, summary data of regional location of PVC site of origin in MI (N = 8) and Sham (N = 7). Analysis of variance (ANOVA) with Bonferroni post-test.

PVCs in the BZ originate at short distances from the scar boundary

We transformed the 3D LV geometry to a 2D polar map, straightened the scar demarcation line (voltage < 0.5 mV, line of reference) and added the line of the outer BZ boundary (voltage > 1.5 mV). We then plotted PVC locations in this XY plot (Fig. 2A). The plot illustrates the variable thickness of the BZ and shows that on average 80% of the PVC were localized within the BZ (Fig. 2B). For this analysis, 1 MI with less than 50 PVCs was not included. Most PVCs originated within 0.2A.U. (~4mm distance) from the scar demarcation (Fig. 2C).

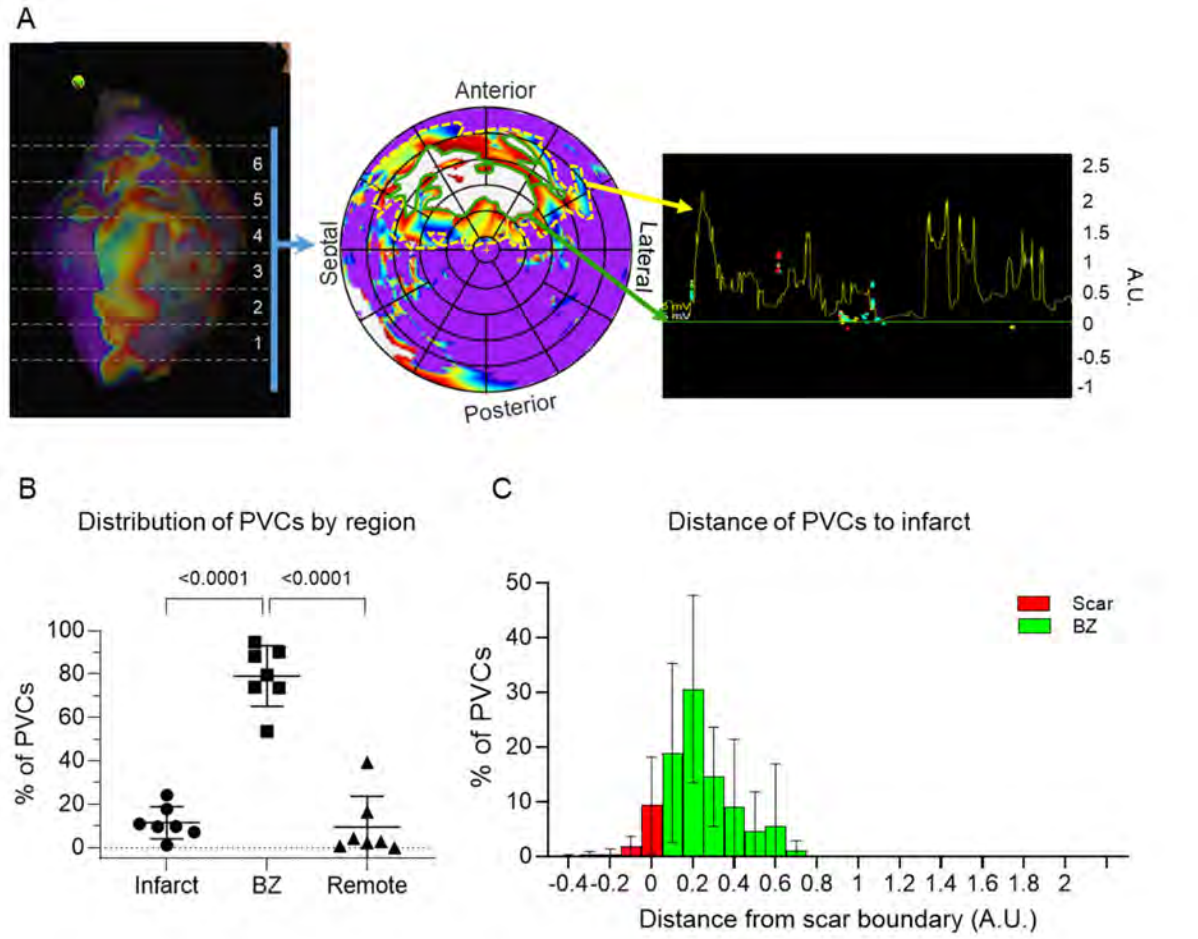

Figure 2. Spatial distribution of PVCs and distances from the scar boundary.

A: The 3D LV geometry (left) is transformed to a 2D polar map (middle) by segmentation into 6 levels with 12 radial spokes. The scar boundary is set as the zero reference and PVC distances calculated in arbitrary units (A.U.) (right).
B: PVCs by region, per pig, N=7. ANOVA with Bonferroni post-test.
C: Distribution of PVCs for distance to the scar boundary, mean ± SD, N=7.

PVCs cluster at discrete sites defining 'hotspots'

We further investigated whether there would be more discrete dominant vulnerable areas, 'hotspots', from which frequent PVCs would originate. We plotted PVC sites on a polar map and applied a custom-written algorithm that identified areas with frequent PVCs occurring in close proximity forming a cluster defined as >5 PVCs originating within a 0.1AU radius (Fig. 3A, see online supplement). In MI, 14/18 animals had most of their PVCs occurring in such clusters, which was particularly evident in animals with large number of PVCs (Fig. 3B). For comparable numbers, clustering in Sham was less pronounced (Fig. 3C). In the subset of animals with contact mapping of the BZ, we found that these PVC clusters were mostly seen in the BZ (Fig. 3D, left) and that BZ PVCs mostly occurred in clusters (Fig. 3D, right).

DADs are more frequent in the BZ and more prevalent at PVC cluster sites

Figure 4A illustrates definition of a site with frequent PVCs, annotated on the electroanatomical map (*, left panel), and LARCA view of the LV model (right panel). Figure 4B shows the resulting the polar map (left) and 3D LV model (right) of all PVC and non-PVC sites. Simultaneous recordings of MAPs at a PVC and non-PVC site (Figure 4C, Suppl. Fig. 4A) show frequent DADs at the PVC site (red arrows). Most, i.e. 82%, of PVC sites in MI had DADs, *vs*. only 40% of non-PVC sites, and *vs*. 50% of PVC sites in Sham (Fig. 4D), indicating the strong association of DADs with PVC-prone sites in MI. Within MI, DADs were found predominantly in the BZ (Fig. 4E). In Sham, no regional prevalence of DADs was detected (Suppl. Fig. 4B). The *in vivo* PVC sites for MAP recording matched with the later off-line defined PVC clusters (Fig. 3) for 21/22 sites in MI and 13/18 sites in Sham.

Capturing triggered action potentials arising from DADs at PVC-prone sites

We investigated whether we could detect a direct link between DADs and PVC *in vivo* and could observe in a number of MAP recordings a DAD that appeared to give rise to an action potential (AP), with the take-off of the AP >10 ms earlier than the associated PVC on the surface ECG (Fig. 5A). Although this phenomenon was rare, it occurred predominantly in MI (89%), where APs triggered by DADs were seen only in PVC sites (Fig. 5B).

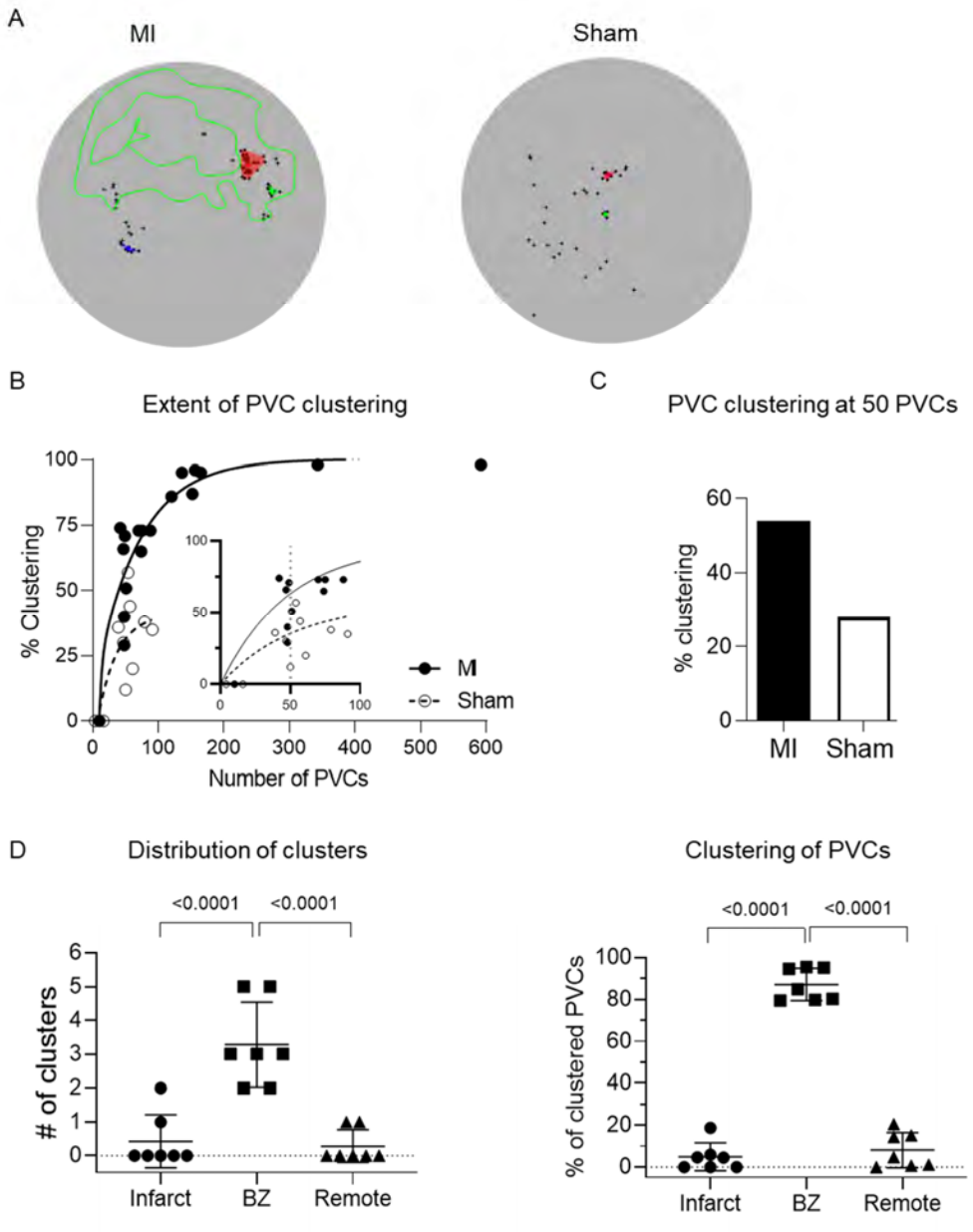

Figure 3. Spatial clustering of PVC sites of origin.
A: Polar maps of PVC sites (+) with identification of clusters (MI scar and BZ delineated): red and green within, blue outside the BZ.
B: Total number of PVCs and the extent of PVC clustering per pig, fitted with an exponential curve. Insert: a zoom into the first 100 PVCs illustrating the early divergent behavior of the fitted curve of MI from Sham. Curve fitting parameters: MI, N = 17, R^2 = 0.85, Tau_{fast} = 3.6; Sham, N = 14, R^2 = 0.55, Tau_{fast} = 29.2.
C: Extent clustering at 50 PVCs extrapolated from the curve fitted in B.
D: Regional distribution of clusters in the subset of MI animals with contact mapping (left) and clustering of PVCs by region (right). N=7, ANOVA with Bonferroni post-test.

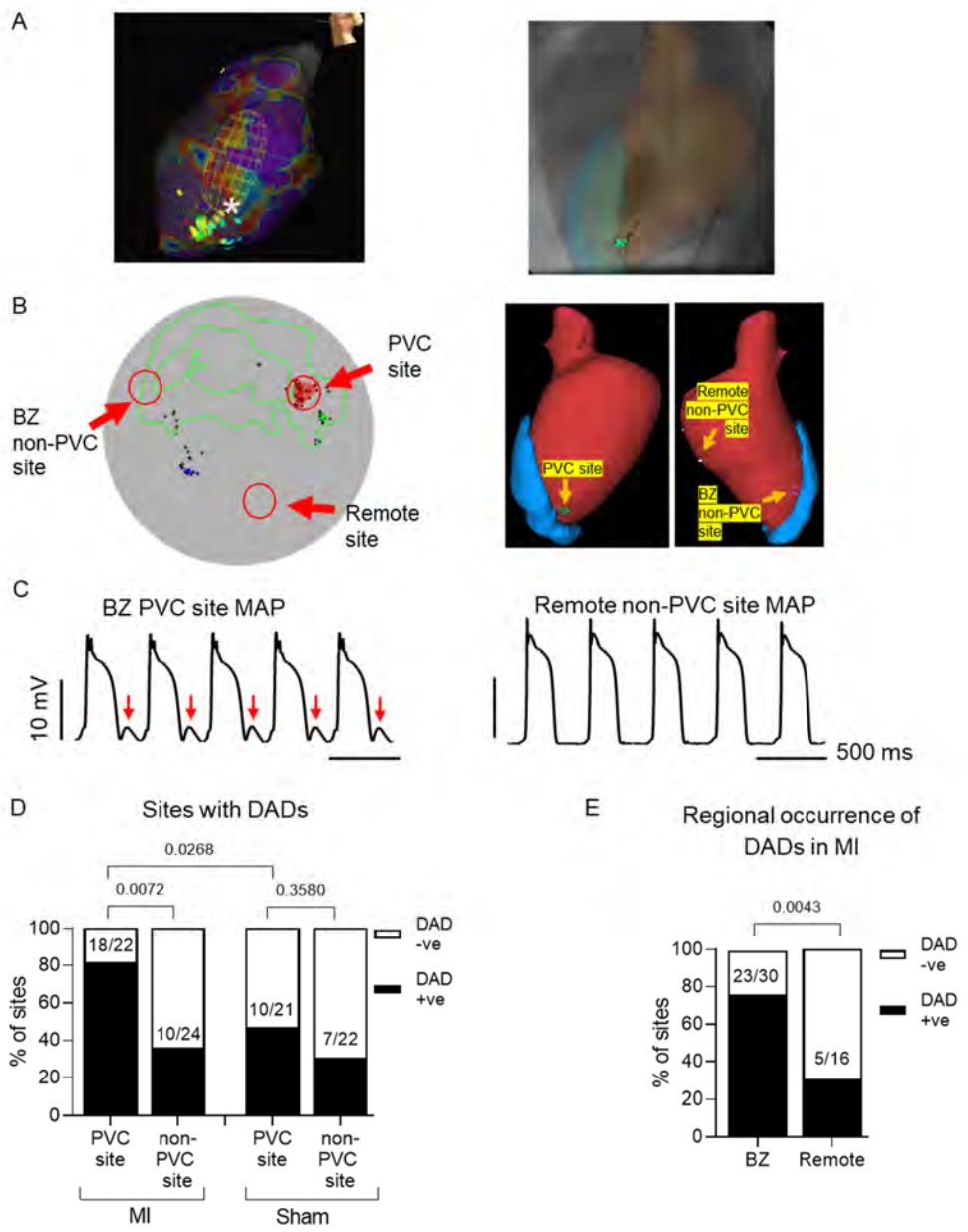

Figure 4. Occurrence of DADs at PVC- and non-PVC sites.
A: Left, EnSite LV mapping model highlighting a BZ PVC site with the mapping catheter marked (*). Right, the corresponding fluoroscopic view of the catheter with the augmented reality overlay of the cMRI model and PVC site tagged with green dots.
B: PVC site and non-PVC sites for site-directed monophasic action potentials (MAP) recordings on the polar map (left), and the 3D segmented cMRI model (right) with superimposed offline-defined clusters.
C: Simultaneously recorded MAPs from a BZ PVC site and remote non-PVC site, illustrating DADs at the BZ PVC site (red arrows).
D: Fraction of PVC- and non-PVC sites with DADs in MI and Sham. MI, N = 14 and Sham, N = 10. Fisher's exact test.
E: Regional distribution of the occurrence of DADs at PVC- and non-PVC sites in MI.

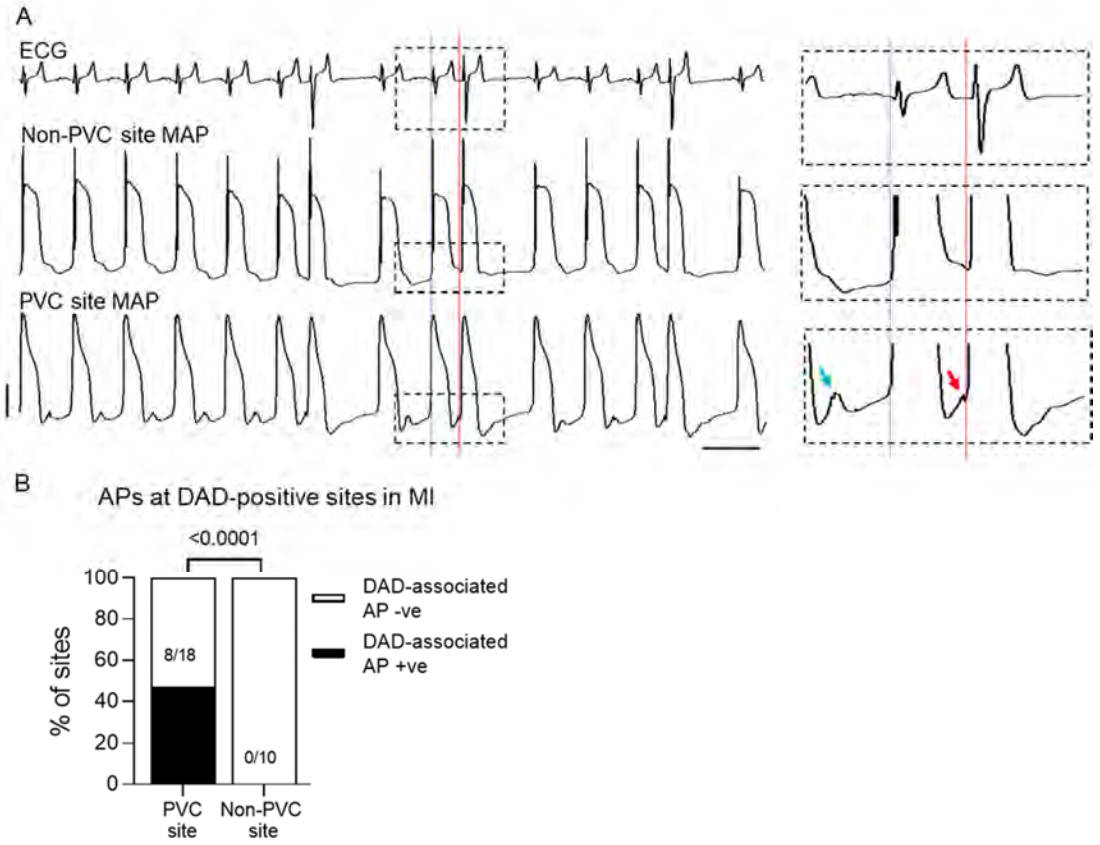

Figure 5. Association of DADs to occurrence of spontaneous action potentials.
A: Example of frequent DADs (blue arrow) that are associated with spontaneous action potential (red arrow) that translates to a PVC on the ECG.
B: Sites with observed DAD-associated APs in MI are restricted to PVC-sites. Fisher's exact test.

Arrhythmogenic remodeling of cardiomyocytes in the BZ

The *in vivo* findings of spontaneous activity suggest that cardiomyocyte remodeling mechanistically contributes to local vulnerability. MI BZ cardiomyocytes were significantly wider than those from MI remote and Sham (Suppl. Fig. 5A, B). The cell morphology was comparable in the anterior and septal BZ as was fibrosis (Suppl. Fig. 5C).

We assessed the cardiomyocytes' susceptibility to DADs and triggered APs under ISO (Fig. 6A). The incidence of triggered APs was significantly higher in MI BZ cardiomyocytes compared to remote and matched Sham cardiomyocytes (Fig. 6B, Suppl. Fig. 6A). However, there was no correlation between *in vivo* observations of a septal vs anterior BZ dominance in PVC origin and DAD incidence in cardiomyocytes from these subregions (Suppl. Fig. 6B). Resting membrane potential (RMP) in the presence of ISO was on average slightly but significantly less negative in BZ cardiomyocytes compared to remote and control cells (Fig. 6C). IK1, recorded as the Ba^{2+}-sensitive current at -30 and -90 mV (Fig. 6D) was reduced in BZ cardiomyocytes under ISO compared to remote and control cells (Fig. 6E).

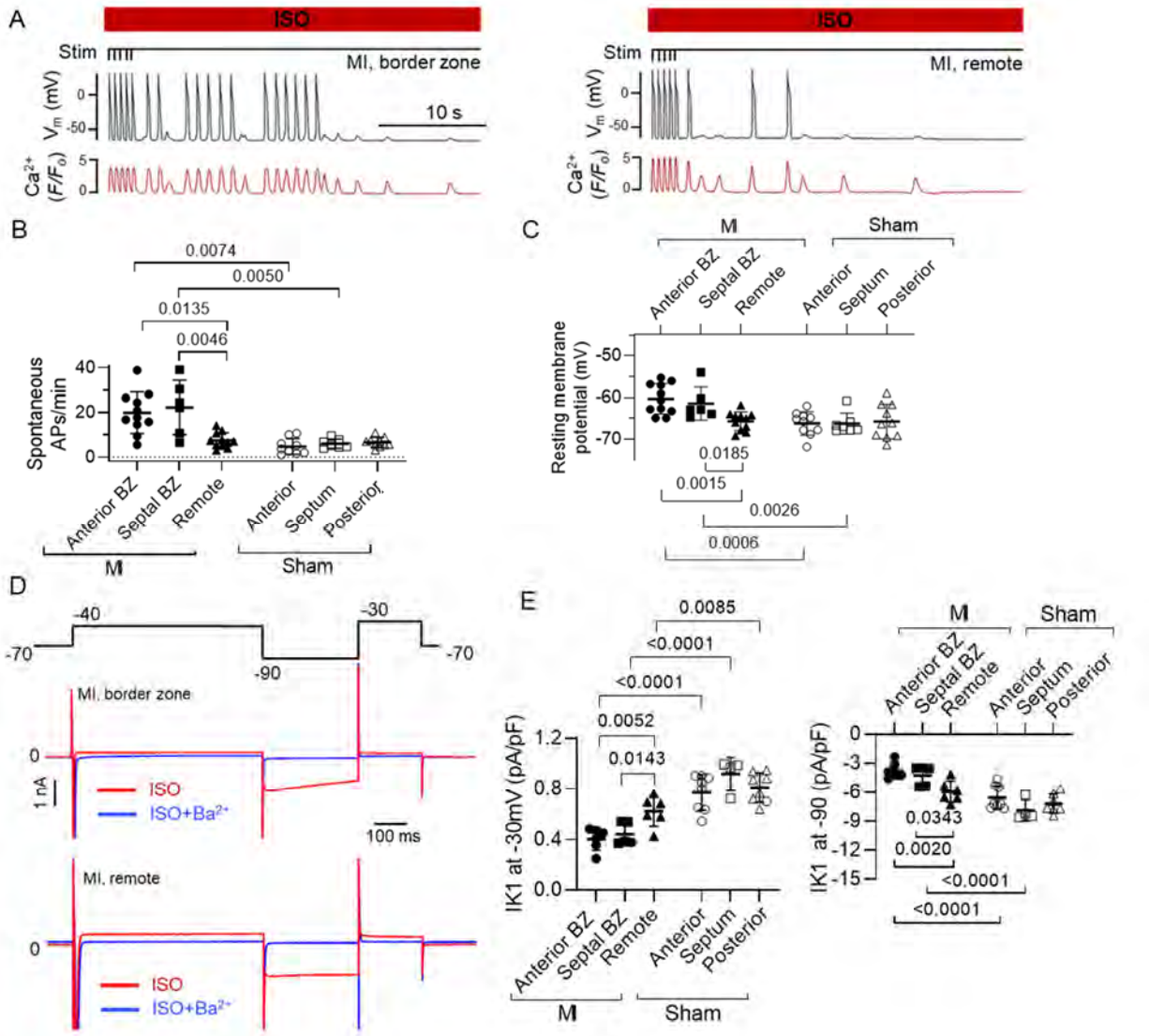

Figure 6. Differential regional remodeling of cardiomyocytes and propensity for DAD-triggered spontaneous action potentials.

A: Left, the last 5 stimulated APs (top) and calcium transients (bottom) of a 1-minute 2 Hz train (Stim) and the 30 seconds observation without stimulation illustrating spontaneous events. Right, the same recording protocol in a remote cardiomyocyte.

B: Frequency of spontaneous APs in regional MI cardiomyocytes matched Sham cells during the 30s observation after pacing under ISO. MI, n_{cells} = 45-70, N- N_{pigs} = 6-11 and Sham, n_{cells} = 39-63, N_{pigs} = 7-10. Mixed model ANOVA with Bonferroni post-test.

C: Resting membrane potential (RMP) under ISO for cells presented in D. Note that RMP was not corrected for junctional potential (~-11 mV).

D: Top, voltage clamp protocol used to record IK1 as the Ba^{2+}-sensitive current under ISO. Middle, example of the currents recorded in a MI BZ cell, and an MI remote cell (bottom).

G: Outward and inward IK1 at -30 mV (left) and -90 mV (right) respectively in cardiomyocytes from MI and Sham. MI, n_{cells} = 14-21, N_{pigs} = 5-6 and Sham, n_{cells} = 16-24, N_{pigs} = 4-8. Mixed model ANOVA with Dunn's post-test.

Threshold for adrenergic response in BZ cardiomyocytes and *in vivo*

The increased incidence of spontaneous calcium release in MI BZ cardiomyocytes could be due to an enhanced adrenergic sensitivity. At 10, 25 and 50 nM ISO, MI cardiomyocytes had significantly more triggered APs than Sham (Fig. 7A). The fitted Hill equation (Fig. 7A, right panel) showed a similar maximal response, with a lower half maximal effective concentration (EC50) in MI than Sham (47 nM vs 72.9 nM, $P < 0.01$) consistent with increased sensitivity.

In vivo, the chronotropic response in MI was similar to Sham while PVC incidence was higher but only at 0.02 µg/kg ISO (Suppl. Fig. 7A, B). This translated into a narrow arrhythmogenic heart rate window of ~90-100 bpm (Fig. 7B). Altered adrenergic sensitivity in cardiomyocytes correlated well with *in vivo* susceptibility (Fig. 7C).

Frequent PVCs and lethal arrhythmias after MI occur during elevated adrenergic tone *in domo*.

Lastly, we explored the relation between adrenergic drive and arrhythmia in awake, freely moving animals. On average, MI animals had higher heart rates (Fig. 8A). We focused on episodes of high heart rate as a proxy for increased adrenergic drive and analyzed ECG strips of episodes with HR > 170bpm in detail (Fig. 8B). MI animals had significantly more PVCs than Sham. We also observed more complex arrhythmias and non-sustained VT (Fig. 8C) as well as sustained VT degenerating to VF and death in 2 of 7 MI animals under monitoring (Fig. 8D).

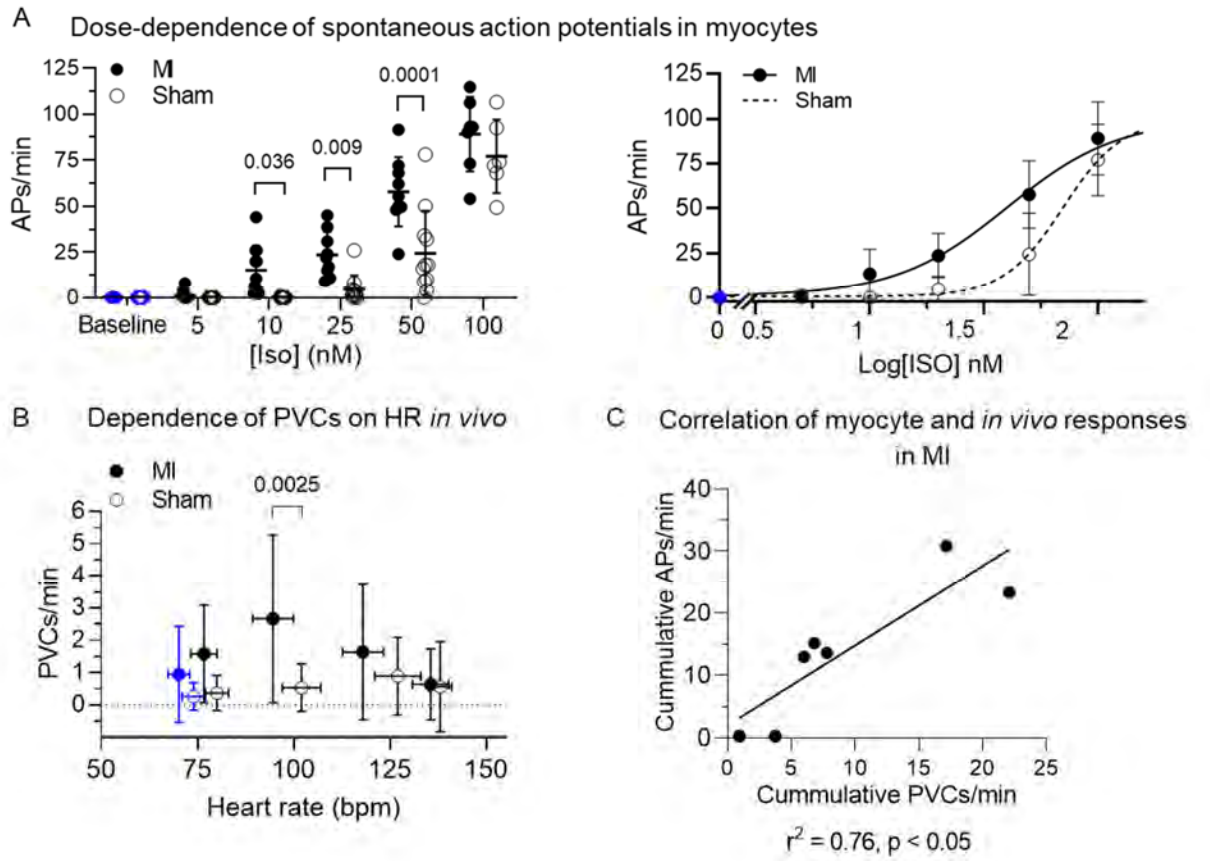

Figure 7. β-adrenergic sensitivity to spontaneous action potentials in cardiomyocytes and *in vivo*.

A: Left, Incidence of spontaneous APs at the various doses of ISO in MI, n_{cells} = 70, N_{pigs} = 11 and Sham, n_{cells} = 63, N_{pigs} = 10. Repeated measures ANOVA with Bonferroni posttest. Right, mean data fitted with a Hill logistic equation.

D: PVC incidence relationship to heart rate *in vivo*.

E: Correlation of the incidence of spontaneous PVCs *in vivo* to the incidence of spontaneous APs in isolated cardiomyocytes from MI, N_{pigs} = 7. Linear regression analysis.

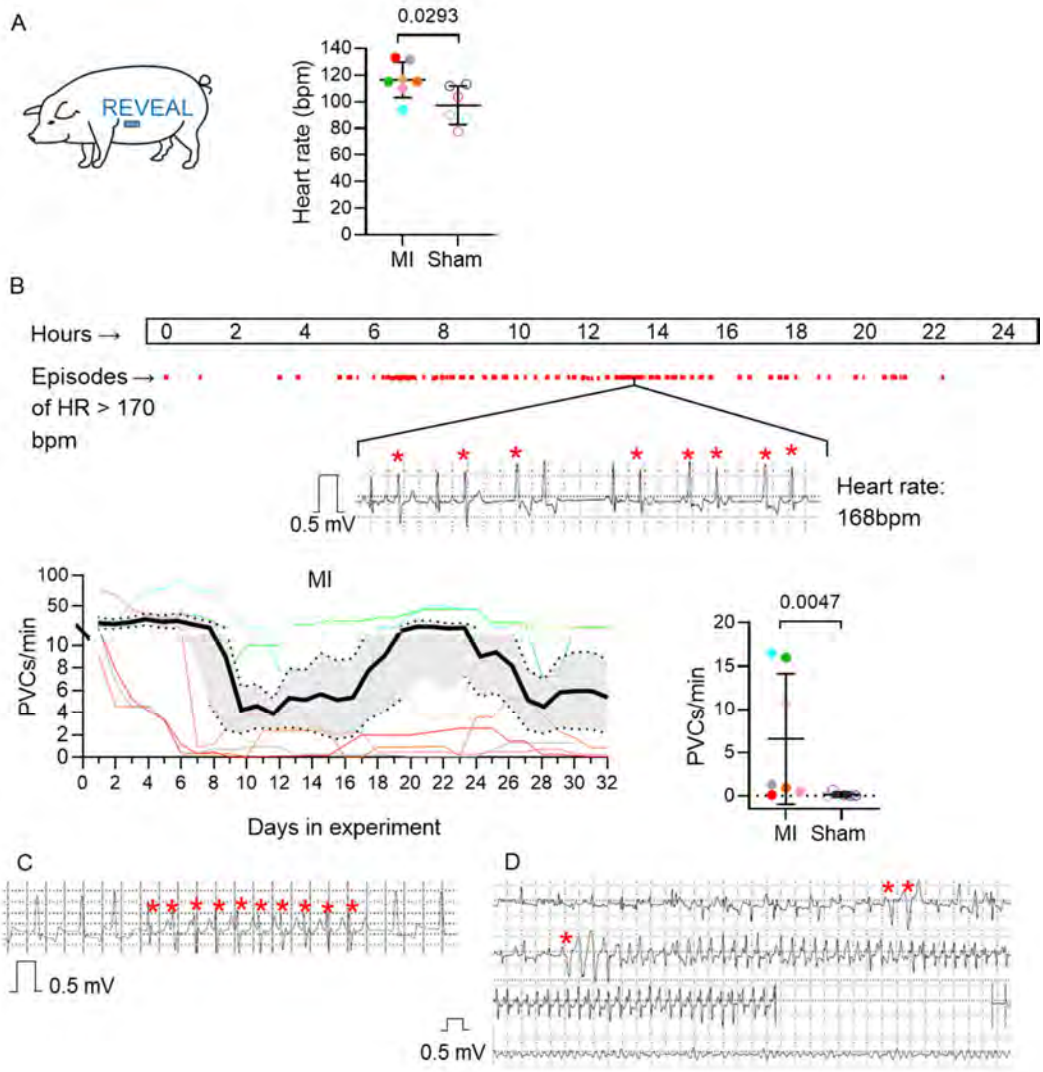

Figure 8. Occurrence of PVCs, complex arrhythmias and sudden cardiac death during moderately elevated adrenergic tone.

A: Average heart rate recorded by the REVEAL loop recorder device during the 4th week, immediately prior to the electrophysiological study. MI, N_{pigs} = 7 and Sham, N_{pigs} = 6. Unpaired t-test.

B: Top, protocol for analysis of REVEAL data. Every 2-3 days, the device was interrogated and the ECG strips of last 20 episodes of HR > 170 bpm were reviewed and PVCs (*) counted. Bottom: daily trends of the PVC burden in MI, N_{pigs} = 7 (left). Summary data of the average PVC incidence during the 4th week, immediately prior to the electrophysiological study (right). MI, N_{pigs} = 7 and Sham, N_{pigs} = 6. Unpaired t-test.

C: Example of a run of non-sustained ventricular tachycardia (*).

D: Example of documented sudden cardiac death in MI. Recurrent PVCs (*) initiate VT degenerating into VF and death.

DISCUSSION

Discrete vulnerable areas within the BZ

We developed a two-stage experimental protocol, combining imaging and electrophysiology, with multi-layered analysis that allowed us to precisely locate hotspots of PVCs under β-adrenergic stimulation, 4 weeks after MI. A major advance was the recording of spontaneous PVCs in an unbiased real-time approach by non-contact mapping [15]. The augmented reality angiography system allowed us to tag PVC sites and record simultaneous MAPs to identify mechanisms involving afterdepolarizations that are not detected by conventional catheter studies.

We identified discrete dominant cluster sites of PVCs close to the infarct border. Point-by-point mapping in post-MI patients also found that frequently PVCs originate from vulnerable areas in low voltage areas around the scar boundary, relating PVC to VT exit sites [7,12,16]. The present data add another dimension to these findings as we recorded spontaneous events and showed they cluster in hotspots. The consistency of observing clusters in the BZ across animals, but in different locations, indicates that in each individual there is a unique BZ remodeling that locally creates vulnerable areas. Until now, post-MI vulnerable areas were mostly viewed from the point of re-entry, which remains the central mechanism for arrhythmia perpetuation, and guides ablation [17]. Whether spontaneous events map to similar sites remains to be investigated.

Role of cardiomyocyte DADs and local environment in ventricular ectopy

We co-localized cardiomyocyte-driven events and PVCs and observed transitions from DADs to triggered APs, providing a basis for DAD-driven triggered activity underlying PVCs. This phenomenon remained infrequent most likely due to the narrow window of observation in space (sampling MAP at one location) and time (MAP recordings for 2 minutes). Other mechanisms including micro-reentry and Purkinje depolarization were not investigated and cannot be excluded.

Taken out of their local environment, BZ cardiomyocytes had unique properties, confirming previous observations [9,11]. Mechanisms that lead to this BZ remodeling signature may include inflammation and activated fibroblasts[14], altered innervation [3,4], and mechanical stress [18]. The thickening of BZ cardiomyocytes, not present in remote regions, points to a local higher wall stress as a result of local wall thinning. Electrophysiological remodeling of ion channels in BZ myocytes occurs [9], particularly IK1 which is reduced to a greater extent during adrenergic stimulation. This translates to a less negative RMP – a lower threshold for triggered activity, and reduced counterbalancing outward currents allowing larger membrane voltage changes for a given DAD [19]. Such unique cardiomyocyte profiles can offer opportunities for local therapy [20].

Local environment further uniquely modulates the BZ cardiomyocyte behavior *in vivo*, as indicated by differential behavior of septal and anterior BZ in individual animals. The likelihood of DAD-triggering of a PVC is increased with diminished cell-cell coupling due to reduced or altered localization of conexin-43 [21], that overcomes source-sink mismatch, as cardiomyocytes are not effectively voltage clamped [22].

Ventricular ectopy and arrhythmias at moderate sympathetic drive

The increased occurrence of DADs and spontaneous APs in BZ cardiomyocytes is due to a leftward-shifted in adrenergic response, which, in cardiomyocytes, can be studied without

concurrent change in heart rate. *In vivo*, with high levels of stimulation, high heart rates may induce overdrive suppression of PVCs, seen in the anesthetized animals. In non-anesthetized animals, arrhythmias occurred during periods of increased adrenergic drive characterized by increased heart rate, higher than in the anesthetized animals, but still below the maximum seen in pigs during exercise [23]. Together this would imply that arrhythmias are likely to be triggered during moderate sympathetic drive.

Limitations

The MEA used for non-contact mapping is an endocardial tool that may increase ectopy if the catheter touches the wall during mapping. We used a biplane ventriculogram to aid catheter positioning, and if contact was suspected, the mapping was redone after positioning the catheter optimally. Another limitation is that the MEA sensitivity cannot capture small amplitude or local events such as Purkinje fiber depolarizations or micro-reentry potentials; neither can it discriminate if the true focus may lie epicardial or intramural.

Cellular correlative studies with discrete PVC sites are limited by lack of site-directed sampling or direct *in situ* study of cardiomyocytes in the BZ environment. Such techniques are currently beyond reach, requiring further technological development.

We used ISO for β-adrenergic stimulation to probe spontaneous events and avoid the confounding peripheral hemodynamic effects of α-adrenergic stimulation. Whether these spontaneous events occur during direct nerve stimulation was not investigated in this study.

Clinical implications and future directions

In preliminary experiments, we established that VT inducibility is greater in animals that have a high burden of PVCs and clustering in the BZ, suggesting that PVC clustering may be a surrogate for arrhythmogenicity. The identification of vulnerable areas within the BZ, where PVCs can arise and trigger arrhythmia during adrenergic stimulation may have clinical relevance in risk stratification for SCD and in the indication to implant a defibrillator in primary prevention.

These findings also support trigger ablation in discrete vulnerable areas of the BZ in the therapeutic approach to post-MI VT, particularly in hemodynamically unstable or unmappable VT where the perpetuating reentry mechanism cannot be untangled [24].

Spontaneous activity in cardiomyocytes, documented in the present study, could be complementary to abnormal Purkinje fiber activity previously reported [25]. A unifying hypothesis to consider is an interplay between cardiomyocyte DADs and the purkinje depolarization resulting in parasystolic modulation and generation of PVCs. Further investigation of these mechanisms *in vivo* and their interplay in the BZ should be a focus of future study.

In conclusion, our data indicate that unique properties of remodeled cardiomyocytes in the infarct BZ together with a facilitating environment define discrete vulnerable areas in the BZ that can initiate arrhythmia under adrenergic stress *in vivo*.

Acknowledgments

The authors thank Patricia Holemans, Roxane Menten and Annemie Biesemans for expert technical assistance with the experimental data acquisition and animal care.

Funding Sources

This work was supported by the Fund for Scientific Research-Flanders (FWO project grants G.0918.15 and G097021N; Senior Clinical Investigator Felloship to RW and Junior Research Fellowship to MA) and by the BOF research fund of KU Leuven (to RW and PC).

REFERENCES

1. Hayashi M, Shimizu W, Albert CM: The Spectrum of Epidemiology Underlying Sudden Cardiac Death. Circ Res 2016; 116:1887–1906.

2. Shen MJ, Zipes DP: Role of the autonomic nervous system in modulating cardiac arrhythmias. Circ Res 2014; 114:1004–1021.

3. Ajijola OA, Yagishita D, Patel KJ, et al.: Focal myocardial infarction induces global remodeling of cardiac sympathetic innervation: Neural remodeling in a spatial context. Am J Physiol - Heart Circ Physiol 2013; 305:1031–1040.

4. Gardner R, Wang L, Lang B, et al.: Targeting protein tyrosine phosphatase σ after myocardial infarction restores cardiac sympathetic innervation and prevents arrhythmias. Nat Commun 2015; 6:1–9.

5. Vaseghi M, Lux RL, Mahajan A, Shivkumar K: Sympathetic stimulation increases dispersion of repolarization in humans with myocardial infarction. Am J Physiol Heart Circ Physiol 2012; 302:H1838-1846.

6. Doytchinova A, Patel J, Zhou S, et al.: Subcutaneous nerve activity and spontaneous ventricular arrhythmias in ambulatory dogs. Heart Rhythm Elsevier, 2015; 12:612–620.

7. Marrouche NF, Verma A, Wazni O, et al.: Mode of initiation and ablation of ventricular fibrillation storms in patients with ischemic cardiomyopathy. J Am Coll Cardiol 2004; 43:1715–1720.

8. Belevych AE, Terentyev D, Terentyeva R, et al.: Shortened Ca 2+ signaling refractoriness underlies cellular arrhythmogenesis in a postinfarction model of sudden cardiac death. Circ Res 2012; 110:569–577.

9. Hegyi B, Bossuyt J, Griffiths LG, et al.: Complex electrophysiological remodeling in postinfarction ischemic heart failure. Proc Natl Acad Sci USA 2018; 115:E3036–E3044.

10. Priori SG, Mantica M, Schwartz PJ: Delayed afterdepolarizations elicited in vivo by left stellate ganglion stimulation. Circulation 1988; 78:178–185.

11. Dries E, Amoni M, Vandenberk B, et al.: Altered adrenergic response in myocytes bordering a chronic myocardial infarction underlies in vivo triggered activity and repolarization instability. J Physiol 2020; 598.

12. Bogun F, Crawford T, Chalfoun N, et al.: Relationship of frequent postinfarction premature ventricular complexes to the reentry circuit of scar-related ventricular tachycardia. Heart Rhythm 2008; 5:367–374.

13. Ector J, De Buck S, Adams J, et al.: Cardiac three-dimensional magnetic resonance imaging and fluoroscopy merging: A new approach for electroanatomic mapping to assist catheter ablation. Circulation 2005; 112:3769–3776.

14. Nagaraju CK, Dries E, Popovic N, et al.: Global fibroblast activation throughout the left ventricle but localized fibrosis after myocardial infarction. Sci Rep Springer US, 2017; 7:1–14.

15. Kim YH, Chen SA, Ernst S, et al.: 2019 APHRS expert consensus statement on three-dimensional mapping systems for tachycardia developed in collaboration with HRS, EHRA, and LAHRS. J Arrhythmia 2020; 36:215–270.

16. Sarrazin JF, Good E, Kuhne M, et al.: Mapping and ablation of frequent post-infarction premature ventricular complexes. J Cardiovasc Electrophysiol 2010; 21:1002–1008.

17. Prakosa A, Arevalo HJ, Deng D, et al.: Personalized virtual-heart technology for guiding the ablation of infarct-related ventricular tachycardia. Nat Biomed Eng Springer US, 2018; 2:732–740.

18. Frisk M, Ruud M, Espe EKS, et al.: Elevated ventricular wall stress disrupts cardiomyocyte t-Tubule structure and calcium homeostasis. Cardiovasc Res 2016; 112:443–451.

19. Pogwizd SM, Schlotthauer K, Li L, Yuan W, Bers DM: Arrhythmogenesis and Contractile Dysfunction in Heart Failure: Roles of Sodium-Calcium Exchange, Inward Rectifier Potassium Current, and Residual Beta-Adrenergic Responsiveness. Circ Res 2001; 88:1159–1167.

20. Sasano T, McDonald AD, Kikuchi K, Donahue JK: Molecular ablation of ventricular tachycardia after myocardial infarction. Nat Med 2006; 12:1256–1258.

21. Aiba T, Noda T, Hidaka I, et al.: Acetylcholine suppresses ventricular arrhythmias and improves conduction and connexin-43 properties during myocardial ischemia in isolated rabbit hearts. J Cardiovasc Electrophysiol 2015; 26:678–685.

22. Lang D, Sato D, Jiang Y, Ginsburg KS, Ripplinger CM, Bers DM: Calcium-Dependent Arrhythmogenic Foci Created by Weakly Coupled Myocytes in the Failing Heart. Circ Res 2017; 121:1379–1391.

23. Stubenitsky R, Verdouw PD, Duncker DJ: Autonomic control of cardiovascular performance and whole body O2 delivery and utilization in swine during treadmill exercise. Cardiovasc Res 1998; 39:459–474.

24. Nogami A: Mapping and Ablating Ventricular Premature Contractions That Trigger Ventricular Fibrillation: Trigger Elimination and Substrate Modification. J Cardiovasc Electrophysiol 2015; 26:110–115.

25. Haissaguerre M, Vigmond E, Stuyvers B, Hocini M, Bernus O: Ventricular arrhythmias and the His–Purkinje system. Nat Rev Cardiol 2016; 13:155–166.

Online Supplement to Amoni et al. *Discrete sites of frequent premature ventricular complexes cluster ...'*

List of Abbreviations

MI	Myocardial infarction
VT/VF	Ventricular tachycardia / fibrillation
SCD	Sudden cardiac death
BZ	Border zone
PVC	Premature ventricular complex
DAD	Delayed afterdepolarization
LV	Left ventricle
ISO	Isoproterenol
cMRI	Cardiac magnetic resonance imaging
MAP	Monophasic action potential
AU	Arbitrary units
LARCA Leuven	augmented reality catheter ablation tool
ECG	Electrocardiogram
AP	Action potential

Expanded Methods

Pig model of myocardial infarction

Domestic pigs (Strain: TN70, Topigs Norsvin) of both sexes (34±4 kg) were used in this study. Forty-three animals entered the study of which thirty-six were included in the final data set. Seven animals were excluded due to anesthesia complications (5), failed vascular access (1) and failure to thrive (1). Animals were housed individually and treated according to the Guide for the Care and Use of Laboratory Animals (National Institute of Health, USA), and the European Directive 2010/63/EU. A standard 14 h light, 10 h dark cycle, 22 ± 2°C temperature and 45-70 % humidity was maintained. A standard chow (Optivo Pro 9041, AVEVE, Belgium) and water were provided *ad libitum* except in the days prior to and after experimental procedures when they were either fasted or fed twice a day (between 7-8am and 12-2pm), with welfare monitoring. The experimental protocols were approved by the in-house ethical committee (Ethische Commissie Dierproeven, KU Leuven), with permit number ECD137/2018.

All *in vivo* interventions were performed under general anesthesia. The protocol consisted of sedation with tiletamine/zolazepam 8 mg/kg and xylazine 2.5 mg/kg IM, induction and maintenance of anesthesia with Propofol 3 mg/kg and 10 mg/kg/h IV respectively, combined with remifentanil 0.2-0.4 µg/kg/h IV. Animals received endotracheal ventilation at 6-10 ml/kg tidal

volume of 50% oxygen-air mixture. Antibiotics (Cefazolin 22-50 mg/kg, IV) and anticoagulation (acetylsalicylic acid, 500 mg and periodic heparin 5 000-10 000 IU, IV) were routinely administered.

We use a coronary occlusion-reperfusion model of MI that reflects clinical practice of reperfusion and is more relevant in infarct size, ejection fraction and arrhythmic risk than the stenosis-induced MI model we have previously used [1]. Before MI induction, all animals were pre-medicated for three days with Amiodarone 300 mg, as well as one day of Aspirin 300 mg and Clopidogrel 300 mg, then randomized to either MI induction or Sham operation on day 0. MI was induced under anesthesia by coronary balloon occlusion-reperfusion as described before [2]. Briefly, via the carotid artery, a 6/7 Fr Judkins-left coronary guiding catheter was positioned in the left main coronary ostium under fluoroscopic guidance. A 2.5-3.0 mm angioplasty balloon, was completely inflated in the left anterior descending (LAD) immediately after the first diagonal branch (D1). Amiodarone 5 mg/kg, IV bolus as given to reduce arrhythmias and an intracoronary bolus of nitroglycerine 250-300 mg to prevent vasospasm. The balloon was inflated to ~12 bar and resulted in total occlusion of the LAD, confirmed by angiography (Suppl. fig. 1A) and evident from ST-segment elevation. Occlusion was maintained for 120 minutes, followed by release and reperfusion with at least 60 minutes monitoring. In the event of sustained ventricular tachycardia or fibrillation, external defibrillation with a shock of 150-200J was applied to restore sinus rhythm. Sham animals, which undergo the same procedure, without occlusion, were included as controls. Post-operatively animals received broad-spectrum antibiotics (Amoxicillin 15mg/kg or Enrofloxacilin 4mg/kg) with analgesia, Buprenorphine HCl 0.02-0.03mg/kg, IM. All animals received Amiodarone for 3 days. Aspirin 100 mg and Clopidogrel 75 mg was given daily for 1 month.

No animals died during MI induction procedure. Early mortality (<5 days post-MI) was 13% (3 MI), due to confirmed (2) or suspected SCD (1) after MI.

Implantable cardiac monitor and arrhythmia monitoring

In a subset of 7 MI and 6 Sham animals, a clinical cardiac monitoring device (REVEAL XT™ or LINQ™, Medtronic, Belgium) was implanted subcutaneously in the left-side of the chest, at the level of the 4th intercostal space (approximating the location of the conventional V2 ECG electrode) to sample cardiac rhythm. The device was secured at the location with the best QRS amplitude. In order to screen the animals for arrhythmias during periods of adrenergic drive (defined as increased heart rate ≥ 170 bpm), the device loop recording parameters were programmed to a VT detection threshold of 170bpm, and atrial sensing off, allowing recording only of ECG strips during high heart rate. The gain and sensitivity settings were adjusted to achieve optimal detection of the QRS complex. To capture sufficient episodes before the loop recording overwrite, the devices were interrogated every 2-3 days and the ECG strips (each approximately 30 seconds) of the last 20 recordings were downloaded for analysis of arrhythmias and premature ventricular complexes (PVCs).

Cardiac magnetic resonance imaging

After 1 month, heart structure, dimensions and function as well as left ventricle (LV) infarct size was assessed by cardiac magnetic resonance imaging (cMRI) using a 3 Tesla whole-body scanner (PRISMA, Siemens, Erlangen, Germany) as previously described [3]. Infarct size and morphology was determined by late gadolinium enhancement (LGE), 12 minutes following a

double dose bolus of Gd (gadoterate meglumine, Dotarem, 0.2 mmol kg^{-1}) (Fig 1A). Suppl. table 1 summarizes the structural and functional remodeling after MI.

The CMR data was analyzed and images segmented with custom software (RightVol; KU Leuven) on an offline workstation to obtain a 3D model of the LV myocardium, the LGE-infarct region, as well as the aortic arch with coronary ostia and brachiocephalic arteries, with millimeter accuracy for use in the *in vivo* study (Suppl. fig. 1B). 2-4 days after the CMR, an *in vivo* electrophysiology (EP) study was performed.

Cardiac electrophysiology study

For *in vivo* electrophysiological studies, animals were sedated with Tiletamine/Zolazepam 8 – 12 mg/kg only, omitting xylazine to avoid its adrenergic blocking effects. For cardiac catheterization, two arteries (carotid or femoral) and two veins (jugular or femoral) were cannulated with an 8 or 9 Fr introducer sheath for arterial access and 7 Fr sheaths for venous access. A single bolus of aspirin (500 mg), and periodic boluses of heparin (5 000-10 000 IU) was administered for anticoagulation. Standard electrophysiology (EP) catheters (Biosense Webster, Diegem, Belgium) were positioned in the coronary sinus (WEBSTER CS decapolar, Biosense Webster, Diegem, Belgium) and the RV apex (DECANAV quadripolar, Biosense Webster, Diegem, Belgium) for orientation and diagnostic signals.

Electroanatomical mapping of the left ventricle (LV) endocardium was performed using the EnSite Precision 2.0 mapping system (Abbott Medical, New Jersey, USA) paired with a BARD Electrophysiology Labsystem Pro EP (Boston Scientific, USA). The EnSite system consists of a 9 Fr 64-electrode multi-electrode array (MEA) catheter for non-contact mapping, and an amplifier system for input of conventional EP catheter signals from the paired BARD, and connected to a workstation, which is used to run the EnSite Precision software [4]. Under bi-plane fluoroscopic guidance, the MEA, was deployed centrally in the LV chamber using the 9 Fr arterial access, with the pigtail in the apex strategically to a stable position without catheter movement and contact with LV. To create an electroanatomical map, the MEA was paired to a mapping EP catheter (decapolar LASSO or quadripolar NAVISTAR DS, Biosense Webster, Diegem, Belgium) used to rove the LV and create and collect points of the endocardial geometry that are registered by the MEA non-contact anatomical map.

After the detailed anatomical map of the LV was created, the roving catheter was withdrawn from the LV and only non-contact mapping was performed using virtual electrograms from the MEA that were sampled at 1.2 kHz and filtered with a bandwidth of 0.1–300Hz. Left ventricular pressure was continuously monitored via the MEA central lumen. Following a stabilization period of approximately 20 minutes, the baseline sinus activation of the LV was recorded by non-contact electroanatomical mapping for 5 minutes. To simulate adrenergic stimulation, Isoproterenol (ISO) was infused in incremental doses of 0.01 µg/kg for 5 minutes until 0.04 µg/kg (4 steps, total duration of 20 minutes) during continuous non-contact mapping.

In a subset of animals (8 MI, 7 Sham), during creation of the detailed anatomical map of the LV, simultaneous contact bipolar voltages were annotated on the map to create an electroanatomical map [5]. This contact based voltage-mapping was used to define the conventional BZ using peak-to-peak voltages with the BZ defined as points with voltage > 0.5 mV and < 1.5 mV (Fig. 1B) [6–8]. In the rest of animals (10 MI, 3 Sham), only a non-contact activation map to identify PVC sites of origin (SOO) was created to reduce mapping time. 2 MI animals had catheter-induced intractable ventricular fibrillation during mapping and could not be

defibrillated leading to circulatory death. While another 2 MI and 2 Sham had high heart rates after ISO and eventually died during recovery, thus excluding them from further study.

A period of at least 1-hour recovery was observed to allow washout of the ISO and off-line mapping and manual annotation of PVC activation on the LV map. The sinus activation was first mapped and annotated (normally a consistent breakout originating in the basal septum (Suppl. fig. 2D). Then, all PVCs were annotated by placing a virtual lesion at the site of earliest activation determined using the tracking virtual and earliest activation of virtual electrodes [9]. Five pigs (3 MI, 2 Sham) had high heart rate (>120 bpm) after mapping and ISO, precluding MAP study. For the MAP study, the top 3 most common occurring PVC sites of origin and morphology were selected for further investigation; PVCs from the RV were not included. To facilitate local recordings, the mapping catheter was positioned at the PVC sites and these were tagged on an anatomical LV model using an augmented reality tool (LARCA, Leuven Augmented Reality Catheter Ablation) [10,11]. Briefly, a bi-plane left ventriculogram in left anterior oblique (LAO) 50° with caudal angulation of 15-20° and right anterior oblique (RAO) 30° was performed with a 50-80% contract-saline mixture delivered via a pressure injector and pigtail in the LV. This was used to fuse the real-time fluoroscopy with the pre-procedural cMRI model of the heart. The quadripolar mapping catheter was then positioned at the top 3 most common PVC-sites identified guided by the EnSite navigation (Fig. 4A). The position of the catheter was then stored on a bi-plane fluoroscopy system and tagged on the LARCA tool. Thereafter, the MEA was withdrawn from the LV and two monophasic action potential (MAP) catheters (MedFact GmbH, Germany) were inserted for local recordings without the MEA obstructing maneuverability (Suppl. Fig4A). The registration error of the LARCA system has been estimated to be approximately 1.5mm in prior work [10,11], and positioning accuracy has been verified to be within ~2mm using the current setup [12] (Amoni *et al.*, Unpublished).

The MAP catheter is a 7Fr deflectable quadripolar Ag-AgCl electrode catheter that was connected to the BARD Labsystem via a 4-pole connector. Under augmented reality fluoroscopic guidance, the MAP catheter was positioned at PVC sites and at selected non-PVC sites (or matched regions in Sham). The CS or RV catheter was then re-positioned in the high right atrium for atrial pacing. Continuous arterial pressure via the 9Fr sheath, the 12-lead electrocardiogram (ECG) and simultaneous MAPs were recorded at 4 kHz with bandwidth filtering between 0.01 – 1000 Hz, using the BARD Labsystem. To eliminate effects of heart rate variations on baseline MAPs, animals were atrially paced at 90 (if sinus rate allowed) and 120 bpm, and recordings were performed at baseline and during infusion with ISO, tailored to the maximum PVC provocative dose observed during the EnSite testing targeting a similar HR increase. At baseline, the following acceptance criteria for MAP recordings were applied: 1) amplitude of at least 10 mV, 2) stable baseline. DADs were defined as an increase in baseline potential exceeding 0.5mV in amplitude and having a positive diastolic angle [13]. MAPs were recorded and analyzed over a period of 2 minutes at baseline and during ISO infusion.

After the MAP study, surgical access was repaired and hemostasis achieved, and the animal recovered with appropriate analgesia (Buprenorphine HCl 0.03-0.05 mg/kg, IM and Fentanyl transdermal patch (12 µg/hr for 72 hr) and antibiotics as appropriate Amoxicillin15mg/kg or Enrofloxacilin 4mg/kg.

After 1-3 days recovery following the EP study, animals were sacrificed for tissue sampling and cell isolation. Procedure-related mortality after EP study was ~16% (4 MI and 2 Sham).

Sacrifice and cell isolation

For sacrifice, animals were sedated as described above, anaesthesia was induced with pentobarbital (20 mg/kg pentobarbital, IV) and artificial ventilation performed. Through a sternotomy, the heart was quickly harvested after anticoagulation with heparin (20 000IU) and placed in cold oxygenated Tyrode's solution. From MI hearts, LV wedges of the anterior BZ, the septal BZ and the non-infarcted remote region were dissected and their perfusing arterial branch cannulated. In Sham hearts, the matching regions from the anterior, septal and posterior LV wall were chosen. The wedges were perfused with a constant flow (3-4 ml/min) at 37°C. The tissue was briefly perfused with normal Tyrode's to washout remaining blood (in mmol/L: NaCl 137, KCl 5.4, $MgCl_2$ 0.5, $CaCl_2$ 1.8, Na-HEPES 11.8, and glucose 10; pH 7.4). Then the tissue was perfused with Ca^{2+}-free Tyrode's, followed by the enzymatic solution (collagenase-A, Roche and protease-XIV, Sigma Aldrich) then low Ca^{2+} Tyrode's (in mmol/L: NaCl 130, KCl 5.4, KH_2PO4 1.2, $MgSO_4$ 1.2, $CaCl_2$ 0.18, Na-HEPES 6, glucose 20, pH 7.2). The digested tissue was minced and filtered, and the isolated myocytes resuspended in normal Tyrode's.

Measurement of Cell Size

Freshly isolated myocytes were placed in a bath and light images taken with Nikon A1R microscope. Cell size (length and width) was measured in random samples of cells from both regions of Sham and MI. Images were collected using a 20x or 40x objective, 1.3 NA oil immersion. Analysis was done using Image J software (NIH, USA).

Cellular electrophysiological and Ca^{2+} recordings

Cells were studied in whole-cell patch clamp mode, using current clamp configuration (Axon 200B amplifier, Axon Instruments). Cells were constantly superfused with normal Tyrode's solution at 37 °C and patch pipettes (2-3 MΩ) (GB 200-8P, Science Products) were filled with (in mmol/L): K-aspartate 120, NaCl 10, KCl 20, K-HEPES 10, MgATP 5, and K_5Fluo-4 0.05; pH 7.2. In steady state, cells were stimulated with a suprathreshold depolarizing pulse of 2-4 nA, at 2 Hz for 1 min, then observed without stimulation for 30 seconds. $[Ca^{2+}]_i$ was monitored using a photometry epifluorescence setup as previously described [1]. This was then repeated in the presence of 5, 10, 20, 50 or 100 nM ISO, to assess β-adrenergic sensitivity by incidence of spontaneous APs. A dose-response curve was fitted with a logistic equation Y=Ymin+(Ymax-Ymin)/(1+10^(LogEC50-x)HillSlope).

In a subset of animals, 6 MI and 8 Sham, a voltage clamp protocol to record IK 1 was performed (figure 6F). Under superfusion of ISO at steady state, from a holding voltage of -70 mV, a step to -40 was made for 600ms to inactivate Na^+-current and allow the Ca^{2+}-transient to return to baseline. There after a hyperpolarizing step to -90 mV for 300 ms was made to record inward IK1, and immediately a depolarizing step to -30 mV for 300 ms to record outward IK1. 5 sweeps were recorded to ensure current stability. Thereafter, Ba^{2+} was superfused and the protocol recorded for another 5 sweeps at steady state. IK1 was derived as the Ba^{2+}-sensitive current at -90 and -30 mV.

Analysis and statistics

Data acquisition was performed by multiple investigators. Investigators were blinded when doing analysis off-line by creating coded data files.

The EnSite review mode was used to analyze all mapping data, in conjunction with the BARD mapping module. To perform spatial analysis of PVCs on the LV, electroanatomical maps were exported from EnSite and represented as a standard bull's eye plot (2D polar map) using custom-built software (RightHemo-MEA, KU Leuven). Cluster analysis of PVCs was performed using a Density-Based Spatial Clustering of Applications with Noise (DBSCAN) algorithm created in Matlab. The criteria for a cluster was fulfilled if 6 PVCs originated within a 0.1AU distance from each other on the polar plot. These criteria were determined from a consensus definition of clusters by three readers (KS, RW, LR).

All data are presented as means ± SD, and mostly presented by animal, or per site as indicted in the figure legends. Data were compared with Student's t-test or a 2-way ANOVA with Bonferroni post- hoc testing as applicable, and using nested design when several measurements were from the same animal. Chi-squared and posttest residuals or Fisher's exact test was used to compare proportions of DADs and spontaneous APs at sites between different groups. Data were considered significantly different when the p-value was < 0.05.

SUPPLEMENTAL DATA

Supplemental Table 1. Left ventricular function and remodeling after MI

	MI (N_{pigs} = 19)	**Sham (N_{pigs} = 13)**	***P* value**
Infarct size (%)	18.8 ± 3.5	0 ± 0	<0.0001
Ejection fraction (%)	40.4 ± 9.6	63.3 ± 4.9	<0.0001
End-diastolic volume (mL)	195.5 ± 25.0	139.6 ± 26.1	<0.0001
End-systolic volume (mL)	117.1 ± 27.3	51.5 ± 12.2	<0.0001
Left ventricular mass (g)	147.4 ± 12.8	124.3 ± 13.1	<0.0001
Heart rate (beats per minute)	88.8 ± 12.2	94.0 ± 13.9	0.2570
Left ventricular peak systolic pressure (mmHg)	97.6 ± 16.2	105.7 ± 18.9	0.1892
Left ventricular mean diastolic pressure (mmHg)	4.02 ± 1.9	2.129 ± 1.4	0.0030

Supplemental figure 1. Timeline of the experimental protocol.

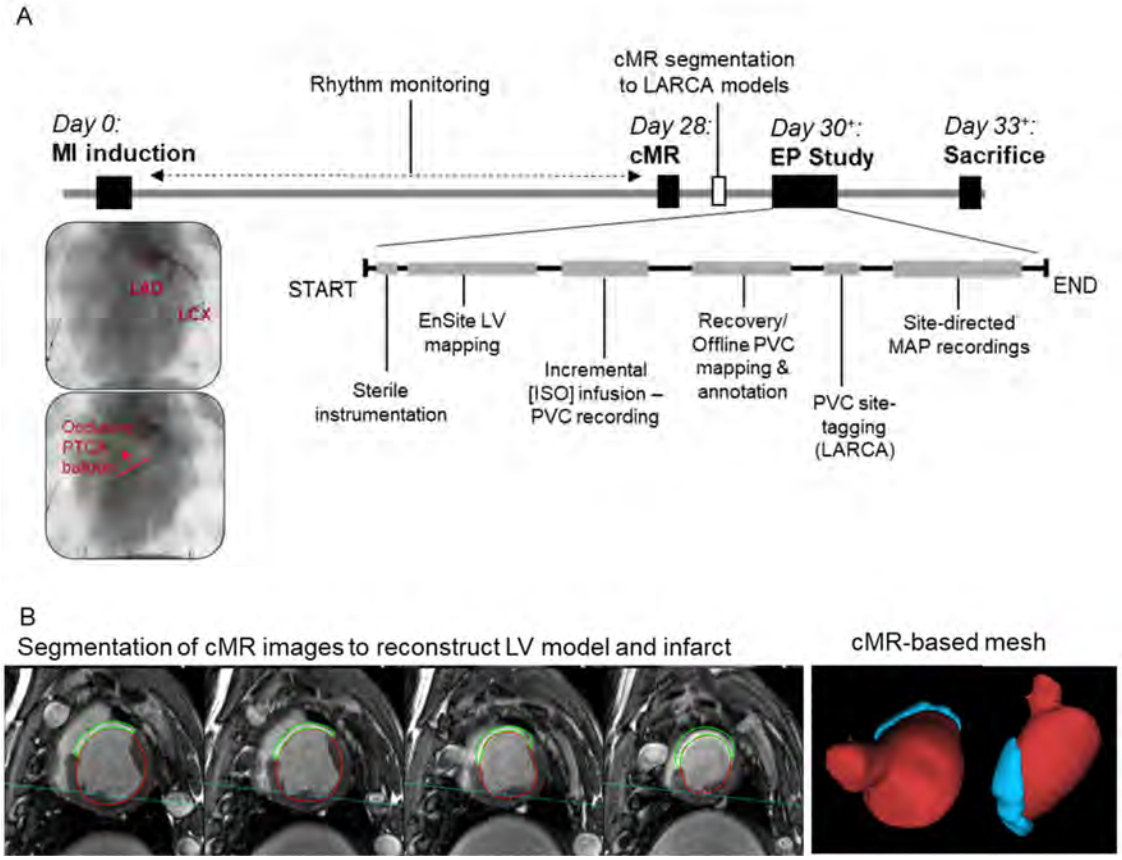

A, Myocardial infarction (MI), or sham operation, was induced by left anterior descending artery (LAD) balloon occlusion-reperfusion on day 0. Animals were kept for 1 month during which time, heart rhythm was monitored regularly using a loop recorder. On day 28, a pre-procedural cardiac magnetic resonance imaging (cMRI) was performed, and processed to produce models of the left ventricle and infarct for augmented reality fluoroscopic guidance in the electrophysiology (EP) study. ~3 days later, an EP study was performed mapping of premature ventricular complexes (PVCs) and site-directed monophasic action potential (MAP) recording during adrenergic stimulation by isoproterenol (ISO) infusion. ~3 days later, the animal was sacrificed for cellular experiments. Insert: anterior-posterior angiographic view of the left coronary arteries illustrating the LAD and left circumflex artery (LCX).
B, Illustration of segmentation of MRI images (left) to reconstruct a 3D LV model and infarct (right).

Supplemental figure 2. Frequent and complex PVCs originate from the BZ during adrenergic stimulation after MI.

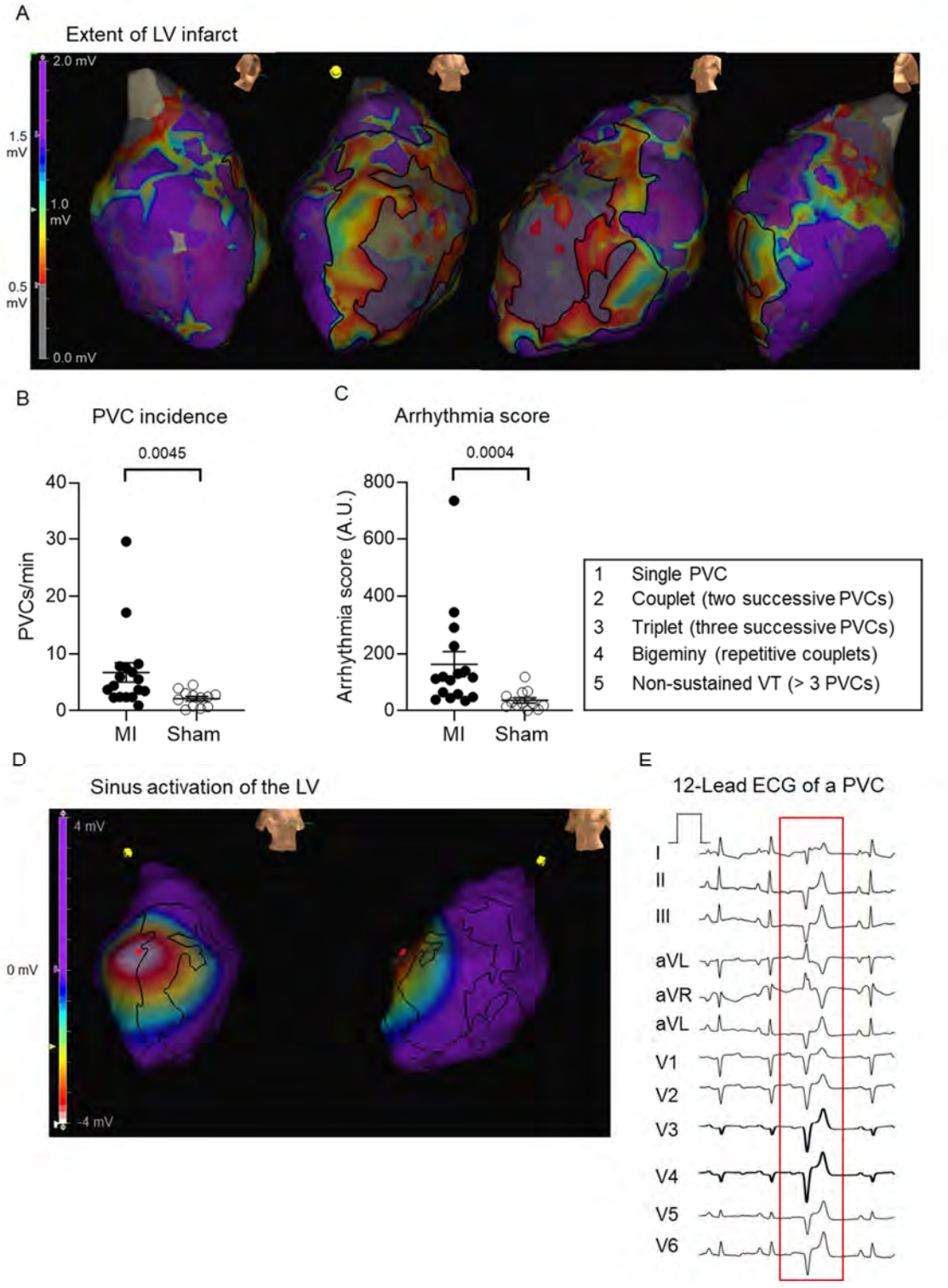

A, Left to right: Right posterior-oblique view, right anterior-oblique view, left anterior-oblique view and left posterior-oblique view of the electroanatomical map of the left ventricle (LV) illustrating the infarct (grey area, voltage < 0.05 mV), border zone (BZ) - the region between 0.5 mV (red) and 1.5 mV (blue), and remote myocardium (purple, voltage > 1.5 mV).
B, Mean data of cumulative number of PVCs during 20 minutes of non-contact mapping in MI (N = 17) and Sham (N = 10); Unpaired t-test, ***P* < 0.01.
C, Right: summary data of the arrhythmia score of MI (N = 17) and Sham (N = 10); Unpaired t-test, ****P* < 0.001. Left: Definition of the arrhythmia scoring of PVCs analysed in B.
D, Right anterior-oblique and left anterior-oblique views of the LV during non-contact mapping of normal sinus activation showing a typical high septal activation breakout.
D, A representative example of the 12-lead ECG of sinus complexes and a PVC.

Supplemental figure 3. Frequent PVCs originate from a preferential region of the BZ after MI.

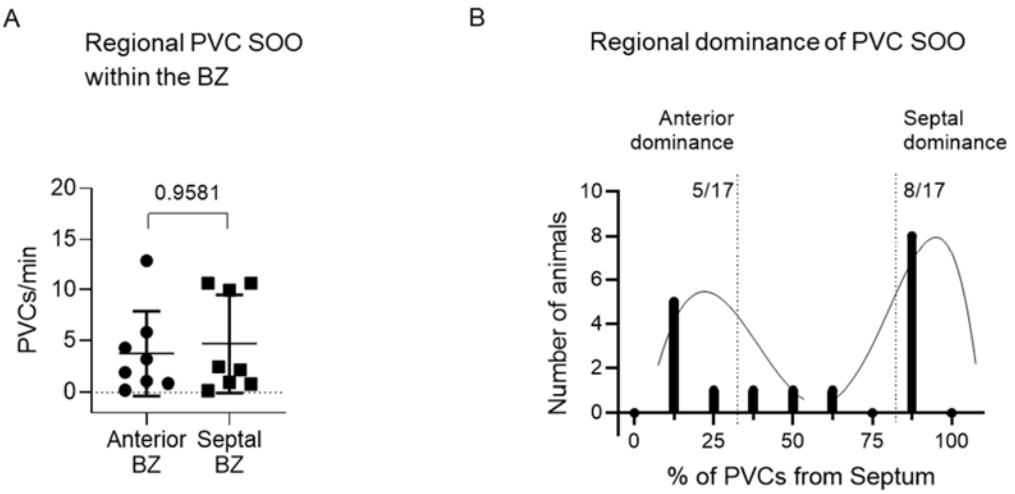

A, Summary data of the incidence of PVCs that originated from the anterior and septal BZ in contact mapping in MI (N = 8). Unpaired t-test.
B, Summary data of the regional dominance of PVC site of origin (SOO) comparing the anterior to septal region in MI (N = 17). Regional dominance of PVC SOO was defined by >75% of PVCs originating from the region.

Supplemental figure 4. Augmented reality angiography for site-directed monophasic action potential recordings (LARCA).

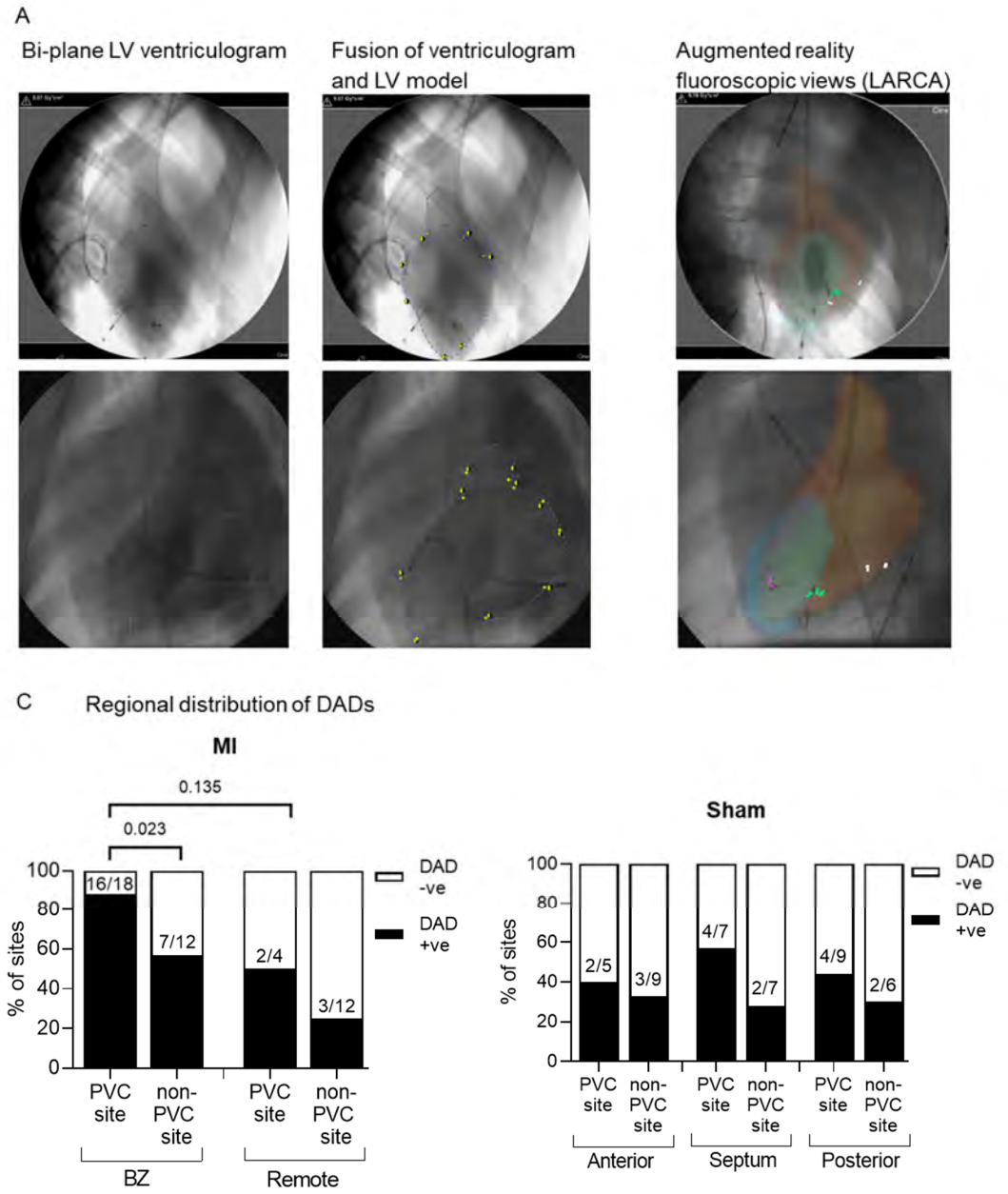

A, Bi-plane ventriculogram of the LV in RAO and LAO views (left). Illustration of the fusion of the LV ventriculogram with the cMR model (middle), and (right) to create the real-time augmented reality fluoroscopic views (LARCA), illustrating simultaneous MAP recording at a PVC site (green dots) and non-PVC site (pink dots).
B, Regional proportion of delayed afterdepolarizations (DADs) at PVC- and non-PVC sites in Sham (N = 10).

Supplemental figure 5. Regional structural remodelling after MI

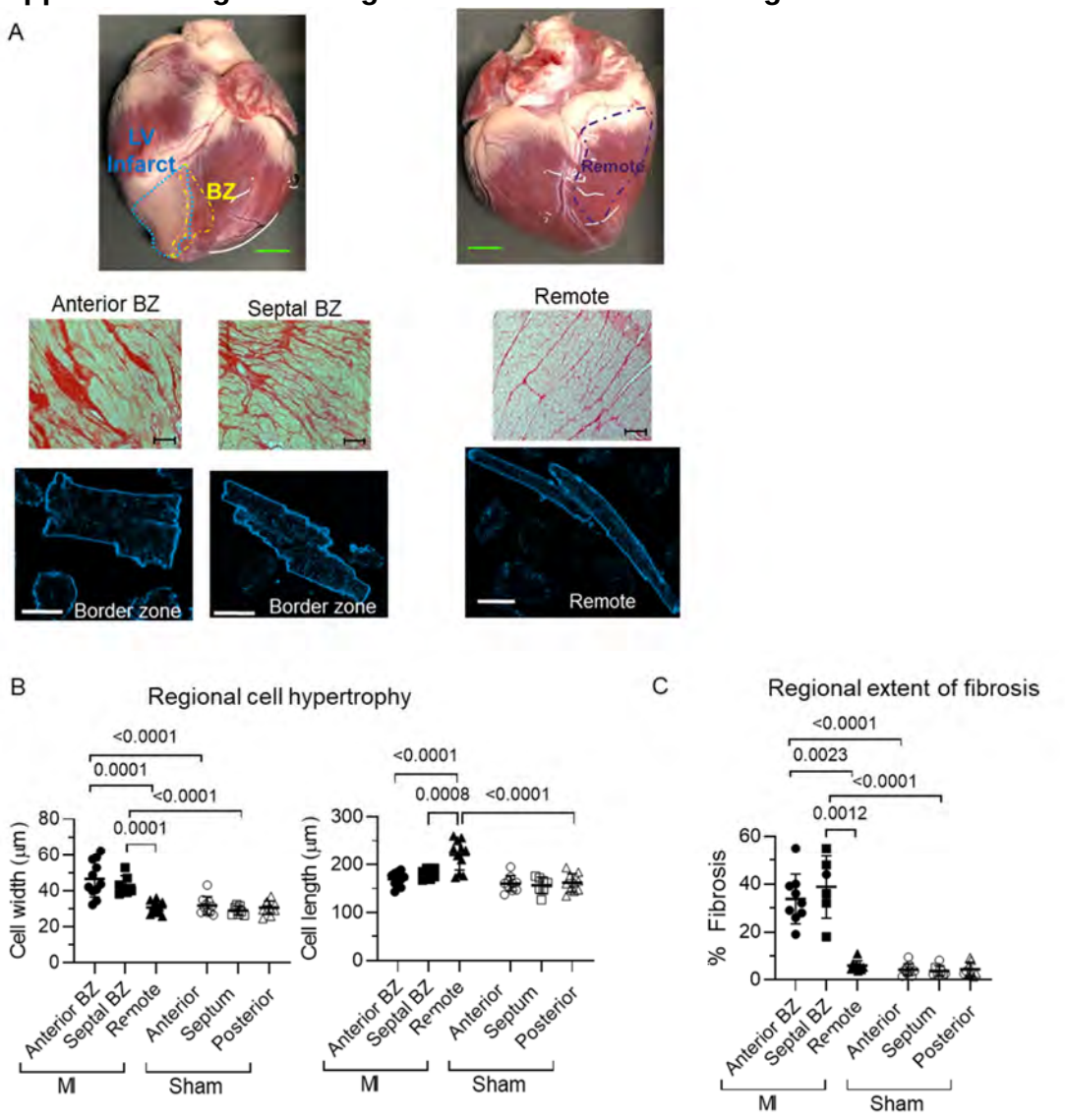

A: Top, MI heart, anterior (left) and posterior (right) view, illustrating the anterior BZ and remote regions used for cell isolation, scale bar = 1 cm. Middle, matching tissue sections illustrating fibrosis (Sirius Red staining, scale bar = 100µm). Bottom, isolated cells illustrate cell morphology (scale bar = 50µm).
B, Regional cell size: cell length (left) and cell width (right) of isolated cells from MI, n_{cells} = 286-420, N_{pigs} = 6-11 and Sham, n_{cells} = 252-375, N_{pigs} = 7-10. Mixed model ANOVA with Bonferroni post-test.
C: Mean data of regional fibrosis in MI and matched Sham regions. Analysis of variance (ANOVA) with Bonferroni post-test.

Supplemental figure 6. Regional cellular electrophysiology and arrhythmogenicity

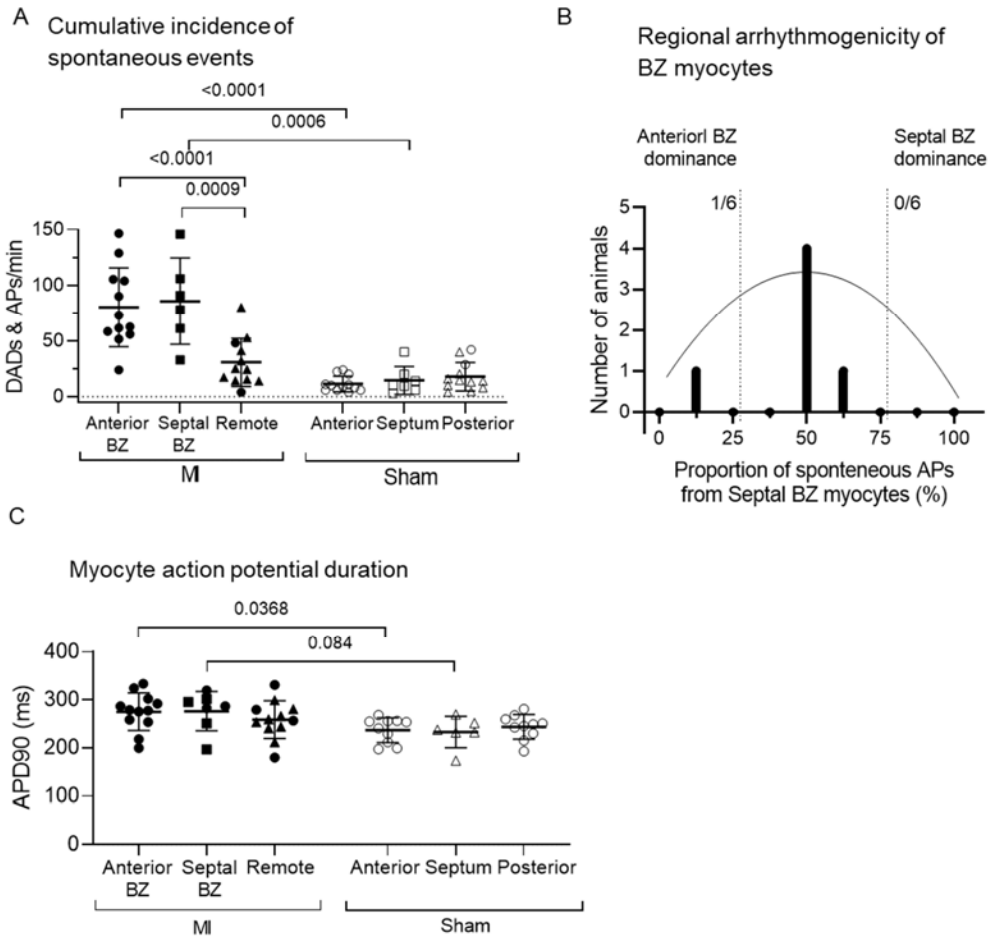

A, Cumulative data of the incidence of spontaneous events DADs and spontaneous APs in anterior BZ, septal BZ and remote myocytes as well as myocytes from matched Sham regions. MI, n_{cells} = 70-45, N_{pigs} = 11-6 and Sham, n_{cells} = 63-39, N_{pigs} = 10-7. Analysis of variance (ANOVA) with Bonferroni post-test.
B, Summary data of the regional dominance of the proportion of spontaneous APs in myocytes comparing the anterior BZ to septal BZ myocytes in MI (N = 6).
C, Summary data of regional dominance of regional myocyte action potential duration from pacing train of cells in A. MI, n_{cells} = 70-45, N_{pigs} = 11-6 and Sham, n_{cells} = 63-39, N_{pigs} = 10-7. Analysis of variance (ANOVA) with Bonferroni post-test.

Supplemental figure 7. *In vivo* HR and PVC dose-response to ISO

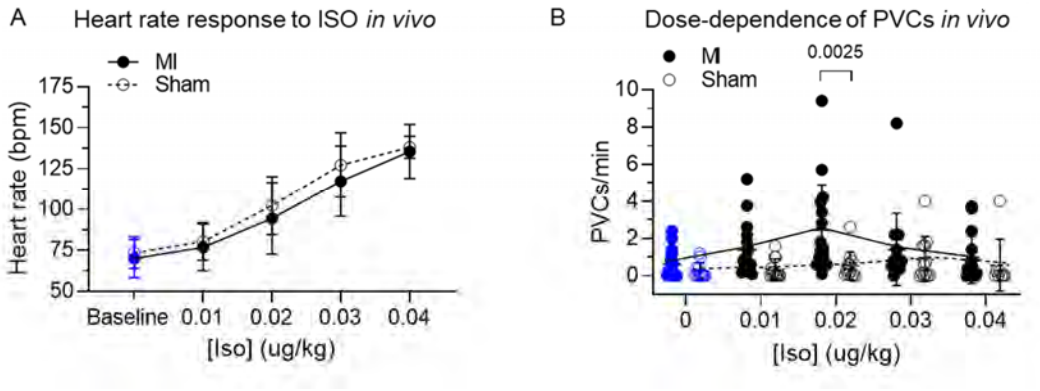

A, Heart rate changes during incremental dose increase of ISO infusion *in vivo* for MI and Sham pigs. MI, N_{pigs} = 17 and Sham, N_{pigs} = 10.
B, Incidence of PVCs at various doses of ISO *in vivo* for MI and Sham pigs. MI, N_{pigs} = 17 and Sham, N_{pigs} = 10. Repeated measures ANOVA with Bonferroni post-test.

Supplement references

1. Dries E, Amoni M, Vandenberk B, et al.: Altered adrenergic response in myocytes bordering a chronic myocardial infarction underlies in vivo triggered activity and repolarization instability. J Physiol 2020; 598.

2. Floré V, Claus P, Antoons G, et al.: Microvolt T-wave alternans and beat-to-beat variability of repolarization during early postischemic remodeling in a pig heart. Heart Rhythm 2011; 8:1050–1057.

3. Galan DT, Bito V, Claus P, et al.: Reduced mitochondrial respiration in the ischemic as well as in the remote nonischemic region in postmyocardial infarction remodeling. Am J Physiol Heart Circ Physiol 2016; 311:H1075–H1090.

4. Peters NS, Jackman WM, Schilling RJ, Beatty G, Davies DW: Human left ventricular endocardial activation mapping using a novel noncontact catheter. Circulation 1997; 95:1658–1660.

5. Klemm HU, Ventura R, Steven D, et al.: Catheter ablation of multiple ventricular tachycardias after myocardial infarction guided by combined contact and noncontact mapping. Circulation 2007; 115:2697–2704.

6. Marchlinski FE, Callans DJ, Gottlieb CD, Zado ES: Linear Ablation Lesions for Control of Unmappable Ventricular Tachycardia in Patients With Ischemic and Nonischemic Cardiomyopathy. Circulation 2000; 101:1288–1296.

7. Cronin EM, Bogun FM, Maury P, et al.: 2019 HRS/EHRA/APHRS/LAHRS expert

consensus statement on catheter ablation of ventricular arrhythmias. Europace 2019; 21:1143–1144.

8. Reddy VY, Wrobleski D, Houghtaling C, Josephson ME, Ruskin JN: Combined epicardial and endocardial electroanatomic mapping in a porcine model of healed myocardial infarction. Circulation 2003; 107:3236–3242.

9. Higa S, Tai CT, Lin YJ, et al.: Focal Atrial Tachycardia: New Insight from Noncontact Mapping and Catheter Ablation. Circulation 2004; 109:84–91.

10. Ector J, De Buck S, Adams J, et al.: Cardiac three-dimensional magnetic resonance imaging and fluoroscopy merging: A new approach for electroanatomic mapping to assist catheter ablation. Circulation 2005; 112:3769–3776.

11. Buck S De, Maes F, Ector J, et al.: An Augmented Reality System for Patient-Specific Guidance of Cardiac Catheter Ablation Procedures. 2005; 24:1512–1524.

12. Dauwe DF, Nuyens D, De Buck S, et al.: Three-dimensional rotational angiography fused with multimodal imaging modalities for targeted endomyocardial injections in the ischaemic heart. Eur Heart J Cardiovasc Imaging 2014; 15:900–907.

13. De Groot SHM, Vos MA, Gorgels APM, Leunissen JDM, Van Der Steld BJ, Wellens HJJ: Combining monophasic action potential recordings with pacing to demonstrate delayed afterdepolarizations and triggered arrhythmias in the intact heart: Value of diastolic slope. Circulation 1995; 92:2697–2704.

CHAPTER 5: Heterogeneous repolarization within the myocardial infarction border zone – A functional substrate for arrhythmias

Manuscript submitted as:

Matthew Amoni, Dylan Vermoortele, Samaneh Ekhteraei-Tousi, Rosa Doñate Puertas, Guillaume Gilbert, Mohamad Youness, Bernard Thienpont, Rik Willems, H. Llewelyn Roderick, Piet Claus, Karin R. Sipido. Myocyte population studies reveal heterogeneous repolarization and cellular remodeling within the myocardial infarction border zone. *(Revision to be submitted to Circulation: Arrhythmia & Electrophysiology)*

Abstract

Background: After myocardial infarction (MI), the infarct border zone (BZ) is the dominant source of life-threatening arrhythmias, where fibrosis and abnormal repolarization due to myocyte remodeling create a local substrate for re-entry. We examined whether repolarization abnormalities are heterogeneous within the BZ *in vivo* and related to heterogeneous cardiomyocyte remodeling.

Methods: MI was induced in domestic pigs by 120-minutes ischemia-reperfusion injury. After 1-month, remodeling of the left ventricle (LV) was assessed by magnetic resonance imaging (MRI). Electro-anatomical mapping was performed to determine local activation-recovery-intervals (ARIs). Cardiomyocytes were isolated, and tissue samples collected from the anterior and septal BZs, and remote regions. Optical recording of action potentials (Di-8-Annepps, stimulation at 1 Hz, 37°C) allowed assessment of repolarization heterogeneity within the cardiomyocyte populations. We used single nuclear RNA sequencing (10x Genomics), to examine heterogeneity of gene expression in the BZ cardiomyocyte population compared to remote regions.

Results: *In vivo*, ARIs in the BZs tended to be longer than remote with increased spatial heterogeneity evidenced by a greater local standard deviation (SD) (3.5±1.3 ms vs remote: 2.0±0.5 ms, P=0.036, N_{pigs}=5). Cellular population studies (N_{cells}=635-862 cells/region) demonstrated longer APD in the BZs with greater heterogeneity than remote (SD: 105.9±17.0 ms vs remote: 73.9±8.6 ms, P=0.001, N_{pigs}=6). Sequencing revealed cell-cell gene expression heterogeneity in the BZ, with increased nuclei Euclidean distances compared to remote (BZ: 12.1(9.2-15.0) vs remote: 10.6(7.5-11.6), P<0.0001). Differentially expressed genes characterizing BZ cardiomyocyte remodeling identified hypertrophic (*NPPB*), stress (*XIRP2*) and ion channel (*KCNT2*, *SCN3B, KCNJ5*) related genes, including genes with high cell-cell variability of expression. In addition, heterogeneity of LV wall thickness was higher in the BZs than remote.

Conclusions: Cardiomyocyte remodeling in the BZ is heterogeneous, driven by uniquely altered gene expression, possibly related to wall stress heterogeneity, and translates to heterogeneous repolarization and arrhythmia vulnerability *in vivo*.

Keywords: myocardial infarction; action potential; electroanatomical mapping; activation-recovery interval; single nucleus RNA-sequencing; cellular heterogeneity.

Novelty and Significance

What is known?

- The infarct and its surrounding border zone (BZ) are the source of arrhythmias after myocardial infarction (MI).
- Structural remodeling with interspersion of fibrosis and cardiomyocytes creates a substrate for re-entry to occur.
- Altered repolarization of cardiomyocytes after MI in the BZ likely contributes to this substrate.

What new information does this article contribute?

- Cardiomyocyte remodeling within the BZ is not homogeneous, with phenotypic heterogeneity of repolarization and hypertrophy
- Cardiomyocyte remodeling is driven by heterogeneous gene expression with key genes including hypertrophy (*NPPB and INPP5F*) and repolarization (*KCNT2*, *SCN3B* and *KCNJ5*) genes, driven by various signalling pathways, some likely activated by a variable wall stress within the BZ.
- Consequently, the heterogenous cellular remodeling translates to local heterogeneity of repolarization *in vivo* that could underlie arrhythmia vulnerability in the BZ

Introduction

Ventricular arrhythmias and sudden death are major complications after myocardial infarction (MI), with a particularly high incidence in the first months after the acute event [1]. The transition zone between the scar and healthy myocardium is the most vulnerable region and prime target for ablation therapy [2,3]. In this border zone (BZ), a mix of surviving cardiomyocytes and fibrous tissue form a perfect substrate for re-entry. Whether the BZ cardiomyocytes also undergo remodeling that enhances the re-entry, distinct from the overall remodeling in the post-MI heart, is likely, but data are scarce.

Many studies to identify mechanisms linking MI and arrhythmias use small animal models, in particular rats or mice, and report on cardiomyocytes isolated from the viable left ventricle (LV) [4-7]. These studies also often use a permanent coronary ligation model, not representative of current clinical practice [8]. Studies in the dog [9] and pig [10] have identified regional AP changes critical for arrhythmogenesis including Purkinje and cardiomyocyte remodeling in the BZ. These studies exploited the advantage that large animal models may be more suitable to identify this vulnerable BZ region within the post-MI heart, as well as to connect *in vivo* and *ex vivo* findings [11]. In the pig with 5-month chronic occlusion, Hegyi et al [12], reported a shortening of the AP in myocytes from the BZ compared to lengthening in the remote region. We also studied regional AP changes 6 weeks after MI without reperfusion, and only found differences between regions during adrenergic stimulation [13].

In current clinical practice, reperfusion is established as soon as possible after acute coronary occlusion. This intervention salvages myocardium but also subjects the BZ to intense remodeling driven by local inflammation [14]. It is conceivable that local differences in perfusion and inflammation lead to further heterogeneity within the BZ, consistent with clinical observations of areas of greater vulnerability within the BZ [2]. In the pig with a MI following ischemia and reperfusion, adrenergic stimulation also uncovered regional vulnerability and heterogeneity, with clusters of premature ventricular beats dispersed within the BZ [15]. Such heterogeneity could result from the different ultrastructure, whether related to fibrosis or innervation, but could also reflect a mix of cardiomyocyte populations.

One of the main challenges in isolated cardiomyocyte studies is the low power resulting from the small number of cardiomyocytes measured in a typical animal study [16]. This is inherent to the time-consuming methodology of single cell patch clamp recording. In healthy animals, small samples, often used in a repeated measurement design during mechanistic studies, may be valid. However, recent evidence has demonstrated that even in healthy hearts, the variability between cardiomyocytes from the same heart can be as large as that between individuals, supporting a need for large datasets [17]. Therefore, if reliable changes are to be detected under pathological conditions that may alter cell type distributions, larger samples sizes are necessary.

Given there is limited information of potential cellular heterogeneity within the BZ, we implemented a higher throughput method for measuring AP duration (APD), and compared cardiomyocytes from different regions of the LV 4 weeks after MI, a time of high arrhythmic risk [1]. Our focus was on the repolarization process, which is a major factor in facilitating re-entry, and on heterogeneity of repolarization, which is a feature of VT circuits after MI [18,19]. Using a recently developed method for mapping *in vivo* repolarization duration at high spatial resolution, we first established that *in vivo* the repolarization within the BZ is not homogeneous. We then isolated cardiomyocytes from the BZ, taking samples from two regions and studied electrical activity in

large populations of these cardiomyocytes using optical methods. We also examined whether regional variability of cellular remodeling could be detected in the degree and type of cardiomyocyte hypertrophy. Mechanistically we examined gene expression at the single cell level.

Methods

Detailed methods are provided in the Supplementary Materials, including the supporting references. The data and analytical methods supporting the findings of this study are available from the corresponding author upon request.

Pre-clinical animal model of MI

Animal handling was in accordance with the National Institutes of Health (NIH) Guide for the Care and Use of Laboratory Animals and the EU Directive for animal research 2010/63/EU. Experimental protocols were approved by the KU Leuven animal ethics committee (ECD137/2018). The experimental workflow is illustrated in Supplemental Figure 1. All animal procedures were performed under general anesthesia. MI was induced in 22 domestic pigs (TN70, Topigs, Norsvin, weight 30-35 kg) by 120 min balloon occlusion of the left anterior descending coronary artery followed by reperfusion, while 11 pigs underwent a Sham procedure [15]. Two MI animals experienced sudden death within 1 week after MI.

Cardiac magnetic resonance imaging

After 1 month, animals underwent cardiac magnetic resonance imaging (cMRI) using a 3T scanner. The LV structural and functional cMRI parameters are summarized in Supplemental Table 1. For regional LV wall analysis, the BZ was defined as the region with signal intensity 20-70% of the maximum intensity (infarct core), and the remote as the posterior wall opposite to the BZ.

In vivo cardiac electrophysiology

Electroanatomical mapping of the LV was performed with an EnSite Precision 2.0 mapping system (Abbott Medical, New Jersey, USA) paired with a BARD Electrophysiology Labsystem Pro EP (Boston Scientific, USA), as previously described [15]. Contact mapping was performed to generate the LV map paired to the EnSite multielectrode array (MEA) and define the BZ as points with bipolar voltage >0.5 mV and <1.5 mV. After ~20 min stabilization, non-contact mapping using the MEA was performed to record 2048 non-contact local electrograms for 5 min.

Mapping data was processed to calculate the local activation-recovery interval (ARI) for each electrogram (Vermoortele et al., under revision). We reconstructed a spatially dense map using a custom-made Matlab software and calculated local heterogeneity as the standard deviation (SD) of ARIs in a 1 cm radius for each of the 2048 points (Figure 1B).

After 1-3 days recovery, animals were sacrificed for tissue harvesting and cellular experiments.

Isolated cardiomyocyte electrophysiology and phenotyping

Cardiomyocytes were isolated from the anterior and septal MI BZ, from the remote region and from similar regions in Sham [15]; each animal thus contributes matched data from the diffferent regions Freshly isolated cardiomyocytes were studied using whole-cell patch clamp mode [13].For optical recording of action potentials, cells were loaded with Di-8-Anepps and imaged on the stage of an inverted microscope (Nikon TiE, Germany). Cells were superfused with Tyrode's solution at 37˚C and field stimulated with suprathreshold 2-4 ms pulses at 1 Hz. APD was defined as the AP duration at 25% (APD25), 50% (APD50) and 90% repolarization (APD90).

Single-nucleus RNA sequencing and gene expression analysis

Isolation of cardiac nuclei

Tissue samples collected under RNase free conditions from the BZ and remote regions were immediately snap frozen in liquid nitrogen and stored at -80˚C. Debris-free suspensions of intact nuclei were generated by tissue homogenization followed by sucrose gradient centrifugation and flow sorting.

10x RNA single nucleus RNA-Seq (snRNA-Seq) and analysis.

Single-nucleus RNAseq libraries were prepared on ~6000 nuclei per sample (10x Genomics) according to the manufacturer's protocol. Libraries were sequenced on Illumina Novaseq 6000 at a depth of ~30,000 reads per nucleus.

Transcriptome datasets per sample were provided by CellRanger V5, followed by removal of ambient RNA and low complexity libraries. Sample datasets were then merged and further processed and cell-type clusters generated using Seurat V4. Clusters were visualized following non-linear dimensional reduction using UMAP (Uniform Manifold Approximation and Projection) approach, and were annotated based on their expression of established cell-type-specific markers [20].

Cellular heterogeneity was analyzed at the cellular level, using the mean of Euclidean distance of each cell relative to other cells in each physiological condition (per animal) and at the level of gene expression variability using BASiCS. Expressed/dispersed genes were identified with an expected false discovery rate (EFDR) < 0.10.

Data and statistical analysis

Off-line data analysis was performed blinded where feasible. Data are presented as mean ± SD, unless otherwise stated. Comparisons between regions and between MI and Sham were made using a 2-way or mixed-effects model ANOVA and Bonferroni post-hoc analysis. For pooled data per animal, means were compared using a linear mixed model with hierarchical analysis. The regional cardiomyocyte subtype proportions were compared by a Chi-square test with Bonferroni correction. Correlations were assessed by linear regression analysis as applicable. All analyses are indicated in the figure legends.

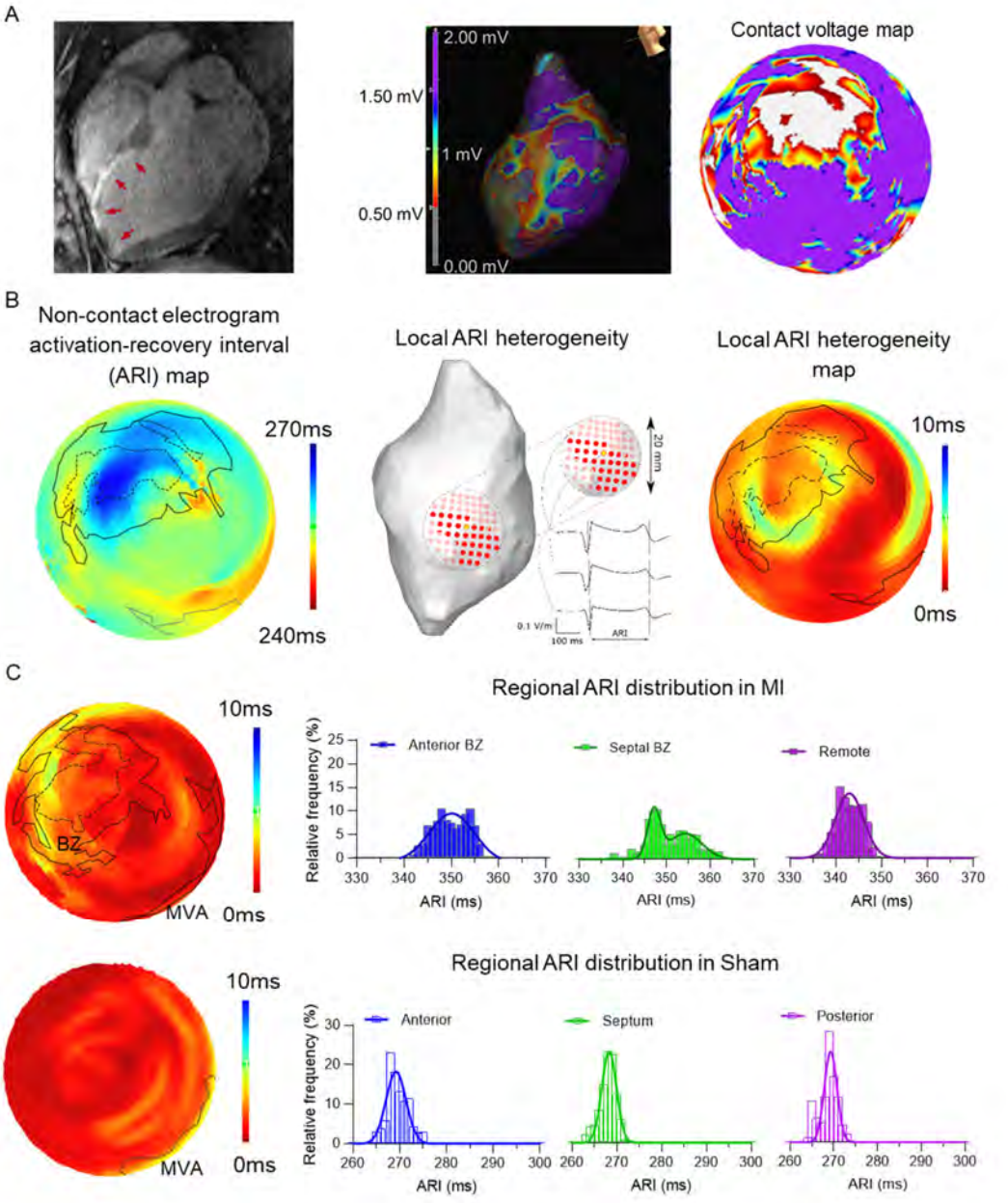

Figure 1. Regional activation-recovery intervals *in vivo* after MI.

A, Example of cMRI (left) with corresponding electroanatomical map (middle) and polar map (right) illustrating the extent of infarct (Infarct size = 18.2% and ejection fraction 46.8%), and the electroanatomical BZ defined as bipolar voltage between 0.5-1.5 mV.
B, Left, the e-field method for quantifying local activation-recovery interval (ARI) heterogeneity using spatially dense LV electrograms (see Online Supplement). Middle, example of resulting ARI map, and right, map of the ARI heterogeneity plotted as local SD of ARIs by e-field.
C, Examples of polar maps the local ARI heterogeneity of the LV (left) and corresponding regional distribution of ARIs (right) in MI (top) and Sham (bottom). BZ – border zone, MVA – mitral valve annulus.

Results

Variable repolarization in the BZ *in vivo*

We assessed the presence of regional variability of repolarization *in vivo*. Using a recently developed algorithm, we mapped the local repolarization time from spatially dense electrograms of non-contact electro-anatomical maps of the LV. Contact mapping defined the infarct, BZ and remote regions, which were translated to polar maps to aid visualization (Figure 1A). The local ARI, as a measure of repolarization, were plotted on the polar map (Figure 1B, left and middle). Heterogeneity of repolarization measured as the SD of ARI values in a region of 1 cm radius around each endocardial point was visualized on the polar map (Figure 1B, right). Electroanatomical maps, ARI maps and heterogeneity maps from different views are shown in Supplemental Figure 2.

Figure 1C shows an example of the ARI heterogeneity polar map and corresponding distribution of ARIs from an MI and Sham animal. The distribution of ARIs from the MI BZ had a wider and skewed profile compared to the remote region, consistent with the visual image of dispersion. Such a profile, indicative of heterogeneity of repolarization, was not seen in the histograms of the ARIs of the remote region nor in matched regions of the example Sham animal.

A similar pattern of ARIs was seen in all MI pigs. Figure 2A shows ARI values for anterior and posterior BZ and the remote region for each pig (Sham data are presented in Supplemental Figure 3). The visual impression of greater heterogeneity of local ARIs in the BZ was quantified as the SD for each pig. These values were significantly larger in the BZ (Figure 2B). Since *in vivo* heart rate influences APD and it is not identical between different pigs, pooling the ARI data was not appropriate. Therefore, we used the magnitude of the regional difference between BZ and remote for each animal to assess mean ARI differences between regions across the group of animals (Figure 2C). These data suggest that the repolarization in the BZ was both more heterogeneous and overall longer than that of the remote region.

Heterogeneity of repolarization within the population of BZ myocytes

To examine whether heterogeneity in cardiomyocyte remodeling underlies this heterogeneity of repolarization in the BZ, we isolated cardiomyocytes from the anterior and septal BZ, the remote region, and similar regions in Sham. In a first set of experiments, we recorded cellular APs using conventional whole-cell patch clamp recording (~5 cells per region in each pig). Figure 3A illustrates the stimulation protocol, with 30 APs recorded at 1 Hz steady state, averaged for analysis; the right panel shows the summary data of all cells. In this substantial data set of 7 MI and 6 Sham animals, each pig contributing 4-9 cells per region (N_{cells}=149), no significant difference in APD between regions was detected. However, it was evident that the APD of BZ cardiomyocytes had a larger range than that of the remote and matched Sham regions of equivalent sample size. This difference between BZ and other regions could reflect an inter-individual variability and/or an intra-regional variability, and by extension obscure differences in mean values.

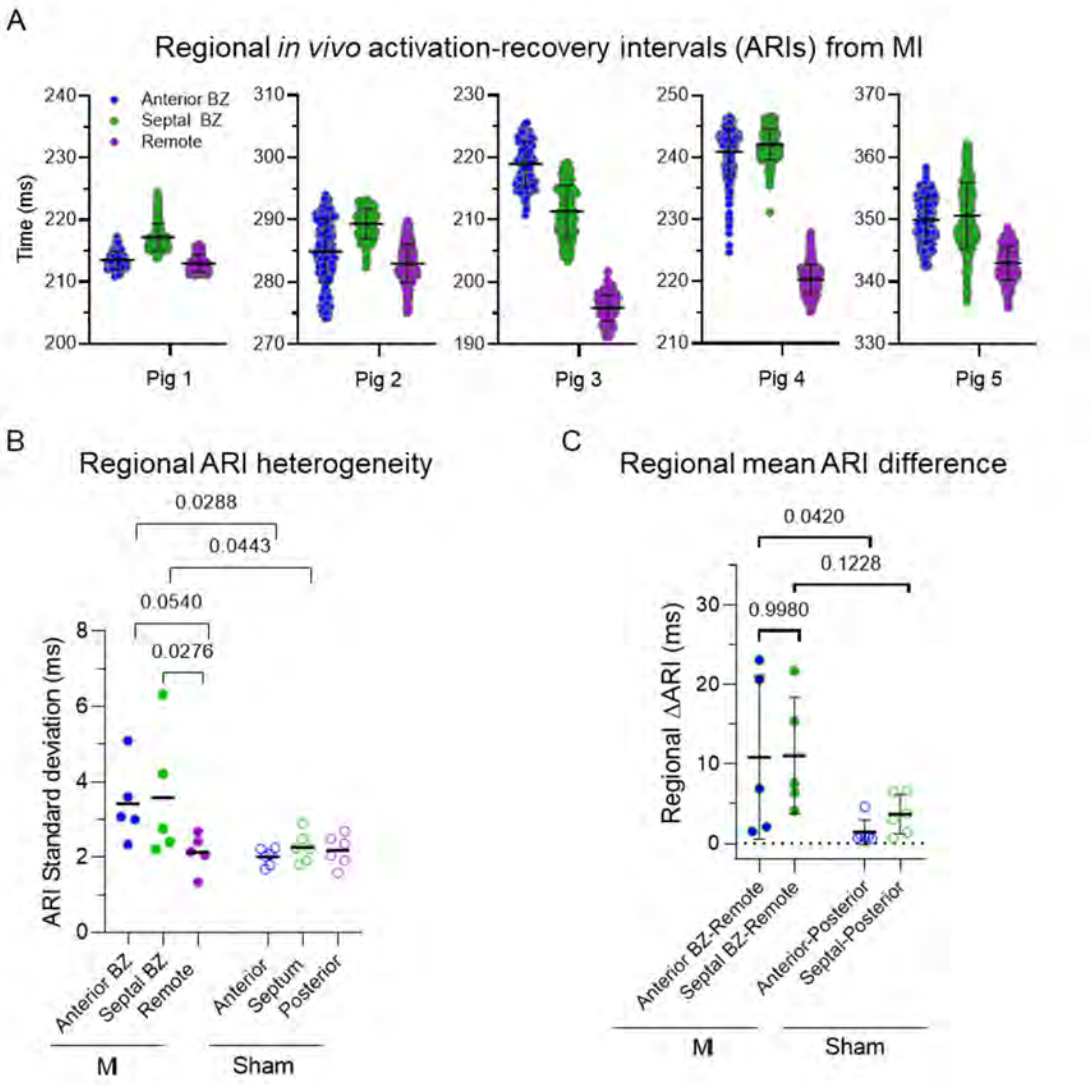

Figure 2. Quantification of *in vivo* heterogeneity of repolarization.
A, Pooled data on ARIs of the different regions *in vivo* from MI (N_{pigs} = 5, n_{ARIs} = 112-468/region).
B, Summary data of ARI heterogeneity quantified by regional standard deviation per pig from (A). Mixed-effects model ANOVA with Bonferroni post-test.
C, Regional differences in ARI dispersion quantified by pig as mean ARI differences. Mixed-effects model ANOVA with Bonferroni post-test.

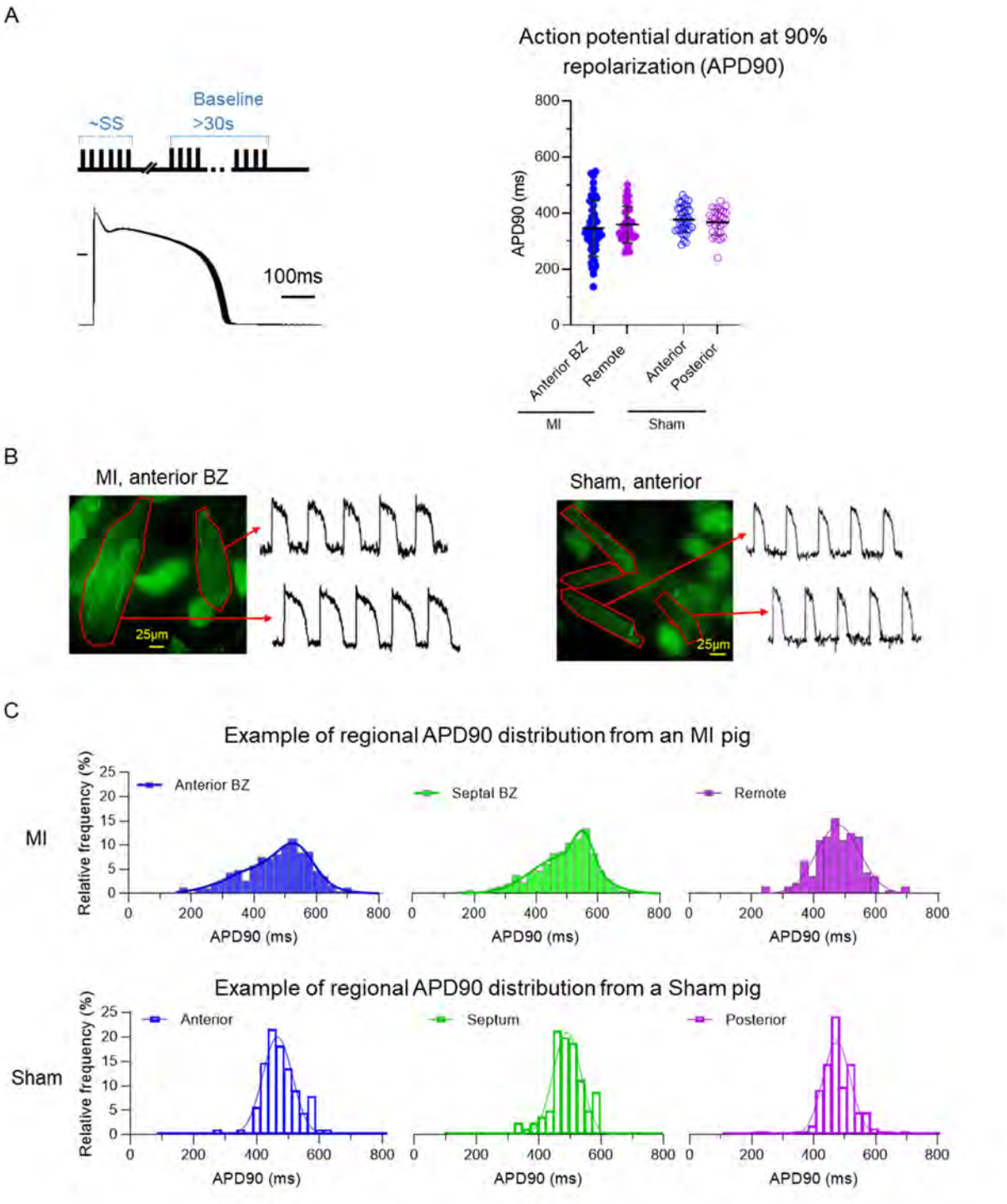

Figure 3. Action potential duration (APD90) of isolated myocytes from different regions. **A,** Left, protocol and representative example of 30 steady-state action potentials recorded under patch clamp. Right, summary of regional cellular action potential duration at 90% repolarization (APD90) profiles from MI (N_{pigs} = 7, n_{cells} = 4-9/region) and Sham (N_{pigs} = 6, n_{cells} = 4-8/region). Multilevel mixed model ANOVA with Bonferroni correction.

B, Examples of BZ (left) and Sham (right) cells loaded with the voltage dye Di-8-annepps and corresponding action potentials recorded. Scale bar = 25µm.
C, Examples of the distribution of cellular APD90 of populations of isolated cells from each region of an MI (n_{cells} = 212-312/region) and Sham pig (n_{cells} = 133-254/region) illustrating increased heterogeneity in the MI BZ.

To gain insights into intra-regional heterogeneity within each animal, we determined that we would need to analyze a greater number of cells We therefore implemented an optical method using voltage-sensitive dyes to record APs from 200-400 cardiomyocytes/pig, in an unbiased manner (Figure 3B). The APs of 10 tracings at the end of a 15 s recording were averaged and APD was measured. Figure 3C illustrates the distribution of cellular APDs in a representative MI and Sham pig. Visually, the BZ distributions were wider and skewed towards a longer APD, in both anterior and septal BZ, which was not seen in the remote region, nor in Sham animals.

Figure 4A represents the complete dataset of 6 MI (dataset of 7 Sham animals is presented in Supplemental Figure 4), illustrating the large spread of cellular APD in MI BZ. Moreover, the effect was apparent at both the anterior and septal subregions. Intra-region heterogeneity of cellular APDs was quantified by the SD in each dataset and animal, and was larger in BZ compared to remote (Figure 4B). These data are in line with our *in vivo* findings, i.e. heterogeneity of repolarization in the BZ, without distinctive features between septal or anterior BZ, but not in the remote region. Furthermore, there was a strong correlation between *in vivo* and cellular heterogeneity (Figure 4C).

With this optical approach for AP analysis and the large data set generated, we could detect an average increase in APD in the BZ compared to remote, and without difference between anterior and septal subpopulations (Figure 4D, APD50 and APD25 data in supplemental Figure 4B). The mean regional APD (Figure 4D) correlated only moderately with the mean of the regional *in vivo* ARI, possibly related to the differences in heart rate *in vivo* vs. stimulation of 1 Hz in cells.

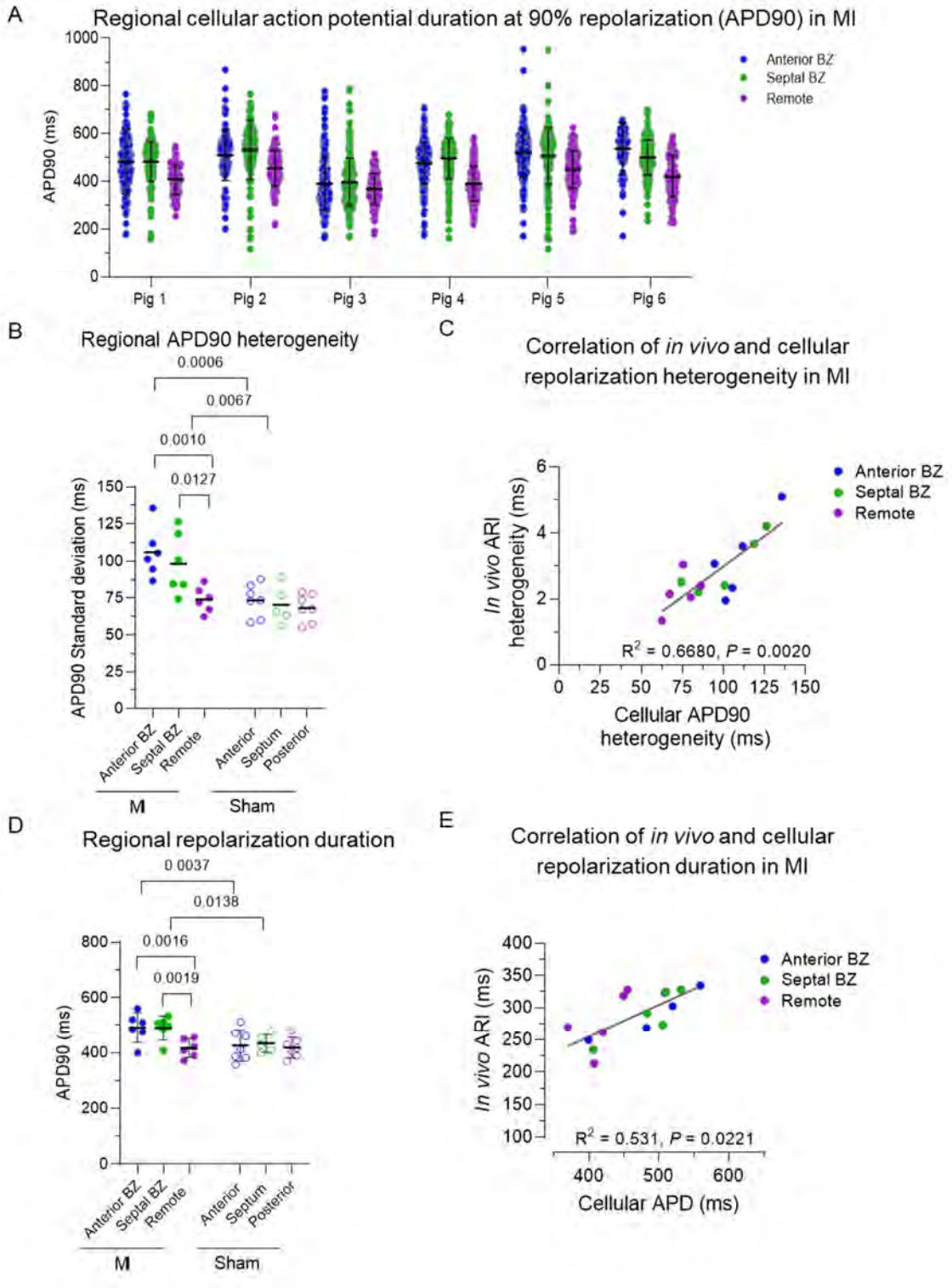

Figure 4. Quantification of regional cellular action potential duration heterogeneity.
A, Individual cellular APD90s of populations of isolated cells from MI N_{pigs} = 6 (n_{cells} = 86-216/region).

B, Summary of cellular APD90 heterogeneity as standard deviation per pig, mixed model ANOVA with Bonferroni posttest.
C, Correlation of regional cellular and *in* vivo heterogeneity in MI (N_{pigs} = 5 MI), linear regression analysis.
D, Mean data of cellular APD90 pooled by pig from (A), mixed model ANOVA with Bonferroni posttest.
E, Correlation of regional cellular and *in* vivo repolarization duration in MI (N_{pigs} = 5), linear regression analysis.

Heterogeneous myocyte hypertrophy in BZ and remote regions

Altered repolarization is but one of the phenotypic manifestations of the cellular remodeling that occurs after MI. We hypothesized that variability in repolarization in the BZ would be associated with a similar differential and heterogenous hypertrophic remodeling. To evaluate this premise, we examined cell dimensions and its heterogeneity within and between regions. Representative images of isolated cardiomyocytes from MI and Sham illustrate characteristic morphologies in the different regions (Figure 5A). Figure 5B, presents an example of the distribution of cell width and length in matched regions of an MI and Sham pig. The BZ is characterized by a wide distribution of cell width compared to the remote region and to Sham, top rows), whereas cell length appears more variable in the remote region (bottom rows). This visual dispersion is confirmed by the greater SD of cell dimensions within each pig (Figure 5C). On average, BZ cells had a significant increase in width but not length, whereas cells in the remote region had an increase in length, but not width (Figure 5D).

To investigate the relationship between AP variability and cell dimension variability, we also extracted cell length and width from the optical AP recordings presented in Figure 3. A linear regression analysis between matched data for APD and cell size however did not detect a correlation between these parameters (R^2 <0.3, P<0.05; Supplemental figure 5).

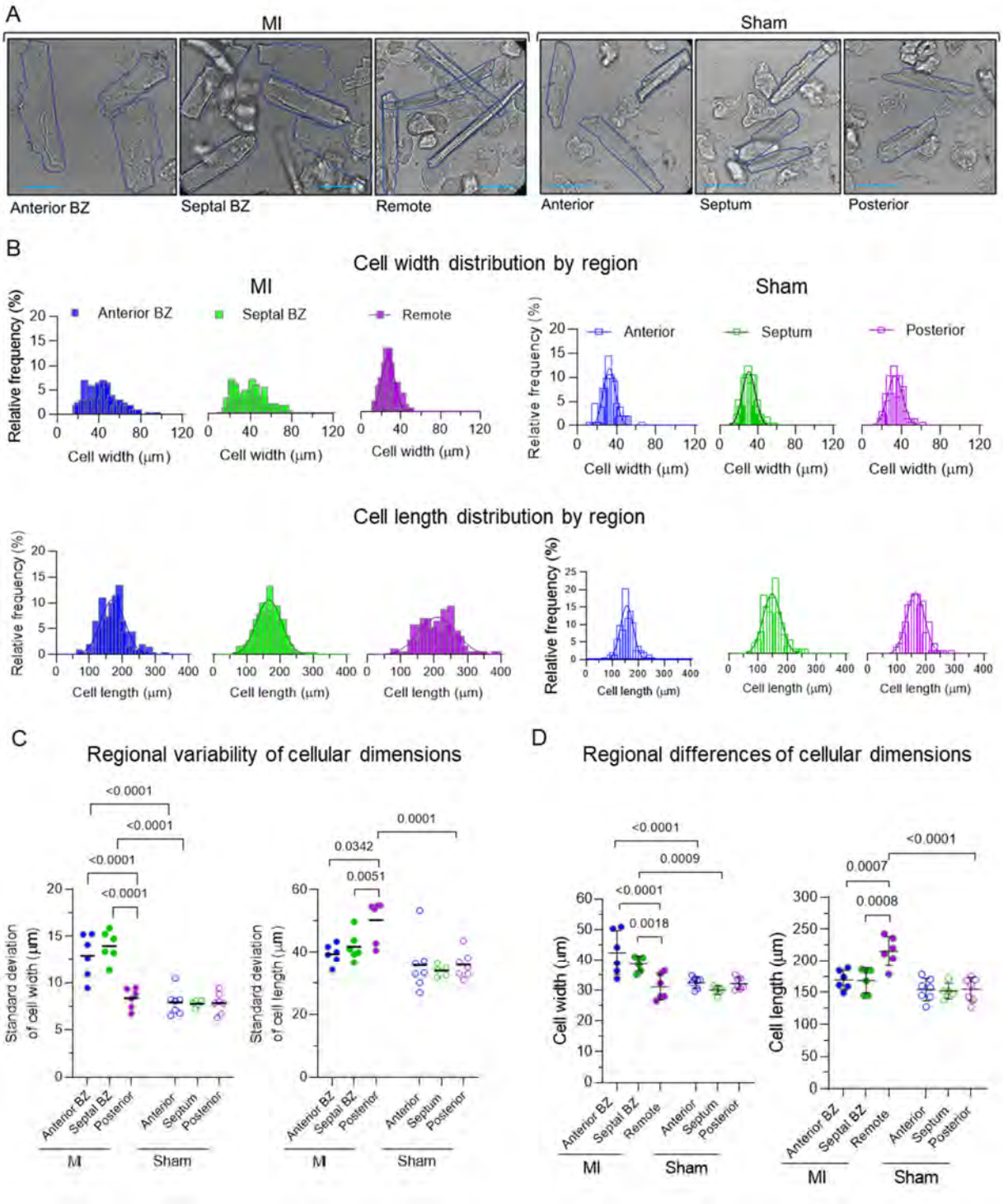

Figure 5. Heterogeneity of cellular hypertrophic remodelling after MI.
A, Examples of isolated cells illustrating regional cell size profiles from MI (left) and sham (right). Scale = 50 μm.
B, An example of the distribution profile of cell width (top) and cell length (bottom) of populations of regionally isolated cells from an MI (left) and Sham (right).

C, Left, variability of regional isolated cell width (left) and cell length (right) as quantified by the standard deviation per pig from MI (N_{pigs} = 6, n_{cells} = 86-216) and Sham (N_{pigs} = 7, n_{cells} = 90-330). Mixed model ANOVA with Bonferroni posttest.
D, Mean data of cell width (right) and cell length (left) per pig from dataset in C.

Border zone gene expression and cell-cell variability of gene expression

The cardiomyocyte AP and hypertrophy data indicate that there are major regional differences in remodeling after MI, and also highlight the cellular heterogeneity within the BZ. We considered that the phenotypic heterogeneity within the BZ could reflect heterogeneous influences that via activation of signaling pathways and downstream induction of transcription would lead to cell-cell variability of gene expression. To examine cellular expression profiles, we again opted for an unbiased approach involving large cell numbers. To this end, we performed single-nucleus droplet-based RNA sequencing (snRNA-Seq) on total nuclei isolated from the BZ and remote regions from a subset of the MI animals (N_{pigs}=3 of both BZ and remote regions) as well as from Sham animals (N_{pigs}=2). This analaysis generated 51860 nuclear transcriptomes, which after filtering yielded 46028 qualified nuclei. Figure 6A (left) illustrates UMAP dimensionality reduction of the total tissue qualified cell nuclei based on their transcriptomic profiles, resulting in clusters representing the different cardiac cell types present in the samples. Nuclei from all samples were represented in all clusters identified, suggesting robust reproducibility and no batch or sample specific effects. As expected, fibroblasts were more numerous in MI than in Sham. This increase in fibroblast proportion was most pronounced in the BZ, which showed significantly greater abundance in comparison with the remote region (Figure 6A, right). Mirroring the increase in fibroblasts, the proportion of cardiomyocytes was significantly decreased in the BZ. Nevertheless, cardiomyocytes were sufficiently numerous in this region (2,981 nuclei) to allow a deeper analysis of differences in their gene expression profiles.

The degree of cardiomyocyte remodeling in the BZ compared to the remote regions was assessed first by differential gene expression analysis (Figure 6B, left). This analysis revealed substantial transcriptional differences (BZ vs Remote: Up: 425, Down: 58; padj <0.05), characterized by altered expression of genes involved in cardiac hypertrophic remodeling, metabolism, and ion channel expression. This difference was further evidenced by the Gene ontology (GO) and Kyoto Encyclopedia of Genes and Genomes (KEGG) pathways enrichment analysis, showing that pathways of advanced cardiomyocyte function (AP and contraction) were downregulated in BZ cardiomyocytes, whereas pathways involved with myofilament rearrangement and ECM production were upregulated (Figure 6B, right).

To explore heterogeneity of cardiomyocytes, a higher resolution re-clustering specifically of the cardiomyocyte population was carried out. From this analysis, five major clusters were identified (Figure 6C). Of these, cluster 2 was most prominent in the BZ, while cluster 0 was significantly lower in BZ than in the remote region. Notably, cluster 2 showed a high level of expression of the hypertrophy marker gene *NPPB*, as well as of the stress related gene *XIRP2* (Figure 6D), previously detected as highly upregulated in the BZ [21,22]. This cluster was also defined by elevated expression of genes involved in the cardiac cytoskeleton and mechanosensing including *NRAP* and *ANKRD1*, and KEGG terms associated with TGF-beta signaling, and acto-myosin organization (data not shown). Clusters 3 and 4 represent the fewest cells in both BZ and remote, although cluster 4 was significantly increased in the BZ at the expense of cluster 3.

While cluster 3 was enriched for KEGG terms in transcription/translation, KEGG terms and genes associated with fibrosis were enriched in cluster 4 (Supplemental figure 6A).

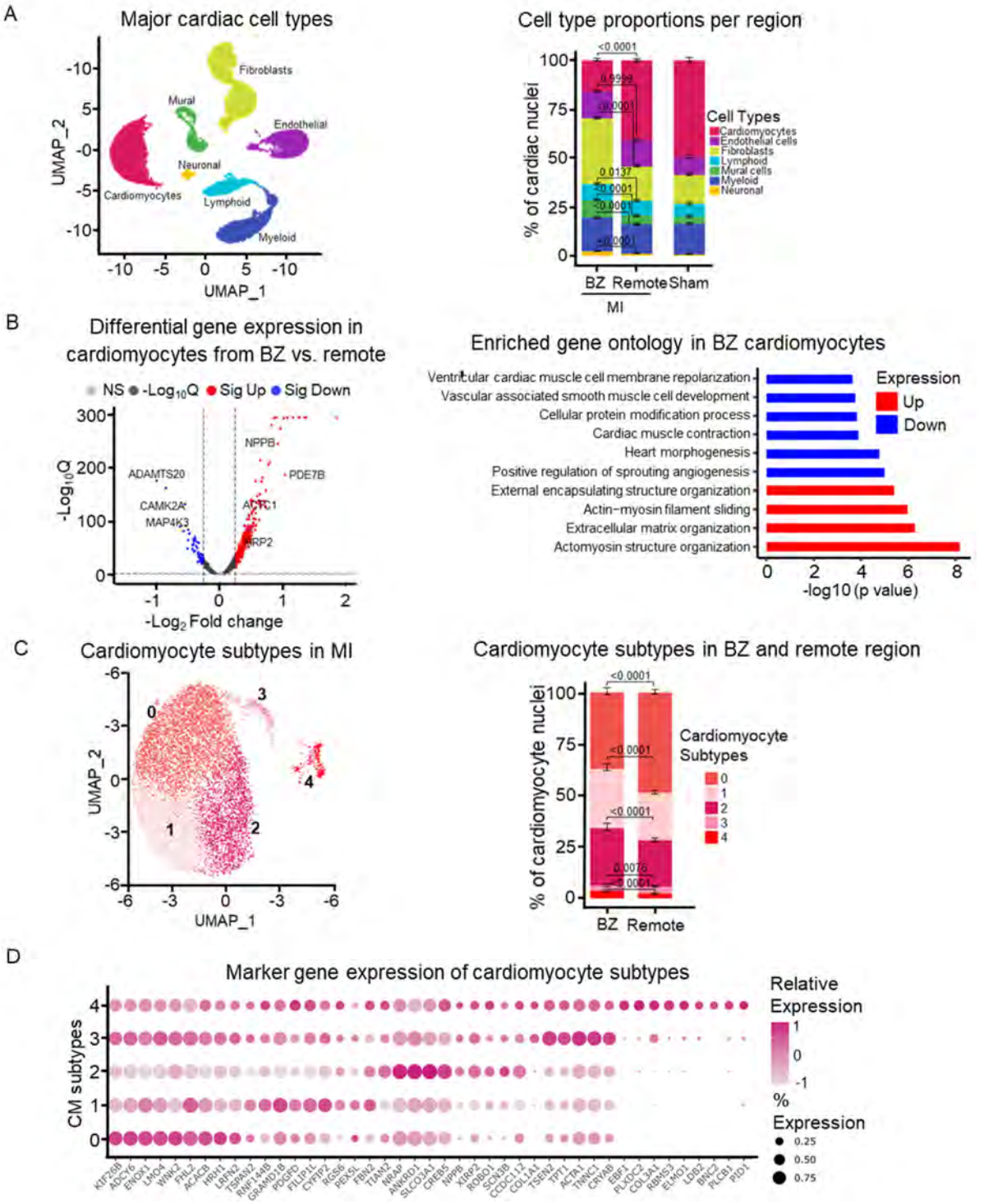

Figure 6. BZ cardiomyocytes have a unique transcriptomic signature.
A, Left, uniform manifold approximation and projection (UMAP) of main cardiac cell types. Right, Right, the fraction of cardiac cell types per region/condition (N_{pigs} = 3 MI, 2 Sham, N_{nuclei} = 46028). Chi-square test with Bonferroni adjustment, error bars represent 95% confidence interval.
B, Left, differentially expressed genes in MI BZ and remote ($p_{adj} < 0.05$, $log_2FC > 0.25$ and < -0.25) detected with DESeq2. Right, GO and KEGG pathway analysis of the differentially expressed genes.
C, Left, clustering of cardiomyocyte nuclei from BZ and remote reveals five cardiomyocyte subtypes. Right, proportion of cardiomyocyte subtypes in MI BZ and remote (N_{pigs} = 3, N_{nuclei} = 10675). Chi-square test with Bonferroni adjustment, error bars represent 95% confidence interval.
D, Gene expression defining the five cardiomyocyte subtypes.

Similar induction of fibrosis-associated genes in cardiomyocytes have been proposed to be associated with proximity to regions of fibrosis [23]. While these data demonstrate the unique nature of the BZ, this analysis did not directly inform upon the phenotypic heterogeneity within the cardiomyocyte population. We therefore next probed the gene expression variability between cells within each region and calculated the Euclidean distance between the individual cardiomyocyte nuclei based on the variable genes in the top 13 significant principal components that defined the cell clusters (Figure 7A). On average, Euclidean distances were significantly greater in the BZ than remote indicating greater cell-cell diversity in their transcriptomes. Using a second approach, we assessed variability at the gene level by quantifying the (residual) over-dispersion [24]. 127 genes showed significantly higher dispersion in the BZ compared to remote, consistent with higher cellular heterogeneity in the BZ (Figure 7B). These highly variable genes (HVGs) were associated with KEGG terms including 'regulation of cardiac muscle hypertrophy', 'ECM formation', 'MAPK signaling' (Supplemental figure 6B). The HVGs were then compared with the list of DEG between the BZ and remote, and with a curated list of genes associated with excitation-contraction coupling (ECC). Figure 7C illustrates that more than half of the HVGs, were also differentially expressed between the BZ and remote, including the hypertrophy markers *NPPB* and *INPP5F*. Further, two HVGs are of interest for ECC, i.e. upregulated *KCNT2* and *SCN3B*. Other genes of interest for ECC are also differentially regulated, including several K^+ channels such as *KCNJ5* which is downregulated (Supplemental Table 2) but do not show greater variability in expression. Figure 7D maps these five differentially regulated HVGs on the BZ myocyte cluster and shows that while *KCNT2* is expressed more diffusely, *SCN3B* and *INPP5F* appear to be expressed in cells that also express *NPPB*. These cells are mostly in sub-cluster 2 (Figure 6C, left).

In a next step, we further studied these *NPPB*+ve cardiomyocytes. Within the BZ, *NPPB*+ve nuclei represented a third of all cardiomyocytes, significantly higher than in remote (Figure 7E). When comparing *NPPB*+ve vs *NPPB*-ve cells, we found marked differences in gene expression (Figure 7F) BZ NPPB+ve vs NPPB-ve: Up: 251 Down:285). Upregulated genes in *NPPB*+ve cardiomyocytes include *SCN3B*, but also *XIRP2* and *ROBO1*. GO pathways include upregulation of muscle contraction pathways, whereas down-regulated ones are enriched in (calcium−dependent) cell−cell adhesion and interaction (Figure 7G), supported by the KEGG analysis (data not shown).

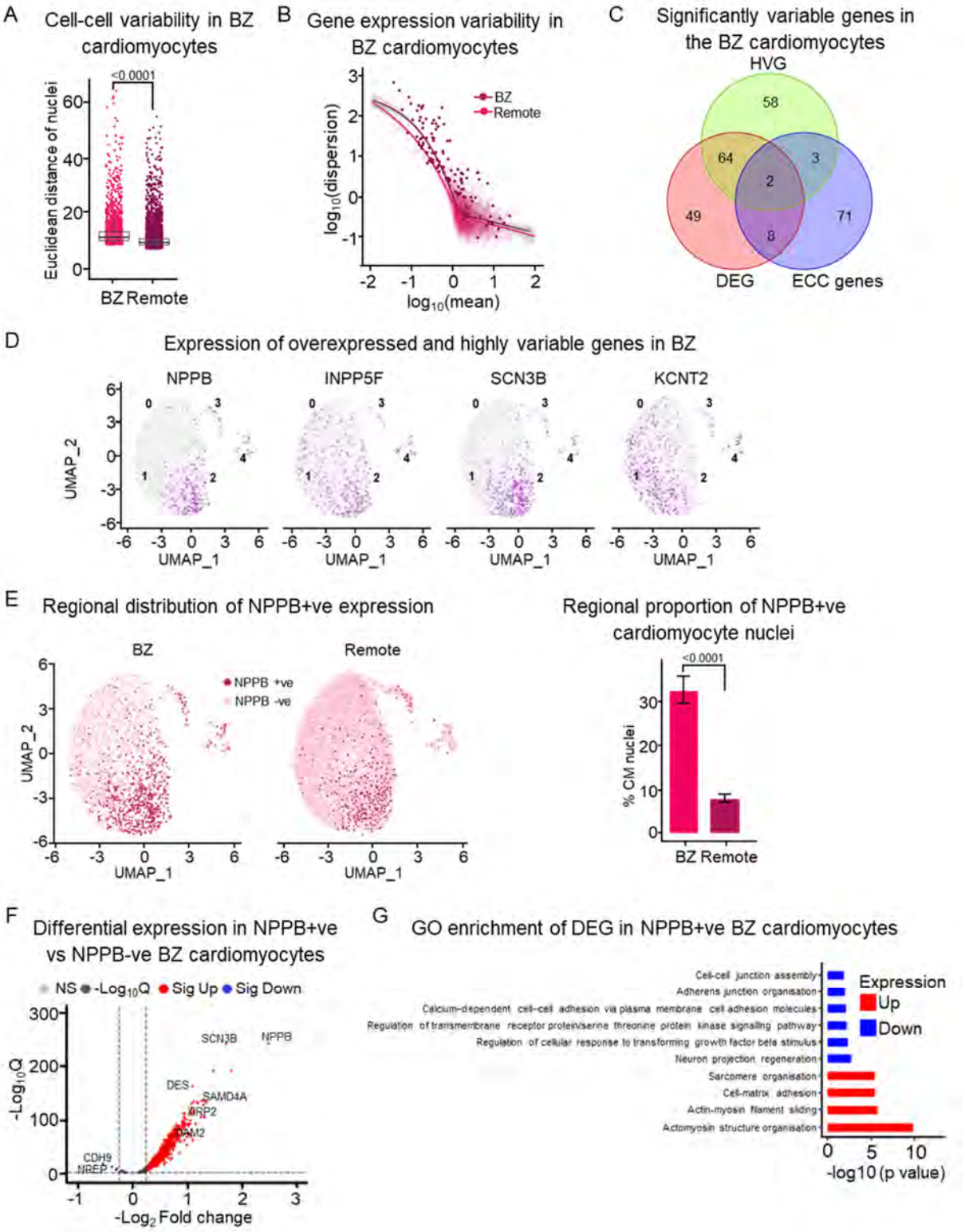
A
Cell-cell variability in BZ cardiomyocytes
<0.0001
Euclidean distance of nuclei
BZ Remote
B
Gene expression variability in BZ cardiomyocytes
BZ
Remote
log10(dispersion)
log10(mean)
C
Significantly variable genes in the BZ cardiomyocytes
HVG
58
64
3
2
49
71
8
DEG
ECC genes
D
Expression of overexpressed and highly variable genes in BZ
NPPB
INPP5F
SCN3B
KCNT2
UMAP_2
UMAP_1
E
Regional distribution of NPPB+ve expression
BZ
Remote
NPPB +ve
NPPB -ve
Regional proportion of NPPB+ve cardiomyocyte nuclei
<0.0001
% CM nuclei
BZ Remote
F
Differential expression in NPPB+ve vs NPPB-ve BZ cardiomyocytes
NS -Log10Q Sig Up Sig Down
-Log10Q
SCN3B
NPPB
DES
SAMD4A
IRP2
DAM2
CDH9
NREP
-Log2 Fold change
G
GO enrichment of DEG in NPPB+ve BZ cardiomyocytes
Cell-cell junction assembly
Adherens junction organisation
Calcium-dependent cell-cell adhesion via plasma membrane cell adhesion molecules
Regulation of transmembrane receptor protein/serine threonine protein kinase signaling pathway
Regulation of cellular response to transforming growth factor beta stimulus
Neuron projection regeneration
Sarcomere organisation
Cell-matrix adhesion
Actin-myosin filament sliding
Actomyosin structure organisation
Expression
Up
Down
-log10 (p value)

Figure 7. Cell-cell variability of cardiomyocytes within the BZ
A, Euclidean distances of cardiomyocyte nuclei re-clustering. N_{nuclei} = 10675, N_{pigs} = 3. Each dot represents a nucleus. The horizontal line in the box plot and the whiskers are median median and interquartile range, error bars are 1.5*interquartile range. Hierarchical t-test.
B, Dispersion of gene expression in BZ compared to remote cardiomyocyte nuclei. The highly variable genes (HVGs) in BZ compared with remote nuclei are marked with bold dots (EFDR < 0.10, the genes with at least 50% increase in biological over-dispersion are defined as HVGs based on a Bayesian inference model). The solid line represents the best fit model of the gene expression variability against expression. The grey bars represent the 95% CI of this model.
C, Overlap between the HVGs, differentially expressed genes (DEGs) in the BZ compared to remote, and excitation-contraction coupling (ECC) related genes.
D, Distribution of expression of the four HVGs, which are also detected as DEGs, across CM subtypes in the BZ.
E, Prominence of NPPB+ve nuclei in MI BZ vs. remote, left. Distribution of NPBB +ve nuclei in BZ compared with Remote, right (Nnuclei = 10675, Npigs = 3 MI). Chi-square test, error bars represent 95% confidence interval.
F, Left, DEGs in NPPB+ve vs. NPPB-ve nuclei in the BZ ($p_{adj} < 0.05$, $log_2FC > 0.25$ and < -0.25).
G, Gene Ontology analysis of the DEGs between NPPB +ve vs NPPB -ve nuclei in the BZ.

Local drivers for heterogeneous remodeling

Local remodeling after MI is complex involving several factors. We investigated the role of local wall stress. Given a homogenous LV chamber pressure distribution and small variations in wall curvature, wall thickness is the main determinant of wall tension. Thus, in the scar, wall tension is high, but compensated by the tensile strength of the fibrous tissue. In the border zone, the number of surviving cardiomyocytes and density of replacement fibrosis is heterogeneous and hence wall thickness and tension can vary within the BZ. MRI data were therefore assessed to determine whether local variations in wall thickness were present in our samples (Figure 8A). The BZ characteristically had more heterogeneity in LGE signal intensity, likely reflecting the heterogeneous fibrosis and cardiomyocyte tissue of the BZ (Figure 8B). We defined the heterogeneity by quantifying the variance (σ^2) of the wall thickness in the radial direction as a metric for local heterogeneity and a stronger assessment than the mean wall thickness. Figure 8C presents the regional distribution of variance of wall thickness in an MI pig with the individual data from each pig presented in Figure 8D (Sham pig data in Supplemental Figure 7A, B). Figure 8E shows that the BZ had a significantly higher variance of wall thickness than remote. Wall curvature did not exhibit a comparable heterogeneity (Supplemental Figure 7C).

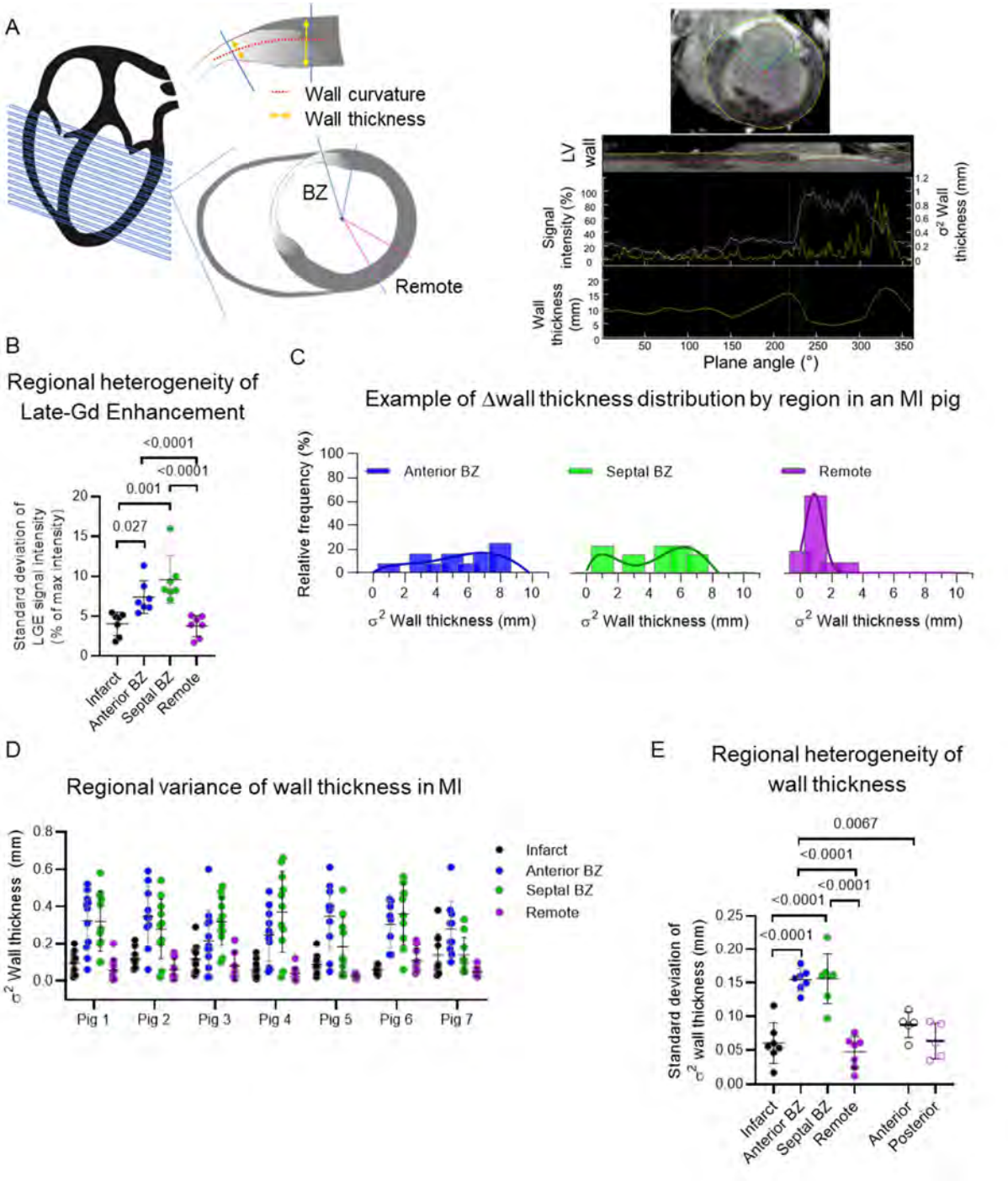

Figure 8. Heterogeneous regional LV wall properties after MI *in vivo*.
A, Left, illustration of short axis MRI slice analysis of regional wall properties of thickness and curvature. Right, example of a cMRI mid-ventricular slice demonstrating LV segmentation and corresponding regional wall property analysis based on signal intensity of the LGE signal.
B, Summary data of variability of mean signal intensity in the cMRI slices from MI (N_{pigs} = 6, n_{slices} = 10-14). One-way ANOVA with Bonferroni posttest.

C, Example of the distribution of regional variance (σ^2) of wall thickness from MI (n_{slices} = 10-14) illustrating increased heterogeneity in the MI BZ.
D, Regional variance (σ^2) of wall thickness *in vivo* from each slice of the cMRI from MI (N_{pigs} = 6, n_{slices} = 10-14).
E, Summary data of the heterogeneity of wall thickness, quantified by standard deviation from (D). Mixed model ANOVA with Bonferroni posttest.

Discussion

Heterogeneity of myocyte remodeling in the MI border zone

In the present data, we found cardiomyocyte heterogeneity at different scales and levels of organization. At the level of the heart, global LV remodeling after MI responds to the increased demand on the surviving myocardium, but the MI injury also leads to regions with distinct cardiomyocyte populations. In comparison to other regions, BZ cardiomyocytes have different morphology, electrical properties and transcription profiles. The present findings for the BZ as a region are in line with earlier reports of differential remodeling in the BZ compared to the remote region [12,13,22], while recently Kelemen *et al.,* [18] described heterogeneous repolarization in arrhythmia-sensitive regions at the BZ. Here we demonstrate the presence of significant heterogeneity within the BZ cardiomyocyte population, supported by a combination of novel and complementary approaches.

Whole-cell patch clamp recording has been the leading method to study altered cellular repolarization and provides insights into underlying member current alterations. Limitations are however the low-throughput, and concomitantly, the potential for selection bias and inter-observer variability. In addition, the interference with cytosolic content is unavoidable. Optical measurements on the other hand have a limitation of the parameters that can be assessed, but have provided us here with a population view on repolarization for 100's of cells per sample, increasing representability for the heart *in vivo* and allowing assessment of population heterogeneity. Single nucleus RNA-sequencing raised the number of cells analyzed yet another order of magnitude, including 1000s of cardiomyocyte nuclei. While a disadvantage here is the small volume of the biopsy sample, the isolation of nuclei by mechanical disruption from the tissue minimizes cell type isolation biases that may occur when comparing fibrotic and non-fibrotic tissues and thus provides a highly representative picture of the *in situ* cell gene expression profile [25]. Across these different scales, analysis of variations within the cardiomyocyte population consistently revealed a higher variability between cardiomyocytes in the BZ than in the remote regions.

Interestingly, across different parameters assessed at cardiomyocyte level, the findings were not necessarily concordant. At cell phenotype level, cell size did not correlate with APD. At transcript level, *NPPB* expression, previously associated with BZ remodeling after MI [22], was a highly variable gene with heterogenous expression in individual BZ cardiomyocytes. It was mostly expressed in a subtype of cardiomyocytes identified as cluster 2, where also *SCN3B* expression was higher. For other ion channels, the distribution was different. *KCNT2*, also displayed highly variable expression, but with different clustering than *SCN3B,* whereas *KCNJ5*, a gene encoding for a GPCR-modulated K^+ channel, was more homogeneously downregulated. The latter

channel may be underlying the reduced inward rectifying current and lability of the resting membrane potential during adrenergic challenge that we previously observed [15]. Altogether, combinations of altered gene expression may lead to the phenotypic heterogeneity that likely contributes to increased arryhtmia susceptibility. These complex changes in gene expression can result from variable activation of signaling pathways.

Mechanisms and drivers of cellular heterogeneity in the BZ

The BZ is highly complex environment where many factors can modulate cardiomyocyte remodeling. During coronary occlusion, the transitional zone between the core ischemic and the fully perfused area is in a state of relative ischemia, and is associated with cell death and remodeling leading to the formation of the future BZ [26]. During reperfusion, further cell death and remodeling occurs with activation of survival pathways, and inflammation initiates a cascade of events that lead to infarct healing [27]. Inflammatory cells remain present for many weeks and months, and contribute to the chronic cardiomyopathy phase. However, whether inflammation and signaling from inflammatory cells is variable within the BZ and thereby contributes to cardimyocyte variability is not known, although recent data highlight the rich cellular environment [23,28]. Similarly, recovery of neurons and heterogeneous nerve ending growth leading to alteration in cardiomyocyte innervation can contribute to the variability in individual cardiomyocyte phenotype [29,30]. The presence of a cell population with neuronal characteristics in the BZ (Figure 6A) supports this concept.

A known key driver of remodeling is mechanical load and stretch, and we noted variation in wall stress along the BZ. The differences in local wall thickness that are responsible for the variable wall stress, can be the consequence of variability in the relative perfusion, consequent cell death, inflammation and replacement fibrosis, and it is difficult to completely disentangle this network. However, there is a well-established link between stretch-induced hypertrophy and local production of Angiotensin II, by cardiomyocytes and fibroblasts [31]. The observation of high levels of XIRP2 (also known as Xin and paralogue of XIRP1/Xin), a protein involved in mechanosensing, cell-cell interaction and component of the intercalated disc, supports the hypothesis that local differences in wall stress contribute to local differences in hypertrophic remodeling. Further, XIRP2 expression is regulated by MEF2A in Angiotensin II-induced cardiomyocyte hypertrophy [28,32]. Consistent with the upregulation of XIRP2, NF2 , which is recruited to intercalated discs and mediates signalling with the Hippo-YAP signalling is also upregulated in the BZ [33].

Contribution of myocyte heterogeneity to *in vivo* repolarization heterogeneity and relevance for arrhythmia

Spatial and temporal heterogeneity of repolarization in the heart facilitate arrhythmias, predominantly as substrate for re-entry. As is well-known from clinical studies, the BZ has areas that are more vulnerable during programmed electrical stimulation to sustain arrhythmias [3]. These vulnerable areas have mostly been seen as regions of irregular fibrosis, identified in MRI and supported by computational studies [2,34]. Whether cell-cell-variability is part of the vulnerability cannot yet be ascertained. The observed heterogeneity of expression of players involved in ECC and some of their regulators may support such a notion. The resultant heterogeneity of repolarization seen in populations of isolated myocytes *ex vivo* is expected to be dampened *in vivo* by cell-cell coupling, but remains present as seen in the ARI data. On average, the ARI durations *in vivo* were shorter than the cellular APDs despite correction of the

ARI for heart rate. It is likely that while cellular AP recordings reflect the cell's native ion channel composition, *in vivo* circulating catecholamines, electrolytes, drugs, mechanical loading, interactions with the matrix and autonomic innervation modulate the resultant APs [35]. These and, importantly, cell coupling may also reduce *in vivo* the extent of APD variability [36]. Nevertheless, we found a correlation between the cardiomyocyte properties and variability *in vivo*, suggesting ion channel composition is an important factor. Pilot data also indicate *in vivo* BZ repolarization variability corelates with arrhythmia susceptibility. As the data suggest that high wall stress in thin fibrotic areas can underlie cardiomyocyte variability, the two mechanisms – heterogeneous cardiomyocyte remodeling and local fibrosis, likely conspire to create *in vivo* vulnerable regions.

Limitations

The study aimed to assess heterogeneity across different scales but technical limitations caution for a full correlation of data. The electroanatomical mapping performed in vivo utilized an endocardial approach that does not provide information on transmural and epicardial heterogeneities, while the cellular isolation reports on the bulk mid-myocardial layer. Moreover, we did not perform atrial pacing maneuvers or investigate the effects of heart rate on regional ARI in vivo, which should be a consideration when interpreting the corroborative in vivo-in vitro data. Finally, the expression data present only a small sample size compared to the other data.

Conclusions

Cardiomyocyte phonotypes in the BZ are heterogeneous, with underlying variability of gene expression between cardiomyocytes. Differences in local wall stress and in microenvironment of innervation and inflammation, could drive this heterogeneous remodeling. The cell-cell heterogeneity will contribute to heterogeneous repolarization *in vivo* and may underlie arrhythmia vulnerability within the BZ.

Acknowledgments

The authors thank Patricia Holemans and Roxane Menten for expert technical assistance with the experimental data acquisition and animal care, and Annemie Biesemans for assistance with cell isolation.

Funding Sources

This work was supported by the Fund for Scientific Research-Flanders (FWO projects G097021N to KRS, RW, HLR, PC; G0C6419N to HLR) and by the BOF research fund of KU Leuven (to RW, PC and HLR); RW is supported as Senior Clinical Investigator and MA as PhD fellow by the Fund for Scientific Research-Flanders (FWO).

Disclosures

RW reports research funding and speakers and consultancy fees from Abbott.

References

1. Solomon SD, Zelenkofske S, McMurray JJV, Finn PV, Velazquez E, Ertl G, Harsanyi A, Rouleau JL, Maggioni A, Kober L, et al. Sudden Death in Patients with Myocardial Infarction and Left Ventricular Dysfunction, Heart Failure, or Both. *N Engl J Med*. 2005;352:2581-2588.

2. Pashakhanloo F, Herzka DA, Halperin H, McVeigh ER, Trayanova NA. Role of 3-Dimensional Architecture of Scar and Surviving Tissue in Ventricular Tachycardia. *Circulation: Arrhythmia and Electrophysiology*. 2018;11:e006131.

3. Martin R, Maury P, Bisceglia C, Wong T, Estner H, Meyer C, Dallet C, Martin CA, Shi R, Takigawa M, et al. Characteristics of Scar-Related Ventricular Tachycardia Circuits Using Ultra-High-Density Mapping. *Circulation: Arrhythmia and Electrophysiology*. 2018;11:e006569.

4. Nieves-Cintrón M, Hirenallur-Shanthappa D, Nygren PJ, Hinke SA, Dell'Acqua ML, Langeberg LK, Navedo M, Santana LF, Scott JD. AKAP150 participates in calcineurin/NFAT activation during the down-regulation of voltage-gated K+ currents in ventricular myocytes following myocardial infarction. *Cell Signal*. 2016;28:733-740.

5. Rossow CF, Minami E, Chase EG, Murry CE, Santana LF. NFATc3-Induced Reductions in Voltage-Gated K+ Currents After Myocardial Infarction. *Circ Res*. 2004;94:1340-1350.

6. Liu M, Liu H, Parthiban P, Kang G-J, Shi G, Feng F, Zhou A, Gu L, Karnopp C, Tolkacheva EG, et al. Inhibition of the unfolded protein response reduces arrhythmia risk after myocardial infarction. *J Clin Invest*. 2021;131:e147836.

7. Qin D, Zhang Z-H, Caref EB, Boutjdir M, Jain P, El-Sherif N. Cellular and Ionic Basis of Arrhythmias in Postinfarction Remodeled Ventricular Myocardium. *Circ Res*. 1996;79:461-473.

8. De Villiers C, Riley PR. Mouse models of myocardial infarction: comparing permanent ligation and ischaemia-reperfusion. *Dis Model Mech*. 2020;13:dmm046565.

9. Baba S, Dun W, Cabo C, Boyden PA. Remodeling in Cells From Different Regions of the Reentrant Circuit During Ventricular Tachycardia. *Circulation*. 2005;112:2386-2396.

10. Sasano T, McDonald AD, Kikuchi K, Donahue JK. Molecular ablation of ventricular tachycardia after myocardial infarction. *Nat Med*. 2006;12:1256-1258.

11. Lindsey ML, Bolli R, Canty JM, Jr., Du XJ, Frangogiannis NG, Frantz S, Gourdie RG, Holmes JW, Jones SP, Kloner RA, et al. Guidelines for experimental models of myocardial ischemia and infarction. *Am J Physiol Heart Circ Physiol*. 2018;314:H812-H838.

12. Hegyi B, Bossuyt J, Griffiths LG, Shimkunas R, Coulibaly Z, Jian Z, Grimsrud KN, Sondergaard CS, Ginsburg KS, Chiamvimonvat N, et al. Complex electrophysiological remodeling in postinfarction ischemic heart failure. *Proceedings of the National Academy of Sciences*. 2018;115:E3036-E3044.

13. Dries E, Amoni M, Vandenberk B, Johnson DM, Gilbert G, Nagaraju CK, Puertas RD, Abdesselem M, Santiago DJ, Roderick HL, et al. Altered adrenergic response in myocytes bordering a chronic myocardial infarction underlies in vivo triggered activity and repolarization instability. *The Journal of Physiology*. 2020;598:2875-2895.

14. Yellon DM, Hausenloy DJ. Myocardial Reperfusion Injury. *N Engl J Med*. 2007;357:1121-1135.

15. Amoni M, Claus P, Dries E, Nagaraju C, De Buck S, Vandenberk B, Ingelaere S, Vermoortele D, Roderick HL, Sipido KR, et al. Discrete sites of frequent premature ventricular complexes cluster within the infarct border zone and coincide with high frequency of delayed afterdepolarizations under adrenergic stimulation. *Heart Rhythm*. 2021;18:1976-1987.

16. Sikkel MB, Francis DP, Howard J, Gordon F, Rowlands C, Peters NS, Lyon AR, Harding SE, Macleod KT. Hierarchical statistical techniques are necessary to draw reliable conclusions from analysis of isolated cardiomyocyte studies. *Cardiovasc Res*. 2017;113:1743-1752.

17. Lachaud Q, Aziz MHN, Burton FL, Macquaide N, Myles RC, Simitev RD, Smith GL. Electrophysiological heterogeneity in large populations of rabbit ventricular cardiomyocytes. *Cardiovasc Res*. 2022;10:cvab375.

18. Kelemen K, Greener ID, Wan X, Parajuli S, Donahue JK. Heterogeneous repolarization creates ventricular tachycardia circuits in healed myocardial infarction scar. *Nature Communications*. 2022;13:830.

19. Ciaccio EJ, Coromilas J, Wit AL, Peters NS, Garan H. Formation of Functional Conduction Block During the Onset of Reentrant Ventricular Tachycardia. *Circulation: Arrhythmia and Electrophysiology*. 2016;9:e004462.

20. Litviňuková M, Talavera-López C, Maatz H, Reichart D, Worth CL, Lindberg EL, Kanda M, Polanski K, Heinig M, Lee M, et al. Cells of the adult human heart. *Nature*. 2020;588:466-472.

21. Cui M, Wang Z, Chen K, Shah AM, Tan W, Duan L, Sanchez-Ortiz E, Li H, Xu L, Liu N, et al. Dynamic Transcriptional Responses to Injury of Regenerative and Non-regenerative Cardiomyocytes Revealed by Single-Nucleus RNA Sequencing. *Dev Cell*. 2020;53:102-116 e108.

22. Van Duijvenboden K, De Bakker DEM, Man JCK, Janssen R, Günthel M, Hill MC, Hooijkaas IB, Van Der Made I, Van Der Kraak PH, Vink A, et al. Conserved NPPB+ Border Zone Switches From MEF2- to AP-1–Driven Gene Program. *Circulation*. 2019;140:864-879.

23. Heras-Bautista CO, Mikhael N, Lam J, Shinde V, Katsen-Globa A, Dieluweit S, Molcanyi M, Uvarov V, Jutten P, Sahito RGA, et al. Cardiomyocytes facing fibrotic conditions re-express extracellular matrix transcripts. *Acta Biomater*. 2019;89:180-192.

24. Eling N, Richard AC, Richardson S, Marioni JC, Vallejos CA. Correcting the Mean-Variance Dependency for Differential Variability Testing Using Single-Cell RNA Sequencing Data. *Cell Systems*. 2019;9:401-413.

25. Denisenko E, Guo BB, Jones M, Hou R, De Kock L, Lassmann T, Poppe D, Clément O, Simmons RK, Lister R, et al. Systematic assessment of tissue dissociation and storage biases in single-cell and single-nucleus RNA-seq workflows. *Genome Biol*. 2020;21:130.

26. Jackson BM, Gorman JH, Moainie SL, Guy TS, Narula N, Narula J, St. John-Sutton MG, Edmunds LH, Gorman RC. Extension of borderzone myocardium in postinfarction dilated cardiomyopathy. *J Am Coll Cardiol*. 2002;40:1160-1167.

27. Frangogiannis NG. The inflammatory response in myocardial injury, repair, and remodelling. *Nature Reviews Cardiology*. 2014;11:255-265.

28. Kuppe C, Ramirez Flores RO, Li Z, Hannani M, Tanevski J, Halder M, Cheng M, Ziegler S, Zhang X, Preisker F, et al. Spatial multi-omic map of human myocardial infarction. *Nature*. 2022;608:766-777.

29. Gardner RT, Wang L, Lang BT, Cregg JM, Dunbar CL, Woodward WR, Silver J, Ripplinger CM, Habecker BA. Targeting protein tyrosine phosphatase σ after myocardial infarction restores cardiac sympathetic innervation and prevents arrhythmias. *Nature Communications*. 2015;6:6235.

30. Zhu C, Rajendran PS, Hanna P, Efimov IR, Salama G, Fowlkes CC, Shivkumar K. High-resolution structure-function mapping of intact hearts reveals altered sympathetic control of infarct border zones. *JCI Insight*. 2022;7:e153913.

31. Malhotra R, Sadoshima J, Brosius FC, Izumo S. Mechanical Stretch and Angiotensin II Differentially Upregulate the Renin-Angiotensin System in Cardiac Myocytes In Vitro. *Circ Res*. 1999;85:137-146.

32. McCalmon SA, Desjardins DM, Ahmad S, Davidoff KS, Snyder CM, Sato K, Ohashi K, Kielbasa OM, Mathew M, Ewen EP, et al. Modulation of Angiotensin II–Mediated Cardiac Remodeling by the MEF2A Target Gene Xirp2. *Circ Res*. 2010;106:952-960.

33. Guo H, Lu YW, Lin Z, Huang Z-P, Liu J, Wang Y, Seok HY, Hu X, Ma Q, Li K, et al. Intercalated disc protein Xinβ is required for Hippo-YAP signaling in the heart. *Nature Communications*. 2020;11:4666.

34. Ashikaga H, Sasano T, Dong J, Zviman MM, Evers R, Hopenfeld B, Castro V, Helm RH, Dickfeld T, Nazarian S, et al. Magnetic resonance-based anatomical analysis of scar-related ventricular tachycardia: implications for catheter ablation. *Circ Res*. 2007;101:939-947.

35. Conrath CE, Opthof T. Ventricular repolarization: an overview of (patho)physiology, sympathetic effects and genetic aspects. *Prog Biophys Mol Biol*. 2006;92:269-307.

36. Glukhov AV, Fedorov VV, Lou Q, Ravikumar VK, Kalish PW, Schuessler RB, Moazami N, Efimov IR. Transmural Dispersion of Repolarization in Failing and Nonfailing Human Ventricle. *Circ Res*. 2010;106:981-991.

Online supplement

Expanded Methods

Animal handling

The experimental protocols of this study were approved by the KU Leuven Animal Ethical Committee (Ethische Commissie Dierproeven, KU Leuven), with permit number ECD137/2018. Animal husbandry and treatment was according to the Guide for the Care and Use of Laboratory Animals (National Institute of Health, USA), and the European Directive 2010/63/EU.

Thirty-four domestic pigs (Sus scrofula domesticus Strain: TN70, Topigs Norsvin) of both sexes were used in this study. Swine were of weight 34±4 kg on entry into the study and were randomized to MI (N = 22) and Sham (N = 11). Two animals were excluded from the final dataset due to sudden cardiac death soon after the induction procedure. Thirteen animals used in this study were also used to gather data presented in a recent study 15.

Animals were housed in single pens with a standard 14 h light, 10 h dark cycle, temperature of 22 ± 2°C and humidity of 45-70%. Animals had free access to a standard chow (Optivo Pro 9041, AVEVE, Belgium) and water. Exception was made in the week of experimentation, animals were fed twice a day (between 7 and 8 am and between 12 and 2 pm, with welfare monitoring) and fasted the day before in vivo procedures.

All invasive procedures and in vivo experiments were performed under general anesthesia (Supplemental figure 1A). The anesthetic regime consisted of an initial sedation with tiletamine/zolazepam 8 mg/kg and xylazine 2.5 mg/kg IM. The animal was then transported to the laboratory where intravenous access was obtained. Then, anesthesia induced with propofol 3 mg/kg, and maintained with a combination of propofol 10 mg/kg/h and remifentanil 0.2-0.4 µg/kg/h IV. Animals were intubated endotracheally with 6-8 Fr standard endotracheal tube and ventilated with a 50% oxygen-air mixture at 6-10 mL/kg tidal volume. During all invasive procedures, antibiotics (cefazolin 22-50 mg/kg, IV) and anticoagulation (acetylsalicylic acid, 500 mg and periodic heparin 5000-10000 IU, IV) were routinely administered. Post-operatively, animals received broad-spectrum antibiotics (amoxicillin 15 mg/kg or enrofloxacilin 4 mg/kg) with analgesia, buprenorphine HCl 0.02-0.03 mg/kg, IM and fentanyl transdermal patch (12 µg/h for 72 h).

Myocardial infarction induction

A clinically relevant ischemia-reperfusion model of MI was used as previously described 15. Briefly, all animals were pre-medicated for three days with amiodarone 300 mg, as well as one day of aspirin 300 mg and clopidogrel 300 mg. Animals were then randomized to either MI induction or Sham operation on day 0. Under anesthesia, the left carotid artery was directly cannulated by surgical cut-down with a 5/6 Fr vascular sheath. Baseline left ventricle (LV) and aorta pressures were recorded using a Millar pressure catheter and PowerLab system (ADInstruments, AU). Then, under fluoroscopic guidance a 5/6 Fr Judkins-left or Amplatz-left

coronary guiding catheter was positioned in the left main coronary ostium. An intracoronary injection of nitroglycerine 250-300 mg was administered intravenously (IV) to prevent vasospasm. 5 mg/kg amiodarone IV was administered as a bolus to reduce arrhythmias. A standard 0.014-inch coronary wire was stabilized in the left anterior descending coronary artery (LAD) and a 2.5-3.0 mm angioplasty balloon, was positioned over-the-wire immediately after the first diagonal branch (D1) and completely inflated to ~12 bar. Ischemia of the anterior-septal territory was induced by complete occlusion of the distal 3/4 of the LAD, and was confirmed by angiography (Supplemental figure 1A). This was also evident from ST-segment elevation. Ischemia, was maintained for 120 minutes after which, the balloon was deflated and the myocardium reperfused. The animal was monitored for at least 60 minutes and the carotid artery repaired. Sham animals, underwent the same procedure, without occlusion, and were included as controls.

During ischemia, sustained ventricular tachycardia or fibrillation, occurred in approximately 17/22 (77%) of animals and was managed by prompt external defibrillation with 150-200 J to restore sinus rhythm. Hypotension (BP < 60/40 mmHg) was treated with noradrenaline 2-5 µg/min or adrenaline 1-10 µg/min infusion and weaned during reperfusion. All animals received amiodarone for 3 days. Aspirin 100 mg and clopidogrel 75 mg was given daily for 1 month.

No animals died during the MI induction. The early mortality (<5 days post-MI) was 9% (2 animals), due to SCD after MI. after ~5 days of observation, animals were transferred to the KU Leuven University farm and returned around ~ day 28 post-MI.

Cardiac magnetic resonance imaging

One month after MI or sham procedure, animals were brought under general anesthesia and cardiac magnetic resonance imaging (cMRI) was performed using a 3T whole-body scanner (PRISMA, Siemens, Erlangen, Germany) as previously described 15. Animals were placed supine in the scanner, electrocardiogram (ECG) leads were placed around the heart and a two phased-array body coils were wrapped around the thorax to increase signal to noise ratio. Acquisition was performed with ECG-gating during periods of apnea, achieved by suspending mechanical ventilation. Standard clinical sequences were adapted to acquire comprehensive views of the heart as well as cine images. Corresponding images of late gadolinium enhancement (LGE) were acquired 12 minutes following a double dose bolus of Gd (gadoterate meglumine, Dotarem, 0.2 mmol/kg) (Fig 1A).

The cMRI data was analyzed and images segmented with custom software (RightVol; KU Leuven) on an offline workstation to assess heart structure, dimensions and function as well as left ventricle (LV) infarct size. Data are summarized in Supplemental table 1.

To assess local variability of LV wall properties in the regions and compare the BZ and remote, we analyzed the wall thickness, curvature and LGE of each slice. The BZ was defined as the region with signal intensity 20-70% of the maximum intensity (infarct core), and the remote as the posterior wall opposite to the BZ. The myocardial curvature and variance ($\sigma 2$) of wall thickness properties of each region were calculated as previously 37.

Two to four days after the cMRI, an in vivo electrophysiology (EP) study was performed.

Cardiac electrophysiology study

The in vivo electrophysiological study was performed under general anesthesia as before, with the exception that sedation was achieved with tiletamine/zolazepam 8 – 12 mg/kg only, omitting xylazine to avoid its adrenergic effects. Vascular access for cardiac catheterization, was obtained by cannulating two arteries (carotid or femoral) and two veins (jugular or femoral). Carotid and jugular veins were exposed by surgical cut-down and femoral vessels were punctured percutaneously under ultrasound guidance. An 8 or 9 Fr vascular sheath was used for arterial access and 7 Fr sheaths for venous access. A single bolus of aspirin (500 mg), and periodic boluses of heparin (5000-10000 IU) were administered for anticoagulation.

Follow-up, LV and Aortic pressures were recorded as described above. Then, electroanatomical mapping of the left ventricle (LV) endocardium was performed using the EnSite Precision 2.0 mapping system (Abbott Medical, New Jersey, USA) paired with a BARD Electrophysiology Labsystem Pro EP (Boston Scientific, USA) as described previously 15. Standard electrophysiology (EP) catheters (Biosense Webster, Diegem, Belgium) were positioned in the coronary sinus and the right ventricle (RV) apex for orientation and diagnostic signals. The 9 Fr 64-electrode multi-electrode array (MEA) catheter for non-contact mapping was positioned centrally in the LV chamber under bi-plane fluoroscopic guidance, with the pigtail in a stable position in the LV apex.

A bi-plane left ventriculogram (left anterior oblique 50° and right anterior oblique 40°) was made under fluoroscopy with 60-80 mL of a 50-80% saline-iodine mixture, to estimate chamber dimensions and guide mapping. An electroanatomical map of the LV was created by roving the LV using a decapolar Lasso and quadripolar linear mapping catheter paired with the MEA. Point-by-point contact mapping was performed by with attention to acquiring bipolar voltages annotated on the map to create an electroanatomical map of the LV. This was used to define the conventional BZ using peak-to-peak voltages of 0.5-1.5 mV.

When the mapping procedure was completed, the mapping catheter was withdrawn from the LV. After a stabilization period of approximately 20 minutes, the sinus electrical activity of the LV was recorded by non-contact mapping for 5 minutes. For non-contact mapping, the 64-electrode MEA was used to distribute 2048 virtual electrodes around the LV anatomical map as previously described 15. Virtual electrograms were then recorded at a sampling rate of 1.2 kHz and filtered with a bandwidth of 0.1-300 Hz.

After the EP study, surgical access was repaired and hemostasis achieved, after which the animal recovered with appropriate analgesia and antibiotics as appropriate - Amoxicillin15 mg/kg or Enrofloxacilin 4 mg/kg. Procedure-related mortality after EP study was ~16% (4 MI and 2 Sham).

In vivo mapping data analysis by E-field

All electroanatomical and electrophysiological data were exported to an offline workstation and analyzed using a custom-made Matlab software (RightHemo-MEA, KU Leuven) and activation repolarization intervals were calculated for the 2048 virtual electrogram positions on the endocardial surface. The analysis methodology is described and validated in a separate study (Vermoortele et al., 2022, manuscript under review).

The local ARI duration for each annotated electrogram were used to construct a spatially dense ARI map incorporating the 2048 electrograms (Supplemental figure 3B). To visualize and assess local ARI heterogeneity, a heterogeneity index (H-index) was determined for each electrogram as the standard deviation of ARIs in a 1 cm radius surrounding each electrograms. The H-index was annotated on each point of the LV and visualized as a polar map (Supplemental figure 3C).

Sacrifice and cell isolation

After 1-3 days for recovery, animals were sacrificed for tissue sampling and cell isolation as previously 15.

For sacrifice, the animals were sedated, and anesthesia was induced with pentobarbital (20 mg/kg, IV) with artificial ventilation. A midline-sternotomy, was performed and the heart exposed by opening the pericardium and mobilized. Full anticoagulation with heparin (20 000 IU) was given and an overdose of anesthesia was given (50 mg/kg pentobarbital, IV). The heart was quickly harvested by dividing the great vessels and placed in cold oxygenated Tyrode's solution on ice and transported to the lab.

All hearts were prepared by rinsing with cold oxygenated Tyrode's solution. The heart was then dissected to isolate the LV. From MI hearts, LV wedges of the anterior BZ, the septal BZ and the non-infarcted remote region were dissected and their perfusing arterial branches cannulated as follows: anterior BZ via the proximal LAD above the 1st diagonal branch and the septal BZ the entire LAD above the 1st conus branch with ligation of leaking branches, finally the remote region was cannulated via the left circumflex or obtuse marginal branch. In Sham hearts, the matching regions from the anterior, septal and posterior LV wall were chosen. A small piece (0.5-1 g) of the anterior BZ, septal BZ and remote territories used for cell isolation were collected and snap frozen in liquid nitrogen and stored at -80 °C for batch processing.

The wedges were perfused by a constant flow Langendorff system (3-4 mL/min) at 37 °C. The tissue was briefly perfused with normal Tyrode's (in mmol/L: NaCl 137, KCl 5.4, MgCl2 0.5, CaCl2 1.8, Na-HEPES 11.8, and glucose 10; pH 7.4) to washout residual blood. Then the tissue was perfused with Ca2+-free Tyrode's, followed by enzyme-containing Ca2+-free Tyrode's solution (collagenase-A, Roche and protease-XIV, Sigma Aldrich). After digestion, low Ca2+ Tyrode's (in mmol/L: NaCl 130, KCl 5.4, KH2PO4 1.2, MgSO4 1.2, CaCl2 0.18, Na-HEPES 6, glucose 20, pH 7.2) was perfused to washout the enzyme. The digested tissue was minced and filtered to liberate single cardiomyocytes in solution. The isolated cardiomyocytes were then resuspended in normal Tyrode's.

Cellular electrophysiological recordings

Cellular action potentials were recorded from the isolated cells by patch-clamp and optical electrophysiological techniques as before 13.

For patch clamp recordings, cells were placed on the stage of an inverted microscope with a setup as previously described 15. Cells were constantly superfused with normal Tyrode's solution at 37 °C. Patch pipettes were fashioned from borosilicate glass (GB 200-8P, Science Products) and pulled to a resistance of 2-3 MΩ when filled with internal solution (in mmol/L): K-

aspartate 120, NaCl 10, KCl 20, K-HEPES 10, MgATP 5, and K5Fluo-4 0.05; pH 7.2. Whole-cell patch clamp mode was employed and cells studied using the current clamp configuration (Axon 200B amplifier, Axon Instruments). Cells were stimulated with a suprathreshold depolarizing pulse of 2-4 nA, until steady state, after which at least 30 APs were recorded.

Patch-clamp data were exported in .abf format and files were analyzed using pClamp software v11 (Molecular Devices, USA). Cell capacitance, resting membrane potential and AP duration (APD) at 90% repolarization (APD90) were analyzed.

For population studies, optical recordings of APs were performed using a voltage-sensitive dye. An aliquot of the freshly isolated cells was incubated at 37 ˚C for 30 minutes with 5 µM Di-8-Anepps (Thermo Fisher Scientific, Belgium), then washed and placed in a recording chamber of an inverted microscope (Nikon Ti-E, Germany), equipped with a 40x oil immersion objective lens, N.A. = 1.3 and refractive index = 1.5. The cells were superfused with Tyrode's solution at 37 ˚C and field stimulated with suprathreshold 2-4 ms pulses at 1 Hz, generated by 2 platinum electrodes placed in the bath. A CoolLED pE340fura illumination system was used for excitation centered at 488 nm, with emission recorded at >535 nm. Fluorescence emission was captured using a sCMOS camera at 200 Hz with an exposure time of 5 ms and 4×4 binning, with resultant voxels of 0.65 µm/pixel (Orca flash-c11440, Hamamatsu). Illumination and image acquisition were controlled with Nikon NIS-Elements (v5) software.

Image files were exported in .ND format. Recordings were analyzed in ImageJ software (NIH, USA) using a semi-automated custom-written macro. Briefly after a pre-processing step, the cells were semi-automatically segmented and identified; then fluorescence changes associated with the AP within the region of interest were converted to an AP waveform. APs were then automatically analyzed in MatLab. The last 10 APs were averaged and the APD at 25% (APD25), 50% (APD50) and 90% repolarization (APD90) were collected.

Single-nucleus RNA sequencing and gene expression analysis

Tissue samples collected under RNase free conditions from the same regions as used for cell isolation were rapidly frozen in liquid nitrogen and stored at -80°C.

Isolation of cardiac nuclei

Debris-free suspensions of intact nuclei were generated by tissue homogenisation followed by sucrose gradient centrifugation and flow sorting with all steps performed at ≤ 4 °C with modifications from Thienpont et al., 38 and Preissl et al., 39. Prior to processing, sample quality and preservation were assessed by Bioanalyzer analysis of RNA isolated from the samples used. Only samples with an RNA Integrity (RIN; Agilent Bioanalyzer) of > 7.6 were used. Approximately 80 mg of snap-frozen cardiac tissue (each sample in duplicate) was cut on ice with a scalpel into 4-5 smaller pieces after which they were placed into gentleMACS M-tubes (Miltenyi Biotec, 130093236) containing 5 mL lysis buffer and thawed on ice (5 mM CaCl2, 3 mM MgAc, 2 mM EDTA, 0.5 mM EGTA, 10 mM Tris-HCL pH 8, supplemented prior to use with 1 mM DDT (Sigma-Aldrich, 646563), 1 µg/mL actinomycin D (Sigma-Aldrich, A1410), 0.05% protease inhibitor cocktail (Sigma-Aldrich, P8340), and 0.04 U/µL RNA inhibitors-RNase OUT (Thermo fisher Scientific, 10777019)). Tissue was then homogenized using a gentleMACS dissociator (Miltenyi Biotec) on program "protein_01" for 1 min. After homogenization, 5 mL lysis buffer

supplemented with 0.1 % NP-40 Surfact-Amps™ (Thermo fisher Scientific, 28324) was added to the cell suspension, which was then filtered through a 30 µm filter to remove non-disrupted tissue and cells (Miltenyi Biotec, 130041407). To recover retained nuclei, the filter was washed with an additional 2 mL lysis buffer containing 0.1 % NP-40 Surfact-Amps™. Nuclei were then harvested by centrifugation (1000 x g, 5 min), after which the pellet was resuspended in and overlayed on sucrose buffer (1 M sucrose, 3 mM MgAc, 10 mM Tris-HCl, pH 8) containing 1 mM DDT, 1 µg/mL actinomycin D, 0.05% protease inhibitor cocktail, 0.04 U/µL RNA inhibitors-RNase OUT, and 2 µg/mL WGA (Sigma-Aldrich, L9640), then pelleted by centrifugation (1000 x g, 5 min). The cardiac nuclei pellet was washed twice (650 x g/ 500 x g, 6 min) in PBS including 0.04 U/µL RNA inhibitors-RNase OUT, 2 µg/mL WGA, and 750 µg/mL UltraPure™ BSA (Thermo fisher Scientific, AM2616), after which nuclei were resuspended in staining buffer (wash buffer containing 0.02 mg/mL DAPI) for 10 min. After centrifugation (500 x g, 6 min), the pellet was resuspended in 300 µl PBS, pooled with the duplicate pellet of each sample, and passed through a 35 µm cell strainer. Cardiac nuclei were sorted into PBS containing 0.04 U/µL RNA inhibitors-RNase OUT and 750 µg/mL UltraPure™ BSA using a BD Influx flow cytometer. Intact debris-free cardiac nuclei were harvested by setting gates for DAPI+ve and particle size. Finally, after counting using a LUNA-FL™ Counter (Logos Biosystems), cardiac nuclei were pelleted by centrifugation at 500 x g for 6 min, and then resuspended into sorting buffer.

Sequencing and analysis of snRNA-seq data

Cardiac nuclear suspensions (~6000 nuclei per animal, based on counting) were loaded on a Chromium Single Cell Instrument (10x Genomics) to generate single-nucleus GEMs. Single-nucleus RNAseq libraries were prepared using Chromium Single-cell 3' Library Version 3 Chemistry, Gel beads, Chip, and Multiplex kit (10x Genomics) following the manufacturer's protocol. Libraries were sequenced on Illumina Novaseq 6000 at a depth of 30,000 reads per nucleus.

Single nucleus transcriptomics analysis

Transcriptome datasets from sequenced reads per lane (each lane contains only one animal sample) of sequencing were provided by CellRanger V5 through aligning the reads to both introns and exons from premature unprocessed nuclear RNAs. Ambient RNAs and low complexity libraries in the raw expression matrices were removed with CellBender 40 and nuclear doublets detected and removed by scDblFinder 41. Singlet nuclei from different datasets were then merged and further processed using Seurat V4 42 in R V4.1.2 (R Core Team (2021)). Nuclei were further filtered according to following QC criteria: These extra QC thresholds are adjusted based on the log10 nGenesPerUMI (> 0.8) as a library complexity index, nUMI (<60000), nGenes (>350) based on the outliers of log10X visualized by boxplot, and the percentage of reads originating from mitochondrial coded RNAs (<5%) and rRNAs (<5%). After library normalization, gene expression scaling, and identification of variable genes, the nearest neighbour graph was constructed based on the Euclidean distance of the nuclei in each top significant principal component (PCs). Next, the main cell types are clustered using the Louvain algorithm at a low resolution (0.1). To visualize clusters, the UMAP (Uniform Manifold Approximation and Projection) non-linear dimensional reduction approach was used to group similar nuclei in a low-dimensional space. Thereafter, the clusters were annotated based on their expression of established cell-type-specific marker expression 20. Cardiomyocyte nuclei with > 700 genes detected were then extracted from the whole merged datasets and integrated using Harmony 43 and re-clustered at a higher resolution (0.25). The proportion of each

cardiomyocyte subtype detected was then quantified per heart region and the ratio of cardiomyocyte cluster 0 to other cardiomyocyte subtypes in each region statistically compared (with Chi Square test).

The genes defining each cardiomyocyte subtype were identified amongst those genes expressed in at least 10% of nuclei in either of the two groups of cardiomyocyte subtypes and visualized by dittoDotPlot 44. The differentially expressed genes in all BZ vs Remote cardiomyocyte nuclei were then determined by DESeq analysis 45 and further analysed by enrichR 46 to identify affected biological pathways. The differentially expressed genes were visualized by an Enhanced Volcano plot 47.

To analyse cellular heterogeneity in each heart physiological region, two approaches were taken. First, to determine heterogeneity at a cellular level, mean of Euclidean distance of each cell relative to other cells in each physio_condition (per animal) was calculated based on the expression of variable genes in the top 13 significant principal components, which defined the cell clustering. The data were visualized using ggplot2/ tidyverse 48 and statistically compared using a hierarchical t-test.

To identify variation at the level of genes, the BASiCS 24,49,50 algorithm was used to determine the significantly (residual) over-dispersed genes after removing very lowly expressed genes (MinCellsWithExpression=2 and MinTotalCountsPerCell/Gene=2). The significant expressed/dispersed genes were identified with an expected false discovery rate (EFDR) < 0.10.

The Venn R package was used to illustrate the overlapped genes in each list of interest. For visualizing the distributed nuclei expressing the candidate genes, the FeaturePlot() function in Seurat package was used. Of note, each individual plot is scaled to the maximum expression value of the gene across the physiological conditions.

Analysis and statistics

Data acquisition was performed by multiple investigators and investigators were blinded when doing analysis off-line by coding or anonymizing data files.

All data are presented as means ± SD or median (IQR) and mostly presented by animal as indicted in the figure legends. Distribution of data was tested by Shapiro-Wilk to determine appropriate statistical tests.

Data were compared with unpaired t-test or a mixed-effects model 1-way or 2-way ANOVA with Bonferroni post-hoc testing as applicable, and using nested design when several measurements from the same animal. Associations were investigated by linear regression analysis. Data were considered significantly different when the p-value was < 0.05.

Supplemental Data

Supplemental table 1.

Cardiac magnetic resonance imaging metrices of structural and functional remodeling 1-month after MI

	MI (N_{pigs} = 13)	**Sham (N_{pigs} = 8)**	***P* value**
Infarct size (%)	18.5 ± 4.5	0 ± 0	<0.0001
Ejection fraction (%)	40.9 ± 8.1	64.5 ± 4.3	<0.0001
End-diastolic volume (mL)	174.9 ± 24.8	121.2 ± 13.3	0.0003
End-systolic volume (mL)	103.7 ± 23.4	49.8 ± 15.5	<0.0001
Left ventricular mass (g)	137.6 ± 16.3	128.4 ± 19.5	0.2992
Heart rate (beats per minute)	85.2 ± 9.0	97.6 ± 18.3	0.0657
Left ventricular peak systolic pressure (mmHg)	98.7 ± 9.9	103.8 ± 19.4	0.4974
Left ventricular mean diastolic pressure (mmHg)	5.0 ± 1.9	1.5 ± 1.6	0.0090

Supplemental table 2.

Differentially expressed genes in the BZ comparedto remote regions.

Gene	Base Mean	log2Fold Change	lfcSE	stat	pvalue	padj
QKI	22.75	0.2663	0.02132	12.49	8.376e-36	2.552e-34
TIAM2	2.198	0.3417	0.02463	13.87	9.369e-44	3.687e-42
PPP1R14C	3.794	0.2526	0.02253	11.21	3.66e-29	8.332e-28
PHACTR2	2.685	0.2766	0.02236	12.37	3.876e-35	1.146e-33
AIG1	3.154	0.3421	0.02521	13.57	6.014e-42	2.268e-40
ARFGEF3	3.067	0.4253	0.02329	18.26	1.783e-74	1.591e-72
MAP3K5	32.3	0.2661	0.02133	12.48	9.779e-36	2.971e-34
MAP7	2.337	0.2911	0.02669	10.91	1.031e-27	2.179e-26
PDE7B	3.617	1.045	0.03557	29.37	1.164e-189	6.845e-187
AHI1	3.549	0.3169	0.02412	13.14	1.959e-39	6.894e-38
CCN2	1.291	0.4884	0.02647	18.45	5.124e-76	4.787e-74
ARHGAP18	1.689	0.4545	0.02317	19.62	1.098e-85	1.322e-83
ENSSSCG00000036671	3.264	0.387	0.02144	18.05	8.21e-73	6.954e-71
BACH2	5.988	0.7401	0.02745	26.97	3.774e-160	1.64e-157
KLHL32	4.454	0.5115	0.02591	19.74	8.969e-87	1.149e-84
ASCC3	2.918	0.261	0.02204	11.84	2.395e-32	6.317e-31
FYN	3.354	0.4536	0.02516	18.03	1.123e-72	9.43e-71
LAMA4	8.968	0.266	0.02263	11.76	6.631e-32	1.691e-30
HS3ST5	4.241	0.3495	0.0285	12.26	1.419e-34	4.099e-33
TENT5A	1.699	0.2733	0.02317	11.8	4.037e-32	1.048e-30
TPM1	13.07	0.2772	0.0223	12.43	1.804e-35	5.398e-34
ENSSSCG00000004598	5.144	0.3097	0.02316	13.37	8.656e-41	3.181e-39
ZNF106	6.88	0.3232	0.02193	14.74	3.575e-49	1.67e-47
SPRED1	1.868	0.4563	0.02291	19.91	3.022e-88	4.028e-86
C15orf41	2.379	0.3519	0.02408	14.61	2.379e-48	1.071e-46
ACTC1	2.73	0.6445	0.02556	25.21	2.779e-140	8.68e-138

CHSY1	1.488	0.3246	0.02459	13.2	8.889e-40	3.151e-38
SERPINB2	1.417	0.428	0.02541	16.84	1.196e-63	7.815e-62
KDSR	2.886	0.2619	0.02622	9.991	1.669e-23	2.803e-22
CCBE1	5.464	0.3971	0.01922	20.66	7.368e-95	1.227e-92
ATP8B1	5.798	0.2842	0.02286	12.43	1.837e-35	5.479e-34
ENSSSCG00000033218	2.269	0.4642	0.02032	22.85	1.595e-115	3.321e-113
UACA	1.875	0.2798	0.02293	12.2	3.171e-34	9.056e-33
MYO9A	6.251	0.3188	0.02129	14.98	1.027e-50	4.959e-49
NID2	4.785	0.2976	0.02367	12.57	2.989e-36	9.193e-35
DAAM1	5.772	0.3224	0.02287	14.1	3.994e-45	1.636e-43
MLLT3	2.808	0.2646	0.02646	9.998	1.548e-23	2.609e-22
NFIB	10.27	0.3368	0.02254	14.94	1.711e-50	8.222e-49
SMARCA2	2.908	0.5338	0.02115	25.24	1.618e-140	5.39e-138
FAM189A2	5.378	0.5176	0.0226	22.91	4.141e-116	8.807e-114
MAMDC2	1.135	0.3578	0.02807	12.75	3.245e-37	1.033e-35
ENSSSCG00000005358	1.684	0.3225	0.0232	13.9	6.026e-44	2.381e-42
ZNF462	3.591	0.3743	0.02402	15.58	9.218e-55	4.875e-53
ENSSSCG00000005518	2.287	0.3784	0.02143	17.66	8.955e-70	7.048e-68
NEK6	1.157	0.2838	0.02797	10.15	3.461e-24	6.026e-23
ATP2C1	3.41	0.2939	0.02046	14.36	8.581e-47	3.665e-45
THRB	32.12	0.4268	0.02164	19.72	1.369e-86	1.732e-84
LRRFIP2	11.37	0.3127	0.02032	15.39	1.897e-53	9.877e-52
ITGA9	2.518	0.4017	0.02377	16.9	4.269e-64	2.845e-62
TOPAZ1	1.789	0.3404	0.02365	14.39	5.71e-47	2.481e-45
TNNC1	2.583	0.2725	0.02005	13.59	4.777e-42	1.809e-40
SLMAP	12.03	0.2819	0.02131	13.23	6.031e-40	2.153e-38
MAGI1	1.837	0.3045	0.02466	12.35	4.95e-35	1.438e-33
ENSSSCG00000036148	3.679	0.5052	0.02887	17.5	1.5e-68	1.127e-66
FRMD4B	17.72	0.4066	0.02288	17.77	1.27e-70	1.032e-68
MITF	15.22	0.3206	0.02211	14.5	1.246e-47	5.486e-46

RYBP	2.626	0.2676	0.0223	12	3.623e-33	9.868e-32
CNTN3	1.092	0.2534	0.02891	8.766	1.856e-18	2.342e-17
LMCD1	1.574	0.3271	0.02519	12.99	1.484e-38	4.928e-37
GRIP2	1.586	0.3472	0.02379	14.59	3.16e-48	1.404e-46
SLC6A6	1.785	1.167	0.02831	41.23	0	0
XPC	1.492	0.341	0.02448	13.93	4.206e-44	1.675e-42
SLC9A9	2.582	0.2567	0.02463	10.42	1.912e-25	3.558e-24
GYG1	2.197	0.2541	0.02358	10.78	4.456e-27	9.145e-26
TSC22D2	3.902	0.3247	0.0235	13.82	1.966e-43	7.677e-42
PHC3	3.421	0.2855	0.02087	13.68	1.342e-42	5.161e-41
TNIK	11.16	0.4849	0.02404	20.17	1.821e-90	2.494e-88
PLD1	9.655	0.3632	0.02397	15.15	7.714e-52	3.874e-50
FNDC3B	13.42	0.393	0.02162	18.17	8.614e-74	7.486e-72
NAALADL2	2.388	0.2681	0.02717	9.868	5.753e-23	9.35e-22
TBL1XR1	6.987	0.2662	0.02234	11.92	9.326e-33	2.499e-31
IGF2BP2	1.708	0.3448	0.02637	13.08	4.493e-39	1.559e-37
ENSSSCG00000040916	1.461	0.2781	0.02491	11.16	6.228e-29	1.396e-27
TP63	1.951	0.5141	0.02795	18.39	1.574e-75	1.417e-73
P3H2	1.123	0.2821	0.02844	9.917	3.519e-23	5.813e-22
ATP13A3	3.412	0.8682	0.02359	36.8	2.049e-296	2.048e-293
ACAP2	2.572	0.2517	0.02135	11.79	4.594e-32	1.187e-30
ENSSSCG00000011851	3.185	0.2905	0.02332	12.46	1.278e-35	3.837e-34
ENSSSCG00000011850	1.502	0.3342	0.02441	13.69	1.195e-42	4.631e-41
STXBP5L	1.938	0.295	0.02636	11.19	4.488e-29	1.013e-27
ARHGAP31	1.879	0.304	0.02347	12.95	2.328e-38	7.704e-37
ZBTB20	12.37	0.2612	0.02249	11.61	3.543e-31	8.808e-30
NECTIN3	1.525	0.2735	0.02466	11.09	1.44e-28	3.171e-27
DZIP3	4.299	0.4749	0.02559	18.56	7.373e-77	7.019e-75
CD47	2.368	0.3201	0.02192	14.6	2.798e-48	1.254e-46
CBLB	7.66	0.4426	0.02229	19.85	1.054e-87	1.369e-85
ALCAM	7.314	0.2667	0.02818	9.466	2.896e-21	4.339e-20

ST3GAL6	2.462	0.2772	0.02224	12.46	1.165e-35	3.508e-34
PROS1	4.905	0.2524	0.02036	12.4	2.573e-35	7.655e-34
ROBO1	2.214	1.374	0.03057	44.93	0	0
ROBO2	1.215	0.2542	0.02747	9.253	2.182e-20	3.076e-19
USP25	5.78	0.3093	0.02162	14.3	2.069e-46	8.689e-45
ENSSSCG00000034679	2.104	0.4055	0.02362	17.17	4.438e-66	3.124e-64
CYYR1	1.997	0.3455	0.0241	14.33	1.335e-46	5.63e-45
RCAN1	3.578	0.3587	0.02502	14.34	1.251e-46	5.299e-45
TTC3	2.564	0.253	0.02152	11.76	6.249e-32	1.601e-30
IL34	4.946	0.3628	0.0241	15.05	3.21e-51	1.58e-49
NDRG4	5.459	0.3775	0.02279	16.57	1.167e-61	7.069e-60
CDH8	3.231	0.3654	0.0287	12.73	3.876e-37	1.23e-35
TERB1	1.486	0.2633	0.02477	10.63	2.199e-26	4.361e-25
TNNT1	1.963	0.4136	0.02485	16.65	3.191e-62	1.957e-60
NPPB	1.614	0.9291	0.02767	33.58	3.759e-247	2.89e-244
SRSF10	3.253	0.4414	0.02009	21.97	5.426e-107	1.043e-104
STX12	1.93	0.3346	0.02228	15.02	5.475e-51	2.669e-49
EPB41L3	36.43	0.364	0.02297	15.84	1.532e-56	8.462e-55
GATA6	7.788	0.2843	0.02204	12.9	4.585e-38	1.493e-36
DSC3	3.297	0.2659	0.02032	13.08	4.091e-39	1.425e-37
MAPRE2	4.467	0.2613	0.02462	10.61	2.571e-26	5.038e-25
ENSSSCG00000039133	1.428	0.3067	0.02511	12.21	2.599e-34	7.464e-33
ENSSSCG00000031521	1.296	0.2921	0.02641	11.06	1.949e-28	4.272e-27
PRKACB	5.447	0.2899	0.02305	12.58	2.78e-36	8.575e-35
GIPC2	7.577	0.3701	0.02531	14.62	1.974e-48	9.007e-47
DNAJB4	8.101	0.3014	0.02162	13.94	3.412e-44	1.364e-42
ENSSSCG00000003771	3.608	0.2525	0.02015	12.53	5.13e-36	1.573e-34
SLC44A5	4.352	0.5378	0.02561	21	6.19e-98	1.085e-95
PTGER3	33.25	0.3471	0.02494	13.92	4.89e-44	1.94e-42
TCTEX1D1	1.902	0.2823	0.02329	12.12	8.305e-34	2.332e-32

PDE4B	5.808	0.4157	0.02372	17.52	9.527e-69	7.269e-67
ROR1	6.485	0.466	0.02792	16.69	1.57e-62	9.807e-61
FAM151A	1.6	0.2549	0.02389	10.67	1.405e-26	2.803e-25
ENSSSCG00000038101	1.549	0.3734	0.02818	13.25	4.291e-40	1.537e-38
PIK3R3	1.449	0.4329	0.02496	17.35	2.032e-67	1.494e-65
ENSSSCG00000014540	1.406	0.2517	0.02549	9.877	5.259e-23	8.574e-22
CTNND1	3.773	0.3886	0.0206	18.87	2.182e-79	2.225e-77
CD44	2.323	0.3073	0.02301	13.35	1.141e-40	4.176e-39
ENSSSCG00000035881	4.668	0.4747	0.02741	17.32	3.368e-67	2.457e-65
FSHB	1.442	0.4532	0.02458	18.44	6.32e-76	5.849e-74
CSRP3	6.189	0.3414	0.02495	13.68	1.288e-42	4.971e-41
ENSSSCG00000033786	2.517	0.3576	0.02489	14.37	8.218e-47	3.525e-45
MICAL2	7.435	0.3962	0.02191	18.08	4.318e-73	3.688e-71
DKK3	1.383	0.5764	0.02498	23.07	9.226e-118	2.005e-115
ENSSSCG00000013880	1.137	0.4185	0.02779	15.06	2.993e-51	1.481e-49
LHFPL2	3.871	0.3114	0.02337	13.33	1.628e-40	5.916e-39
SSBP2	7.079	0.3383	0.02673	12.65	1.077e-36	3.364e-35
MEF2C	8.254	0.4586	0.02216	20.69	4.06e-95	6.879e-93
ENSSSCG00000035571	2.529	0.3003	0.02555	11.75	6.737e-32	1.713e-30
ENSSSCG00000014161	2.116	0.2516	0.02462	10.22	1.655e-24	2.926e-23
SLCO6A1	1.546	0.3271	0.03147	10.39	2.639e-25	4.894e-24
PAM	10.64	0.4828	0.02372	20.36	4.043e-92	5.856e-90
EFNA5	19.05	0.3397	0.0252	13.48	2.019e-41	7.559e-40
MCC	6.776	0.2576	0.02526	10.2	2.016e-24	3.541e-23
PRR16	10.14	0.4652	0.02466	18.86	2.272e-79	2.294e-77
ZNF608	3.027	0.2693	0.02339	11.51	1.152e-30	2.814e-29
FBN2	3.587	1.259	0.03105	40.54	0	0
ADAMTS19	1.118	0.3136	0.02894	10.84	2.248e-27	4.662e-26
KLHL3	2.526	0.4318	0.02191	19.71	1.91e-86	2.328e-84
MYOT	5.842	0.2763	0.02486	11.12	1.044e-28	2.308e-27
DPYSL3	4.259	0.2545	0.02407	10.58	3.816e-26	7.392e-25

PPP3CC	10.65	0.3403	0.02034	16.73	7.938e-63	5.053e-61
ADRA1A	4.496	0.3502	0.02716	12.89	4.809e-38	1.551e-36
PTK2B	1.536	0.4002	0.02406	16.63	3.979e-62	2.425e-60
ADGRD1	1.741	0.2778	0.02423	11.47	1.939e-30	4.692e-29
CLIP1	7.872	0.2962	0.02258	13.11	2.719e-39	9.504e-38
MYL2	10.92	0.3617	0.02063	17.53	8.541e-69	6.567e-67
MTMR3	5.998	0.4767	0.0212	22.49	5.498e-112	1.121e-109
ACTN2	29.87	0.2851	0.02211	12.9	4.642e-38	1.507e-36
SIPA1L2	4.684	0.2673	0.02399	11.14	7.807e-29	1.742e-27
ACTA1	4.287	0.3658	0.02316	15.79	3.451e-56	1.895e-54
FAM13C	1.766	0.3253	0.02383	13.65	1.954e-42	7.454e-41
RHOBTB1	2.893	0.5421	0.02458	22.06	8.533e-108	1.706e-105
ARID5B	2.488	0.433	0.02322	18.65	1.321e-77	1.294e-75
LRRTM3	6.539	0.8243	0.02294	35.94	6.644e-283	6.037e-280
HERC4	6.578	0.4126	0.02167	19.04	7.746e-81	8.237e-79
STOX1	2.744	0.4393	0.02308	19.03	9.559e-81	1.006e-78
MICU1	4.206	0.2585	0.02186	11.83	2.828e-32	7.418e-31
MCU	3.235	0.4208	0.02681	15.7	1.618e-55	8.697e-54
VCL	6.989	0.3967	0.02236	17.74	1.926e-70	1.552e-68
RASSF4	1.522	0.252	0.02449	10.29	7.805e-25	1.408e-23
SGMS1	5.53	0.3763	0.02228	16.89	5.727e-64	3.791e-62
ENSSSCG00000010440	2.78	0.2833	0.02197	12.89	4.883e-38	1.569e-36
ANKRD1	27.79	0.2604	0.02673	9.741	2.019e-22	3.203e-21
SH3PXD2A	2.359	0.3493	0.02184	15.99	1.489e-57	8.503e-56
NRAP	12.39	0.3002	0.02578	11.64	2.522e-31	6.286e-30
INPP5F	1.965	0.4073	0.0236	17.26	9.658e-67	6.846e-65
PLEKHA1	2.277	0.2519	0.02103	11.98	4.567e-33	1.24e-31
MGMT	3.546	0.3123	0.03037	10.29	8.186e-25	1.474e-23
ENSSSCG00000031528	1.824	0.6843	0.02369	28.88	1.884e-183	1.046e-180

ENSSSCG00000023746	2.159	0.3023	0.02694	11.22	3.125e-29	7.148e-28
R3HDM1	8.842	0.331	0.02231	14.83	8.811e-50	4.194e-48
RAB3GAP1	2.736	0.2598	0.02175	11.95	6.785e-33	1.828e-31
ENSSSCG00000023479	9.391	0.406	0.01988	20.42	1.048e-92	1.611e-90
SLC35F5	2.58	0.3256	0.02088	15.6	7.773e-55	4.132e-53
EPB41L5	4.546	0.2656	0.02098	12.66	1.038e-36	3.252e-35
ENSSSCG00000034187	1.698	0.4276	0.02272	18.82	5.213e-79	5.159e-77
PDLIM3	1.592	0.3827	0.02656	14.41	4.648e-47	2.029e-45
SORBS2	106.5	0.292	0.02299	12.7	5.869e-37	1.845e-35
GALNT13	1.242	0.5716	0.02778	20.57	4.688e-94	7.437e-92
ACVR1	4.28	0.2766	0.02138	12.94	2.804e-38	9.189e-37
RBMS1	6.63	0.3777	0.02256	16.74	7.009e-63	4.491e-61
FIGN	3.298	0.2757	0.02477	11.13	9.031e-29	2.01e-27
XIRP2	2.571	0.4823	0.02809	17.17	4.614e-66	3.225e-64
CERS6	1.224	0.4692	0.02738	17.14	7.985e-66	5.542e-64
MAP3K20	6.151	0.3707	0.02326	15.94	3.589e-57	2.015e-55
ITPRID2	1.564	0.3406	0.02402	14.18	1.232e-45	5.066e-44
FRZB	1.847	0.9701	0.0273	35.54	1.212e-276	1.01e-273
NCKAP1	3.056	0.282	0.02125	13.28	3.232e-40	1.162e-38
ITGAV	3.47	0.6691	0.02361	28.35	9.416e-177	4.482e-174
GULP1	12.22	0.2736	0.02245	12.19	3.602e-34	1.026e-32
MYO1B	1.161	0.4536	0.02765	16.41	1.757e-60	1.027e-58
CAVIN2	2.038	0.3704	0.02247	16.48	4.886e-61	2.907e-59
SLC39A10	2.267	0.375	0.02244	16.71	1.137e-62	7.147e-61
HECW2	3.04	0.652	0.02695	24.19	2.712e-129	6.611e-127
PLCL1	1.78	0.2829	0.02399	11.79	4.261e-32	1.103e-30
CLK1	2.771	0.3081	0.01899	16.23	3.342e-59	1.931e-57
STRADB	9.089	0.2844	0.02212	12.86	7.933e-38	2.533e-36
ENSSSCG00000036410	2.179	0.5744	0.02021	28.43	9.441e-178	4.718e-175

CYP20A1	3.665	0.3681	0.02163	17.02	6.211e-65	4.252e-63
ENSSSCG00000016119	1.994	0.4233	0.02279	18.57	5.181e-77	5.027e-75
DES	3.976	0.3197	0.02315	13.81	2.177e-43	8.465e-42
EPHA4	1.251	0.4373	0.02646	16.53	2.304e-61	1.387e-59
KCNJ13	1.514	0.3141	0.02437	12.89	5.017e-38	1.607e-36
ENSSSCG00000014850	1.978	0.5208	0.02565	20.31	1.147e-91	1.614e-89
CTSC	9.082	0.4092	0.02487	16.45	8.495e-61	5.024e-59
ENSSSCG00000038831	5.182	0.2595	0.02207	11.76	6.43e-32	1.644e-30
NAALAD2	2.338	0.4393	0.02255	19.48	1.634e-84	1.921e-82
MAML2	3.16	0.6303	0.02895	21.77	4.694e-105	8.53e-103
CEP126	4.482	0.6016	0.023	26.16	8.047e-151	3.217e-148
PDGFD	3.433	1.275	0.02907	43.87	0	0
GRIA4	1.095	0.2594	0.02904	8.934	4.116e-19	5.363e-18
SIK2	1.09	0.2778	0.02884	9.631	5.892e-22	9.145e-21
ENSSSCG00000015027	1.345	0.2547	0.02604	9.782	1.35e-22	2.156e-21
NCAM1	7.255	0.4702	0.02444	19.24	1.698e-82	1.886e-80
CADM1	2.553	0.3593	0.03022	11.89	1.373e-32	3.671e-31
SIK3	5.66	0.2953	0.02262	13.05	6.151e-39	2.113e-37
ARHGEF12	5.076	0.3037	0.02112	14.38	7.199e-47	3.102e-45
GRAMD1B	5.505	0.5453	0.02477	22.01	2.158e-107	4.23e-105
SCN3B	1.862	1.022	0.02779	36.8	1.992e-296	2.048e-293
ATP2B4	6.004	0.2596	0.02411	10.77	5.01e-27	1.022e-25
ENSSSCG00000028035	3.414	0.2653	0.01977	13.42	4.599e-41	1.702e-39
AKAP9	6.053	0.2661	0.01951	13.64	2.401e-42	9.124e-41
PPP1R9A	7.537	0.2546	0.02294	11.1	1.315e-28	2.902e-27
THSD7A	7.282	0.3166	0.02619	12.09	1.219e-33	3.405e-32
ETV1	1.288	0.6378	0.02558	24.93	3.418e-137	1.005e-134
BZW2	3.426	0.3995	0.02158	18.51	1.581e-76	1.491e-74

HDAC9	15.3	0.4268	0.02254	18.93	6.027e-80	6.211e-78
ITGB8	2.328	0.3669	0.02487	14.75	2.895e-49	1.359e-47
FAM126A	4.837	0.5286	0.02595	20.37	3.003e-92	4.414e-90
CACNA2D1	11.88	0.3324	0.02182	15.24	2.043e-52	1.047e-50
PTPN12	2.549	0.2626	0.02106	12.47	1.095e-35	3.315e-34
TPK1	8.508	0.2663	0.02387	11.16	6.735e-29	1.506e-27
XPR1	4.033	0.6835	0.0278	24.59	1.79e-133	4.588e-131
STX6	2.964	0.41	0.02333	17.57	3.833e-69	2.97e-67
LAMC1	7.681	0.3359	0.0239	14.05	7.501e-45	3.035e-43
NMNAT2	2.457	0.3323	0.02521	13.18	1.129e-39	3.986e-38
LCORL	4.372	0.2685	0.02293	11.71	1.156e-31	2.896e-30
APBB2	3.176	0.257	0.02335	11.01	3.502e-28	7.609e-27
LIMCH1	5.403	0.467	0.02415	19.34	2.69e-83	3.055e-81
GABRA4	3.877	0.5756	0.02626	21.92	1.725e-106	3.252e-104
GABRB1	9.078	0.3815	0.02598	14.68	8.217e-49	3.82e-47
GASK1B	2.672	0.4175	0.02249	18.56	6.445e-77	6.194e-75
TMEM144	3.486	0.3099	0.02267	13.67	1.503e-42	5.756e-41
TECRL	27.24	0.3863	0.02557	15.11	1.404e-51	7.017e-50
ADAMTS3	2.571	0.4835	0.02711	17.84	3.591e-71	2.942e-69
SEPT11	1.709	0.2664	0.0232	11.48	1.576e-30	3.832e-29
FRAS1	1.741	0.3024	0.02633	11.48	1.605e-30	3.893e-29
TRIM2	5.533	0.2618	0.02323	11.27	1.865e-29	4.325e-28
INPP4B	16.05	0.4481	0.02202	20.36	4.124e-92	5.889e-90
RNF150	14.51	0.2873	0.02539	11.32	1.06e-29	2.498e-28
MAML3	2.849	0.5672	0.02877	19.71	1.627e-86	2.007e-84
FAT4	1.325	0.2841	0.02645	10.74	6.415e-27	1.303e-25
MYOZ2	25.21	0.474	0.02163	21.92	1.828e-106	3.383e-104
SYNPO2	11.83	0.4215	0.0252	16.72	8.92e-63	5.643e-61
SEC24D	1.973	0.2958	0.02264	13.06	5.284e-39	1.821e-37
NDST3	1.542	0.2717	0.02475	10.98	4.827e-28	1.042e-26

NPNT	1.386	0.3799	0.02588	14.68	9.224e-49	4.248e-47
ARHGAP24	7.703	0.4103	0.0244	16.81	2.035e-63	1.312e-61
GPAT3	3.936	0.3075	0.02557	12.03	2.595e-33	7.126e-32
ANTXR2	3.169	0.2714	0.02402	11.3	1.34e-29	3.143e-28
HSPB1	1.438	0.2814	0.02511	11.21	3.812e-29	8.658e-28
HIP1	2.054	0.2752	0.02116	13.01	1.144e-38	3.836e-37
RABGEF1	1.726	0.3094	0.02296	13.47	2.259e-41	8.424e-40
ENSSSCG00000035273	1.358	0.5149	0.02695	19.1	2.426e-81	2.607e-79
TACR1	1.653	0.2681	0.02655	10.09	5.823e-24	9.932e-23
SPRED2	1.436	0.5072	0.02463	20.59	3.323e-94	5.356e-92
CCDC85A	7.756	0.31	0.02854	10.86	1.717e-27	3.582e-26
RTN4	2.793	0.2984	0.02511	11.88	1.435e-32	3.825e-31
ENSSSCG00000035426	2.97	0.5392	0.02296	23.49	5.716e-122	1.298e-119
PREPL	2.224	0.3954	0.02249	17.58	3.523e-69	2.751e-67
ENSSSCG00000008451	2.477	0.2658	0.02132	12.47	1.13e-35	3.413e-34
EML4	2.009	0.2624	0.02222	11.81	3.645e-32	9.487e-31
ENSSSCG00000008496	1.623	0.25	0.02385	10.48	1.02e-25	1.931e-24
LTBP1	1.967	1.353	0.02787	48.54	0	0
TRIM54	3.55	0.2575	0.02226	11.57	6.036e-31	1.497e-29
EFR3B	1.639	0.2905	0.02352	12.35	4.732e-35	1.383e-33
ROCK2	4.864	0.3617	0.02265	15.97	2.216e-57	1.258e-55
MBOAT2	2.55	0.3039	0.02258	13.46	2.784e-41	1.034e-39
MTSS1	3.75	0.2653	0.02194	12.09	1.197e-33	3.352e-32
ENSSSCG00000034048	2.287	0.6462	0.02055	31.45	4.521e-217	3.227e-214
TMEM65	9.547	0.448	0.02253	19.89	5.238e-88	6.889e-86
EXT1	12.95	0.4704	0.02327	20.21	7.379e-91	1.024e-88
ENSSSCG00000006008	1.311	0.3186	0.02616	12.18	4.196e-34	1.191e-32
ANGPT1	1.168	0.4948	0.02724	18.16	9.962e-74	8.584e-72
YWHAZ	4.103	0.4431	0.02312	19.17	7.246e-82	7.959e-80
PTDSS1	7.451	0.3315	0.02318	14.3	2.112e-46	8.831e-45

RUNX1T1	7.468	0.3433	0.02342	14.66	1.159e-48	5.313e-47
CPNE3	11.61	0.2761	0.02064	13.38	8.169e-41	3.013e-39
PAG1	4.47	0.3689	0.02495	14.79	1.763e-49	8.312e-48
ZC2HC1A	2.424	0.2803	0.02108	13.3	2.385e-40	8.636e-39
CSPP1	2.08	0.2783	0.02228	12.49	8.235e-36	2.517e-34
PDE7A	8.027	0.2738	0.02214	12.37	3.895e-35	1.148e-33
KIFAP3	2.011	0.3092	0.02164	14.29	2.471e-46	1.029e-44
ATP1B1	5.35	0.3874	0.02106	18.39	1.479e-75	1.344e-73
DPT	1.458	0.2641	0.02499	10.57	4.149e-26	8.021e-25
NES	1.163	0.2681	0.02796	9.59	8.767e-22	1.346e-20
ARHGEF2	2.746	0.2776	0.02145	12.94	2.676e-38	8.798e-37
RNF115	3.053	0.3473	0.02233	15.56	1.406e-54	7.357e-53
MAGI3	2.213	0.2505	0.02512	9.974	1.973e-23	3.292e-22
CDC14A	2.099	0.7965	0.02553	31.2	1.21e-213	8.066e-211
PALMD	7.166	0.4971	0.02434	20.42	1.075e-92	1.628e-90
MID1	1.22	0.2858	0.02726	10.49	9.834e-26	1.865e-24
CNKSR2	3.357	0.4767	0.0249	19.14	1.102e-81	1.197e-79
PHEX	2.955	0.3681	0.02276	16.17	7.644e-59	4.391e-57
NONO	2.66	0.2673	0.02053	13.02	9.038e-39	3.073e-37
ENSSSCG00000012403	3.378	0.3964	0.01932	20.52	1.548e-93	2.418e-91
ATRX	5.214	0.2583	0.02091	12.35	4.832e-35	1.408e-33
ENSSSCG00000035722	1.746	0.3907	0.02261	17.28	6.954e-67	5.037e-65
COL4A5	2.974	0.4389	0.02317	18.94	5.228e-80	5.443e-78
AMMECR1	1.948	0.337	0.02164	15.57	1.084e-54	5.701e-53
PLS3	1.865	0.344	0.02377	14.47	1.792e-47	7.854e-46
ENSSSCG00000025028	3.128	0.3314	0.02195	15.1	1.613e-51	8.021e-50
ENSSSCG00000012700	3.064	0.26	0.02292	11.34	8.102e-30	1.928e-28
ATP11C	3.004	0.4346	0.02433	17.87	2.157e-71	1.781e-69
PHACTR1	7.254	0.3808	0.02723	13.99	1.913e-44	7.681e-43
KIF13A	7.194	0.3029	0.02073	14.61	2.319e-48	1.049e-46
RNF144B	3.164	0.7196	0.02846	25.29	4.509e-141	1.554e-138

ENSSSCG00000037166	1.526	0.2589	0.02661	9.728	2.301e-22	3.638e-21
MBOAT1	2.058	0.3622	0.02378	15.23	2.218e-52	1.131e-50
ENSSSCG00000001097	2.88	0.2625	0.0227	11.57	6.197e-31	1.533e-29
ENSSSCG00000030197	1.833	0.5682	0.02357	24.11	2.129e-128	5.067e-126
HDGFL3	2.37	0.2716	0.02196	12.37	3.909e-35	1.149e-33
BTBD1	4.036	0.314	0.02182	14.39	6.131e-47	2.653e-45
PEAK1	4.857	0.6256	0.02466	25.37	5.594e-142	2.071e-139
PTPN9	2.444	0.2628	0.02203	11.93	8.497e-33	2.283e-31
STXBP6	8.894	0.4358	0.02546	17.12	1.031e-65	7.105e-64
ENSSSCG00000031822	2.021	0.51	0.02068	24.66	2.658e-134	6.991e-132
SLCO3A1	13.95	0.3682	0.02618	14.07	6.188e-45	2.514e-43
ENSSSCG00000002259	6.069	0.3044	0.02335	13.04	7.462e-39	2.545e-37
SIPA1L1	2.172	0.2811	0.02269	12.39	2.978e-35	8.831e-34
RGS6	2.641	1.863	0.02941	63.32	0	0
NRXN3	1.205	0.501	0.03008	16.65	2.785e-62	1.719e-60
ENSSSCG00000021315	1.457	0.7373	0.03033	24.31	1.585e-130	3.96e-128
FLRT2	1.079	0.2709	0.02904	9.328	1.074e-20	1.545e-19
C12orf75	1.317	0.2726	0.02628	10.37	3.292e-25	6.049e-24
TEX49	2.918	0.4996	0.01981	25.22	2.156e-140	6.95e-138
RASSF3	4.177	0.4382	0.02576	17.01	7.162e-65	4.87e-63
ENSSSCG00000034610	1.206	0.4432	0.02699	16.42	1.298e-60	7.631e-59
FAR2	4.083	0.2686	0.02607	10.3	6.81e-25	1.238e-23
PPFIBP1	8.347	0.515	0.02211	23.29	5.13e-120	1.139e-117
STK38L	6.934	0.2764	0.02244	12.32	7.131e-35	2.066e-33
RASSF8	4.046	0.312	0.02466	12.65	1.116e-36	3.476e-35
LMNTD1	7.724	0.2659	0.03015	8.819	1.157e-18	1.473e-17
LDHB	4.521	0.3579	0.02048	17.48	2.197e-68	1.639e-66
ENSSSCG00000036623	1.996	0.4078	0.02113	19.3	5.386e-83	6.049e-81

MGST1	1.744	0.3615	0.02267	15.95	2.857e-57	1.613e-55
RERG	1.115	0.3626	0.02851	12.72	4.525e-37	1.427e-35
OLR1	1.629	0.3313	0.02368	13.99	1.766e-44	7.118e-43
CCND2	1.816	0.2543	0.02268	11.21	3.528e-29	8.051e-28
DCP1B	2.035	0.3819	0.02099	18.2	5.512e-74	4.833e-72
SLC38A1	2.313	0.3046	0.02341	13.01	1.069e-38	3.599e-37
SLC38A2	2.026	0.2824	0.0215	13.13	2.16e-39	7.575e-38
FGD6	2.225	0.5636	0.02363	23.86	8.653e-126	2.011e-123
TMTC2	3.268	0.3229	0.02391	13.51	1.457e-41	5.474e-40
CDH18	1.462	0.5436	0.02555	21.28	1.878e-100	3.352e-98
CDH9	1.639	0.4537	0.02569	17.66	8.666e-70	6.874e-68
PLPP1	6.426	0.345	0.0242	14.26	4.127e-46	1.712e-44
IL6ST	3.701	0.2669	0.0211	12.65	1.165e-36	3.617e-35
RNF180	6.207	0.2844	0.0264	10.77	4.6e-27	9.422e-26
RGS7BP	2.913	0.2539	0.02487	10.21	1.779e-24	3.136e-23
ADAMTS6	6.343	0.4845	0.02492	19.44	3.48e-84	4.045e-82
ERBIN	4.384	0.3137	0.02138	14.68	9.141e-49	4.23e-47
MAST4	7.032	0.5888	0.02364	24.91	5.787e-137	1.653e-134
MAP1B	2.47	0.3017	0.02576	11.71	1.113e-31	2.795e-30
TNPO1	3.276	0.2554	0.02007	12.72	4.405e-37	1.393e-35
SH3PXD2B	2.366	0.3409	0.02182	15.62	5.165e-55	2.761e-53
STK10	1.355	0.3736	0.02559	14.6	2.883e-48	1.287e-46
WWC1	1.225	0.4506	0.02673	16.86	9.266e-64	6.093e-62
CYFIP2	3.557	0.7805	0.02533	30.81	2.064e-208	1.289e-205
GRIA1	12.24	0.7124	0.02827	25.2	4.167e-140	1.262e-137
ENSSSCG00000009341	5.248	0.3056	0.02149	14.22	6.625e-46	2.736e-44
PDS5B	3.167	0.2595	0.02186	11.87	1.6e-32	4.241e-31
ENSSSCG00000038414	2.379	0.2757	0.02343	11.77	5.777e-32	1.484e-30

LHFPL6	2.901	0.463	0.03022	15.32	5.489e-53	2.828e-51
TPT1	1.524	0.2693	0.02444	11.02	3.086e-28	6.72e-27
TSC22D1	2.262	0.3166	0.02125	14.9	3.135e-50	1.499e-48
LMO7	13.64	0.2565	0.01989	12.9	4.727e-38	1.529e-36
TGFB2	1.835	0.2609	0.02455	10.63	2.226e-26	4.397e-25
ENSSSCG00000038646	2.108	0.4174	0.0246	16.96	1.527e-64	1.025e-62
CDC42BPA	4.967	0.304	0.02096	14.5	1.186e-47	5.246e-46
ENSSSCG00000027557	4.465	0.3977	0.02302	17.28	7.092e-67	5.099e-65
FANCC	1.517	0.2604	0.02452	10.62	2.392e-26	4.707e-25
AOPEP	20.65	0.2525	0.02102	12.01	3.023e-33	8.256e-32
FRMD4A	1.717	0.908	0.02385	38.06	0	0
ARHGAP21	3.767	0.3337	0.02195	15.2	3.427e-52	1.739e-50
NEBL	129.8	0.3701	0.02012	18.39	1.448e-75	1.327e-73
ITGB1	3.749	0.2755	0.02112	13.04	7.008e-39	2.399e-37
DLC1	64.24	0.342	0.02178	15.71	1.359e-55	7.344e-54
TUSC3	2.995	0.3604	0.02285	15.77	4.976e-56	2.718e-54
VDAC3	2.25	0.2634	0.02023	13.02	9.115e-39	3.088e-37
DSTN	1.88	0.286	0.02421	11.81	3.311e-32	8.664e-31
C20orf194	2.573	0.2781	0.02306	12.06	1.732e-33	4.795e-32
DLGAP4	1.961	0.6435	0.02436	26.41	9.416e-154	3.922e-151
TGM2	2.284	0.4692	0.02578	18.2	4.893e-74	4.328e-72
NCOA3	2.942	0.2514	0.02181	11.52	9.897e-31	2.424e-29
SULF2	1.393	0.399	0.02517	15.85	1.429e-56	7.937e-55
TANC2	2.69	0.4583	0.02352	19.49	1.432e-84	1.704e-82
ATP6V0A1	2.234	0.3136	0.02145	14.62	2.153e-48	9.779e-47
NF1	5.325	0.2838	0.0215	13.2	8.796e-40	3.129e-38
NLK	5.104	0.3055	0.02346	13.02	9.565e-39	3.23e-37
NXN	1.565	0.3165	0.02588	12.23	2.167e-34	6.243e-33
ENSSSCG00000038144	1.631	0.3136	0.02424	12.94	2.849e-38	9.307e-37
CREB3L2	2.074	0.2799	0.02337	11.98	4.598e-33	1.246e-31

CHRM2	16.07	0.6364	0.02572	24.74	3.965e-135	1.101e-132
CALD1	7.577	0.4119	0.0247	16.68	1.943e-62	1.206e-60
ENSSSCG00000035751	3.004	0.5116	0.02009	25.47	4.257e-143	1.637e-140
MKLN1	5.123	0.39	0.022	17.73	2.453e-70	1.961e-68
UBE2H	9.333	0.3412	0.0222	15.37	2.77e-53	1.434e-51
STRIP2	3.011	0.3305	0.022	15.02	5.067e-51	2.482e-49
CAV1	2.061	0.4638	0.02319	20	5.146e-89	6.951e-87
MDFIC	1.259	0.2932	0.02679	10.94	7.094e-28	1.518e-26
DOCK4	4.256	0.6481	0.02562	25.29	3.783e-141	1.35e-138
SEPT7	2.167	0.2618	0.0208	12.59	2.49e-36	7.706e-35
DPY19L1	1.923	0.2583	0.02246	11.5	1.327e-30	3.235e-29
NPSR1	3.679	0.2735	0.03436	7.96	1.72e-15	1.782e-14
CREB5	6.812	0.5862	0.02824	20.76	1.027e-95	1.77e-93
KCNT2	1.615	1.08	0.02515	42.94	0	0
UST	3.386	-0.2759	0.02627	-10.5	8.366e-26	1.596e-24
NHSL1	3.45	-0.2835	0.024	-11.81	3.447e-32	8.997e-31
EYA4	2.582	-0.4928	0.02854	-17.27	8.431e-67	6.019e-65
PTPRK	12.94	-0.4939	0.02505	-19.72	1.539e-86	1.923e-84
HEY2	1.97	-0.2696	0.0238	-11.33	9.711e-30	2.305e-28
DAPK2	1.768	-0.4134	0.02538	-16.29	1.166e-59	6.773e-58
ADAMTSL1	9.748	-0.2901	0.0264	-10.99	4.331e-28	9.37e-27
TPM2	14.47	-0.3544	0.02104	-16.84	1.278e-63	8.294e-62
TSEN2	1.825	-0.2825	0.02732	-10.34	4.534e-25	8.284e-24
GREB1L	1.705	-0.2556	0.02527	-10.11	4.783e-24	8.2e-23
OSBPL5	2.286	-0.4138	0.02369	-17.47	2.647e-68	1.96e-66
MACROD1	3.228	-0.3977	0.02341	-16.99	9.5e-65	6.416e-63
ENSSSCG00000036669	4.441	-0.3848	0.02683	-14.34	1.165e-46	4.955e-45
MYBPC3	14.79	-0.2621	0.02018	-12.99	1.441e-38	4.8e-37
LDLRAD3	2.702	-0.2558	0.02582	-9.906	3.913e-23	6.443e-22
LGR4	2.459	-0.2933	0.02539	-11.55	7.512e-31	1.849e-29

NREP	3.121	-0.2677	0.0268	-9.989	1.703e-23	2.856e-22
FGF1	5.449	-0.26	0.0254	-10.23	1.394e-24	2.484e-23
ARHGAP26	7.178	-0.3715	0.02357	-15.77	5.398e-56	2.932e-54
PPARGC1B	3.681	-0.2939	0.02204	-13.34	1.425e-40	5.199e-39
CAMK2A	6.192	-0.5457	0.02206	-24.74	4.433e-135	1.197e-132
LPL	7.154	-0.2529	0.02363	-10.7	9.702e-27	1.951e-25
LZTS1	1.883	-0.3013	0.025	-12.05	1.924e-33	5.298e-32
RYR2	154.3	-0.3818	0.02182	-17.5	1.413e-68	1.07e-66
NID1	5.006	-0.2967	0.02469	-12.02	2.812e-33	7.7e-32
PRKG1	5.726	-0.3463	0.03363	-10.3	7.23e-25	1.311e-23
ZBTB16	10.95	-0.284	0.02537	-11.19	4.379e-29	9.901e-28
KCNJ5	1.292	-0.283	0.02885	-9.807	1.05e-22	1.685e-21
SLC41A1	4.738	-0.35	0.02308	-15.16	6.21e-52	3.135e-50
CDK6	6.754	-0.3046	0.02548	-11.95	6.224e-33	1.681e-31
SYT14	1.74	-0.2782	0.02912	-9.555	1.235e-21	1.882e-20
KIAA1211	1.876	-0.3295	0.02699	-12.21	2.708e-34	7.755e-33
ENSSSCG00000036217	1.386	-0.4068	0.02892	-14.07	5.914e-45	2.413e-43
SRL	8.898	-0.3255	0.01971	-16.52	2.802e-61	1.677e-59
MAP4K3	2.45	-0.5329	0.02585	-20.61	2.099e-94	3.44e-92
PTP4A3	2.44	-0.2562	0.02106	-12.17	4.508e-34	1.276e-32
COL14A1	2.382	-0.3369	0.02431	-13.86	1.147e-43	4.494e-42
TRPS1	1.56	-0.4244	0.02864	-14.82	1.101e-49	5.216e-48
FKBP5	3.247	-0.318	0.02958	-10.75	5.972e-27	1.216e-25
VEGFA	4.773	-0.3888	0.02158	-18.02	1.36e-72	1.133e-70
PLA2G7	4.876	-0.2794	0.02487	-11.24	2.686e-29	6.187e-28
ACO2	7.758	-0.2855	0.02197	-13	1.296e-38	4.332e-37
SUN2	2.714	-0.2546	0.02588	-9.837	7.794e-23	1.257e-21
ITGA5	2.311	-0.2613	0.02225	-11.74	7.779e-32	1.968e-30
ADAMTS20	2.2	-0.9973	0.03502	-28.48	2.339e-178	1.23e-175
STC2	1.82	-0.2993	0.0248	-12.07	1.518e-33	4.225e-32

TENM2	2.159	-0.5734	0.02951	-19.43	4.314e-84	4.956e-82
ENSSSCG00000017019	2.503	-0.6231	0.03053	-20.41	1.328e-92	1.981e-90
MARC2	2.426	-0.2883	0.02205	-13.07	4.773e-39	1.651e-37
KIF26B	11.06	-0.8484	0.03107	-27.31	3.435e-164	1.561e-161
DAPK1	3.218	-0.3042	0.02774	-10.97	5.626e-28	1.209e-26
RIN2	4.167	-0.3371	0.02539	-13.28	3.138e-40	1.132e-38
ACSS1	2.096	-0.4764	0.02528	-18.84	3.31e-79	3.308e-77
KCNH2	1.704	-0.328	0.02534	-12.94	2.606e-38	8.597e-37
TSPAN12	17.88	-0.2571	0.0235	-10.94	7.323e-28	1.564e-26
ADCYAP1R1	1.612	-0.4219	0.02654	-15.9	6.521e-57	3.641e-55
ENSSSCG00000032599	1.595	-0.2941	0.02644	-11.12	9.768e-29	2.165e-27
ENSSSCG00000032395	5.477	-0.506	0.0337	-15.02	5.816e-51	2.822e-49

Supplemental Figure 1

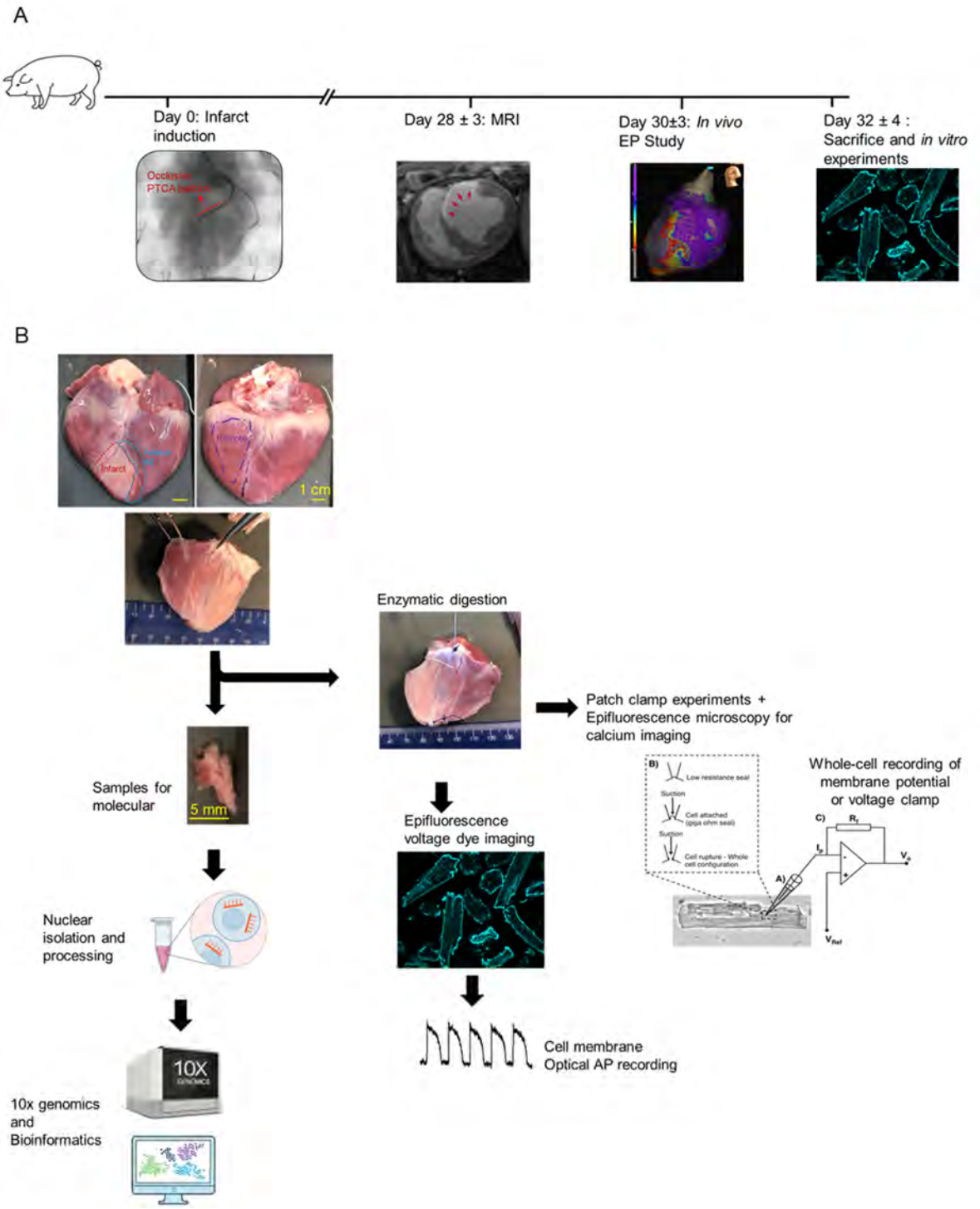

Supplemental Figure 1. Experimental design and tissue sampling.
A, Timeline of the experimental protocol.
B, Anterior (left) and posterior view (right) of the heart, and illustration of the workflow for cellular and molecular studies.

Supplemental Figure 2

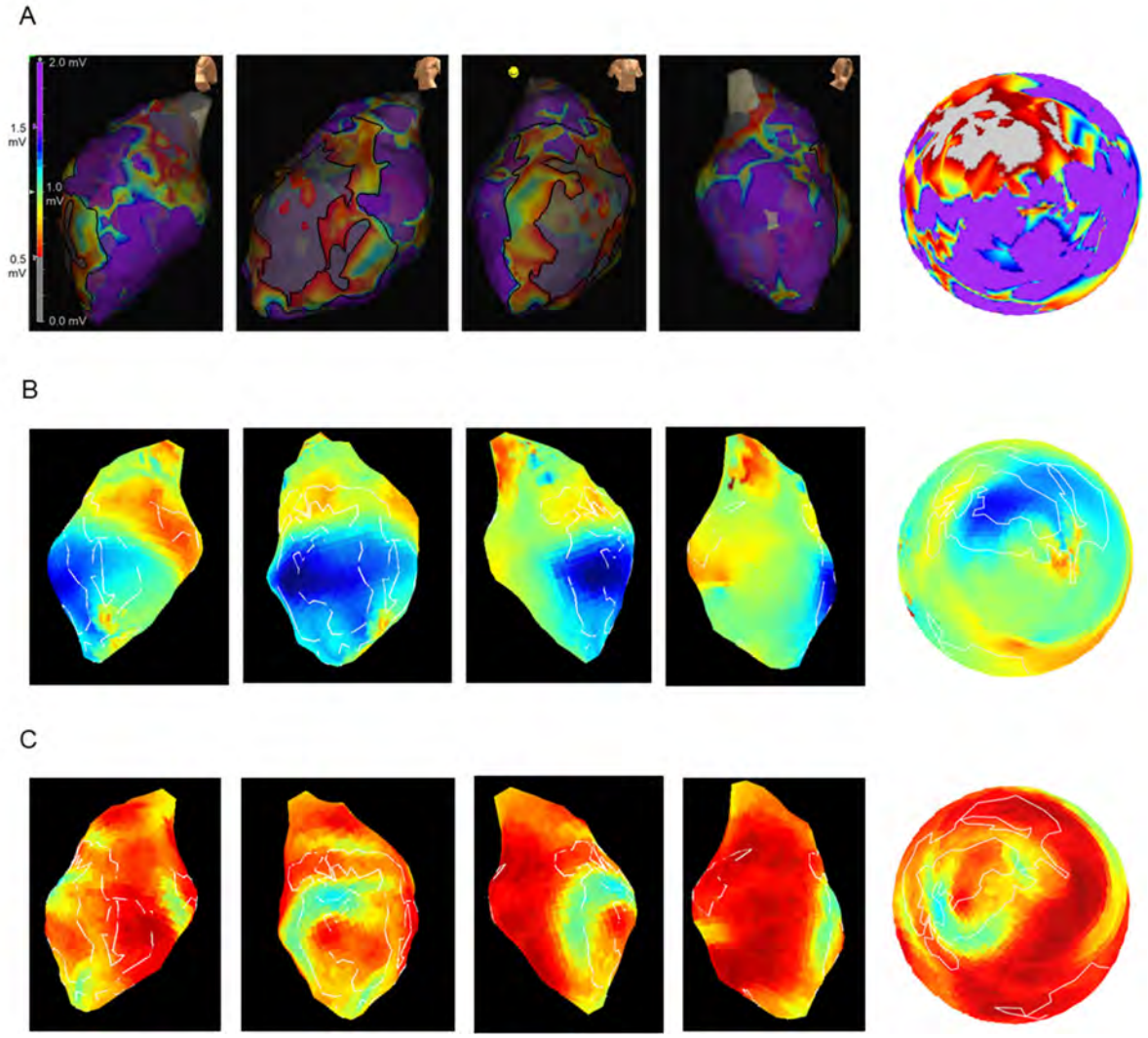

Supplemental Figure 2. Assessing regional heterogeneity of local activation-recovery interval (ARI) *in vivo* after MI.
A, Example of lateral, left-anterior oblique, right-anterior oblique and posterior views of electroanatomical mapping model generated to define the BZ as the region of bipolar voltage 0.5-1.5 mV. This model is visualized in 2D as a polar map (right).
B, Corresponding non-contact mapping model illustrating the local ARI and translation to a polar map.
C, Local ARI heterogeneity quantified as the standard deviation of the electrogram ARIs in a 1 cm radius for each electrogram.

Supplemental Figure 3

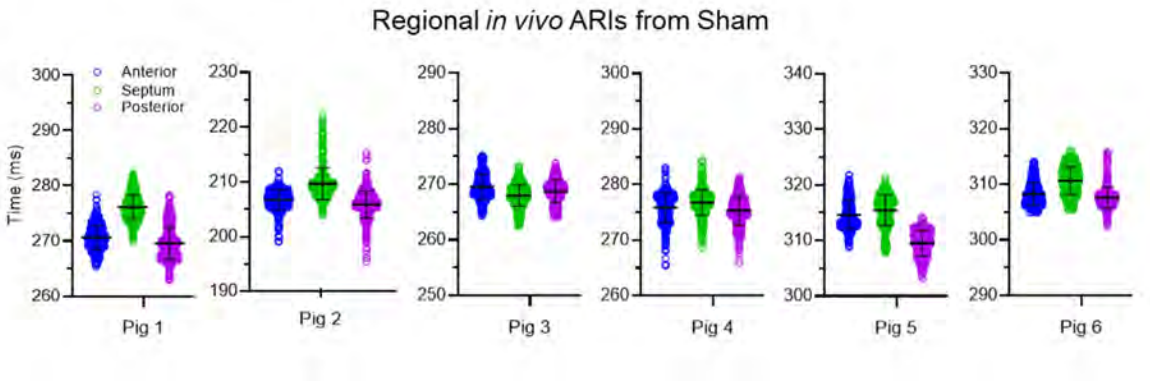

Supplemental Figure 3. Quantification of *in vivo* heterogeneity of repolarization.
Pooled data on ARIs of different regions *in vivo* from Sham (N_{pigs} = 6, n_{cells} = 321-568/region).

Supplemental Figure 4

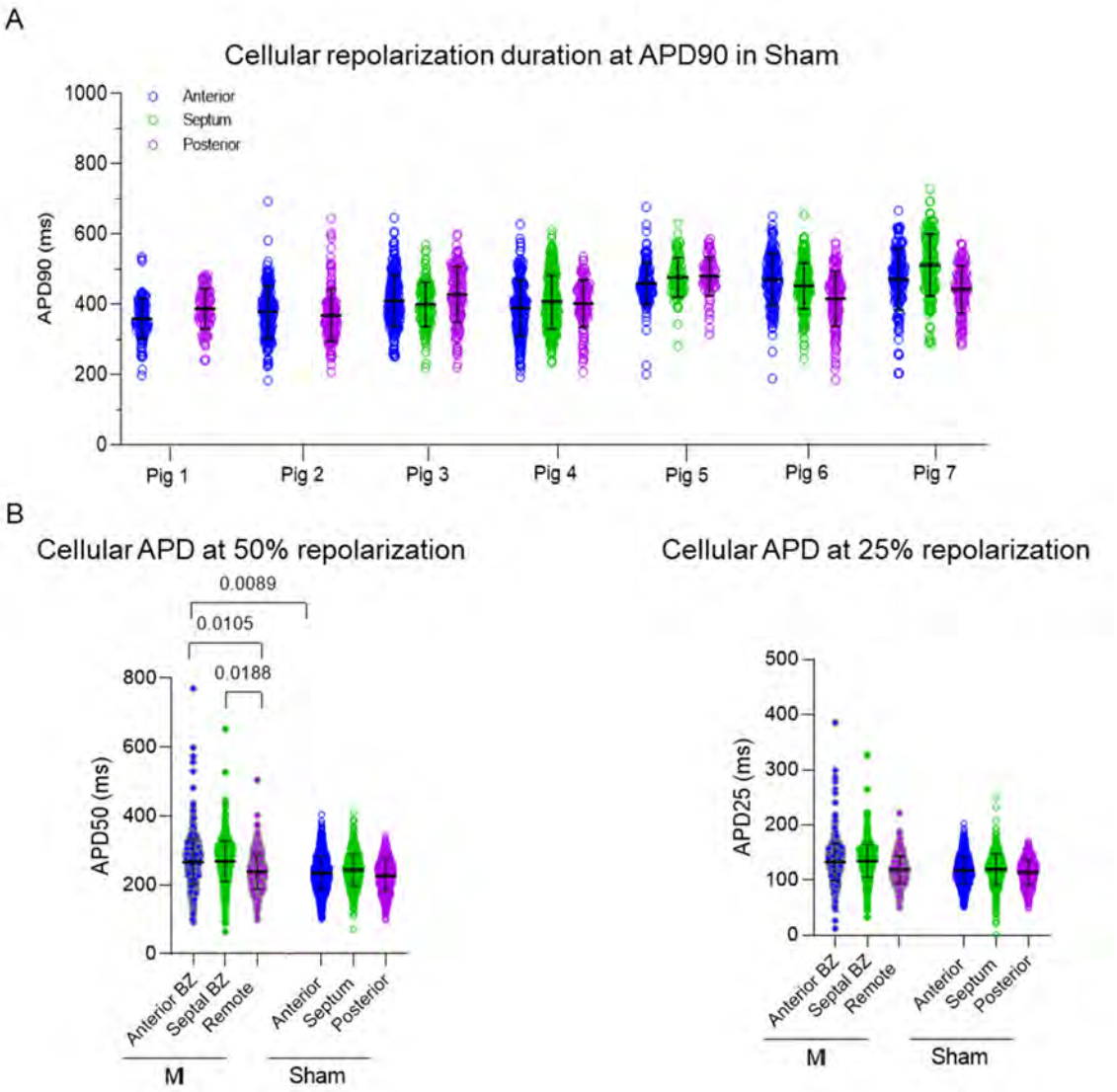

Supplemental Figure 4. Heterogeneity of early repolarization after MI.
A, Pooled individual cellular APD90 of populations of isolated cells from Sham (N_{pigs} = 7, n_{cells} = 90-330/region).
B, Summary data of pooled regional cellular APD50 (left) and APD25 (right). Multilevel mixed model with Bonferroni correction.

Supplemental Figure 5

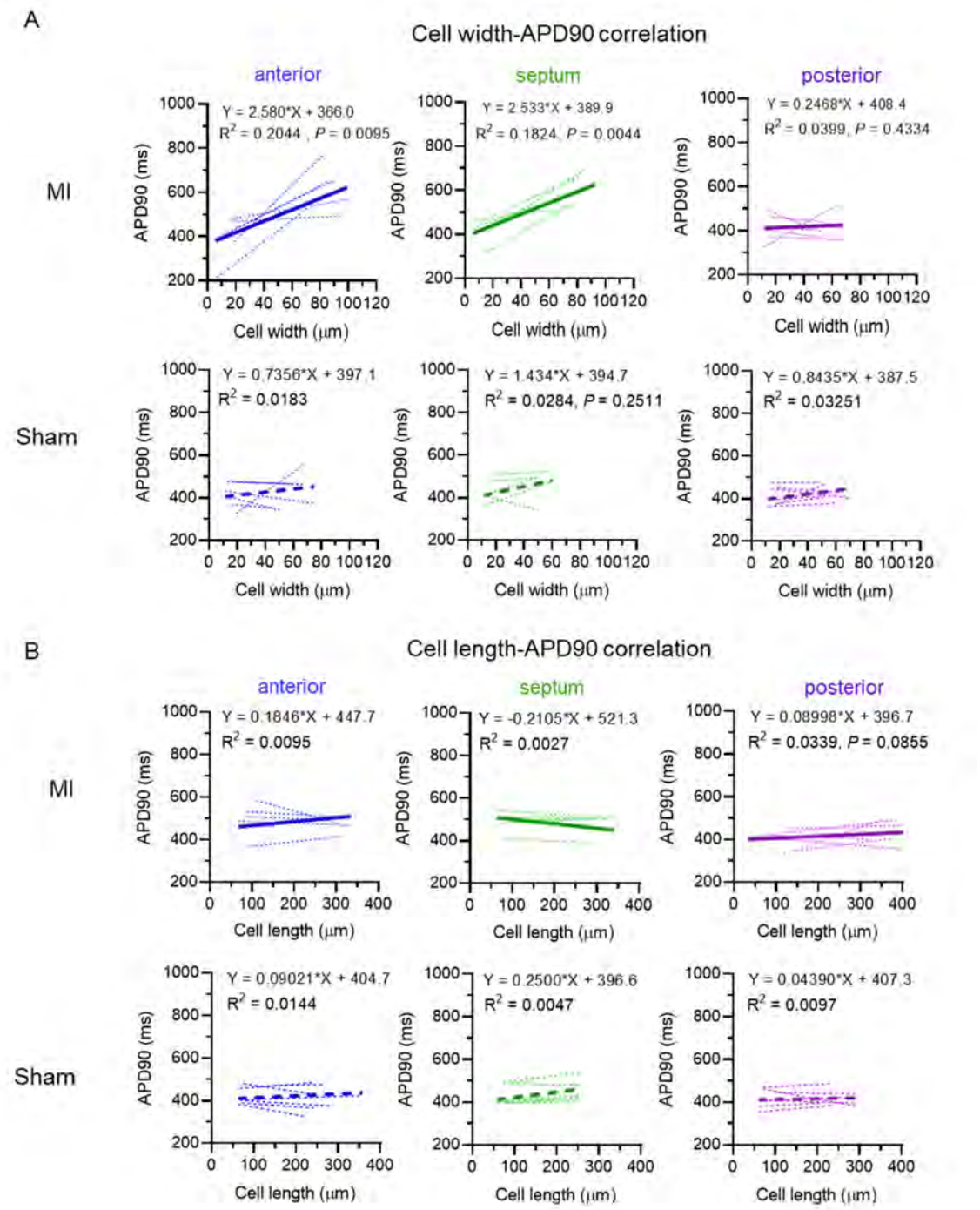

Supplemental Figure 5. Cell size correlation of action potential duration.
A, Correlation between cell width and APD90 from MI (N_{pigs} = 6, n_{cells} = 86-216) and Sham (N_{pigs} = 7, n_{cells} = 90-330). Linear regression analysis.
B, Correlation between cell length and APD90 from MI, N_{pigs} = 6, n_{cells} = 86-216 (top) and Sham, N_{pigs} = 7, n_{cells} = 90-330 (bottom). Linear regression analysis.

Supplemental Figure 6

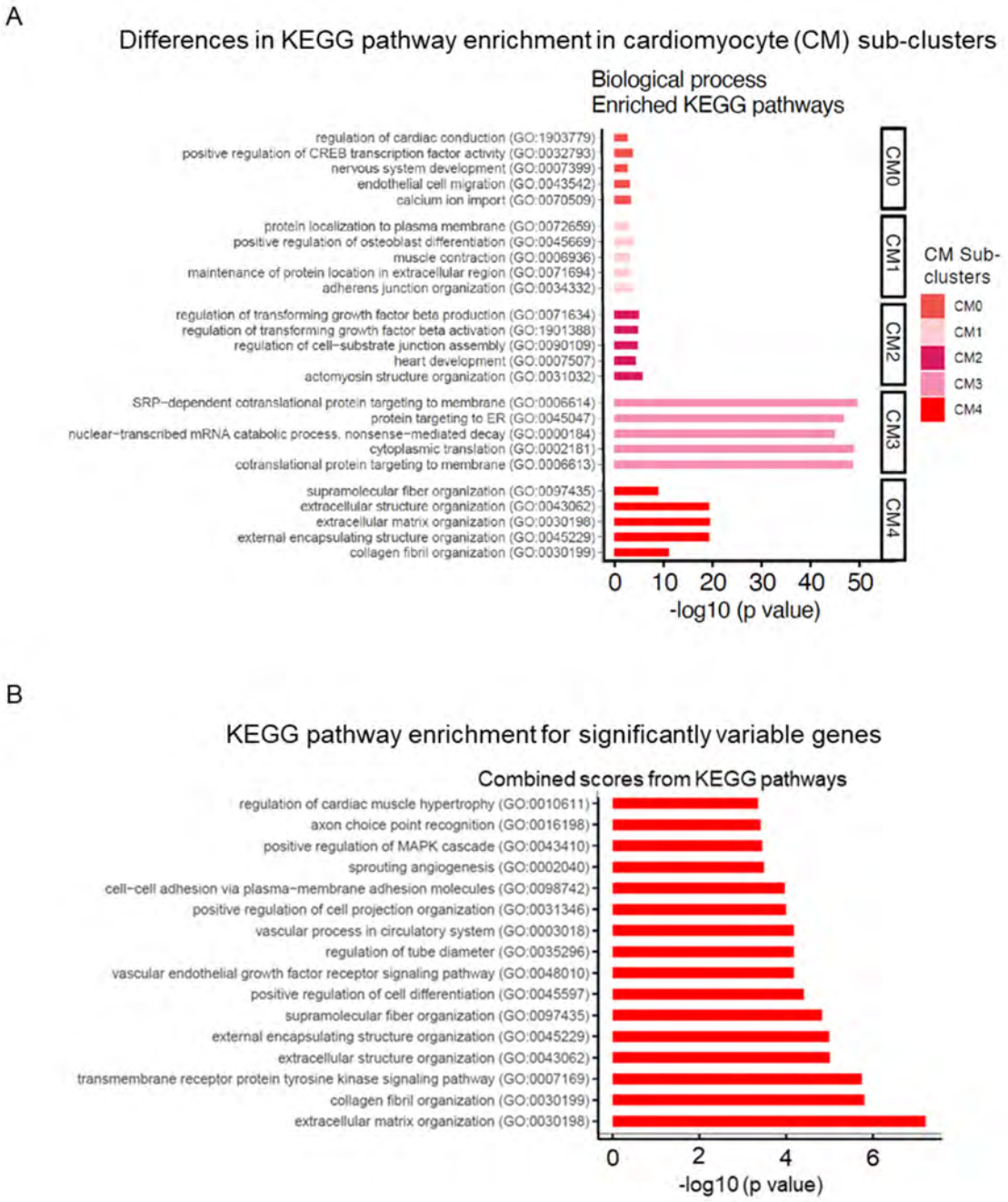

Supplemental Figure 6. Gene expression analysis of BZ vs. Remote cardiac myocytes.
A, GO and KEGG pathway analysis characterizing cardiomyocyte (CM) sub-clusters.
B, GO and KEGG pathway analysis of the highly variable genes (detected by a Bayesian inference model) in BZ compared with Remote cardiomyocyte nuclei.

Supplemental Figure 7

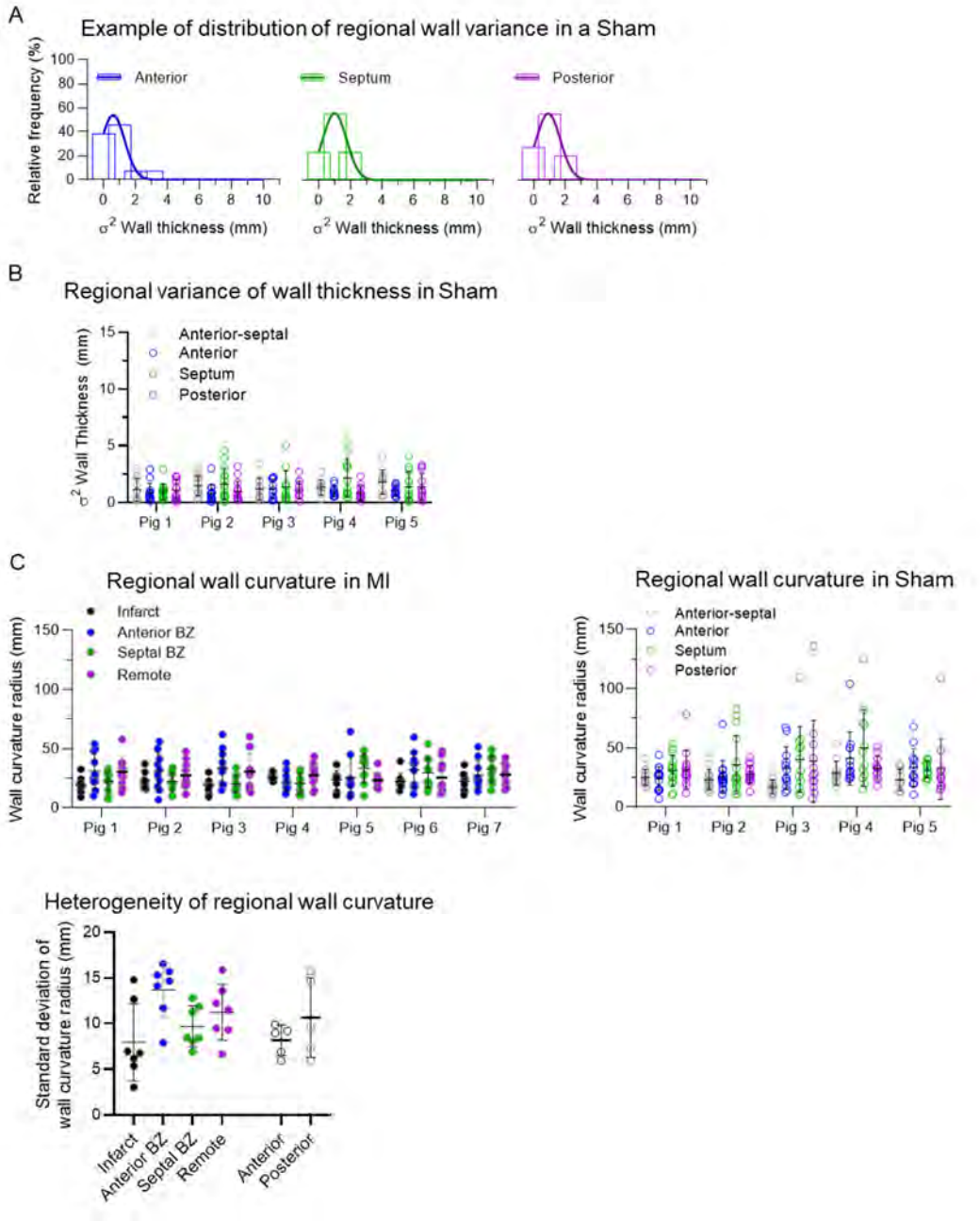

Supplemental Figure 7. Regional wall properties from MRI image analysis.
A, Example of the distribution of regional variance (σ^2) in wall thickness from Sham (n_{slices} = 10-13) illustrating uniformity in the different regions.
B, Regional wall variance (σ^2) in vivo from each slice of the cMRI from Sham (N_{pigs} = 5, n_{slices} = 10-14).
C, Regional wall curvature in vivo from MI (left, N_{pigs} = 6, n_{slices} = 10-14) and Sham (N_{pigs} = 5, n_{slices} = 10-14).
D, Summary data of the heterogeneity of wall curvature, quantified by standard deviation from (C). Mixed model ANOVA with Bonferroni posttest.

Supplemental references

37. Galan DT, Bito V, Claus P, Holemans P, Abi-Char J, Nagaraju CK, Dries E, Vermeulen K, Ventura-Clapier R, Sipido KR, et al. Reduced mitochondrial respiration in the ischemic as well as in the remote nonischemic region in postmyocardial infarction remodeling. *American Journal of Physiology-Heart and Circulatory Physiology*. 2016;311:H1075-H1090.

38. Thienpont B, Aronsen JM, Robinson EL, Okkenhaug H, Loche E, Ferrini A, Brien P, Alkass K, Tomasso A, Agrawal A, et al. The H3K9 dimethyltransferases EHMT1/2 protect against pathological cardiac hypertrophy. *J Clin Invest*. 2016;127:335-348.

39. Preissl S, Schwaderer M, Raulf A, Hesse M, Grüning BA, Köbele C, Backofen R, Fleischmann BK, Hein L, Gilsbach R. Deciphering the Epigenetic Code of Cardiac Myocyte Transcription. *Circ Res*. 2015;117:413-423.

40. Fleming SJ, Marioni JC, Babadi M. CellBender remove-background: a deep generative model for unsupervised removal of background noise from scRNA-seq datasets. In: bioRxiv: Cold Spring Harbor Laboratory; 2019.

41. Germain P-L, Lun A, Macnair W, Robinson MD. Doublet identification in single-cell sequencing data using scDblFinder. *F1000Research*. 2021;10:979.

42. Hao Y, Hao S, Andersen-Nissen E, Mauck WM, Zheng S, Butler A, Lee MJ, Wilk AJ, Darby C, Zager M, et al. Integrated analysis of multimodal single-cell data. *Cell*. 2021;184:3573-3587.e3529.

43. Korsunsky I, Millard N, Fan J, Slowikowski K, Zhang F, Wei K, Baglaenko Y, Brenner M, Loh P-R, Raychaudhuri S. Fast, sensitive and accurate integration of single-cell data with Harmony. *Nature Methods*. 2019;16:1289-1296.

44. Bunis DG, Andrews J, Fragiadakis GK, Burt TD, Sirota M. dittoSeq: universal user-friendly single-cell and bulk RNA sequencing visualization toolkit. *Bioinformatics*. 2021;36:5535-5536.

45. Love MI, Huber W, Anders S. Moderated estimation of fold change and dispersion for RNA-seq data with DESeq2. *Genome Biol*. 2014;15:550.

46. Kuleshov MV, Jones MR, Rouillard AD, Fernandez NF, Duan Q, Wang Z, Koplev S, Jenkins SL, Jagodnik KM, Lachmann A, et al. Enrichr: a comprehensive gene set enrichment analysis web server 2016 update. *Nucleic Acids Res*. 2016;44:W90-W97.

47. Blighe K, Rana S, Lewis M. EnhancedVolcano: Publication-ready volcano plots with enhanced colouring and labeling. GitHub, Inc. 2021.

48. Wickham H. *ggplot2: Elegant Graphics for Data Analysis*. New York, NY: Springer New York, NY; 2016.

49. Vallejos CA, Marioni JC, Richardson S. BASiCS: Bayesian Analysis of Single-Cell Sequencing Data. *PLoS Comput Biol*. 2015;11:e1004333.

50. Vallejos CA, Richardson S, Marioni JC. Beyond comparisons of means: understanding changes in gene expression at the single-cell level. *Genome Biol*. 2016;17:70.

CHAPTER 6: Electrocardiogram beat-to-beat variability of repolarization (BVR) during acute ischemia.

Manuscript submitted as:

Matthew Amoni, Sebastian Ingelare, Jonathan Moeyersons, Dries Wets, Aldo Tanushi, Sabine Van Huffel, Carolina Varon, Karin Sipido, Piet Claus, Rik Willems. “Regional beat-to-beat variability of repolarization increases during ischemia and predicts imminent arrhythmias in a pig mode ofl myocardial infarction.” (American Journal of Physiology – Heart and Circulatory Physiology – revision to be submitted).

Abstract

Background

Ventricular tachycardia (VT) and fibrillation (VF) can complicate acute myocardial ischemia (AMI) leading to sudden cardiac death. Regional repolarization instability during AMI can contribute to the substrate for VT/VF. QT Beat-to-beat variability of repolarization (BVR), a measure of repolarization lability increases during AMI. We hypothesized that its surge precedes VT/VF. We studied the spatial and temporal BVR changes in relation to VT/VF during AMI.

Methods

In 24 pigs, baseline BVR was quantified on 12-lead electrocardiogram (ECG) simultaneously recorded at 200 Hz, 1- and 4 kHz to assess the impact of sampling frequency on BVR. AMI was then induced in 16 pigs by percutaneous coronary artery occlusion (MI), while 8 underwent sham-operation (Sham). Changes in BVR were assessed in 1 kHz signals at 5-minutes after occlusion, 5- and 1-minute pre-VF in animals that developed VF during AMI, or individually matched time points in pigs without VF. Serum troponin and ST deviation were measured. After 1-month, magnetic resonance imaging and VT induction by programmed electrical stimulation were performed.

Results

During AMI, BVR increased significantly in inferior-lateral leads correlating with ST-deviation and troponin increase. BVR was maximal 1-minute pre-VF (3.78±1.36 vs 5-minutes pre-VF: 1.67±1.56, $P < 0.0001$). After 1-month, BVR was higher in MI than sham and correlated with the infarct size (1.43±0.50, vs 0.57±0.30, $P = 0.009$). VT was inducible in all MI animals and the ease-of-induction, correlated with BVR ($R^2 = 0.67$, $P = 0.022$).

Conclusion

BVR increases during AMI, and temporal BVR changes predicted imminent VT/VF supporting a possible role in monitoring and early-warning systems. Post-AMI BVR correlated to arrhythmia vulnerability suggesting utility in risk stratification.

Keywords: acute myocardial ischemia, beat-to-beat variability of repolarization, myocardial infarction, sudden cardiac death, ventricular fibrillation

Introduction

Sudden cardiac death (SCD) is a leading cause of death, and occurs predominantly due to unexpected ventricular tachycardia (VT) and fibrillation (VF) with subsequent sudden cardiac arrest (1). The majority of SCDs occur in patients with ischemic heart disease (IHD) and is often the first presentation of acute myocardial ischemia (AMI) (2). Several factors contribute to the occurrence of an AMI including the characteristics of the coronary lesion, particularly thin-walled atherosclerotic plaques, and hypercoagulability (3). However, the vulnerability to SCD during AMI and factors predicting SCD as a manifestation of AMI remain under investigation (4). Structural elements such as the severity and extent of the infarcted area, cellular electrophysiological changes during AMI and sympathetic hyperresponsiveness promote SCD (5). Identifying and monitoring electrophysiological factors that predict imminent arrhythmia can provide a better identification of patients at risk and an opportunity to prevent SCD via monitoring in wearables and early warning systems (6).

The timing and prediction of SCD in AMI in patients is poorly defined because it is difficult to capture extensive data of these rare and unexpected events. Insights are gained from pre-clinical animal models, where lethal arrhythmias occur early in AMI during Phase I (<30 minutes), and fewer occur in Phase II (1-24 hours) (7, 8). Early arrhythmias can be ‘immediate’ (Phase 1a), within 10 mins, or ‘delayed’ (Phase 1b), within 12-30 minutes of AMI, when most arrhythmias occur (8). The principal mechanism is functional re-entry and involves progressive cell uncoupling and reduced membrane potential with electrical propagation and repolarization abnormalities in the infarct and border zone leading to unidirectional block and rotors (9). It would be of interest to understand why some individuals are vulnerable to SCD during this time window and to predict the occurrence of these arrhythmias preferably by non-invasive means, to perform novel or more strict primary prevention of atherosclerotic heart disease and possibly to offer monitoring with future wearable technology in these individuals.

Beat-to-beat variability of repolarization (BVR) is an electrocardiographic predictor of imminent arrhythmia in the dog-model of Torsades de Pointes (TdP) during pro-arrhythmic drug infusion (10, 11). Temporal changes in BVR have been recently proposed for prediction of non-sustained ventricular tachycardia (nsVT) in chronic IHD patients at risk of SCD (12, 13). During AMI BVR and its predictive value for SCD has not been evaluated. However, repolarization abnormalities including including increased BVR (14), T-wave alternans (TWA) (15), QT dispersion (16) and non-TWA repolarization variability (17) occur during and after AMI. Data from intracardiac monitoring of monophasic action potential (MAP) during AMI demonstrate increased BVR (18) during AMI, although its relationship to SCD was not evaluated.

Therefore, we hypothesized that BVR increases during AMI, and is detectable on the surface ECG. Furthermore, we posit BVR exhibits a spatial pattern with higher indices in leads directed to the vulnerable territory of regional ischemia. In this study we used a pig model of AMI to study ECG-BVR. We studied the evolution of BVR during AMI and its relation to imminent SCD events and we evaluated BVR in the chronic phase after AMI and assessed its correlation to the inducibility of ventricular arrhythmia. To optimize BVR recordings in these experiments, we first studied the impact of signal sampling frequency on BVR.

Materials and Methods

Twenty-four domestic pigs (Strain TN70, Topigs, Norsvin) of both sexes were used in this study. Animal husbandry was in accordance with international guidelines (European Directive 2010/63/EU) and protocols were approved by the KU Leuven institutional ethical committee (ECD137/2018).

All experiments were performed under general anesthesia with mechanical ventilation. Animals were sedated with tiletamine/zolazepam 8 mg/kg and xylazine 2.5 mg/kg, intramuscular (IM), anesthesia was induced with propofol 3 mg/kg and maintained with 10 mg/kg/h, intravenous (IV) combined with remifentanil 0.2-0.4 µg/kg/h, IV. Endotracheal ventilation was performed at 6-10 ml/kg with 50% oxygen-air mixture. Antibiotics (pre-operative cefazolin 25-50 mg/kg, IV and post-operative amoxicillin 15mg/kg or enrofloxacilin 4mg/kg, IM) and anticoagulation (acetylsalicylic acid 500 mg, IV and periodic heparin 5 000-10 000 IU, IV) were routinely administered during procedures.

Pig model of acute myocardial ischemia

All animals were premedicated with oral amiodarone 300 mg for 3 days as well as aspirin 300 mg and clopidogrel 300 mg for one day. AMI was induced by balloon occlusion of the left anterior descending coronary artery in 16 animals as previously described (MI) (19). Briefly, the right carotid artery was dissected and cannulated with a 6/7 Fr vascular sheath. A 6/7 Fr Judkins-left coronary guiding catheter was positioned in the left main coronary ostium under fluoroscopic guidance. A 2.5-3.0 mm angioplasty balloon, was completely inflated in the left anterior descending (LAD) immediately after the first diagonal branch, resulting in anterior-septal ischemia (Figure 1A). Occlusion was maintained for 120 minutes, followed by release and reperfusion with 60 minutes monitoring under anesthesia. In the event of sustained VT/VF, external defibrillation with a shock of 150-200J was applied to restore sinus rhythm. Eight sham-operated animals were included as controls (Sham). Animals were randomly asigned to either MI or Sham. No animals died during the procedure. Post-operatively animals received broad-spectrum antibiotics (Amoxicillin 15mg/kg or Enrofloxacilin 4mg/kg) with analgesia, Buprenorphine HCl 0.02-0.03mg/kg, IM. All animals received Amiodarone for 3 days. Aspirin 100 mg and Clopidogrel 75 mg was given daily for 1 month.

Electrocardiogram recording and analysis

To assess the impact of sampling frequency and recording systems on BVR, three sets of ECGs were simultaneously recorded at 200 Hz (Holter device; Microport, Belgium), 1 kHz (Powerlab system; ADInstruments, UK) and 4 kHz (Labsystem Pro electrophysiology system; BARD, Boston Scientific, USA). All systems employed a 50 Hz lowpass filter. The ECG electrodes were positioned to mimic the clinical ECG, and precordial placement was modified to adapt to the orientation of the heart in the pig (Figure 1B). All recordings were exported and analyzed on an offline workstation. To assess the impact of sampling frequency on BVR assessment, lead A of Holter recordings and equivalent lead II of 12-lead ECG were used at baseline.

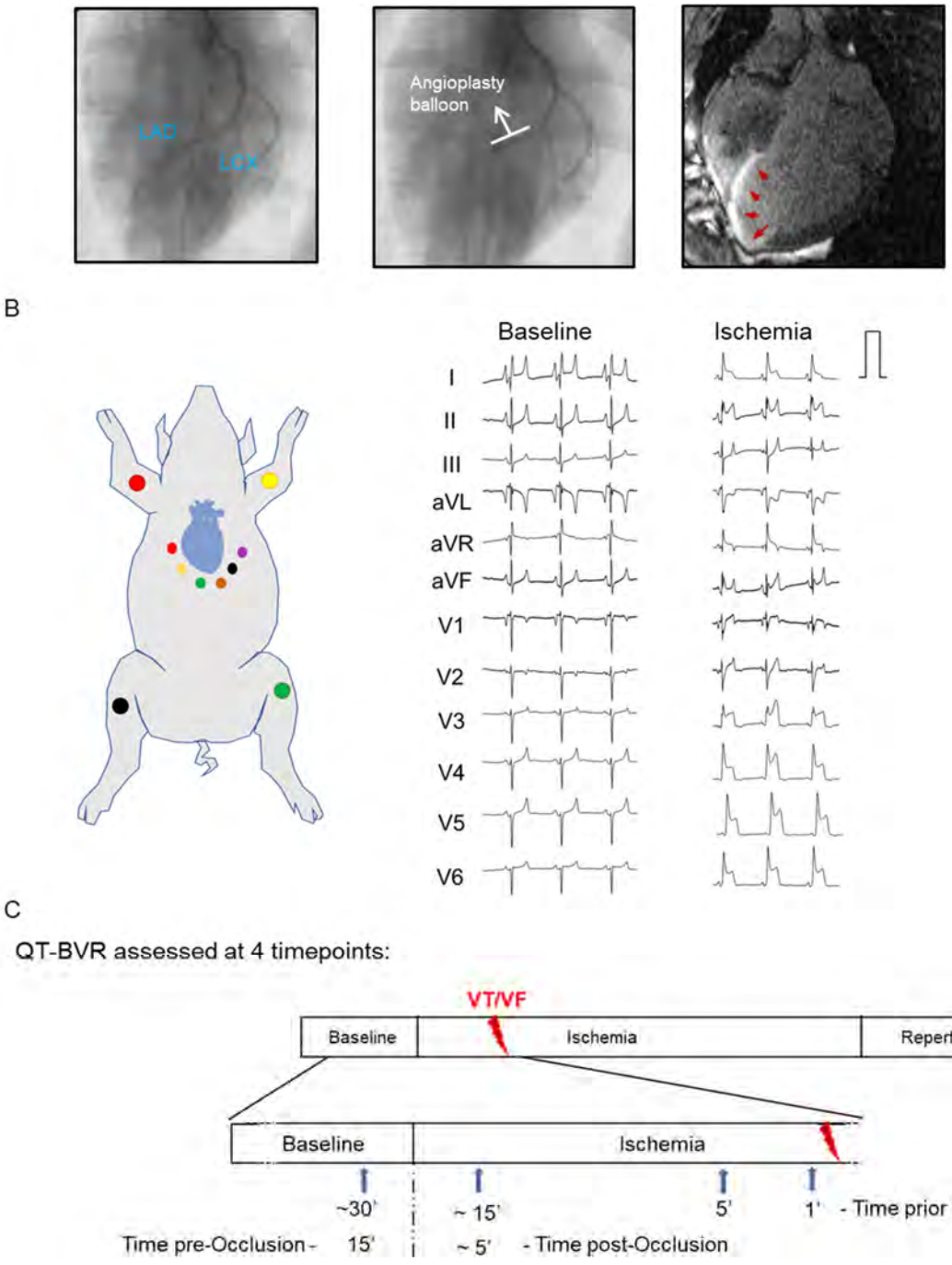

Figure 1, Assessment of beat-to-beat variation of repolarization (BVR) in a pig model of myocardial infarction and sudden cardiac death.
A, AP angiographic views of the left coronary arteries (left) illustrating occlusion of the mid-left anterior descending artery (middle). Right, cardiac magnetic resonance imaging of the infarcted heart 1 month after I/R illustrating 21% infarction of left ventricular mass.
B, Schematic illustrating the ECG electrode placement in the pig (left) and examples of the 12-lead ECG at baseline and during ischemia (right), note the dramatic ST changes in V1-6.
C, Illustration of the experimental design and selected taken to analyze BVR.

Baseline was defined as a 1-minute segment, 15 minutes prior to coronary occlusion. For assessment of the spatial changes in BVR during AMI, a 1-minute segment during early ischemia (5 minutes post-occlusion), from all leads of the 1 kHz, 12 lead ECG were compared to baseline. To assess the BVR changes preceding VT/VF, animals subjected to AMI were subdivided into 2 groups: those that developped VF (VF+ve), n = 10, and those without VF (VF-ve), n = 6. The first episode of VF was annotated and 2 time points: 5-minutes and 1-minute prior to the spontaneous VF were defined (Figure 1C). VF-ve animals were matched by weight and sex to 6 VF+ve animals, and individually matched timepoints from the start of coronary occlusion were used to define the 5-minute and 1-minute pre-VF timepoints. A 1-minute ECG segment at these time points was used for analysis. ECG segments were coded to blind the investigator and analyzed using R-DECO: a modified fiducial point detection custom-made MATLAB software (20). Correct annotation of fiducial points was checked and manually adjusted where necessary. All ventricular premature complexes as well as the preceding (if the premature complex occurred before the end of the T-wave) and the succeeding sinus beats were excluded from the analysis. Repolarization lability in the ECG QT-BVR was then calculated using : $\Sigma(|QT_{n+1} - QT_n|) / [nbeats \times \sqrt{2}]$ (10).

Premature ventricular complexes were counted in 5-minute intervals within the 30-minutes after occlusion and documented.

Serum biomarker assessment

Serum troponin and creatinine kinase were determined prior to and during AMI as well as 1-month post-procedure, as a surrogate of severity of myocardial injury. Blood was collected at baseline, defined as a time at least 15-minutes prior to occlusion, as well as at the end of 120-minutes of ischemia, using EDTA and Li-heparin tubes. Blood samples were analyzed by the routine clinical assays of the clinical laboratory of the university hospitals Leuven.

Cardiac magnetic resonance imaging

After 1-month, cardiac dimensions and function as well as left ventricle (LV) infarct size were assessed by magnetic resonance imaging (MRI) under general anesthesia with artificial ventilation in 19 of the 24 pigs, 12 MI and 7 Sham (2 MI pigs succumbed to SCD in the first week after MI induction and 3 animals, 1 Sham and 2 MI, had high heart rates (>150bpm) not suitable for imaging). The protocol of cMRI performed with a 3T, PRISMA-tim whole-body scanner (Siemens, Erlangen, Germany) have been described previously (19). Infarct size was determined by late gadolinium enhancement (LGE), 12 minutes following a double dose bolus of Gd (gadoterate meglumine, Dotarem, 0.2 mmol kg^{-1}). Structural and functional assessment parameters are summarized in table 1.

Cardiac electrophysiology study

Two to four days after the cardiac MRI, a follow- *in-vivo* electrophysiology (EP) study was performed in a subset of 15 pigs (9 MI and 6 Sham). Under general anesthesia, a 12-lead ECG was recorded at 1kHz as described prior. for at least 5 minutes. Then, the femoral vein, jugular vein and carotid artery were cannulated with 7-8Fr vascular sheaths. Standard EP catheters (Decanav Biosense Webster, Belgium) were positioned in the LV, right ventricle (RV) and coronary sinus as described previously (19). One MI pig was exculeded due to a vascular access complication. A modified-Wellens clinical ventricular arrhythmia induction protocol was performed by programmed electrical stimulation (PES) from the RV apex adapted from (14, 21)

in 8 MI and 6 Sham. To avoid induction of a nonspecific VF, stimulation in the LV and burst pacing were not done. Animals without arrhythmias in this single site protocol were considered non-inducible.

The inducibility of VT/VF as a surrogate of arrhythmia vulnerability was assessed using a scale constructed from the stepwise progression of the PES protocol where the first step (S1 = 600ms and 1 extrasystole, S2 = 400 ms) was 100% and the last most aggressive step (S1 = 350 ms and 3 extrasystoles, S2 = 200 ms, S3 = 180 ms, S4 = 150 ms) marked non-inducibility as 0%, adapted from León *et al.* (21).

Statistical analysis

All data are presented as mean ± SD or number (percentage). Distribution of data was tested by Shapiro-Wilk. Data were analyzed with Student's t-test or Mann-Wiitney test, 1-way or 2-way mixed-effects model ANOVA with Bonferroni post-hoc testing or Kruskal-Wallis test with Dunn's post-hoc testing, Fisher's exact test, and linear regression analysis as applicable and indicated in the figure legends. $P < 0.05$ was considered statistically significant.

Table 1. Cardiac magnetic resonance imaging data of structural and functional remodeling 1-month after MI

	MI (N_{pigs} = 12)	**Sham (N_{pigs} = 7)**	***P* value**
Infarct size (%)	19.3 ± 4.2	0 ± 0	<0.0001
Ejection fraction (%)	38.5 ± 10.3	62.3 ± 3.2	<0.0001
End-diastolic volume (mL)	170.7 ± 22.6	142 ± 24.7	0.0014
End-systolic volume (mL)	104.9 ± 25.9	51.0 ± 10.1	<0.0001
Left ventricular mass (g)	132.1 ± 17.7	133.9 ± 24.5	0.1298
Heart rate (beats per minute)	81.6 ± 10.8	74 ± 16.9	0.0876
Left ventricular peak systolic pressure (mmHg)	94.3 ± 12.2	103.0 ± 18.2	0.1949
Left ventricular mean diastolic pressure (mmHg)	5.7 ± 4.7	1.5 ± 1.4	0.0184

Results

Sampling rate influences BVR assessment.

To determine the optimal experimental set-up, we assessed the impact of sampling rate on BVR assessment, because BVR detects subtle variation in the QT interval that can be misannotated in an undersampled signal. Figure 2A illustrates the ECG analysis and QT-interval detection methods for BVR calculation and visualization. At baseline, BVR of ECGs recorded at 200 Hz was significantly higher than the BVR simultaneously recorded at 1 kHz (200 Hz: 2.02 ± 0.72ms, vs 1 kHz: 0.31 ± 0.18ms, $P < 0.0001$). The magnitude of BVR recorded at 1 kHz was comparable to the 4 kHz ECG (1 kHz: 0.31 ± 0.18ms vs 4 kHz: 0.36 ± 0.21ms, P = 0.9800; figure 2B, C). To investigate whether the lower sampling frequency indeed produced higher BVR, we downsampling the 1 kHz baseline signal to 200Hz (Figure 3). This reproduced the increased BVR magnitude observed in the 200Hz signal recorded by the Holter.

There was no difference between MI and sham BVR at baseline in both the low sampling 200 Hz and high sampling 1kHz and 4kHz signals. These findings demonstrate that BVR magnitude is influenced by the sampling frequency and reinforce the requirement of uniform sampling frequency for comparison.

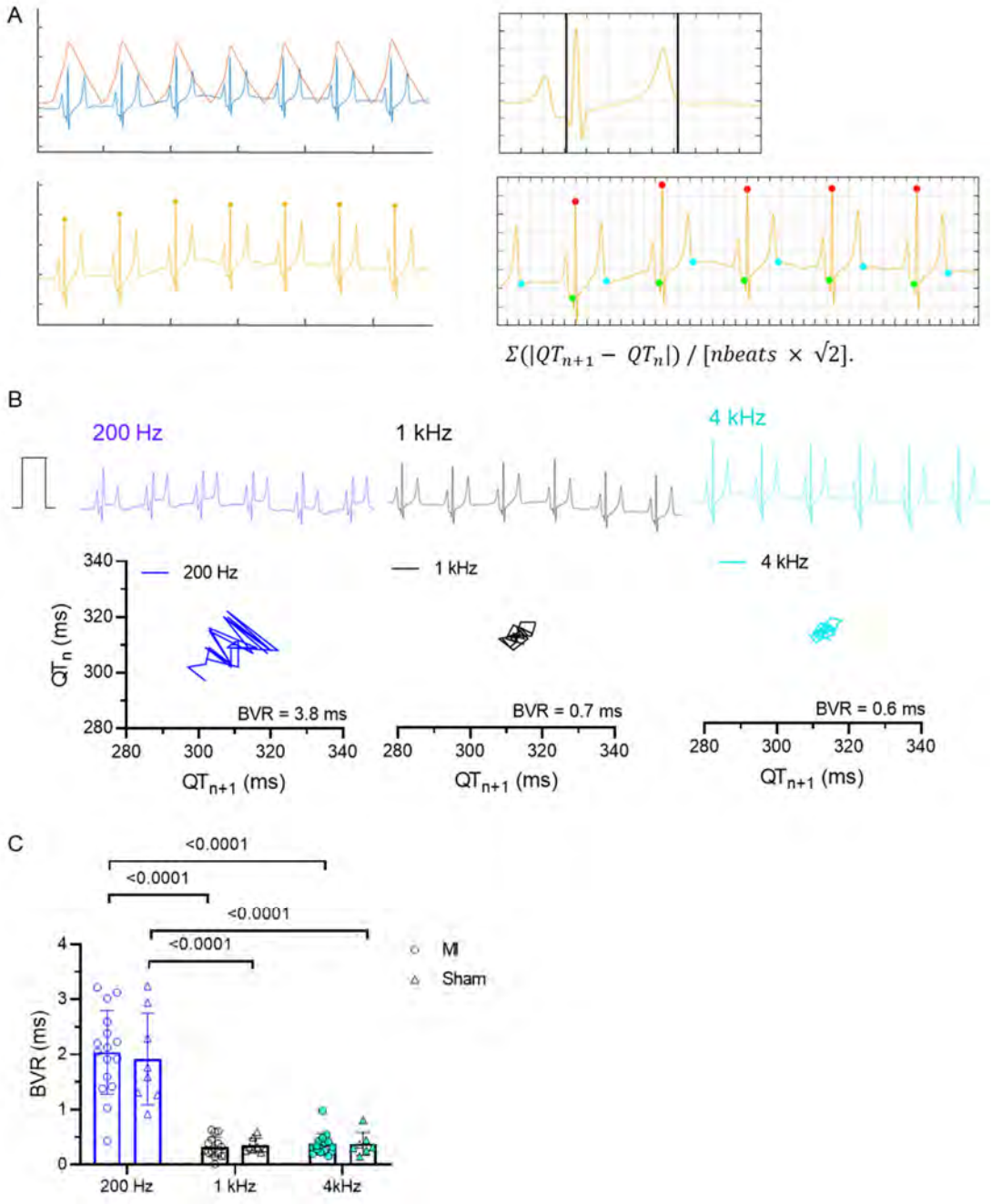

Figure 2. Impact of sampling rate on BVR assessment.
A, Illustration of the R_DECO interface used to analyse the electrocardiogram (ECG). Left, an enveloping algorithm (top) is employed to enhance QRS complex detection (bottom). Right, Template-based algorithm (top) is used for QT interval determination and calculation of the QT BVR (bottom).
B, Examples of of baseline ECG (top) and corresponding Poincaré plots (bottom) recorded by 200 Hz Holter system (left), 1 kHz PowerLab system (middle) and 4 kHz BARD system (right)
C, Summary data of BVR from low and high sampling rate ECG (right). N = 16 MI, 8 Sham. Mixed-effects model analysis of variance (ANOVA) with Bonferroni post-test.

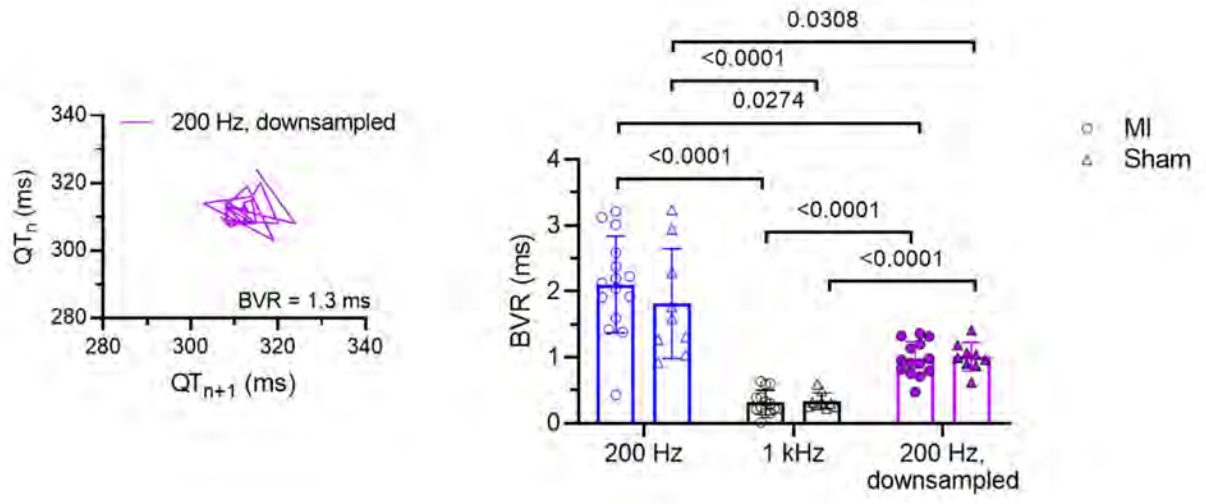

Figure 3. Reducing ECG samples increases magnitude of BVR.
Example of Poincaré plots of baseline ECG segments recorded at 1 kHz signal downsampled to 200 Hz (left). Summary data of BVR from baseline 1kHz ECGs and downsampled to 200Hz from MI and Sham replicates the increased BVR observed in 200Hz Holter. Mixed-effects model ANOVA with Bonferroni posttest (right).

BVR increases during regional ischemia proportional to the extent of injury.

Using the high-sampling 1 kHz ECG, we investigated the impact of AMI on BVR. During AMI, the ST-segment deviated from baseline in all leads, mean absolute deviation of 0.23 ± 0.15 mV and was largest in leads II, and V4, consistent with the anterior-septal AMI (Figure 4A). The serum troponin rose significantly (AMI: 34.60 ± 15.54 µg/L vs baseline: 0.01 ± 0.01 µg/L, P < 0.0001), but did not correlate strongly with infarct size (R^2=0.56, *P*=0.003), possibly reflecting the discrepancy between the sampling time, i.e. serum sampling immediately after MI compared to the imaging after 1-month with additional reperfusion injury and remodelling in between the time-points. Figure 4B presents BVR changes on the 12-lead ECG during AMI. BVR increased significant in leads covering the territory of injury including II, III, aVF, V3, V4 and V5, while sham animals showed no significant changes at matched timepoints.

The cumulative BVR correlated with the cumulative ST-segment deviation of all leads (R^2 = 0.567, P = 0.0002) (Figure 4C), and lead II and V4 had the highest correlations (Supplemental figure S1). The maximal BVR in each pig also correlated with the serum troponin levels (R^2 = 0.612, P = 0.0038) (Figure 4C). There was no significant change in heart rate between baseline and AMI, or between MI and sham (Figure 5A). Although the QT duration was not different between baseline and AMI, the QT dispersion increased during ischemia (Figure 5). Together, these data suggest that BVR increases during acute ischemia in keeping with the region and extent of injury.

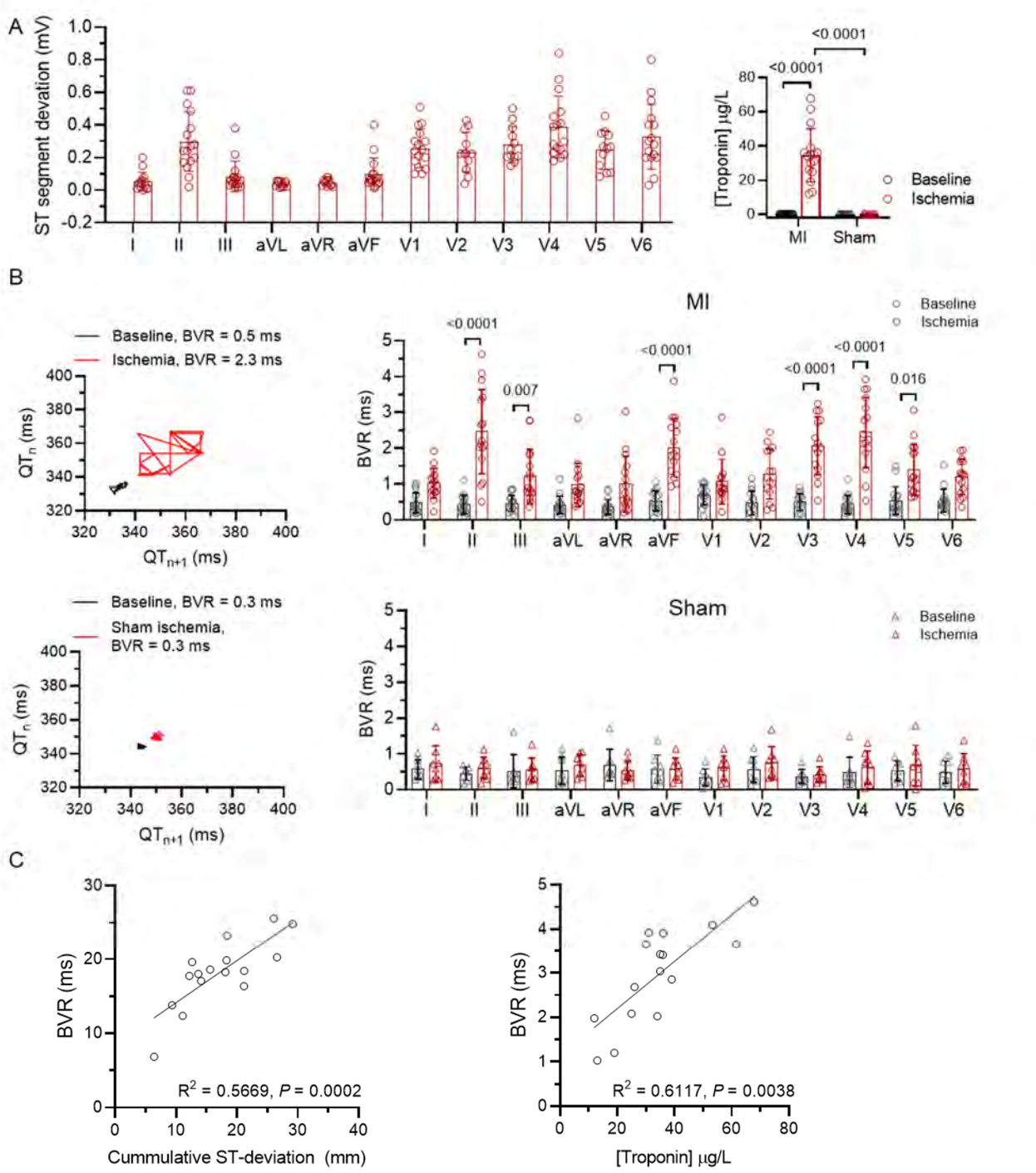

Figure 4. BVR increases during regional ischemia and is related to the extent of injury.
A, Summary data of 12-lead ECG ST segment deviation (left) and serum troponin after 120 minutes AMI (right). N = 16 MI and 8 Sham. One-way and Mixed-effects model ANOVA with Bonferroni posttest respectively.
B, Left, example of Poincaré plots of the QT interval at baseline and during ischemia in MI (top) and Sham animals (bottom). Right, summary data of 12-lead ECG BVR. N = 16 MI and 8 Sham.

Mixed-effects model ANOVA with Bonferroni post-test. **C,** Left, correlation between cumulative BVR and ST deviation in all 12 ECG leads. Right, correlation between cumulative BVR and serum troponin. N = 16 MI. Linear regression analysis.

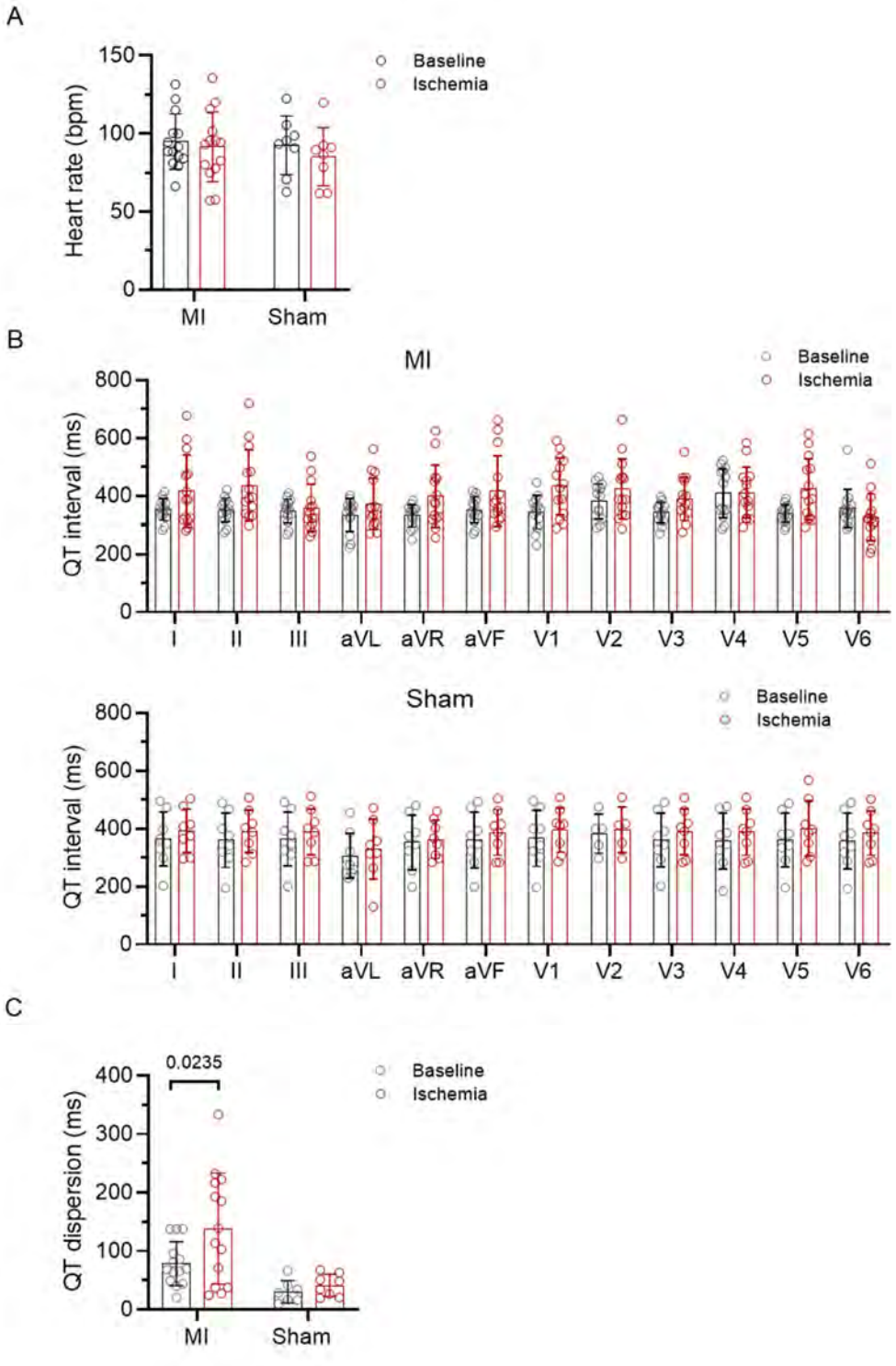

Figure 5. Heart rate and QT interval changes are negligible during ischemia.
A, Summary data of heart rate at baseline and during ischemia.
B, Summary data of QT interval duration in the 12 ECG leads at baseline and during ischemia in MI (top) and sham (bottom).
C, Summary data of QT dispersion at baseline and during ischemia. N = 16 MI and 8 Sham. Mixed-effects model ANOVA with Bonferroni post-test.

BVR increases prior to spontaneous VT/VF during ischemia

We assessed the behavior of BVR prior to spontaneous onset VF in our model of AMI in lead II or V4 as appropriate. Figure 6A shows a typical example of a spontaneous onset VF. VF occurred in 72% of cases at 15-23 minutes after AMI. Figure 6B presents the changes in BVR in VF+ve and VF-ve animals during AMI. In VF+ve cases, BVR at 5-minutes prior to VF was comparable to BVR in early ischemia, 5-minutes AMI (5-minutes pre-VF: 1.67 ± 1.56ms, vs 5-minutes AMI: 2.49 ± 0.98ms, P = 0.3468). In the minute prior to VF, BVR increased significantly (3.78 ± 1.36ms, vs 5-minutes pre-VF: 1.67 ± 1.56ms, P < 0.0001). In animals that did not have VF (VF-ve), BVR changes were assessed using a matched timepoint during AMI, BVR did not increase significantly between the matched time-points during AMI (2.04 ± 1.42ms, vs 5-minutes pre-matched: 1.47 ± 0.51ms, P = 0.5926) and compared to early ischemia (vs 5-minutes AMI: 2.10 ± 0.66ms, P = 0.7997). Thus, after a similar duration of ischemia (17.5 ± 5.4minutes, corresponding to the 1-minute before VF), a significant difference was observed in the change in BVR between the animals that developed VF (VF+ve) and the ones that did not (VF-ve) (2.23 ± 0.81ms, vs VF-ve: 0.66 ± 1.00ms, *P* = 0.0164; figure 6B). Furthermore, in Sham animals, no temporal changes in BVR were observed at matched timepoints (Supplemental figure S2). These data suggest that BVR changes can be a predictor of imminent VF during AMI.

We also examined the occurrence of PVCs that could provide the triggers that initiate VF. Figure 6C shows the temporal incidence of PVCs, which exhibited a similar pattern of temporal behavior as BVR. The coupling interval of the PVC that initiated the VF and PVCs in the 1-minute prior to VF were similar and short (218 ± 28ms vs 1-minutes pre-VF: 225 ± 46ms, P = 0.9122), and tended to be shorter than PVCs observed in the early ischemic period (5-minutes AMI: 302 ± 96ms, P = 0.0865). These observations highlight the possible importance of PVC timing and an evolution during MI until the ideal timing and substrate coincide to initiate and sustain VF.

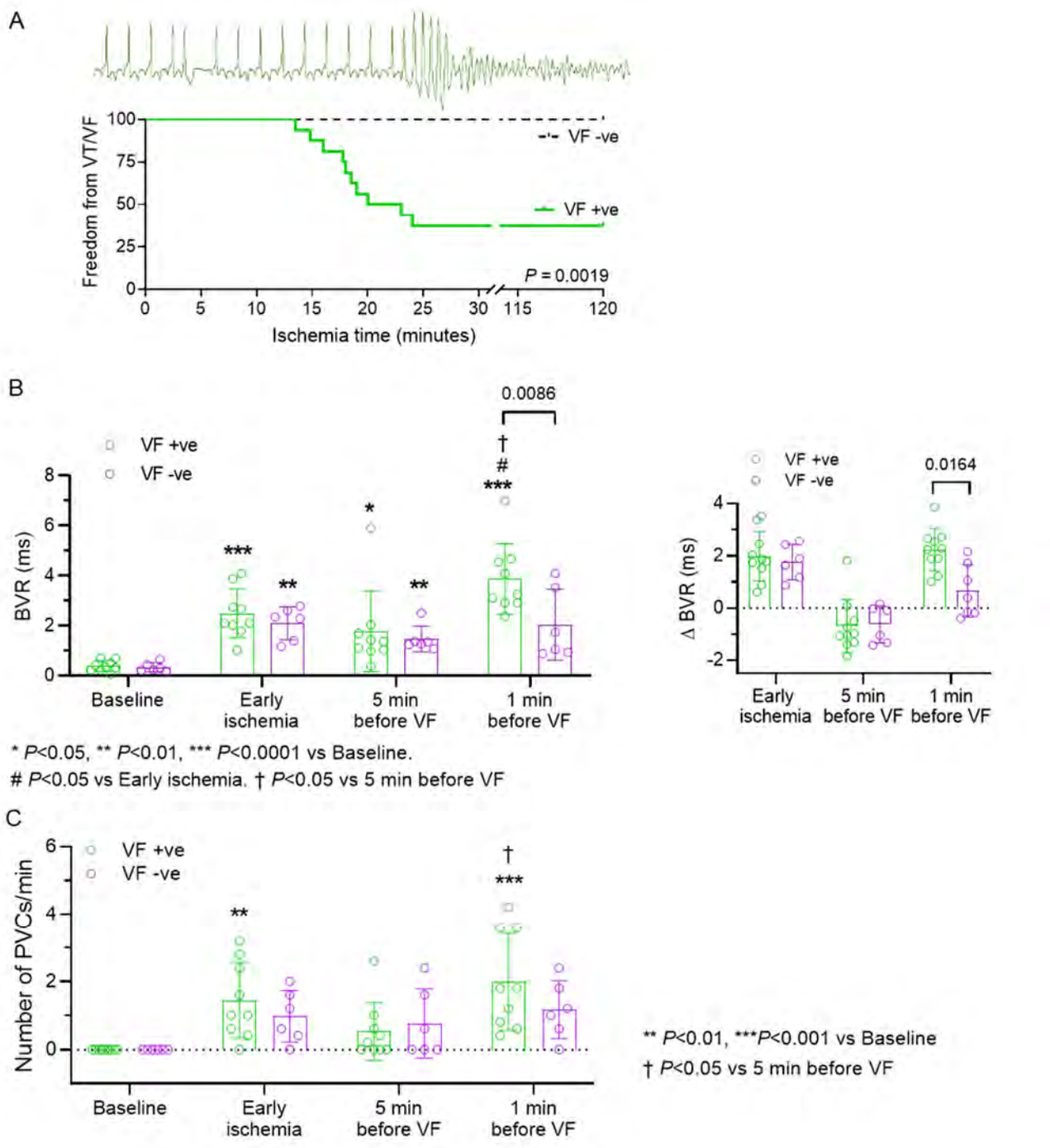

Figure 6. BVR increases further prior to spontaneous ventricular fibrillation (VF) during ischemia.

A, A typical example of spontaneous onset ventricular fibrillation during AMI (top), and Kaplan–Meier plots of freedom from VT/VF during AMI. Log-rank test.

B, Left, summary data of temporal BVR changes during AMI in relation to the occurrence of VF and matched time-points (by duration of ischemia) in 6 sex- and weight-matched animals without VF. Right, summary data of the change in BVR from (left). N = 10 VF+ve and 6 VF-ve. Multilevel

mixed-effects linear model with Bonferroni correction.
C, Summary data of the incidence of premature ventricular complexes (PVCs) during AMI. N = 10 VF+ve and 6 VF-ve. Multilevel mixed-effects linear model with Bonferroni correction.

The electrocardiographic and clinical parameters of severity of injury during AMI comparing VF+ve and VF-ve animals are presented in table 2. The maximum frequency of PVCs was higher in VF+ve animals 2.5 ± 1.0/minute vs VF-ve: 1.4 ± 0.6/minute, P = 0.025) and serum troponin levels tended to be greater (35.8 ± 14.2 µg/L vs VF-ve: 21.3 ± 9.9 µg/L, P = 0.0780). However, other parameters including heart rate, QT interval, ∆QT and QT dispersion were not greater in VF+ve animals, suggesting the extent or severity of injury may contribute to arrhythmogenesis.

Table 2. Electrocardiographic and AMI injury characteristics of VF+ve and VF-ve animals.

	VF+ve (N_{pigs} = 10)	**VF-ve (N_{pigs} = 6)**	***P* value**
Serum Troponin (µg/L)	35.87 ± 14.21	21.27 ± 9.857	0.0708
Infarct size (% LV mass)	20.40 ± 4.498	17.74 ± 3.936	0.1893
ST-segment deviation (mm)	5.230 ± 1.978	3.793 ± 1.226	0.1102
Heart rate (bpm)	89.22 ± 20.91	98.41 ± 24.49	0.4608
QT (ms)	458.8 ± 137.9	457.5 ± 89.85	0.9845
QT dispersion (ms)	129.9 ± 109.0	161.3 ± 66.84	0.5420
Max PVC frequency (PVCs/min)	2.520 ± 1.025	1.367 ± 0.5715	0.0250

Myocardial infarction results in sustained BVR elevation

Finally, we investigated the long-term impact of MI on repolarization lability by assessing ECG BVR in lead II or V4 as appropriate. Figure 7A illustrates the extent of infarction 1-month after AMI, showing a 19.0% LV infarct, illustrated by a mid-ventricular slice of the cMRI of an MI animal. BVR correlated with the infarct size (R^2 = 0.69, P = 0.006). Serum CK increases during ischemia but retuned to baseline values at 1-month after AMI (11116.45 ± 5256.56 U/L, vs Baseline: 1074.0 ± 486.10 U/L, vs 1-month: 1634.45 ± 1122.68 U/L, P < 0.0001) confirming absence of ongoing ischemia at this time-point (figure 7B). 1-month after AMI, BVR under anesthesia was elevated in MI animals compared to sham (1.43 ± 0.50ms, vs sham: 0.57 ± 0.30ms, P = 0.009) (Figure 7C). BVR in MI animals was lower after 1-month than immediately post AMI (AMI: 2.03 ± 0.86ms vs 1-month: 1.47 ± 0.57ms, *P* = 0.013), but did not normalize (Baseline: 0.40 ± 0.20ms vs 1-month: 1.47 ± 0.57ms, *P* = 0.001). In addition, the effective refractory period (ERP), the shortest first-extrasystole (S2) coupling interval at the 400 ms drive

train that did not capture the ventricle was longer in MI animals (215 ± 30ms vs Sham 160 ± 10ms, P = 0.009). This suggests an altered repolarization reserve and excitability.

We further tested the hypothesis that BVR could be used for the prediction of arrhythmia vulnerability, using PES to induce VT/VF and quantified the ease-of-induction (figure 7D). In all MI animals, VT/VF could be induced while only 1 in 6 shams was inducible (Supplemental figure S3). The inducibility of arrhythmia correlated with the infarct size (R^2 = 0.71, *P* = 0.086) and the magnitude of baseline BVR after infarction (R^2 = 0.67, P =0.022).

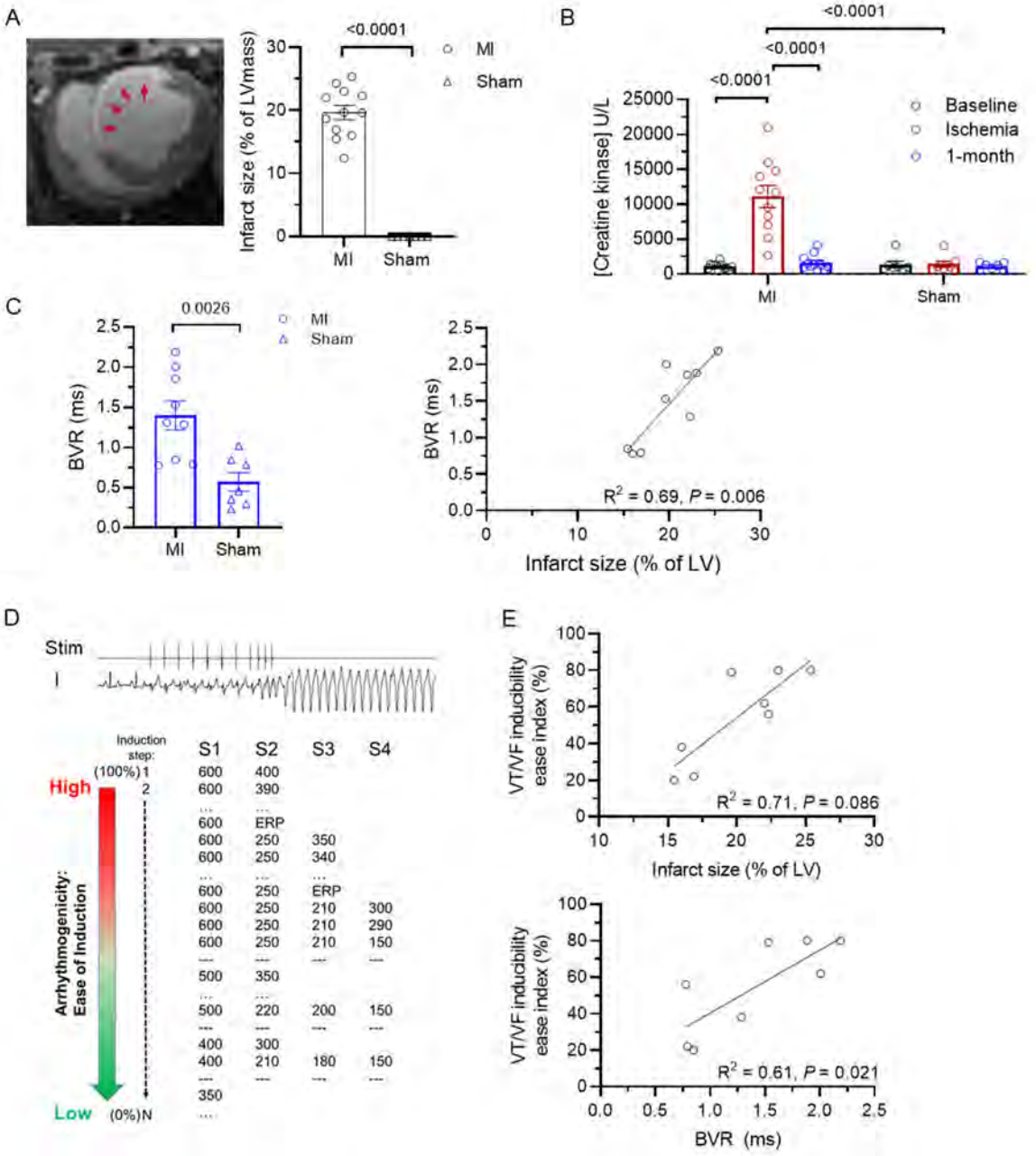

Figure 7. BVR is elevated and associated with arrhythmia vulnerability in chronic MI.
A, Left, example of mid-ventricular short axis cMRI indicating 19.0% infarction (red arrows) after 1-month and right, summary data of infarct size, N = 12 MI and 7 Sham. Two tailed t-test.
B, Serum creatinine kinase concentration at baseline, ischemia and after 1 month. Mixed-effects model ANOVA with Bonferroni posttest.
C, Left, summary data of BVR after 1-month in MI (N = 9) and Sham (N = 7), 2 tailed t-test. Right, Correlation between infarct size and BVR. N = 9 MI. Linear regression analysis.
D, Illustration of programmed stimulation protocol to induce VT/VF (top) and the algorithm used to assess inducibility index based on aggressiveness of stimulation protocol (bottom).
E, Top, Correlation between infarct size and VT/VF inducibility and bottom, correlation between BVR and VT/VF inducibility. N = 8 MI. Linear regression analysis.

Discussion

This study evaluated BVR during AMI in a pre-clinical animal model. The main findings were that BVR is increased on the surface ECG during AMI and surges in the minute preceding VT/VF. In the chronic phase, BVR remains elevated compared to normal hearts and correlates with arrhythmogenicity. In addition, from a methodologically perspective, we showed that BVR assessment is highly influenced by the ECG sampling rate and a sampling frequency of at least 1kHz is desired for BVR assessment.

Spatial and temporal repolarization variability during AMI

In the acute setting of ischemia, repolarization liability has been demonstrated experimentally, non-invasively by ECG analysis of BVR (14), invasively by assessment of BVR (17, 18) and TWA (15, 22). Our findings are congruent with and extend these observations. We demonstrated that BVR increased within the first 5 minutes of AMI in a spatial pattern congruent with ST deviation. Significant ST deviation was observed in II, aVF, and precordial leads V1-6, a pattern reflecting the extensive anteroseptal ischemia (23, 24). The pattern of BVR increase in the 12 leads had remarkable similarity to ST patterns, and a strong correlation to injury by cumulative scores (25). These findings are comparable to patterns of TWA that were unique to regional injury reflecting the regional repolarization vectors (15). However, we did not observe significant changes in QT duration during AMI, although QT dispersion and BVR were increased. Together, these findings suggest an interplay between temporal- and spatial liability in AMI.

The electrophysiological changes producing ST-segment changes during AMI are attributable to altered cellular electrophysiology, and also underlie repolarization lability (26, 27). Potassium currents including K_{ATP} and voltage gated K-currents are modulated by increased extracellular potassium [K_o], ATP depletion, pH changes and ROS during ischemia. Calcium handling is also compromised manifesting characteristically as calcium alternans due to SERCA dysfunction and Calcium-handling proteins. In addition, cell-to-cell uncoupling during AMI contributes to conduction abnormalities in local or regional differences and dispersion of repolarization (28).

Temporal changes in BVR herald imminent SCD during AMI

Arrhythmias occur frequently during AMI and a significant proportion are severe leading to SCD (2), however, factors predicting onset of VF in AMI continue to be investigated (4). In our study,

VF was observed frequently at approximately 20 minutes after onset of the AMI. Prior reports described two distinct arrhythmia phases in AMI: 1a (<10mins) and 1b (15-30mins) (7, 28). The change in BVR in our study exhibited a similar pattern with a distinct increase in the early AMI phase. BVR increased significantly after 5 minutes of AMI as did the number of PVCs. In animals that developed VF, the increased BVR during AMI surged 1-minute prior to VF, and more frequent PVCs were observed in this period. These findings suggest a distinct surge in BVR heralds arrhythmia during AMI, and that there may be a threshold of repolarization lability required for the occurrence of VF (9). Furthermore, we observed PVCs as the triggering event in our model. The coupling interval of PVCs initiating VT/VF tended to be shorter than those during early ischemia. These findings support recent reports of acute BVR increase preceding nsVT in ICD patients on Holter monitoring (12, 13). However, contrasting findings have been reported by Sachdev et al., (29) who did not observe QT variability preceding arrhythmias in AMI patients admitted to CCU. An important difference that may explain this difference is that QT variation was sampled at time intervals of 1 hour, which could have made it possible to miss an acute temporary increase in repolarization lability.

Together, these data suggest an interplay between triggers and substrate in line with classical arrhythmia framework and the R-from-T phenomenon (30, 31).

Increased BVR in chronic MI and arrhythmia vulnerability

Temporal variability of repolarization has been extensively studied in chronic cardiac remodeling including the CAVB dog model (10, 32), the pig MI model (14, 33), and validated in clinical reports (34). In this model BVR is increased 1-month post-AMI and correlated with infarct size, suggesting that the degree of remodeling may contribute to repolarization lability. An increased BVR reflects a reduced repolarization reserve (27) consistent with reduced repolarizing potassium currents and abnormal calcium handling in myocytes form chronic infarcted hearts (33, 35).

We observed a correlation between infarct size and arrhythmia inducibility in agreement with previous reports and likely still an important factor (21, 36). Recent studies have taken this further and advocate a role fordetailed analysis of the infarct to be considered in risk assessment, but are yet to be incorporated into clinical practice guidelines (37, 38). We utilized a clinical PES protocol as a surrogate for arrhythmogenicity. In our model, monomorphic VT, considered to be specific, could be induced all MI animals, but only in one sham instrumented animal. The ERP of MI animals was longer suggesting a reduced excitability and conduction that facilitated conduction block and re-entrant arrhythmias. The finding that VT inducibility was correlated to BVR suggests that repolarization lability may be a factor in the arrhythmia mechanism.

Sampling frequency and methodological considerations for BVR assessment

QT BVR on the ECG has been described to be in the magnitude of <5ms, reflecting subtle QT variations sensitive to error (39, 40). To accurately detect millisecond variations in the QT, a signal with a sampling frequency in the order of half the measured parameter, is required in line with the Nyquist–Shannon sampling theorem (41). In the current study, BVR was significantly higher with a larger spread when analyzed on a 200 Hz sampled ECG signal compared to that at 1 kHz. Downsampling the 1 kHz signal to 200 Hz reproduced the higher BVR observed in the 200 Hz signal supporting the importance of sampling rate. These findings are in line with earlier work on STV, suggesting that the assessment of BVR is influenced by a low sampling frequency

(42). Although it should be noted that, despite the potential sampling error at lower sampling rates, the assessment of ECG parameters has reasonable accuracy as observed in other assessments including HRV (43).

Methodological aspects of QT analysis may also impact BVR assessment. We employed an semi-automated fiducial segment averaging with tangent method for manual correction where necessary (20). Our prior assessment showed that this was the most consistently accurate method for QT detection (44). A recent study proposed a novel method of T-wave end detection using an area-under-the-curve method that remains to be rigorously validated and reproduced (45). These concerns highlight the need for standardized technical practices in addition to the guidelines on the methodological assessment that must be considered with the increasing use of automated QT analysis and non-invasive assessment of repolarization in clinical practice.

Clinical implications

The key finding of this study is that BVR increases during AMI and surges prior to arrhythmia onset. This suggests that differences in BVR should be examined in patients who do or not develop ventricular arrhythmia during acute coronary syndromes and that monitoring BVR may be useful in the acute setting, for monitoring the risk of VF after AMI in the critical or coronary care unit settings. Beyond this, monitoring BVR may have value in implantable cardiac devices or wearables. Recently, the intracardiac electrogram was used to calculate BVR and detect and prevent imminent arrhythmia (46). Our data derived from a clinically relevant setting of AMI support the role of BVR monitoring even in the setting of dynamic T-wave changes, although further validation in humans is needed.

Arrhythmia and SCD risk stratification after MI remain challenging, with LVEF as the most important predictor of in the clinical setting. Electrophysiological parameters including inducible VT and spontaneous nsVT occurrence are important and considered in risk stratification. The correlation between BVR and inducibility suggest that BVR may also be a non-invasive and useful surrogate for this parameter.

Limitations

Aspects of the AMI model employed in this study should be considered when interpreting the results. The use of general anesthesia may impact on arrhythmogenesis as anesthetic drugs are known to influence arrhythmias. Moreover, all animals were pre-medicated with amiodarone for 3 days to avoid excess mortality, the individual effect of amiodarone may be a confounder. In addition, AMI was induced in young healthy pigs, which is quite different from the clinical phenotype of IHD that occurs usually in older persons with comorbidities including obesity, diabetes and hypertension. In addition, modulatory factors including sympathetic stimulation, mechanoelectrical feedback and local electrolyte imbalance may contribute to initiation of VT/VF, but were not investigated in this study.

The analysis of BVR during AMI was limited to defined timepoints. In an ideal situation, a continuous record of the sequential and dynamic changes in BVR would provide a complete picture. This should be addressed by future work on adaptive algorithms and machine-learning to allow continuous monitoring of the QT and BVR.

The pattern of BVR dispersion observed in the 12 lead ECG was not validated with direct measurements of local and regional repolarization. Future work should evaluate the interplay

between spatial and temporal variability in AMI with the use of mapping tools that were beyond the scope of this study.

Conclusion

AMI induced temporal and spatial repolarization variability which was consistent with the extent and severity of injury. There was a distinct surge in BVR prior to arrhythmia onset, which identifies BVR as a possible useful parameter for monitoring and early warning systems. In the chronic MI setting, BVR remained elevated increased reflecting a reduced repolarization reserve, which correlated to arrhythmia vulnerability suggesting BVR may also be useful in future arrhythmia risk stratification. Finally, the assessment of BVR was influenced by sampling frequency and QT detection methods, which highlights a need for consensus and standardization of automated QT detection and analysis for reproducible data.

Acknowledgements

The authors thank Patricia Holemans and Roxane Menten for their excellent technical assistance.

Grants

MA is supported as supported as doctoral researcher by the Fund for Scientific Research Flanders (FWO). RW and PC are supported by a KU Leuven grant BOF-C1 (C14/18/079). RW is supported as senior clinical researcher by the FWO. This research received funding from the Flemish Government (AI Research Program). to SH and JM. CV acknowledges the financial support of the European Space Agency (ESA), BELSPO - NEPTUNE.

Disclosures

RW reports research funding from Abbott, Biotronik, Boston Scientific, Medtronic; speakers and consultancy fees from Medtronic, Boston Scientific, Biotronik, Abbott.

References

1. **Adabag AS, Luepker RV, Roger VL, and Gersh BJ**. Sudden cardiac death: epidemiology and risk factors. *Nature Reviews Cardiology* 7: 216-225, 2010.

2. **Yannopoulos D, Bartos JA, Aufderheide TP, Callaway CW, Deo R, Garcia S, Halperin HR, Kern KB, Kudenchuk PJ, Neumar RW, and Raveendran G**. The Evolving Role of the Cardiac Catheterization Laboratory in the Management of Patients With Out-of-Hospital Cardiac Arrest: A Scientific Statement From the American Heart Association. *Circulation* 139: 2019.

3. **Naghavi M, Libby P, Falk E, Casscells SW, Litovsky S, Rumberger J, Badimon JJ, Stefanadis C, Moreno P, Pasterkamp G, Fayad Z, Stone PH, Waxman S, Raggi P, Madjid M, Zarrabi A, Burke A, Yuan C, Fitzgerald PJ, Siscovick DS, De Korte CL, Aikawa M, Juhani Airaksinen KE, Assmann G, Becker CR, Chesebro JH, Farb A, Galis ZS, Jackson C, Jang I-K, Koenig W, Lodder RA, March K, Demirovic J, Navab M, Priori SG, Rekhter MD, Bahr R, Grundy SM, Mehran R, Colombo A, Boerwinkle E, Ballantyne C, Insull W, Schwartz RS, Vogel R, Serruys PW, Hansson GK, Faxon DP, Kaul S, Drexler H, Greenland P, Muller JE, Virmani R, Ridker PM, Zipes DP, Shah PK, and Willerson JT**. From Vulnerable Plaque to Vulnerable Patient. *Circulation* 108: 1664-1672, 2003.

4. **Gheeraert PJ, De Buyzere ML, Taeymans YM, Gillebert TC, Henriques JPS, De Backer G, and De Bacquer D**. Risk factors for primary ventricular fibrillation during acute myocardial infarction: a systematic review and meta-analysis. *European Heart Journal* 27: 2499-2510, 2006.

5. **Naghavi M, Libby P, Falk E, Casscells SW, Litovsky S, Rumberger J, Badimon JJ, Stefanadis C, Moreno P, Pasterkamp G, Fayad Z, Stone PH, Waxman S, Raggi P, Madjid M, Zarrabi A, Burke A, Yuan C, Fitzgerald PJ, Siscovick DS, de Korte CL, Aikawa M, Airaksinen KE, Assmann G, Becker CR, Chesebro JH, Farb A, Galis ZS, Jackson C, Jang IK, Koenig W, Lodder RA, March K, Demirovic J, Navab M, Priori SG, Rekhter MD, Bahr R, Grundy SM, Mehran R, Colombo A, Boerwinkle E, Ballantyne C, Insull W, Jr., Schwartz RS, Vogel R, Serruys PW, Hansson GK, Faxon DP, Kaul S, Drexler H, Greenland P, Muller JE, Virmani R, Ridker PM, Zipes DP, Shah PK, and Willerson JT**. From vulnerable plaque to vulnerable patient: a call for new definitions and risk assessment strategies: Part II. *Circulation* 108: 1772-1778, 2003.

6. **Wellens HJJ, Schwartz PJ, Lindemans FW, Buxton AE, Goldberger JJ, Hohnloser SH, Huikuri HV, Kaab S, La Rovere MT, Malik M, Myerburg RJ, Simoons ML, Swedberg K, Tijssen J, Voors AA, and Wilde AA**. Risk stratification for sudden cardiac death: current status and challenges for the future. *European Heart Journal* 35: 1642-1651, 2014.

7. **Janse MJ, and Wit A**. Electrophysiological mechanisms of ventricular arrhythmias resulting from myocardial ischemia and infarction. *Physiol Rev* 69: 1049-1169, 1989.

8. **Sattler SM, Skibsbye L, Linz D, Lubberding AF, Tfelt-Hansen J, and Jespersen T**. Ventricular Arrhythmias in First Acute Myocardial Infarction: Epidemiology, Mechanisms, and Interventions in Large Animal Models. *Front Cardiovasc Med* 6: 158, 2019.

9. **Pandit SV, and Jalife J**. Rotors and the Dynamics of Cardiac Fibrillation. *Circulation Research* 112: 849-862, 2013.

10. **Thomsen MB, Verduyn SC, Stengl M, Beekman JDM, De Pater G, Van Opstal J, Volders PGA, and Vos MA**. Increased Short-Term Variability of Repolarization Predicts d - Sotalol–Induced Torsades de Pointes in Dogs. *Circulation* 110: 2453-2459, 2004.

11. **Thomsen MB, Volders PGA, Beekman JDM, Matz J, and Vos MA**. Beat-to-Beat Variability of Repolarization Determines Proarrhythmic Outcome in Dogs Susceptible to Drug-Induced Torsades de Pointes. *Journal of the American College of Cardiology* 48: 1268-1276, 2006.

12. **Smoczyńska A, Loen V, Sprenkeler DJ, Tuinenburg AE, Ritsema Van Eck HJ, Malik M, Schmidt G, Meine M, and Vos MA**. Short-Term Variability of the QT Interval Can be Used for the Prediction of Imminent Ventricular Arrhythmias in Patients With Primary Prophylactic Implantable Cardioverter Defibrillators. *Journal of the American Heart Association* 9: 2020.

13. **Amoni M, Ingelaere S, Moeyersons J, Vandenberk B, Claus P, Lemmens R, Van Huffel S, Sipido K, Varon C, and Willems R**. Temporal Changes in Beat-to-Beat Variability of Repolarization Predict Imminent Nonsustained Ventricular Tachycardia in Patients With Ischemic and Nonischemic Dilated Cardiomyopathy. *Journal of the American Heart Association* 2022.

14. **Flore V, Claus P, Antoons G, Oosterhoff P, Holemans P, Vos MA, Sipido KR, and Willems R**. Microvolt T-wave alternans and beat-to-beat variability of repolarization during early postischemic remodeling in a pig heart. *Heart Rhythm* 8: 1050-1057, 2011.

15. **Martinez JP, Olmos S, Wagner G, and Laguna P**. Characterization of repolarization alternans during ischemia: time-course and spatial analysis. *IEEE Trans Biomed Eng* 53: 701-711, 2006.

16. **Al-Zaiti SS, Callaway CW, Kozik TM, Carey MG, and Pelter MM**. Clinical Utility of Ventricular Repolarization Dispersion for Real-Time Detection of Non-ST Elevation Myocardial Infarction in Emergency Departments. *J Am Heart Assoc* 4: 2015.

17. **Al-Zaiti SS, Alrawashdeh M, Martin-Gill C, Callaway C, Mortara D, and Nemec J**. Evaluation of beat-to-beat ventricular repolarization lability from standard 12-lead ECG during acute myocardial ischemia. *Journal of Electrocardiology* 50: 717-724, 2017.

18. **Lubberding AF, Sattler SM, Grunnet M, Sørensen US, Tfelt-Hansen J, and Jespersen T**. Arrhythmia development during inhibition of small-conductance calcium-activated potassium channels in acute myocardial infarction in a porcine model. *EP Europace* 21: 1584-1593, 2019.

19. **Amoni M, Claus P, Dries E, Nagaraju C, De Buck S, Vandenberk B, Ingelaere S, Vermoortele D, Roderick HL, Sipido KR, and Willems R**. Discrete sites of frequent premature ventricular complexes cluster within the infarct border zone and coincide with high frequency of delayed afterdepolarizations under adrenergic stimulation. *Heart Rhythm* 2021.

20. **Moeyersons J, Amoni M, Van Huffel S, Willems R, and Varon C**. R-DECO: an open-source Matlab based graphical user interface for the detection and correction of R-peaks. *PeerJ Computer Science* 5: e226, 2019.

21. **León DG, López-Yunta M, Alfonso-Almazán JM, Marina-Breysse M, Quintanilla JG, Sánchez-González J, Galán-Arriola C, Castro-Núñez F, González-Ferrer JJ, Ibáñez B, Pérez-Villacastín J, Pérez-Castellano N, Fuster V, Jalife J, Vázquez M, Aguado-Sierra J, and Filgueiras-Rama D**. Three-dimensional cardiac fibre disorganization as a novel parameter for ventricular arrhythmia stratification after myocardial infarction. *EP Europace* 21: 822-832, 2019.

22. **Muñoz LM, Gelzer ARM, Fenton FH, Qian W, Lin W, Gilmour RF, and Otani NF**. Discordant Alternans as a Mechanism for Initiation of Ventricular Fibrillation In Vitro. *Journal of the American Heart Association* 7: 2018.

23. **Lubberding AF, Sattler SM, Flethøj M, Tfelt-Hansen J, and Jespersen T**. Comparison of hemodynamics, cardiac electrophysiology, and ventricular arrhythmia in an open- and a closed-chest porcine model of acute myocardial infarction. *American Journal of Physiology-Heart and Circulatory Physiology* 318: H391-H400, 2020.

24. **Lukacs E, Magyari B, Toth L, Petrasi Z, Repa I, Koller A, and Horvath I**. Overview of large animal myocardial infarction models (review). *Acta Physiol Hung* 99: 365-381, 2012.

25. **Desmet WJ, Mesotten LV, Maes AF, Heidbuchel HP, Mortelmans LA, and Van de Werf FJ**. Relation between different methods for analysing ST segment deviation and infarct size as assessed by positron emission tomography. *Heart* 90: 887-892, 2004.

26. **Di Diego JM, and Antzelevitch C**. Acute myocardial ischemia: cellular mechanisms underlying ST segment elevation. *J Electrocardiol* 47: 486-490, 2014.

27. **Varro A, and Baczko I**. Cardiac ventricular repolarization reserve: a principle for understanding drug-related proarrhythmic risk. *Br J Pharmacol* 164: 14-36, 2011.

28. **Smith WTt, Fleet WF, Johnson TA, Engle CL, and Cascio WE**. The Ib phase of ventricular arrhythmias in ischemic in situ porcine heart is related to changes in cell-to-cell electrical coupling. Experimental Cardiology Group, University of North Carolina. *Circulation* 92: 3051-3060, 1995.

29. **Sachdev M, Fetics BJ, Lai S, Dalal D, Insel J, and Berger RD**. Failure in short-term prediction of ventricular tachycardia and ventricular fibrillation from continuous electrocardiogram in intensive care unit patients. *J Electrocardiol* 43: 400-407, 2010.

30. **Liu MB, Vandersickel N, Panfilov AV, and Qu Z**. R-From-T as a Common Mechanism of Arrhythmia Initiation in Long QT Syndromes. *Circulation: Arrhythmia and Electrophysiology* 12: 2019.

31. **Amoni M, Dries E, Ingelaere S, Vermoortele D, Roderick HL, Claus P, Willems R, and Sipido KR**. Ventricular Arrhythmias in Ischemic Cardiomyopathy-New Avenues for Mechanism-Guided Treatment. *Cells* 10: 2021.

32. **Thomsen M, Oros A, Schoenmakers M, Vanopstal J, Maas J, Beekman J, and Vos M**. Proarrhythmic electrical remodelling is associated with increased beat-to-beat variability of repolarisation. *Cardiovascular Research* 73: 521-530, 2007.

33. **Dries E, Amoni M, Vandenberk B, Johnson DM, Gilbert G, Nagaraju CK, Puertas RD, Abdesselem M, Santiago DJ, Roderick HL, Claus P, Willems R, and Sipido KR**. Altered adrenergic response in myocytes bordering a chronic myocardial infarction underlies in vivo triggered activity and repolarization instability. *The Journal of Physiology* 598: 2875-2895, 2020.

34. **Berger RD, Kasper EK, Baughman KL, Marban E, Calkins H, and Tomaselli GF**. Beat-to-beat QT interval variability: novel evidence for repolarization lability in ischemic and nonischemic dilated cardiomyopathy. *Circulation* 96: 1557-1565, 1997.

35. **Hegyi B, Bossuyt J, Griffiths LG, Shimkunas R, Coulibaly Z, Jian Z, Grimsrud KN, Sondergaard CS, Ginsburg KS, Chiamvimonvat N, Belardinelli L, Varró A, Papp JG, Pollesello P, Levijoki J, Izu LT, Boyd WD, Bányász T, Bers DM, and Chen-Izu Y**. Complex

electrophysiological remodeling in postinfarction ischemic heart failure. *Proceedings of the National Academy of Sciences* 115: E3036-E3044, 2018.

36. **Pride YB, Appelbaum E, Lord EE, Sloan S, Cannon CP, Sabatine MS, Gibson CM, and Group TS**. Relation between myocardial infarct size and ventricular tachyarrhythmia among patients with preserved left ventricular ejection fraction following fibrinolytic therapy for ST-segment elevation myocardial infarction. *Am J Cardiol* 104: 475-479, 2009.

37. **Roes SD, Borleffs CJW, Van Der Geest RJ, Westenberg JJM, Marsan NA, Kaandorp TAM, Reiber JHC, Zeppenfeld K, Lamb HJ, De Roos A, Schalij MJ, and Bax JJ**. Infarct Tissue Heterogeneity Assessed With Contrast-Enhanced MRI Predicts Spontaneous Ventricular Arrhythmia in Patients With Ischemic Cardiomyopathy and Implantable Cardioverter-Defibrillator. *Circulation: Cardiovascular Imaging* 2: 183-190, 2009.

38. **Haghbayan H, Lougheed N, Deva DP, Chan KKW, Lima JAC, and Yan AT**. Peri-Infarct Quantification by Cardiac Magnetic Resonance to Predict Outcomes in Ischemic Cardiomyopathy. *Circulation: Cardiovascular Imaging* 12: 2019.

39. **Thomsen MB, Truin M, Opstal JM, Beekman JDM, Volders PGA, Stengl M, and Vos MA**. Sudden cardiac death in dogs with remodeled hearts is associated with larger beat?to?beat variability of repolarization. *Basic Research in Cardiology* 100: 279-287, 2005.

40. **Berger RD, Kasper EK, Baughman KL, Marban E, Calkins H, and Tomaselli GF**. Beat-to-Beat QT Interval Variability. *Circulation* 96: 1557-1565, 1997.

41. **Luke HD**. The origins of the sampling theorem. *IEEE Communications Magazine* 37: 106-108, 1999.

42. **Oosterhoff P, Thomsen MB, Maas JN, Atteveld NJM, Beekman JDM, Van Rijen HVM, Van Der Heyden MAG, and Vos MA**. High-Rate Pacing Reduces Variability of Repolarization and Prevents Repolarization-Dependent Arrhythmias in Dogs With Chronic AV Block. *Journal of Cardiovascular Electrophysiology* 21: 1384-1391, 2010.

43. **Mahdiani S, Jeyhani V, Peltokangas M, and Vehkaoja A**. Is 50 Hz high enough ECG sampling frequency for accurate HRV analysis? 5948-5951, 2015.

44. **Moeyersons J, Goovaerts G, Huijghebaert S, Vandenberk B, Willems R, and Van Huffel S**. Automated T Wave End Detection Methods - Comparison of Four different methods of T wave end detection. In: *10th International Joint Conference on Biomedical Engineering Systems and Technologies*. Porto, Portugal: Biosignals, 2017, p. 92-98.

45. **Smoczynska A, Sprenkeler DJ, Aranda A, Beekman JDM, Bossu A, Dunnink A, Wijers SC, Stegemann B, Meine M, and Vos MA**. Evaluation of a Fully Automatic Measurement of Short-Term Variability of Repolarization on Intracardiac Electrograms in the Chronic Atrioventricular Block Dog. *Front Physiol* 11: 1005, 2020.

46. **Smoczyńska A, Loen V, Aranda A, Beekman HDM, Meine M, and Vos MA**. High-rate pacing guided by short-term variability of repolarization prevents imminent ventricular arrhythmias automatically by an implantable cardioverter-defibrillator in the chronic atrioventricular block dog model. *Heart Rhythm* 17: 2078-2085, 2020.

Online supplement…

Supplemental data

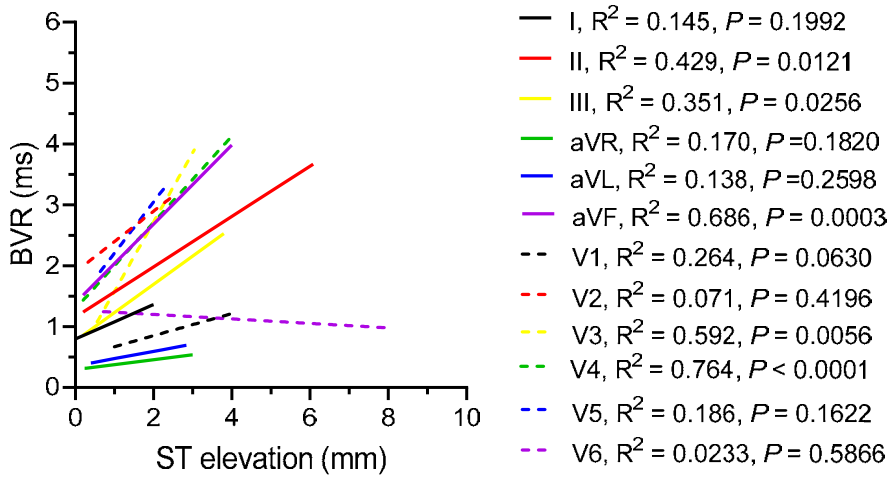

Supplemental figure S1. Correlation between ST segment deviation and BVR
Correlation between ST deviation and BVR in each lead. N = 16 MI. Linear regression analysis

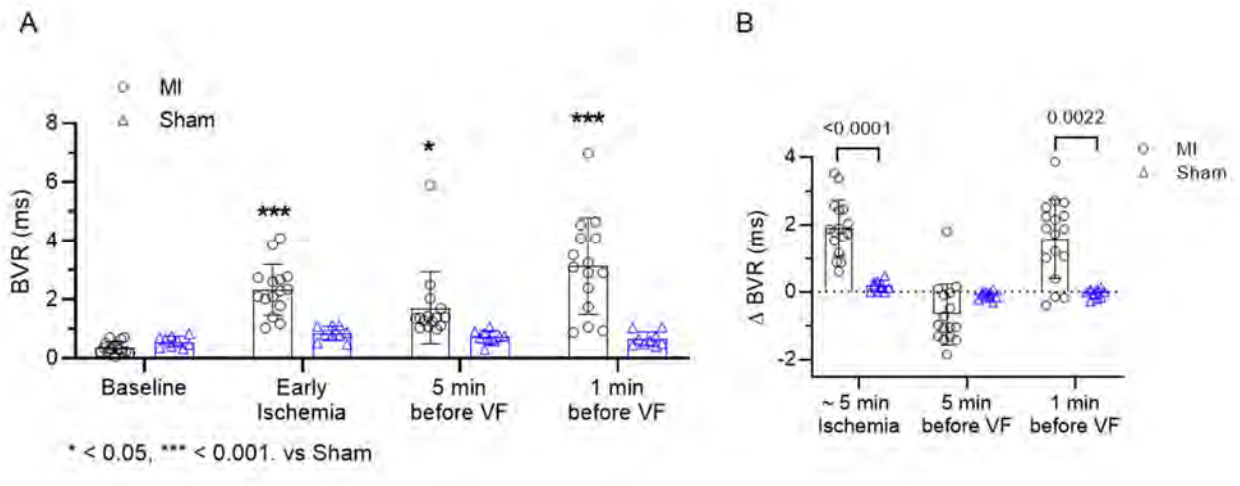

Supplemental figure S2. Temporal BVR does not change in sham animals at matched VF timepoints
A, Summary data of temporal maximal BVR changes during ischemia in relation to the occurrence of VF and matched time-points in sham animals.
B, Summary data of the slope of BVR change from (left). N = 16 MI and 8 Sham. Mixed-effects model ANOVA with Bonferroni post-test.

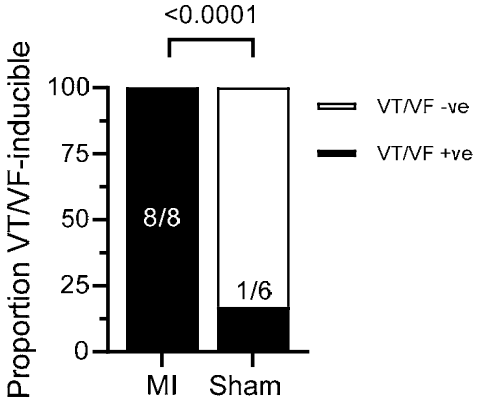

Supplemental figure 3. Inducibility of ventricular tachycardia (VT) or fibrillation (VF) as surrogate for arrhythmia vulnerability.
Proportion of VT/VF inducible pigs in MI and sham. MI, N = 8 and Sham N = 6. Chi-square with Fisher's exact.

CHAPTER 7: Temporal changes in BVR can predict imminent arrhythmias in high risk patients

Published as:

Matthew Amoni, Sebastian Ingelaere, Jonathan Moeyersons, Bert Vandenberk, Piet Claus, Robin Lemmens, Sabine Van Huffel, Karin Sipido, Carolina Varon, Rik Willems. “Temporal Changes in Beat-to-Beat Variability of Repolarization Predict Imminent Nonsustained Ventricular Tachycardia in Patients with Ischemic and Nonischemic Dilated Cardiomyopathy.” J Am Heart Assoc. 2022 Jul 5;11(13): e024294. doi: 10.1161/JAHA.121.024294. Epub 2022 Jun 22.

ABSTRACT

Background: An increase in beat-to-beat variability of repolarization (BVR) predicts arrhythmia onset in experimental models, but its clinical translation is not well established. We investigated the temporal changes in BVR prior to non-sustained ventricular tachycardia (nsVT) in implantable cardioverter defibrillator (ICD) patients.

Methods and Results: Patients with nsVT on 24-hour Holter prior to ICD implantation for ischemic cardiomyopathy (ICM+nsVT, n = 43) or dilated cardiomyopathy (DCM+nsVT, n = 37), matched ICD candidates without nsVT (ICM-nsVT, n = 29 and DCM-nsVT, n = 26) and non-ICD patients without structural heart disease, SHD (n = 50) were studied. Digital Holter recordings from these patients were analyzed using a modified fiducial segment averaging technique to detect the QT interval. The nsVT episodes were semi-automatically identified and QT-BVR was assessed 1-, 5- and 30- minutes prior to nsVT, and at rest (at 3:00am). Resting BVR, was higher in ICD patients compared to controls without SHD. In ICD patients with nsVT, BVR increased significantly 1-minute pre-nsVT in ICM (2.21 ± 0.59ms, vs 5-minutes pre-nsVT: 1.78 ± 0.50ms, $P<0.001$) and DCM (2.09 ± 0.57ms, vs 5-minutes pre-nsVT: 1.58 ± 0.51ms, $P<0.001$), but not in patients without nsVT. In multivariable Cox regression analysis, pre-nsVT BVR was a significant predictor for appropriate therapy during follow-up.

Conclusion: Baseline BVR is elevated and temporal changes in BVR predict imminent nsVT events in ICD patients independent of underlying etiology. Real time BVR monitoring could be used to predict impending ventricular arrhythmia and allow preventive therapy to be incorporated into ICDs.

Keywords: non-sustained ventricular tachycardia, beat-to-beat variability of repolarization, Holter, arrythmia prediction

Clinical perspective

- Beat-to-beat variability of repolarization (BVR) increase predicts imminent arrhythmias in experimental models. Its usefulness in clinical practice of impending arrhythmia risk prediction needs to be established.
- BVR is increased in patients with structural heart disease selected for implantable cardioverter defibrillator (ICD) implantation compared to patients without structural heart disease.
- BVR reproducibly increases in the minute preceding non-sustained ventricular tachycardia in ICD candidates regardless of underlying cardiomyopathy (ischemic and non-ischemic).
- The magnitude of BVR in the minute preceding arrhythmia is a predictor of future appropriate ICD shocks as a surrogate for SCD risk.

Non-standard Abbreviations and Acronyms

SCD	Sudden cardiac death
nsVT	Non-sustained ventricular tachycardia
BVR	Beat-to-beat variability of repolarization
STV	Short-term variability
ICM	Ischemic cardiomyopathy
DCM	Dilated cardiomyopathy
SHD	Structural heart disease
ESUS	Embolic stroke of unknown source
APT	Appropriate ICD therapy
Bpm	Beats per minute
∆ BVR	Delta-BVR (BVR at 1-minute pre-nsVT minus BVR at 5-minutes pre-nsVT)
EU-CERT	European Comparative Effectiveness Research to Assess the Use of Primary Prophylactic Implantable Cardioverter Defibrillators

INTRODUCTION

Sudden cardiac death (SCD) by sustained ventricular tachycardia (VT) and ventricular fibrillation (VF), remains a major mode of death. Patients with advanced heart disease or cardiomyopathy are at a high risk of SCD [1]. Implantable cardioverter defibrillators (ICD) are currently the most effective intervention to prevent SCD in these high-risk patients [2]. ICDs continuously monitor the cardiac rhythm, detect sustained VT or VF rapidly and provide anti-tachycardia pacing or shocks to restore sinus rhythm upon detection.

Identification of patients at increased risk remains challenging as current guidelines utilize clinical assessment with left ventricular ejection fraction (LVEF) as a main factor to identify high risk patients [3]. However, several other parameters have been shown to be powerful tools in risk stratification. Further risk assessment using non-invasive tools and parameters including cardiac imaging (for underlying pathology including fibrosis and infarction), electrocardiogram (ECG) analysis (for conduction abnormalities, fragmentation, repolarization abnormalities among other risk markers) and 24-hour Holter monitoring (to capture rare events such as non-sustained VT (nsVT) or VT/VF) can be used to improve stratification [4].

In high-risk patients, prediction of imminent arrhythmia could have a cardinal role in the management of patients with ICDs by triggering preventive device therapy [5]. Device algorithms incorporating known risk factors for SCD are being implemented in early warning systems that can preventatively manage arrhythmias by monitoring and analyzing cardiac electrical activity [6]. Electrical instability is a hallmark of the substrate that sustains arrhythmia. Thus, measures of labile or heterogeneous repolarization have been proposed for identification of short-term arrhythmia vulnerability [4].

Beat-to-beat variability of repolarization (BVR) or short-term variability (STV) is a measure of temporal dispersion that first showed excellent predictive value in predicting drug-induced Torsades de Pointes (TdP) in experiments using a dog-model of chronic AV block and cardiac hypertrophy [7]. BVR also has been shown to be elevated in cardiomyopathy patients, suggesting its usefulness in identifying long-term high-risk patients [8]. However, evidence supporting its usefulness in predicting imminent events in the clinical setting remains limited and it is unclear if this depends on the etiology of the underlying cardiomyopathy [9].

In this study, we compare the behavior of BVR in patients with an underlying ischemic or non-ischemic cardiomyopathy with and without non-sustained VT and a matched control group of patients without overt cardiovascular disease. We also assess the clinical value of BVR in predicting appropriate ICD therapy during follow-up in our cohort.

METHODS

The data presented in this manuscript are available from the corresponding author upon reasonable request.

Patient population and Study design

This retrospective study, in accordance with the Declaration of Helsinki, was approved by the ethical committee of the University Hospitals of Leuven (S56074). In view of the retrospective

nature of the study the ethical committee waived the necessity of informed consent. All patients who had a first ICD implanted at the University Hospitals of Leuven are included in an electronic registry as described previously [10]. All patients in this registry from 01 January 2008 until 31 December 2018, who had a minimum follow-up of one year were considered for this study. Patients with ischemic (ICM) or dilated non-ischemic (DCM) cardiomyopathy and indication for an ICD in primary or secondary prevention of SCD under current guidelines were screened for inclusion [11]. Only ICD candidates with a pre-procedural Holter, that was digitally available were further considered in the study. ICD candidates who experienced an episode of nsVT (defined as 3 or more consecutive ventricular complexes > 100 bpm) during the 24h Holter monitoring were included as cases divided into two groups according to their underlying cardiomyopathy: ICM+nsVT group 1 and DCM+nsVT group 2 (Figure 1). ICD candidates without nsVT were matched by age and sex to into two control groups: ICM-nsVT group 3 and DCM-nsVT group 4 (Figure 1).

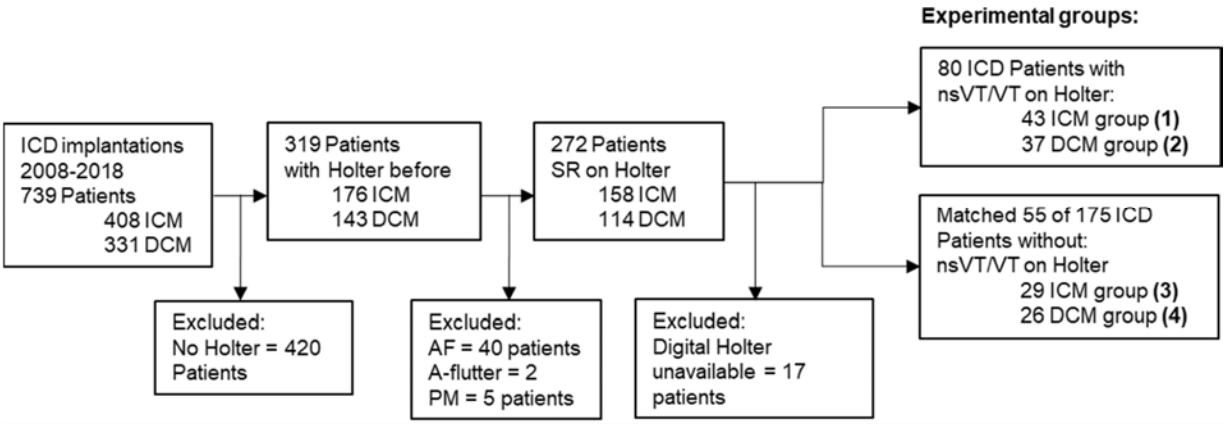

Figure 1. Experimental design.
Study flow chart illustrating patient inclusion and study groups. Ischemic heart disease (IHD) and dilated cardiomyopathy (DCM) admitted for implantable cardiac defibrillator (ICD) implantation were considered. All patients without a prior Holter recording or where the Holter was unavailable, patients with atrial fibrillation (AF) or permanent pacing (PM) were excluded. nsVT – non-sustained ventricular tachycardia, VT – ventricular tachycardia, AF – atrial fibrillation, A-Flutter – atrial flutter, PM – pacemaker device, SHD – structural heart disease, SR – sinus rhythm.

A control group of cryptogenic stroke patients, in whom no obvious structural heart disease (SHD) was present based on medical history, ECG, echocardiography, 24h Holter monitoring and duplex ultrasound of the carotid arteries (meeting the criteria for embolic stroke of unknown source, ESUS) in the period between 2008-2018 were screened. From this ESUS group, 50 patients, matched individually by age and sex to 50 randomly selected ICD candidates (from the 80 ICD patients with nsVT (28 ICM+nsVT and 22 DCM+nsVT), were studied (Figure S1). Given that acute stroke may alter cardiac repolarization [12], the electrocardiographic and Holter assessments were conducted after the period of the acute stroke was resolved. For all patients baseline demographic data including age, sex and body mass index (BMI); clinical data including medical history, medications, LVEF and serum creatinine; as well as electrophysiological parameters from baseline 12-lead ECG were collected from hospital records

(Table 1 and table S1). The baseline ECG QT interval was corrected using the Fridericia or Rautaharju formula for narrow and broad QRS complexes respectively [13].

A two-part study with a case-control followed by cohort study design was employed. In the first part, we performed a case-control study investigating the predictive value of repolarization lability (BVR) in the minutes preceding nsVT. The ICD candidates with nsVT (ICM+nsVT and DCM+nsVT) were cases while patients without nsVT (ICM-nsVT and DCM-nsVT) were controls. In the second part of the study, the cohort of ICD patients with nsVT (ICM+nsVT and DCM+nsVT) on pre-implantation Holter, were investigated for factors predicting appropriate ICD therapy during follow-up in patients with nsVT."

Holter analysis

Twenty-four-hour ambulatory two- or three-channel Holter ECG recordings were performed using standard 200 Hz Spiderview recorders (Microport, France). Holter recordings of all patients included in the study were processed and exported as ISHNE-files using Synescope Holter software (Microport, France). Holter processing utilized a template based-algorithm to analyze the 24-hour Holter for baseline electrophysiological parameters including the duration of time analyzed of the total recorded time as a quality parameter, average heart rate, number of bradycardia episodes defined as heart rate <50 beats per minute (bpm), number of pauses > 2000 ms, number of atrial- and ventricular extrasystoles as well as non-sustained (<30 seconds) and sustained VT episodes. The Holter recordings were semi-automatically analyzed and manually corrected where necessary.

The ISHNE files were then imported and analyzed using R-DECO, a custom-made signal analysis software developed in MATLAB (Mathworks, Natick MA, USA) [14]. The Holter recordings were filtered using a backward/forward high-pass second order Butterworth filter to exclude low frequency variation specifically respiration motion with a cut-off frequency of 0.5 Hz, and a notch filter at 50 Hz to suppress electrical interference and high frequency noise. Then, a modified fiducial segment averaging technique was employed to analyze the QT duration of complexes in the segment as described previously [14]. Briefly, the QRS complex of each beat was detected using an envelope-based algorithm combined with an adaptive thresholding. Correct detection and annotation of the QRS complexes was manually checked and corrected where necessary. All ventricular premature complexes as well as the preceding (if the premature complex occurred before the end of the T-wave) and the succeeding sinus beats were excluded from the analysis.

The annotated sinus QRS complexes were aligned by the dominant R/Q wave and used to create template complexes. The onset of the Q-wave and end of the T-wave, were detected by modified compression and integration algorithms based on the template complex as previously described [15]. Annotations were used to determine the QT duration of each complex. Correct Q-onset and T-end detection were checked and manually adjusted using the tangent method where necessary. Poincaré plots were then constructed from 30 consecutive sinus beats. QT-BVR was calculated using the established formula $\sum|QT_{n+1} - QT_n| / N \times \sqrt{2}$; where N is the number of beats [7].

In all patients, we defined a 1-minute segment of uninterrupted sinus rhythm at 03:00am as baseline. If there were any ventricular extrasystoles at 03:00am, a segment an hour later at 04:00am was used. This timepoint was selected as it is in the middle of the period when extrasystoles were lowest and least influenced by physical activity and sympathetic nervous signaling during sleep [16,17]. In ICD patients, the first nsVT episode after the 03:00am time-point

was semi-automatically detected and annotated. To assess the temporal changes in repolarization lability prior to the arrhythmic event, three time-points were defined based on the nsVT episode as follows: 1-minute, 5-minutes and 30-minutes prior to the nsVT event. Per definition, control patients did not have nsVT on Holter, therefore time-points matched to time of day to respective corresponding ICD patients were selected and BVR was assessed at 1-minute, 5-minutes and 30-minutes prior to this time. At these time points, QT-BVR was measured from the lead equivalent to ECG lead II. If this lead was noisy or had a flat T-wave, the alternate lead was used.

In patients who had more than one nsVT episode, a second episode more than 1-hour following the index was selected to perform the same analysis to assess reproducibility.

Retrospective clinical endpoints

The primary endpoint in patients with underlying cardiomyopathy was considered the first appropriate ICD therapy (APT). APT was defined as either appropriate ICD shock or anti-tachycardia pacing. The date and precipitating event (VT or VF) of the appropriate ICD shock or anti-tachycardia pacing was verified from source documents of ICD interrogation by the treating cardiac electrophysiologist. All clinical endpoints were collected until death, heart transplantation or the last available outpatient visit before 31 December 2021.

Statistical analysis

Data are expressed as mean ± standard deviation (SD), median (interquartile range, IQR) or number and percentage as appropriate. Two-tailed t-test, Chi-square test with Fisher's exact or two-way analysis of variance (ANOVA) with Bonferroni post-hoc analysis was used to compare clinical variables between groups. A mixed effects model with Bonferroni post hoc correction was employed to compare temporal changes in BVR and between groups. Cox hazard regression analysis was used to compare the contribution of clinical parameters to the endpoint. Retrospective clinical analysis of appropriate ICD therapy was performed by survival analysis. Kaplan-Meier graphs with Log-rank analysis were plotted to assess this endpoint. Univariate Cox regression analysis was performed for available clinical parameters: underlying cardiomyopathy, age, sex and LVEF; electrophysiological parameters: heart rate, QRS duration and QTc duration; number of non-sustained episodes on Holter; BVR parameters: resting BVR, BVR in the minute preceding nsVT (pre-nsVT BVR) and temporal change in BVR from preceding timepoint. Multivariable Cox regression analysis was performed using a backward elimination strategy including all variables with a p-value <0.100 in univariate analysis. Proportional hazard assumptions were assessed using Schoenfeld residuals and visual interpretation of the proportional hazard plots. Collinearity in the final model was assessed using a covariance matrix of the final model. The Harrell's C-index was calculated for the final model. A *P*-value <0.05 was considered significant. All statistical analysis was performed using GraphPad Prism v8, SPSS IBM Statistics v27 and Stata v17.

RESULTS

Patient characteristics

The demographic and clinical characteristics of the patients are presented in table 1. A total of 80 ICD candidates with nsVT, 43 ICM+nsVT, aged 66 (57-70) years and 90.6% male, and 37 DCM+nsVT, aged 57 (44-57) years and 70.3% male); 55 ICD candidates without nsVT, 29 ICM-nsVT, aged 66 (58-70) years and 89% male, and 26 DCM-nsVT, aged 54 (46-67) years and 74% male were studied. DCM patients were younger than ICM patients (P = 0.041 and P = 0.043, with and without nsVT respectively). The patients in all groups were predominantly male, although the ICM+nsVT group had a higher proportion than the DCM+nsVT group (P = 0.024).

More ICM+nsVT patients had diabetes (44.1% vs ICM-nsVT: 17.9%, P = 0.037) and fewer DCM patients had hypertension (DCM+nsVT 21.6% vs ICM+nsVT: 67.4%, P<0.001; DCM-nsVT: 34.6% vs ICM-nsVT: 71.4%, P = 0.015). Medications were not different between ICM and DCM, with the exception of more aspirin use in DCM+nsVT patients (DCM+nsVT: 32.4% vs ICM+nsVT: 79.9%, P<0.001; DCM+nsVT: 32.4% vs DCM-nsVT: 69.2%, P = 0.005). There were no differences in ECG parameters between ICM and DCM groups.

Table 1. Patient baseline characteristics

		ICD candidates with nsVT		ICD candidates without nsVT	
		ICM	DCM	ICM	DCM
n		43	37	29	26
Age (years)		66 (57-70)	57 (44-67) *	66 (58-70)	59 (46-67) #
Sex					
	Male (%)	39 (90.6)	26 (70.3) *	26 (89.6)	18 (69.2)
	Female (%)	4 (9.3)	11 (29.7) *	3 (10.3)	8 (30.8)
BMI		27 ± 4.0	25.4 ± 4.6	25 ± 4.6	26.7 ± 5.0
NYHA (%)					
	1	15 (34.9)	8 (21.6)	9 (31.0)	6 (23.1)
	2	16 (34.9)	19 (51.4)	11 (37.9)	11 (42.3)
	3	12 (27.9)	10 (27.0)	9 (31.0)	9 (34.6)
	4	1 (2.3)	0 (0)	0 (0.0)	0 (0.0)
LVEF (%)		28.6 ± 8.8	27.3 ± 10.5	28.1 ± 9.2	29.7 ± 11.5
Indication (%)					
	Primary	36 (83.7)	35 (94.6)	22 (78.5)	24 (88.9)

	Secondary	7 (16.2)	2 (5.4)	6 (21.4)	3 (11.1)
History (%)					
	Stroke/TIA	6 (14.0)	4 (10.8)	5 (17.2)	2 (7.7)
	Diabetes	19 (44.1)	9 (24.3) *	5 (17.2) *	4 (15.4)
	Atrial fibrillation	5 (11.6)	2 (5.4)	8 (27.6)	5 (19.2)
	Hypertension	29 (67.4)	8 (21.6) ***	20 (69.0)	9 (34.6) ‡
Creatinine (mg/dL)		1.10 ± 0.39	1.10 ± 0.31	1.24 ± 0.38	1.21 ± 0.48
Medications (%)					
	Beta-blocker	40 (93.0)	33 (89.2)	26 (89.7)	24 (92.3)
	Statin	42 (97.7)	16 (43.2)	25 (86.2)	20 (76.9)
	ACE-I/ ARB	42 (97.7)	31 (83.2)	26 (89.7)	24 (92.3)
	Loop diuretic	14 (32.0)	22 (59.4)	18 (62.1)	11 (42.3)
	MRA	27 (62.2)	28 (75.7)	16 (55.2)	15 (57.7)
	Aspirin	34 (79.9)	12 (32.4) ***	22 (75.9)	18 (69.2) ‡
	VKA	11 (25.5)	7 (18.1)	10 (34.5)	6 (23.1)
	NOAC	0 (0)	1 (2.0)	2 (6.9)	0 (0)
	Amiodarone	7 (16.6)	4 (10.7)	3 (10.3)	1 (3.8)
	Other AAD	1 (2.3)	2 (5.4)	2 (6.9)	2 (7.7)
ECG					
	Heart rate (bpm)	67.7 ± 12.6	66.4 ± 14.9	63.6 ± 13.4	67.7 ± 12.6
	QRS (ms)	123.5 ± 28.2	119.8 ± 29.9	130.3 ± 35.4	126.0 ± 26.7
	QT (ms)	424 (412-444)	422 (397-449)	434 (418-486)	426 (408-445)
	QTc (ms)	448 ± 41.8	439 ± 37.1	432 ± 42.9	443 ± 33.9
	LBBB (%)	11 (25.6)	11 (29.7)	5 (17.2)	8 (30.7)
	RBBB (%)	4 (9.3)	1 (2.7)	2 (6.9)	1 (3.8)

Data expressed as n (%) and mean ± SD or median (interquartile range). ICD – implantable cardioverter defibrillator, nsVT – non-sustained ventricular tachycardia, ICM – ischemic cardiomyopathy, DCM – dilated cardiomyopathy, BMI – body mass index, NYHA – New York Heart Association classification of heart failure, LVEF – left ventricular ejection fraction, TIA – transient ischemic attack, AF – atrial fibrillation, ACE-I – Angiotensin converting enzyme inhibitor / Angiotensin receptor blocker, MRA – mineralocorticoid receptor antagonist, VKA – vitamin K

antagonist, NOAC – novel oral anticoagulant, AAD – anti-arrhythmia drug, QTc – QT corrected by (Fridericia or Rautaharju formula for narrow and broad QRS complexes respectively11, bpm – beats/minute, LBBB – left bundle branch block, RBBB – right bundle branch block. 2-way ANOVA or Fisher's exact with Bonferroni post hoc analysis. **P*<0.05, ****P*<0.001, vs ICM+nsVT; #*P*<0.05, ##*P*<0.01, vs DCM+nsVT and ‡*P*<0.01, vs ICM-nsVT.

Holter electrophysiological parameters

The baseline parameters of the Holter recordings are presented in table 2 and table S2. ICD candidates with nsVT had more ventricular extrasystoles per hour than ICD candidates without nsVT (ICM+nsVT: 80.8 (25.0-273.2) vs ICM-nsVT: 3.1 (0.5-10.8), *P*<0.001 and DCM+nsVT: 62.2 (10.3-190.7) vs DCM-nsVT: 7.3 (0.5-29.1), *P*<0.001). In addition, ICM+nsVT had more ventricular extrasystoles than DCM+nsVT (*P* = 0.004). There were no other differences in electrophysiological parameters.

Table 2. Holter electrophysiological parameters

	ICD candidates with nsVT		ICD candidates without nsVT	
	ICM	DCM	ICM	DCM
n	43	37	29	26
Holter Quality (Hours analyzed)	22.7 ± 3.5	22.5 ± 3.9	23.0 ± 0.22 #	23.0 ± 0.26 #
Heart rate (bpm)	70.9 ± 11.5	69.4 ± 12.2	66.1 ± 12.7	68.3 ± 10.6
Bradycardia episodes	0 (0-12.8)	8.5 (0-49.5)	15 (0-78.8)	0 (0-23.0)
Pauses	0 (0)	0 (0)	0 (0-1)	0 (0-2)
Atrial extrasystoles per hr	3.5 (0.8-13.3)	1.3 (0.3-8.9)	1.0 (0.2-5.6)	0.5 (0.1-5.0)
Ventricular extrasystoles per hr	80.8 (25.0-273.2)	62.2 (10.3-190.7) **	3.1 (0.5-10.8) ###	7.3 (0.5-29.1) ##
Non-sustained VT				
number of episodes	10.1 ± 6.4	7.9 ± 4.7	0	0
average rate (bpm)	148.1 ± 30.2	150 ± 26.2	N/D	N/D
average duration (s)	2.4 (1.7-3.9)	2.4 (1.6-3.1)	N/D	N/D
Sustained VT				
number of patients	4	1	0	0
average rate (bpm)	123.5 ± 18.4	130.4 ± 0.6	N/D	N/D

Data expressed as n (%) and mean ± SD or median (IQR). *P<0.05 vs Control. Bpm – beats per minute, AV block – atrioventricular block episodes, VT – ventricular tachycardia. 1-way ANOVA, Fisher's exact with Bonferroni post hoc analysis or two-tailed t-test. **P<0.01, ***P<0.001, vs ICM+nsVT; ##P<0.01, vs DCM+nsVT.

The first nsVT episode of the day, used in subsequent analysis, occurred at all hours of the day without distinguishable preferred time-of-day patterns in both groups (Figure 2A). There tended to be more nsVT episodes in ICM+nsVT than DCM+nsVT but this was not statistically significant (ICM+nsVT: 10.1 ± 6.4 vs DCM+nsVT: 7.9 ± 4.7, P = 0.094). The number of complexes and rate of the nsVT episodes considered for analysis were comparable (P = 0.676 and P = 0.582, figure 2B).

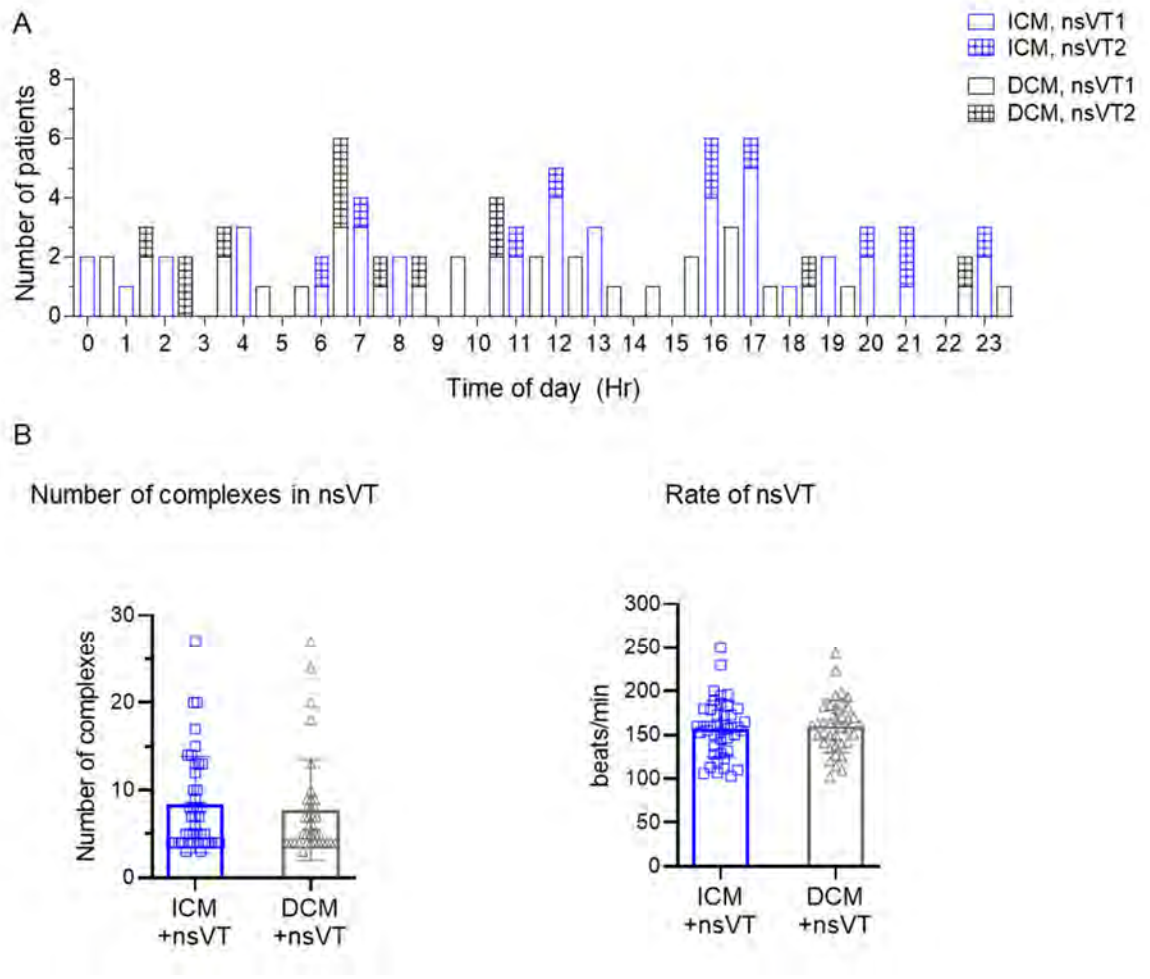

Figure 2. Characteristics of non-sustained ventricular tachycardia (nsVT) episodes.
A, Time of occurrence during the day of the first and second nsVT episode used for analysis.
B, Summary data of the number of complexes in the nsVT episodes analyzed (left) and the heart rate during the nsVT episodes (right). N = 43 (ICM+nsVT), 37 (DCM+nsVT). 2-tailed t-test.

Resting BVR in ICD patients

Figure 3A illustrates the fiducial point detection used to determine the QT interval and an example of the Poincaré plot constructed from 30 consecutive sinus beats to assess the QT-BVR. At baseline, there was no difference in heart rate between the ICD patient groups (ICM+nsVT: 66.9 ± 11.71ms vs ICM-nsVT 61.2 ± 9.19ms, *P* = 0.188; DCM+nsVT: 63.41 ± 10.95ms vs DCM-nsVT: 67.29 ± 12.39, *P* = 0.527) (Figure 3B). QT-BVR was also not significantly different between the groups (ICM+nsVT: 1.48 ± 0.35ms vs ICM-nsVT 1.44 ± 0.20ms, *P* = 0.957; DCM+nsVT: 1.43 ± 0.29ms vs DCM-nsVT: 1.41 ± 0.27, *P* = 0.983) (Figure 3B).

However, the resting BVR in ICD patients both with ICM and DCM was more than that of the control group of patients without SHD (Control: 1.25 ± 0.23ms vs ICM: 1.46 ± 0.32ms, *P*<0.001 and DCM: 1.43 ± 0.28ms, *P* = 0.003), although the resting heart rate was not different (Figure S2).

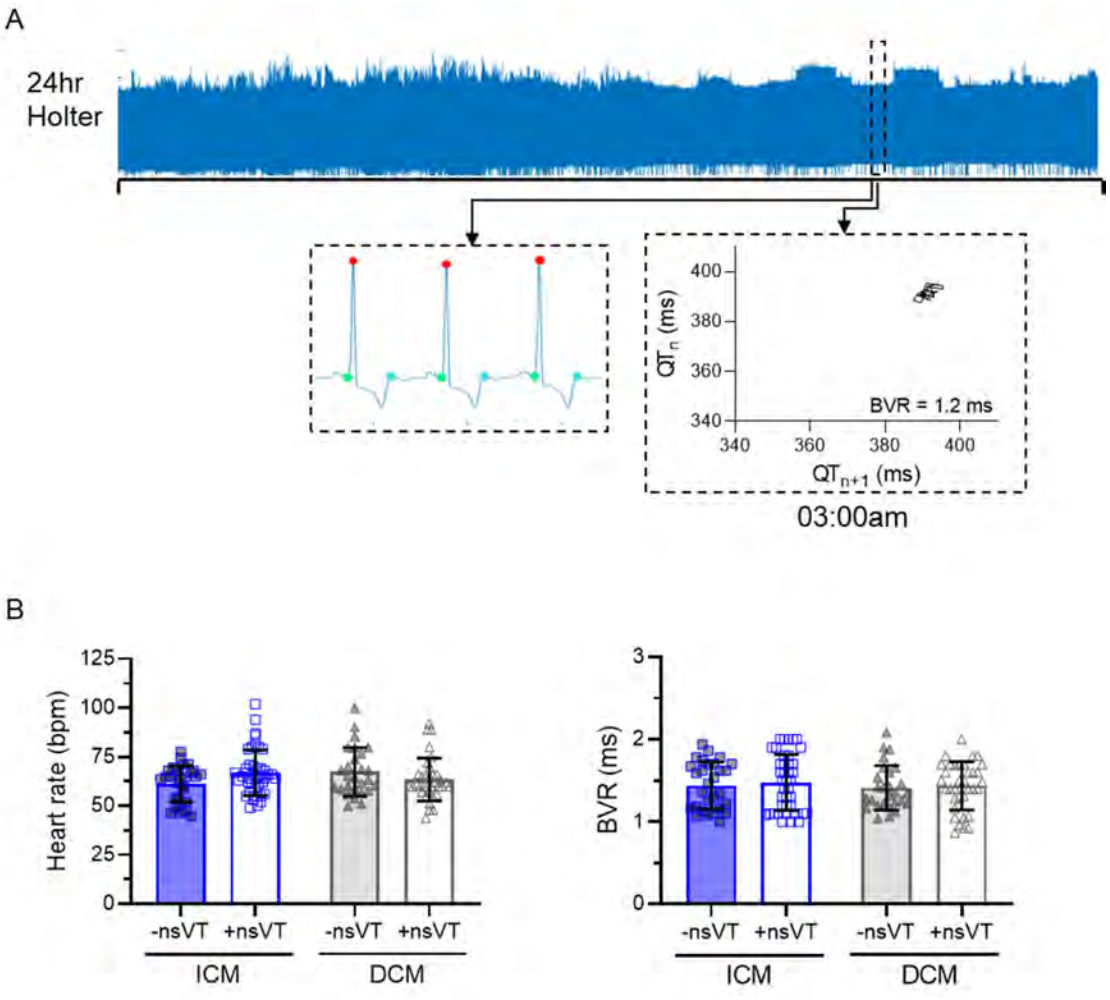

Figure 3. Beat-to-beat variation of repolarization (BVR) at rest.
A, Example of a condensed 24-hour Holter illustrating the fiducial point QRS, and QT detection and baseline QT-BVR Poincaré plot of an ICM patient.
B, Summary data of baseline heart rate (left) and QT-BVR (right) of ICM and DCM patients with and without nsVT, taken at 3:00am. N = 29 (ICM-nsVT), 43 (ICM+nsVT), 26 (DCM-nsVT), 37 (DCM+nsVT). 2-way ANOVA with Bonferroni post hoc analysis.

Temporal changes in BVR predict imminent ventricular arrhythmias

Figure 4A illustrates the temporal analysis of QT-BVR before the occurrence of a nsVT event (top insert), or matched timepoints in ICD candidates without nsVT, and examples of the Poincaré plots at 30-minutes, 5-minutes and 1-minute before the nsVT used for QT-BVR calculation (bottom insert). The timepoints used for analysis in the control groups were matched to nsVT-timepoints of the respective ICD patients in figure 2A. The time-of-day profile matched timepoints are presented in figure S3 and reflect the random distribution of nsVT in ICD patients (P = 0.989).

In ICM ICD candidates with nsVT (ICM+nsVT), the QT-BVR at baseline (1.48 ± 0.35ms at 03:00am) was not different 30-minutes prior to nsVT (1.41 ± 0.54ms, P = 0.985), but thereafter, increased to 1.78 ± 0.50ms at 5-minutes (P = 0.011) and further increased to 2.21 ± 0.59ms at 1-minute prior to nsVT (P<0.001). In contrast, there was no significant change in temporal BVR at matched timepoints in ICM ICD candidates without nsVT (ICM-nsVT) (P = 0.975, figure 4B). A similar pattern was seen in the DCM ICD candidates with nsVT (DCM+nsVT), at baseline (03:00am), BVR was 1.43 ± 0.29ms, comparable to 1.38 ± 0.33ms at 30-minutes before nsVT (P = 0.757), and tended to increase to 1.58 ± 0.51ms at 5-minutes (P = 0.133), then significantly increased to 2.09 ± 0.57ms at 1-minute before nsVT (P<0.001). In DCM ICD candidates without nsVT (DCM-nsVT) no significant BVR differences were observed at matched timepoints (P = 0.945, figure 4B). Furthermore, in control patients without SHD, no differences in BVR were observed at matched timepoints (P = 0.952, figure S4).

There was no significant difference between the temporal behaviour of BVR of the ICM+nsVT compared to DCM+nsVT groups (P = 0.406), neither was there a significant difference between the change in BVR (P = 1.000) (Figure 4C). QT-BVR changes in time were similar between ICM+nsVT and DCM+nsVT, but the magnitude of change at 5-minutes to 1-minute before the nsVT was higher in ICM+nsVT than DCM+nsVT (ICM: 0.48 ± 0.54ms vs DCM: 0.23 ± 0.35, P<0.001) (Figure 4C).

These temporal changes in BVR occurred without temporal changes in heart rate in ICM patients with nsVT (03:00am: 66.9 ± 11.7bpm, 30-minutes pre-matched nsVT time: 70.5 ±15.0bpm, 5-minutes pre-matched nsVT time 68.2 ± 14.5bpm and 1-minutes pre-matched nsVT time 71.6 ± 16.0bpm, P = 1.000) and DCM patients with nsVT (03:00am: 63.4 ± 10.9bpm, 30-minutes pre-matched nsVT time: 68.8 ± 11.2bpm, 5-minutes pre-matched nsVT time 72.2 ± 11.0bpm and 1-minutes pre-matched nsVT time 69.9 ± 13.1bpm, P = 0.985) (Figure S5).

A total of 17 patients (11 ICM and 6 DCM) had more than 1 nsVT episode at least 1-hour later. This second event analyzed also occurred at all hours of the day without distinguishable time-of-day patterns in both groups (Figure S6). In these patients, temporal BVR showed a similar

pattern to the index event and increased from 1.34 ± 0.60ms (30-minutes before nsVT) to 1.84 ± 0.76ms (5-minutes before nsVT) and 2.41 ± 0.79ms (1-minute before nsVT), *P*<0.001.

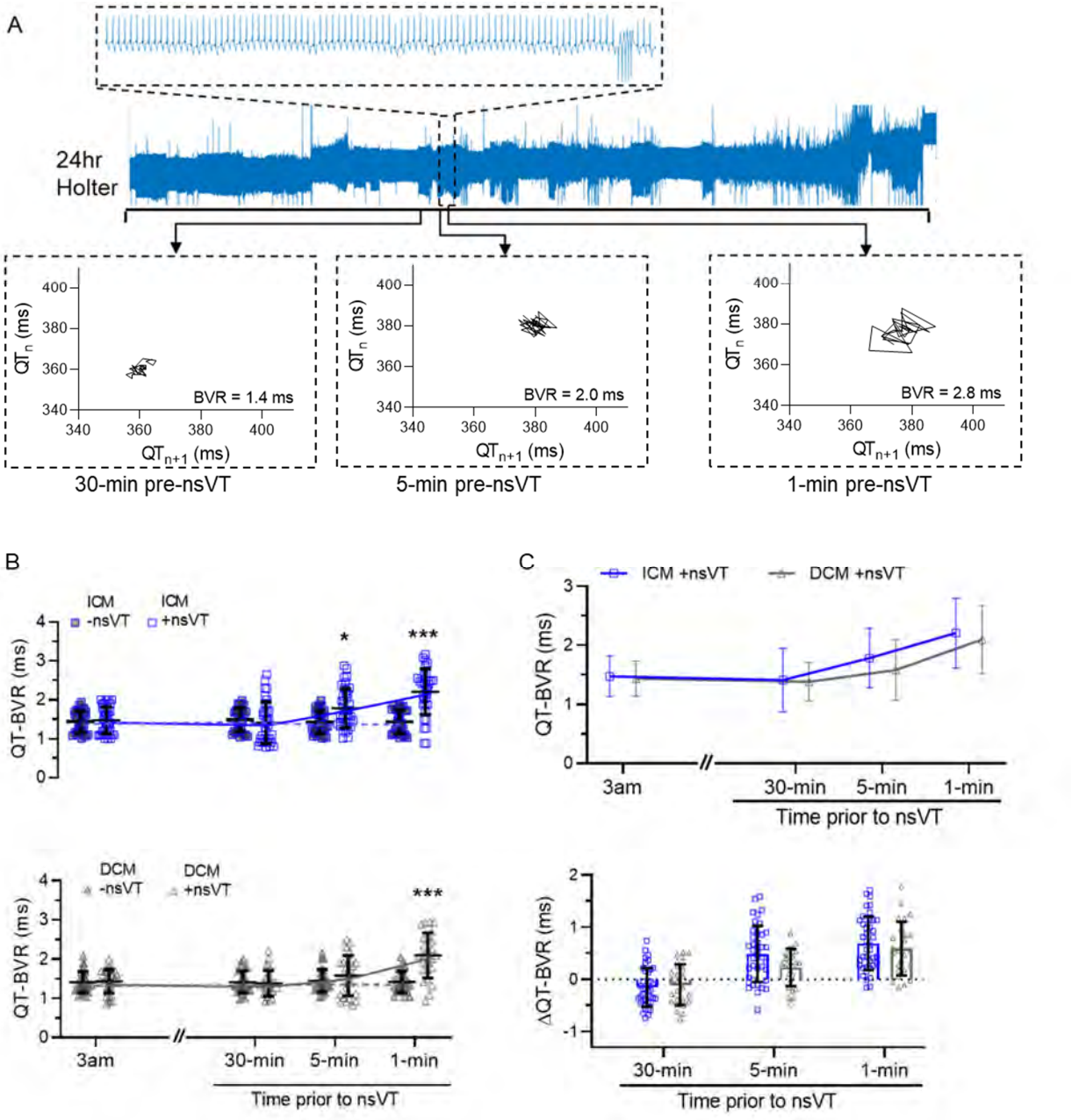

Figure 4. Temporal changes in BVR predict non-sustained ventricular tachycardia (nsVT).

A, Example of a condensed 24-hour Holter illustrating the time points with pre-nsVT ECG segment, and examples of the QT-BVR Poincaré plots from each segment.
B, Summary data of temporal changes in QT-BVR in patients with and without nsVT, with ICM (top) and DCM (bottom). N = 29 (ICM-nsVT), 43 (ICM+nsVT), 26 (DCM-nsVT), 37 (DCM+nsVT). Mixed effects model analysis with Bonferroni correction. **P*<0.05, ****P*<0.001 vs preceding timepoint.

C, Mean data of the temporal BVR changes in patients with nsVT comparing ICM and DCM patients (top), and summary data of the change in BVR (bottom) between timepoints for patients with nsVT groups, comparing ICM and DCM patients. Mixed effects model analysis with Bonferroni correction.

Multivariable clinical analysis

The second part of the study considered the predictive value of BVR analyzed on the pre-ICD implantation Holter, for predicting future events and ICD appropriate therapy in patients with pre-implantation nsVT. Twenty of the 80 ICD patients with nsVT (23.8%) received appropriate therapy during follow-up (ICM+nsVT – 13 patients (10 VT and 3 VF) and DCM+nsVT – 7 patients (7 VT)). There was no difference in event-free survival between ICD and DCM (*P* = 0.359, figure 5). Table 3 presents the regression analysis of clinical and electrophysiological parameters that were assessed as contributors to appropriate ICD therapy. Univariate analysis identified history of atrial fibrillation, number of nsVT episodes on Holter, and all BVR measurements as significant predictors of appropriate ICD therapy. In multivariable Cox regression analysis atrial fibrillation and pre-nsVT BVR as independent predictors of appropriate ICD therapy (Harrell's C-index of the final model = 0.834).

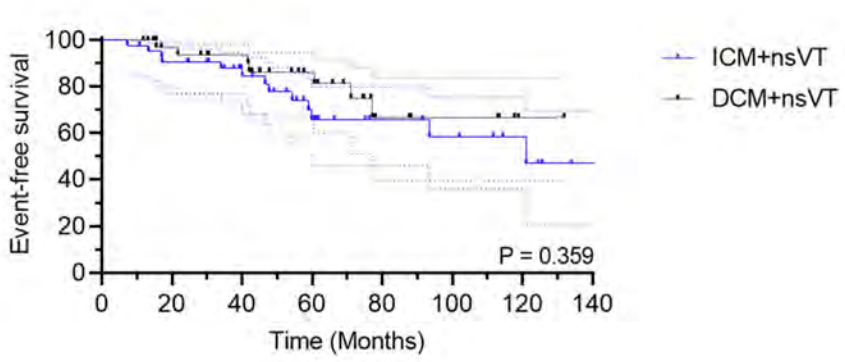

Figure 5. Kaplan-Meier graphs of freedom from appropriate therapy in ICD patients with nsVT.

N = 43 (ICM+nsVT), 37 (DCM+nsVT). Log-rank test.

In this cohort of ICD patients with pre-ICD nsVT, we further compared the clinical variables and BVR in the patients who experienced appropriate therapy to those who did not (Table S3). The number of nsVT episodes, baseline BVR, max BVR and ΔBVR were higher in patients who received appropriate therapy, with max BVR having the most significant difference (2.59 ± 0.47ms, vs APT-ve: 1.93 ± 0.54ms, *P*<0.001).

Table 3. Cox regression analysis for appropriate ICD therapy in patients with pre-implantation nsVT on Holter.

Clinical Variable	Univariate regression		Multivariate regression model	
	P value	Hazard ratio (95% CI)	*P* value	Hazard ratio (95% CI)
N = 80				
Male	0.879	1.090 (0.359 – 3.307)		
Age (/y)	0.161	1.029 (0.989 – 1.071)		
ICM	0.363	1.538 (0.609 – 3.885)		
LVEF (/%)	0.225	1.025 (0.985 – 1.066)		
Atrial fibrillation (AF)	0.018	3.831 (1.254 – 11.706)	0.004	6.247 (1.809 – 21.573)
ECG				
Heart rate (/bpm)	0.288	1.019 (0.984 – 1.055)		
QRS (/ms)	0.829	1.002 (0.986 – 1.018)		
QTc (/ms)	0.094	1.009 (0.998 – 1.020)		
Holter				
Ventricular extrasystoles (/unit increase)	0.647	1.000 (1.000 – 1.000)		
Number of nsVT episodes (/unit increase)	0.003	1.787 (1.212 – 2.365)		
BVR				
Resting (/ms)	0.009	5.508 (1.527 – 19.874)		
pre-nsVT BVR (/ms)	<0.001	8.026 (2.855 – 22.563)	<0.001	7.848 (2.638 – 23.352)
∆ BVR (/ms)	0.020	2.891 (1.186 – 7.047)		

ICM – ischemic cardiomyopathy, LVEF – left ventricular ejection fraction, bpm – beats per minute, nsVT – non-sustained ventricular tachycardia, BVR – beat-to-beat variability of repolarization. Resting BVR defined as BVR measured at 3:00am.

Variables for the multivariable analysis model were selected by backward elimination model and tested for collinearity.

DISCUSSION

The main findings from this study are (1) resting BVR is increased in ICD candidates with both underlying ICM and DCM, (2) BVR increases significantly in the minute preceding nsVT events in both ICM and DCM, and (3) is associated with appropriate therapy during follow-up. These findings support the further exploration of BVR in clinical risk stratification and prediction of imminent arrhythmia risk in ICD patients.

Labile repolarization in ICD patients and arrhythmia vulnerability

Resting BVR taken at a time-point when the patient is assumed to be asleep and physical activity is unlikely, revealed that ICD patients, regardless of underlying cardiomyopathy (ICM and DCM) and presence of nsVT, had higher BVR compared to matched patients without SHD. These findings are consistent with clinical reports of increased BVR in patients with cardiomyopathy [18,19] and heart failure [8].

The relevance of BVR as a measure of temporal dispersion of repolarization has been demonstrated in different animal models. Increased BVR is present in the remodeled heart of chronic AV block dogs susceptible for Torsades de Pointes [7], in pigs after myocardial infarction [20] and in rabbits with long QT syndrome [21]. At a cellular level, BVR is a measure of repolarization reserve and an increased BVR represents a reduced reserve [22]. Thus, increased BVR is a consequence of remodeling of cellular ion channels that contribute to the cellular action potential, particularly repolarizing potassium currents [23], and calcium handling [22,24]. Such cellular remodeling has been observed in human myocytes isolated from cardiomyopathy and heart failure patients, which demonstrated reduced repolarizing potassium currents and calcium handling leading to the characteristic prolonged action potential [25]. This may contribute to altered ventricular repolarization and to a prolongation of the QT interval observed in heart failure models [26,27] and patients [28]. This is consistent with our observations of longer QTc in ICM and DCM patients compared to controls without SHD in the current study.

Our findings support the hypothesis that cardiomyopathy patients have reduced repolarization reserve, which renders them at increased risk of arrhythmia. They also reinforce the value of assessing repolarization heterogeneity in arrhythmogenesis and its targeting in the prevention of SCD in high risk patients.

Usefulness of BVR in predicting imminent arrhythmias

Our data suggest that BVR increases in the minutes preceding nsVT. We observed a similar pattern of BVR increase in ICM and DCM patients prior to nsVT but not at matched timepoints in ICM and DCM patients without nsVT or SHD. At 1-minute before VT BVR was increased compared to the preceding 30-minute time point as well as compared to resting BVR in the ICD groups.

BVR has been extensively studied in a dog model of Torsades de Pointes by the group of M. Vos (Utrecht, The Netherlands) who first demonstrated that this measure of temporal dispersion of repolarization precedes the onset of TdP [7]. Smoczyńska et al. from this group recently demonstrated similar findings in the EU-CERT cohort of ICD patients [99]. In this study, of the 2331 EU-CERT patients, 170 primary prophylactic ICD patients with either ICM or DCM and nsVT on 24-hour Holter were included and 37 randomly selected ICD patients without nsVT were selected as controls. They found that short-term variability or BVR increased by ~50% in

the minute prior to nsVT. These results are in line with our results, but compared to our analysis Smoczyńska et al. did not report possible differences depending on the etiology of the underlying cardiomyopathy and the results were compared only to patients with similar underlying heart disease and not to a control population.

These results are however in contrast to Sachdev et al., [29] who have not observed repolarization variability in monitoring of acutely ill patients admitted to the Coronary Care Unit who had ventricular arrhythmia during 24-hour ECG monitoring. The confounding effects of sustained autonomic activation in these acutely ill patients, which is in contrast to our cohort of stable cardiomyopathy patients, likely contributes to the lack of elevated BVR in this study.

Clinical implications

In clinical practice, currently no parameters are available that accurately predict the onset of spontaneous arrhythmia. The finding of an increased BVR immediately before ventricular arrhythmia is of importance as it reinforces its value in prediction of imminent arrhythmia events in high-risk patients and support its translation to clinical practice, especially for ICD monitoring. Predicting the onset of arrhythmias, particularly in cardiomyopathy patients, is of clinical importance, because it can open possibilities for preventive strategies to avoid ICD shocks. Sustained arrhythmia and the appropriate ICD shocks are associated with negative cardiac and neurohormonal remodeling that worsen function and may contribute to heart failure [30]. The psychological impact of the arrhythmia-shock sequence of events including anxiety and pain is of importance to a patient's holistic well-being and together with the physiological symptomatology is reflected in negative impact on patient quality of life.[31] Alternative approaches could be to use the prediction of imminent arrhythmia to prevent ventricular arrhythmia by high-rate pacing or over-drive suppression [32], or to allow the possibility of automated drug administration [33]. Recent experimental studies have demonstrated that ICDs can be programmed to monitor BVR and initiate high-rate pacing to prevent TdP in animal models [32].

BVR was also associated with appropriate therapy during follow-up in our patient cohort. In the multivariable analysis, pre-nsVT BVR was the strongest predictor of appropriate therapy, and was higher in patients who received appropriated therapy. The pre-nsVT BVR may reflect the degree of repolarization reserve and thus patients with lowest reserve would be most likely to develop sustained arrhythmia. Resting BVR is likely to be less informative because it does not provide insight into the repolarization under challenge.

Limitations

In our study, the digital Holter recordings were recorded at a sampling frequency of 200Hz, compared to experimental studies which were performed at 1000Hz or more. Thus, this difference may have influenced the accuracy of BVR calculation, and should be considered when interpreting these data.

It is conceivable that BVR may increase without the occurrence of arrhythmia. The current technical challenges of automated fiducial point detection limit us from assessing BVR over the complete 24 hours of monitoring. We however did see stable values of BVR in our control patients without peaks in BVR at timepoints spread over the day.

Mortality in the patient cohort was low and a majority of these deaths occurred out-of-hospital and the cause was not ascertained. Therefore, an analysis of mortality was not performed. Future work could benefit from prospective longitudinal follow-up of patients to assess the long-term predictive value of BVR on arrhythmic death.

Conclusion

BVR is increased in high-risk ICM and DCM patients suggesting a reduced repolarization reserve in these patients. BVR increases further immediately prior to nsVT predicting imminent arrhythmia in both ICM and DCM patients. Real time monitoring of BVR could possibly be used for predicting impending ventricular arrhythmia in high-risk patients.

Acknowledgements

The authors would like to thank Sofie van Soest for excellent technical assistance.

Sources of funding

This research received funding from the Flemish Government (AI Research Program) to SVH. KS is supported by a project grant, RW as postdoctoral clinical researcher and MA as a PhD fellow by the Fund for Scientific Research-Flanders. BV is supported by a research grant from the Frans Van de Werf Fund.

Disclosures

RW reports research funding from Abbott, Biotronik, Boston Scientific, Medtronic; speakers and consultancy fees from Medtronic, Boston Scientific, Biotronik, Abbott.

SUPPLEMENTARY MATERIALS

Figures S1-6 and Tables S1-3.

REFERENCES

1. Myerburg RJ, Interian A, Mitrani RM, Kessler KM, Castellanos A. Frequency of sudden cardiac death and profiles of risk. *Am J Cardiol*. 1997;80:10F-19F.

2. Gama F, Ferreira J, Carmo J, Costa FM, Carvalho S, Carmo P, Cavaco D, Morgado FB, Adragão P, Mendes M. Implantable Cardioverter-Defibrillators in Trials of Drug Therapy for Heart Failure: A Systematic Review and Meta-Analysis. *J Am Heart Assoc*. 2020;9:e015177.

3. Al-Khatib SM, Stevenson WG, Ackerman MJ, Bryant WJ, Callans DJ, Curtis AB, Deal BJ, Dickfeld T, Field ME, Fonarow GC, et al. 2017 AHA/ACC/HRS Guideline for Management of Patients With Ventricular Arrhythmias and the Prevention of Sudden Cardiac Death. A Report of

the American College of Cardiology/American Heart Association Task Force on Clinical Practice Guidelines and the Hea. ; 2018: 1-272–391. doi:10.1161/CIR.0000000000000549.

4. Nielsen JC, Lin YJ, de Oliveira Figueiredo MJ, Shamloo AS, Alfie A, Boveda S, Dagres N, Di Toro D, Eckhardt LL, Ellenbogen K, et al. European Heart Rhythm Association (EHRA)/Heart Rhythm Society (HRS)/Asia Pacific Heart Rhythm Society (APHRS)/Latin American Heart Rhythm Society (LAHRS) expert consensus on risk assessment in cardiac arrhythmias: Use the right tool for the right outcome. *Europace*. 2020;22:1147–1148.

5. Wathen MS, Sweeney MO, Degroot PJ, Stark AJ, Koehler JL, Chisner MB, Machado C, Adkisson WO. Shock Reduction Using Antitachycardia Pacing for Spontaneous Rapid Ventricular Tachycardia in Patients With Coronary Artery Disease. *Circulation*. 2001;104:796–801.

6. Varma N, Cygankiewicz I, Turakhia MP, Heidbuchel H, Hu YF, Chen LY, Couderc JP, Cronin EM, Estep JD, Grieten L, et al. 2021 ISHNE/HRS/EHRA/APHRS Expert Collaborative Statement on mHealth in Arrhythmia Management: Digital Medical Tools for Heart Rhythm Professionals: From the International Society for Holter and Noninvasive Electrocardiology/Heart Rhythm Society/European H. *Circ Arrhythmia Electrophysiol*. 2021;14:234–283.

7. Thomsen MB, Verduyn SC, Stengl M, Beekman JDM, de Pater G, van Opstal J, Volders PGA, Vos MA. Increased short-term variability of repolarization predicts d-sotalol-induced torsades de pointes in dogs. *Circulation*. 2004;110:2453–2459.

8. Tereshchenko LG, Cygankiewicz I, Mcnitt S, Vazquez R, Bayes-genis A, Han L, Sur S, Couderc J, Berger RD, Luna AB De. Predictive value of beat-to-beat QT variability index across the continuum of left ventricular dysfunction: competing risks of noncardiac or cardiovascular death and sudden or nonsudden cardiac death. *Circ Arrhythmia Electrophysiol*. 2012;5:719–727.

9. Smoczyńska A, Loen V, Sprenkeler DJ, Tuinenburg AE, Ritsema van Eck HJ, Malik M, Schmidt G, Meine M, Vos MA. Short-term variability of the qt interval can be used for the prediction of imminent ventricular arrhythmias in patients with primary prophylactic implantable cardioverter defibrillators. *J Am Heart Assoc*. 2020;9:1–9.

10. Vandenberk B, Garweg C, Voros G, Floré V, Marynissen T, Sticherling C, Zabel M, Ector J, Willems R. Changes in Implantation Patterns and Therapy Rates of Implantable Cardioverter Defibrillators over Time in Ischemic and Dilated Cardiomyopathy Patients. *Pacing Clin Electrophysiol*. 2016;39:848–857.

11. Al-Khatib SM, Stevenson WG, Ackerman MJ, Bryant WJ, Callans DJ, Curtis AB, Deal BJ, Dickfeld T, Field ME, Fonarow GC, et al. 2017 AHA/ACC/HRS guideline for management of patients with ventricular arrhythmias and the prevention of sudden cardiac death: Executive summary. *Heart Rhythm*. 2018;15:e190–e252.

12. Afsar N, Fak AS, Metzger JT, Van Melle G, Kappenberger L, Bogousslavsky J. Acute stroke increases QT dispersion in patients without known cardiac diseases. *Arch Neurol*. 2003;60:346–350.

13. Vandenberk B, Vandael E, Robyns T, Vandenberghe J, Garweg C, Foulon V, Ector J, Willems R. Which QT correction formulae to use for QT monitoring? *J Am Heart Assoc*. 2016;5:e003264.

14. Moeyersons J, Amoni M, Huffel SV, Willems R, Varon C. R-DECO: An open-source Matlab based graphical user interface for the detection and correction of R-peaks. *PeerJ Comput Sci*. 2019;5:1–20.

15. Moeyersons J, Goovaerts G, Huijghebaert S, Vandenberk B, Willems R, Van Huffel S. Automated T Wave End Detection Methods: Comparison of Four Different Methods for T Wave End Detection. *BIOSIGNALS*. 2017;4:92–98.

16. Black N, D'Souza A, Wang Y, Piggins H, Dobrzynski H, Morris G, Boyett MR. Circadian rhythm of cardiac electrophysiology, arrhythmogenesis, and the underlying mechanisms. *Heart Rhythm*. 2019;16:298–307.

17. Bas HD, Baser K, Hoyt J, Yokokawa M, Labounty T, Morady F, Bogun F. Effect of circadian variability in frequency of premature ventricular complexes on left ventricular function. *Heart Rhythm*. 2016;13:98–102.

18. Berger RD, Kasper EK, Baughman KL, Marban E, Calkins H, Tomaselli GF. Beat-to-Beat QT Interval Variability: Novel Evidence for Repolarization Lability in Ischemic and Nonischemic Dilated Cardiomyopathy. *Circulation*. 1997;96:1557–1565.

19. Hinterseer M, Beckmann B-M, Thomsen MB, Pfeufer A, Ulbrich M, Sinner MF, Perz S, Wichmann H-E, Lengyel C, Schimpf R, et al. Usefulness of short-term variability of QT intervals as a predictor for electrical remodeling and proarrhythmia in patients with nonischemic heart failure. *Am J Cardiol*. 2010;106:216–220.

20. Floré V, Claus P, Antoons G, Oosterhoff P, Holemans P, Vos MA, Sipido KR, Willems R. Microvolt T-wave alternans and beat-to-beat variability of repolarization during early postischemic remodeling in a pig heart. *Heart Rhythm*. 2011;8:1050–1057.

21. Brunner M, Zehender M, Koren G, Brunner M, Peng X, Liu GX, Ren X, Ziv O, Choi B, Mathur R, et al. Mechanisms of cardiac arrhythmias and sudden death in Mechanisms of cardiac arrhythmias and sudden death in transgenic rabbits with long QT syndrome. 2008;118:2246–2259.

22. Varró A, Baczkó I. Cardiac ventricular repolarization reserve : a principle for understanding drug-related proarrhythmic risk. *Br J Pharmacol*. 2011;164:14–36.

23. Volders PGA, Sipido KR, Vos MA, Kulcsár A, Verduyn SC, Wellens HJJ. Cellular basis of biventricular hypertrophy and arrhythmogenesis in dogs with chronic complete atrioventricular block and acquired torsade de pointes. *Circulation*. 1998;98:1136–1147.

24. Dries E, Amoni M, Vandenberk B, Johnson D., Gilbert G, Nagaraju CK, Puertas RD, Abdesselem M, Santiago DJ, Roderick HL, et al. Altered adrenergic response in myocytes bordering a chronic myocardial infarction underlies in vivo triggered activity and repolarization instability. *J Physiol*. 2020;598:2875–2895.

25. Piacentino V. Cellular Basis of Abnormal Calcium Transients of Failing Human Ventricular Myocytes. *Circ Res*. 2003;92:651–658.

26. O'Rourke B, Kass DA, Tomaselli GF, Ka S, Tunin R, Marba E. Mechanisms of Altered Excitation-Contraction Coupling in Canine Tachycardia-Induced Heart Failure, I Experimental Studies. *Circ Res*. 1999;19:562–570.

27. Akar FG, Spragg DD, Tunin RS, Kass DA, Tomaselli GF. Mechanisms underlying conduction slowing and arrhythmogenesis in nonischemic dilated cardiomyopathy. *Circ Res*. 2004;95:717–725.

28. Vrtovec B, Delgado R, Zewail A, Thomas CD, Richartz BM, Radovancevic B. Prolonged QTc Interval and High B-Type Natriuretic Advanced Heart Failure. *Circulation*. 2003;107:1764–1769.

29. Sachdev M, Fetics BJ, Lai S, Dalal D, Insel J, Berger RD. Failure in short-term prediction of ventricular tachycardia and ventricular fibrillation from continuous electrocardiogram in intensive care unit patients. *J Electrocardiol*. 2010;43:400–407.

30. Hasdemir C, Shah N, Rao AP, Acosta H, Matsudaira K, Neas BR, Reynolds DW, Po S, Lazzara R, Beckman KJ. Analysis of troponin I levels after spontaneous implantable cardioverter defibrillator shocks. *J Cardiovasc Electrophysiol*. 2002;13:144–150.

31. Kamphuis HCM, de Leeuw JR, Derksen R, Hauer RNW, Winnubst JAM. Implantable cardioverter defibrillator recipients: Quality of life in recipients with and without ICD shock delivery: A prospective study. *Europace*. 2003;5:381–389.

32. Smoczyńska A, Loen V, Aranda A, Beekman DM, Meine M, Vos MA. High-rate pacing guided by short-term variability of repolarization prevents imminent ventricular arrhythmias automatically by an implantable cardioverter-defibrillator in the chronic atrioventricular block dog model. *Heart Rhythm*. 2020;17:2078–2085.

33. Raviele A, Brignole M, Menozzi C, Giada F, Dorigo A. Development of an Implantable Drug Delivery System for the Treatment of Vasovagal Syncope: a Dream or a Real Prospect? In: Raviele A, ed. Cardiac Arrhythmias. Springer Milano; 1997: 422–427.

SUPPLEMENTAL FIGURES AND FIGURE LEGENDS

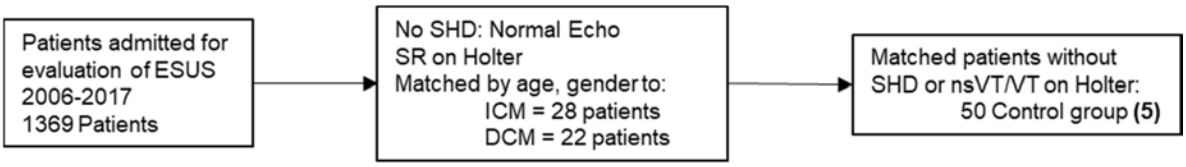

Figure S1. Experimental design.
Study flow chart illustrating patient inclusion of matched control patients without structural heart disease. Patients admitted for evaluation of embolic stroke of undetermined source (ESUS) in 2006-2017 were considered. Patients with a Holter recording were matched to ICM (28) and DCM (22) patients from the ICD candidates with nsVT on Holter. SHD – structural heart disease, SR – sinus rhythm, nsVT – non-sustained ventricular tachycardia.

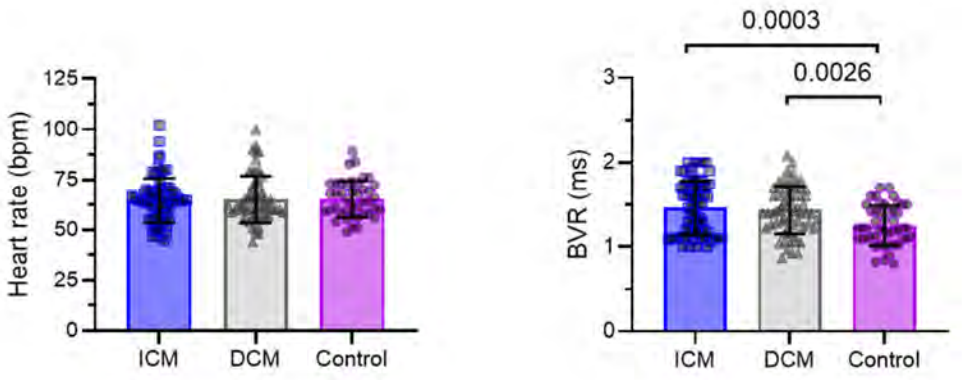

Figure S2. Beat-to-beat variation of repolarization (BVR) at rest.

Summary data of baseline heart rate (left) and QT-BVR (right) of control, ICM and DCM patients taken at 3:00am. N = 72 ICM, 63 DCM and 50 Control.1-way ANOVA with Bonferroni post hoc analysis. *$P < 0.05$, **$P < 0.01$ vs Control,

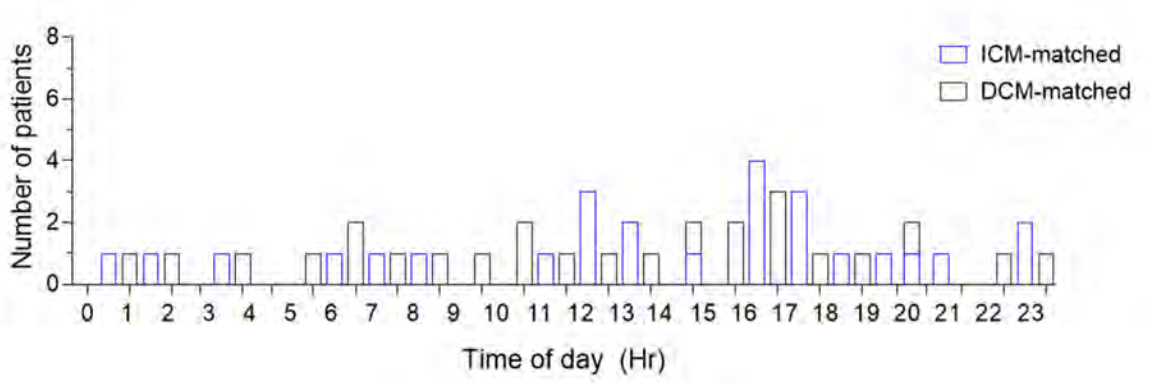

Figure S3. Distribution of matched nsVT timepoint in control patients.

Time of day of the ICM/DCM-matched timepoint of nsVT used for analysis, notably similar to the profile seen in Fig. 2.

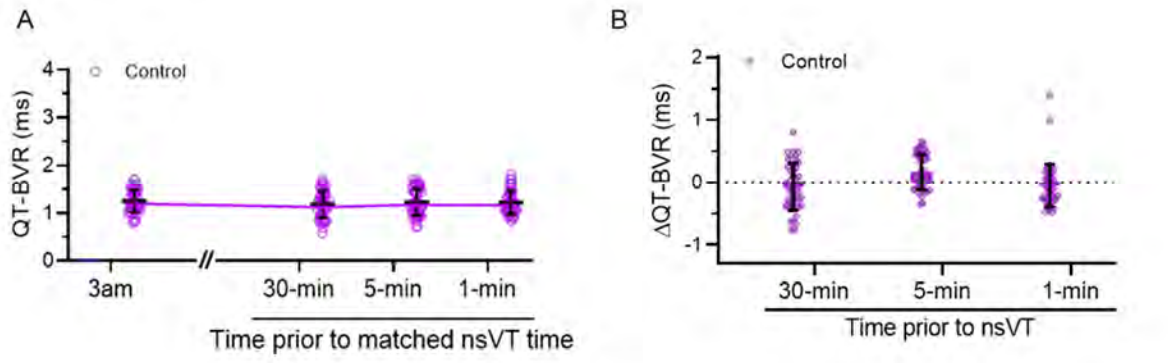

Figure S4. Temporal changes in BVR at matched timepoints in control patients without structural heart disease.

A, Summary data of temporal changes in QT-BVR of control patients. Timepoints are matched to nsVT timepoints of ICD patients in Figure 4.
B, Summary data of the change in BVR between timepoints presented in A.

N = 50 patients. Mixed effects model analysis with Bonferroni post hoc correction.

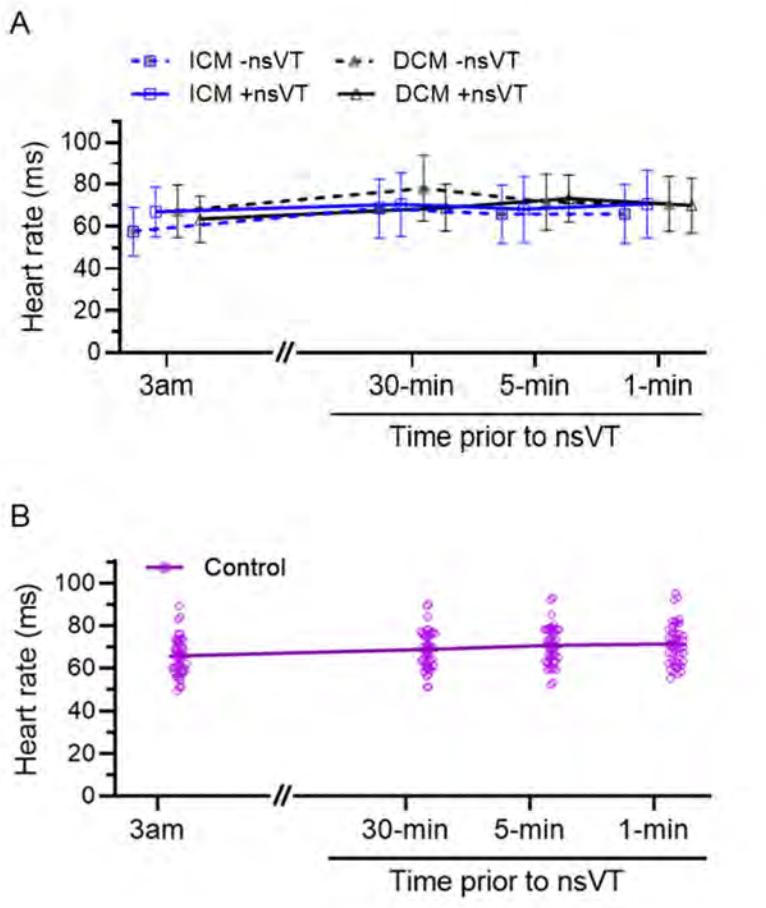

Figure S5. Temporal changes in heart rate in relation to nsVT.

A, Mean data of the temporal changes in heart rate at rest and prior to nsVT, comparing the groups and timepoints. Mixed effects model with Bonferroni post hoc correction. N = 72 ICM, 63 DCM and 50 Control. **B,** Summary of the temporal changes in heart rate at rest and prior to nsVT. Repeated measures ANOVA with Bonferroni post hoc. N = 50 patients.

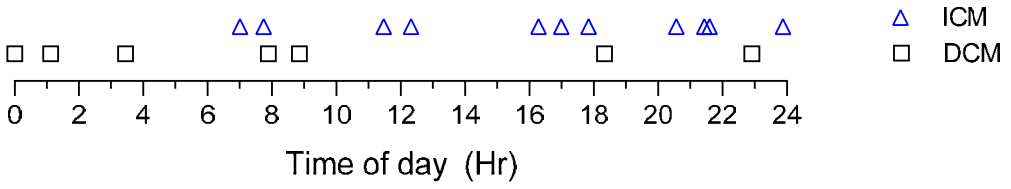

Figure S6. Occurance of the second non-sustained ventricular tachycardia (nsVT) episode.

Time of occurrence during the day of the second nsVT considered for analysis that was at least 1 hour after the index nsVT presented in fig. 2A

SUPPLEMENTAL TABLES AND SUPPORTING INFORMATION

Table S1. Patient baseline characteristics of control patients without structural heart disease (ESUS group).

		Control
n		50
Age (years)		60 ± 12.5
Sex		
	Male (%)	41 (82)
	Female (%)	9 (18)
BMI		25.3 ± 4.3
NYHA (%)		
	1	31 (59.6)
	2	17 (32.7)
	3	3 (5.8)
	4	1 (1.9)
LVEF (%)		59.8 ± 9.7
Indication (%)		
	Primary	
	Secondary	
History (%)		
	Stroke/TIA	14 (28.8)
	Diabetes	9 (17.3)
	Atrial fibrillation	1 (1.9)
	Hypertension	29 (55.8)
Creatinine (mg/dL)		0.98 ± 0.30
Medications (%)		
	Beta-blocker	12 (23.1)
	Statin	26 (50.0)

	ACE-I/ ARB	14 (26.9)
	Loop diuretic	2 (3.8)
	MRA	4 (7.7)
	Aspirin	24 (46.2)
	VKA	2 (3.8)
	NOAC	1 (1.9)
	Amiodarone	2 (3.8)
	Other AAD	7 (13.4)
ECG		
	Heart rate (bpm)	71.1 ± 16.1
	QRS (ms)	113.3 ± 25.1
	QT (ms)	404 ± 40.2
	QTc (ms)	419 ± 26.3
	LBBB (%)	2 (3.8)
	RBBB (%)	8 (16)

Data expressed as n (%) or mean ± SD. ICM – ischemic cardiomyopathy, DCM – dilated cardiomyopathy, BMI – body mass index, NYHA – New York Heart Association classification of heart failure, LVEF – left ventricular ejection fraction, ACE-I – Angiotensin converting enzyme inhibitor / Angiotensin receptor blocker, MRA – mineralocorticoid receptor antagonist, VKA – vitamin K antagonist, NOAC – novel oral anticoagulant, AAD – anti-arrhythmia drug, bpm – beats/minute, LBBB – left bundle branch block, RBBB – right bundle branch block. Stroke/TIA defined as history of stroke/TIA prior to index admission.

ICD candidates had lower LVEF (ICM+nsVT: 28.6 ± 8.8%, DCM+nsVT: 27.3 ± 10.5%, ICM-nsVT: 28.1 ± 9.3%, DCM-nsVT: 29.7 ± 11.5% vs control: 59.8 ± 9.7%, P <0.01) and higher New York Heart Association classification of heart failure (NYHA) with more ICM+nsVT in class 1 than DCM+nsVT (34.9% vs DCM+nsVT: 21.6%, P<0.05). In addition, ICD candidates had longer QTc intervals (ICM+nsVT: 448 ± 41.8 ms, DCM+nsVT: 439 ± 37.1 ms, ICM-nsVT: 443 ± 33.9 and DCM-nsVT: 432 ± 42.9 vs control: 419 ± 26.3 ms) and more left bundle branch block (LBBB) compared to controls (ICM+nsVT: 25.6%, DCM+nsVT: 29.7%, ICM-nsVT: 18.5% and DCM-nsVT: 44.4%, vs 3.8%, P<0.01).

Table S2. Holter electrophysiological parameters of control patients without structural heart disease (ESUS group).

	Control
n	50
Quality – % of Holter analyzed	96.7 ± 2.1
Heart rate (bpm)	71.8 ± 11.9
Bradycardia episodes	2.5 (0-21.5)
Pauses	0 (0-2)
Atrial extrasystoles per hr	4.8 (0.9-32.4)
Ventricular extrasystoles per hr	1.0 (0-4.5)
Non-sustained VT	
number of episodes	0
average rate (bpm)	N/D
average duration (s)	N/D
Sustained VT	
number of patients	0
average rate (bpm)	N/D

Data expressed as n (%) or mean ± SD. Bpm – beats per minute, hr – hour, AV block – atrioventricular block episodes, VT – ventricular tachycardia.

ICD patients, both ICM and DCM patients had more extrasystoles than non-CVD controls (*P* = 0.0035 and 0.0391 respectively).

Table S3. Characteristics of patients with and without appropriate ICD therapy

Clinical variable	APT+ve	APT-ve	*P* value
N	20	60	
ICM %	14 (73.6%)	31 (50.8%)	0.112
Primary prophylaxis %	15 (78.9%)	52 9 (85.5%)	0.496
Sex	16 (80.0%)	49 (81.7%)	0.998
Age	61.3 ± 11.1	58.1 ± 14.8	0.374
LVEF	30.7 ± 7.7	27.1 ± 9.9	0.152
Atrial fibrillation	2 (10.5%)	4 (6.6%)	0.613
ECG			
Heart rate (bpm)	66.9 ± 12.5	67.2 ± 13.97	0.935
QRS (ms)	123.4 ± 30.2	121.3 ± 28.4	0.778
QT (ms)	444.2 ± 60.8	426.0 ± 37.3	0.103
Holter			
Ventricular extrasystoles	252.3 ± 327.8	190.6 ± 325.6	0.470
Number of nsVT episodes	1.9 ± 1.3	1.2 ± 0.7	0.008
BVR			
Rest	1.7 ± 0.3	1.4 ± 0.3	0.019
Max BVR	2.6 ± 0.4	1.9 ± 0.5	<0.001
∆ BVR	0.9 ± 0.4	0.5 ± 0.4	0.003

ICM – ischemic cardiomyopathy, LVEF – left ventricular ejection fraction, ECG – electrocardiogram, bpm – beats per minute, nsVT – non-sustained ventricular tachycardia, BVR – beat-to-beat variability of repolarization, max – maximum. Chi-squared test with Fisher's exact or two-tailed t-test.

CHAPTER 8: General discussion and future perspectives

Ventricular arrhythmias leading to sudden cardiac death (SCD), are a major complication of ischemic heart disease (IHD) and remain a priority for health care. The mechanisms underlying arrhythmias are complex and still incompletely understood, which have been an important hamartia in development of effective therapies. The overall theme of this doctoral study was insight into to the mechanisms and targeting of ventricular arrhythmias in IHD.

Cardiomyocyte remodelling and arrhythmia vulnerability

In the first study (**chapter 3**), we investigated regional cardiomyocyte remodelling as the source of regional arrhythmia vulnerability after myocardial infarction. We found that during adrenergic stress, cardiomyocytes in the peri-infarct border zone (BZ) are susceptible to spontaneous Ca^{2+} release events that are a common mechanism underlying both delayed after depolarizations (DADs) that can trigger premature ventricular complexes, and repolarization instability that can contribute to the substrate maintaining arrhythmias.

The distinction of this study was that we employed a large pre-clinical animal model of myocardial infarction (MI) with a macroscopic peri-infarct BZ and used *in vivo* and *in vitro* electrophysiology to obtain correlative information on regional arrhythmogenic remodelling of cardiomyocytes. There is a paucity of correlative evidence linking cardiomyocyte observations *in vitro* to *in vivo* mechanisms. Few experimental studies have demonstrated the occurrence of DADs *in vivo*, and none to our knowledge in MI, where recording in a defined region can be challenging. Generally, there is not much information on regional arrhythmogenic remodelling of cardiomyocytes after MI, which requires isolation from both the remote region and more importantly the BZ, which in the commonly used rodents is sub-millimetre and thereby unideal. The observation of DADs in cells isolated from the peri-infarct BZ cells validates the *in vivo* findings and informed on Ca^{2+} handling as an important underlying mechanism. Thus, our observation of regional susceptibility to DADs provides important insight into targetable mechanisms of arrhythmia triggers and substrates in the BZ.

Targeting Ca^{2+} handling remains a promising avenue for anti-arrhythmia therapy and was investigated in this study. We showed that pathological Ca^{2+} release could be suppressed by the calmodulin-dependent protein kinase II (CAMKII) inhibitor, Autocamtide-2-Related Inhibitory Peptide (AIP). CAMKII-inhibition is a valid target to pursue and has shown promise in several experimental preparations and human cells (Gaido et al., 2022). Effective and selective small molecule CAMKII-inhibitors have emerged such as RA-608 and NP202 and re-enforced interest in translation. Recently a clinical trial demonstrated that NP202 was safe, although it did not improve left ventricular (LV) function (Boyle et al., 2021). More importantly, its effect on arrhythmias and SCD was not an endpoint, thus not reported, and needs to be assessed in longitudinal studies.

Arrhythmia vulnerability within the border zone: restricted or ubiquitous

The initiation of arrhythmias after MI is predominantly by a premature ventricular complex (PVC), and associated with sympathetic activation. The initiation of arrhythmia after MI has received far less attention than the substrate. Frequent PVCs can trigger ventricular tachycardia (VT) or fibrillation (VF) post-MI, however, sites of origin of these PVCs, spatial vulnerability and the

mechanisms underlying them is unclear. In the preceding study, we observed DADs at randomly studied sites in the BZ, however, direct evidence of triggering PVCs and characterization of vulnerable sites were beyond the experimental setup.

A limitation of the previous study in its perspective to clinical practice was the use of a non-reperfused infarct model. Therefore, in the subsequent work (chapter 4-6) we used an animal model of ischemia-reperfusion MI, which is more representative of current clinical presentation of post-MI arrhythmias.
In **chapter 4**, we aimed to localize the sites of origin of arrhythmias. In a first step, employing longitudinal monitoring with an implanted loop recorder, we observed frequent PVCs in freely moving animals during periods of increased adrenergic drive after MI. In 2 of 7 animals, these PVCs initiated spontaneous VT/VF leading to SCD. In a second step, we recapitulated this in anaesthetized animals and mapped these frequent PVCs to discrete vulnerable sites in the BZ, where frequent DADs were observed directly triggering a spontaneous action potential (AP) and PVC. Hereby we provided important characterization that vulnerable areas in the BZ are discrete: approximately ~1cm^2; few: 1-3 clusters; and close to the scar boundary: within 0.5-1cm. Importantly, DAD-triggered activity at these discrete sites *in vivo* is generally considered the principal mechanism underlying PVCs after MI, but with limited in vivo documentation which we here provided. Furthermore, at cellular level, we showed that cardiomyocyte adrenergic sensitivity is increased. These data support targeting adrenergic signalling and calcium handling to be important avenues for mechanism-guided pharmacotherapy (Njegic et al., 2020).

The concept of targeting frequent PVCs, particularly PVCs triggering arrhythmias is gaining support (Nogami, 2015). However, documentation (12-lead electrocardiogram) of these events is often limited. Novel approaches propose the use electrograms documented from implantable devices (e.g. loop recorder) to guide pace mapping and ablation procedures (Salazar et al., 2022). Our data reinforce the value of PVC monitoring and mapping in the treatment of post MI arrhythmias.

Other mechanisms underlying PVCs are to be considered that could not be addressed in this study, including the role of purkinje cells. The role of purkinje cells has been implicated in experimental studies by the Boyden group (Pinto, 1999). A unifying concept is that cardiomyocytes and purkinje cells interplay by parasystolic modulation (Moe, 1984). Recently, experimental data has demonstrated that at purkinje–myocardial junction, cardiomyocyte DADs trigger action potentials in adjacent purkinje cells (Blackwell et al., 2022), calling for further investigation into this mechanism. Finally, consideration should also be given to the innervation of the myocardium which is altered and remodelled by myocardial infarction. Interrogation of the role of adrenergic innervation in defining arrhythmia vulnerable sites in re-entry has been proposed (Irie et al., 2017), and requires further study.

Heterogeneous repolarization in the border zone: implications for arrhythmias after MI

It has been well established that the BZ is the culprit site of arrhythmia maintenance where the fibrosis forms a structural substrate for arrhythmias. Here, re-entry related to the fixed obstacles is the central mechanism and has been extensively studied. However, structural obstacles do not account for conduction block and electrical heterogeneity required for re-entry. Local differential restitution properties, resulting from repolarization dispersion, can facilitate

unidirectional conduction block that is critical to the re-entry circuit (Coronel et al., 2009). Electrical remodelling of cardiomyocytes can result in local repolarization dispersion and this functional substrate, however, evidence for this is scarce.

Using high throughput techniques to assess large datasets we demonstrated that cardiomyocyte remodelling in the BZ is distinctly heterogeneous and translates to heterogenous repolarization in the BZ *in vivo* (**chapter 5**). This increased local repolarization heterogeneity correlated strongly with arrhythmogenicity. Although altered repolarization in the BZ has been reported in few experimental and computational studies, none were sufficiently powered to evaluate regional heterogeneity. Thus, our data provide novel evidence of local repolarization heterogeneity and the dynamic substrate in the BZ. In the clinical context, these data support a role for functional substrate-based strategies. Recent advances are building on non-invasive substrate identification for non-invasive targeted therapy. Here, non-invasive electrocardiographic-imaging (ECGi) and MRI-based computational modelling are applied to identify the functional substrate for non-invasive stereotactic ablation strategies (Cuculich et al., 2017). Such techniques circumvent the conventional time-consuming VT mapping procedures and can allow for safer therapy. These strategies have shown great promise in small studies and results of randomized control trials are eagerly awaited (Blanck et al., 2020).

An important question from this study is what are the spatial patterns of the heterogeneity in the BZ and how do these relate to the re-entry circuit? Preliminary analysis of the repolarization maps suggests that there are circumscribed areas of large repolarization gradients. Some evidence suggests that re-entry occur at sites of unique or sharp repolarization gradients (Kelemen et al., 2022; Srinivasan et al., 2021). It is conceivable that such unique gradients would be rare and define re-entry critical sites in the BZ. This is supported by the notion that fibrosis and conduction slowing phenomena are ubiquitous while re-entry circuits are discrete within the scar and BZ (Haqqani et al., 2009; Nayyar et al., 2014).

The single nuclei sequencing data corroborated the regional heterogenous cardiomyocyte remodelling in the BZ. Only recently have we begun to explore the transcriptomic changes and underlying regulatory mechanisms (Kuppe et al., 2022). In this study, we explored the unique gene expression profile of BZ cardiomyocytes. Although we could identify highly variable repolarization (*KCNT2*, *SCN3B* and *KCNJ5*) genes, validating our *in vitro* and *in vivo* observations, this comprehensive dataset of single nuclei sequencing yielded a wealth of information that can yield far greater insights into signalling pathways and identifying therapeutic targets.

Predicting imminent arrhythmias and sudden cardiac death in ischemic cardiomyopathy

Complementing these mechanistic studies in an experimental model of post-MI arrhythmias, we undertook a translational study into monitoring the dynamic substrate of repolarization lability for non-invasive arrhythmia prediction in IHD.

SCD in IHD is unpredictable and carries a very high mortality, thus posing a unique clinical challenge. Risk stratification is a cornerstone in SCD management, where appropriate therapy is based on clinical assessment of overall risk. However, does not inform or predict the moment of

SCD. Identifying the onset of arrhythmia or the period of vulnerability prior to arrhythmia onset may allow for preventative therapies.

Beat-to-beat variability of repolarization (BVR) is a measure of repolarization lability that has demonstrated value in predicting arrhythmia onset in experimental model of Torsade de Pointes; however, no studies have previously assessed its clinical utility. In **chapter 7**, we investigated the changes in electrocardiogram (ECG) QT-interval BVR preceding the onset of arrhythmia in high-risk patients. We demonstrated that BVR increases prior to non-sustained VT, a novel observation that was in agreement with a complementary study performed simultaneously by an independent group (Smoczyńska et al., 2020), reinforcing its validity. We further demonstrated the reliability of this finding by testing if the increased BVR in the minute preceding arrhythmia recurred when a second arrhythmia in the same patient was evaluated, suggesting BVR may be a sensitive predictor of imminent arrhythmia.

The value of predicting the onset of arrhythmias is the ability to prevent their occurrence in patients with an ICD or patients being monitored. Here, the benefit is the avoidance of sustained arrhythmias and the shocks needed to defibrillate them that cause injury and adverse remodelling, as well as progression of heart failure with increased mortality. This can be done primarily by overdrive suppression pacing or pharmacotherapy.

An important consideration from the current study was that sustained arrhythmias VT/VF were seldom observed in the Holter recordings (5 of 80 patients). Thus, to address this and obtain further insights on BVR in IHD, we extended our investigation of BVR preceding arrhythmias to the experimental setting.

Further insights into BVR and arrhythmia prediction

In parallel with our clinical study we proceeded to further characterize BVR in IHD. BVR has been shown to be increased during AMI in experimental as well as in clinical studies. In chapter 6, we employed an animal model of AMI with spontaneous ventricular tachycardia (VT) or fibrillation (VF), and demonstrated that BVR surges prior to VT/VF. These data set a strong rationale for the usefulness of in this clinically relevant setting.

Finally, we also tackled a methodological question in the assessment of BVR. We employed a semi-automated fiducial detection algorithm to improve accuracy that was validated in a prior report (Moeyersons et al., 2017). Automation of analysis is proposed to outperform manual analysis by eliminating bias and error. This is particularly important in BVR assessment where millisecond errors can make assessment inaccurate, compounded by the elusive definition of the T-wave end especially in the setting of AMI where the T-wave can be highly dynamic. However, although basic automated ECG analysis is established, complex parameters including BVR are still in infancy calling for further technical developments.

These studies on BVR yielded important insights, however, pertinent questions remain. 1) Can we monitor BVR continuously, and is it a specific predictor of arrhythmia onset? To the best of our knowledge, no studies have examined the pattern of continuous BVR and whether increases in BVR are limited to moments of arrhythmia vulnerability. This would be an important step in defining sensitivity and specificity of BVR in heralding arrhythmias.

2) Can we devise a universal definition for ‘normal’ and ‘increased/pathological’ BVR? In reviewing clinical reports on BVR, we observed widely varying values of baseline BVR (range of 2ms while others up to 6ms). This is likely a reflection of ECG recording and pre-processing (sampling frequency, filtering and smoothing), analysis methodology and manual correction. Thus, there remains a need for standardization of the recording setup and analysis methodology for BVR assessment (Baumert et al., 2016).

General conclusion and future perspectives

Ventricular arrhythmias remain a challenge in IHD, while the understanding of underlying mechanisms is incomplete. Two important insights from this study need to be unified and taken into consideration in arrhythmia studies. Firstly, the cellular remodelling in the BZ is heterogenous and differential compared to the remote region. This leads to heterogeneous repolarization in the BZ that contributes to the dynamic substrate. Secondly, despite heterogenous remodelling and fibrosis throughout the BZ, the vulnerable areas in the BZ are discrete. Thus, in order to obtain better understanding, identification and further study of these areas is required. We have developed a pipeline to map vulnerable sites *in vivo* and harvest them for *in vitro* studies in a pilot study not included in this thesis manuscript, but which will be used for identifying the unique signature of these sites.

Targeting ubiquitous ion channels has had limited success and complicated by paradoxical pro-arrhythmia highlighting the importance of differential and heterogenous remodelling. An avenue to understanding this heterogenous complex remodelling may be systematic analysis of the gene expression and transcriptome to identify drivers of pathological or arrhythmogenic remodelling and development of effective therapeutics. Another important tool that has emerged in recent years is the multicellular preparation that provides a bridging tool to between cellular and *in vivo* setting. This work will be continued ion the group of Experimental Cardiology.

A central theme in arrhythmia mechanisms that we exploited in our studies was the interplay with adrenergic signalling. We did not study receptor subtypes, but of interest, the switch in the β receptor-subtype in the BZ from β1 to β2 dominance opens a new area of further research. Recent advances in our understanding of β3-signalling in remodelling and cardiac function have opened this as a potential target, which have been translated to clinical trials (Pouleur et al., 2018). Further investigation is need for its role in arrhythmias post-MI. Other small molecules have shown excellent promise in targeting Ca^{2+} handling, including a flecainide-derivative without the unwanted Na^{+} channel inhibition (Kryshtal et al., 2021), and novel RYR inhibitors (Pabel et al., 2020). However, these still need further testing in the post-MI remodelling setting and importantly, evidence in relevant large animal models.

The pertinence of arrhythmias in IHD is that they are unpredictable and can lead to SCD, therefore, measures that can predict not only overall risk, but the moment of arrhythmia onset would be invaluable. BVR, may offer a monitorable parameter that predicts imminent arrhythmia in IHD and allow for intervention to prevent arrhythmias and curb SCD. However, much work remains in developing the methodology of continuous BVR assessment and validating the sensitivity and specificity of its arrhythmia predictive value.

References

Baumert, M., Porta, A., Vos, M. A., Malik, M., Couderc, J. P., Laguna, P., Piccirillo, G., Smith, G. L., Tereshchenko, L. G., & Volders, P. G. (2016). QT interval variability in body surface ECG: measurement, physiological basis, and clinical value: position statement and consensus guidance endorsed by the European Heart Rhythm Association jointly with the ESC Working Group on Cardiac Cellular Electrophysiology. *Europace: European Pacing, Arrhythmias, and Cardiac Electrophysiology*, *18*(6), 925-944.

Blackwell, D. J., Faggioni, M., Wleklinski, M. J., Gomez-Hurtado, N., Venkataraman, R., Gibbs, C. E., Baudenbacher, F. J., Gong, S., Fishman, G. I., Boyle, P. M., Pfeifer, K., & Knollmann, B. C. (2022). The Purkinje–myocardial junction is the anatomic origin of ventricular arrhythmia in CPVT. *JCI Insight*, *7*(3).

Blanck, O., Buergy, D., Vens, M., Eidinger, L., Zaman, A., Krug, D., Rudic, B., Boda-Heggemann, J., Giordano, F. A., Boldt, L.-H., Mehrhof, F., Budach, V., Schweikard, A., Olbrich, D., König, I. R., Siebert, F.-A., Vonthein, R., Dunst, J., & Bonnemeier, H. (2020). Radiosurgery for ventricular tachycardia: preclinical and clinical evidence and study design for a German multi-center multi-platform feasibility trial (RAVENTA). *Clinical Research in Cardiology*, *109*(11), 1319-1332.

Boyle, A. J., Schultz, C., Selvanayagam, J. B., Moir, S., Kovacs, R., Dib, N., Zlotnick, D., Al-Omary, M., Sugito, S., Selvarajah, A., Collins, N., & McLachlan, G. (2021). Calcium/Calmodulin-Dependent Protein Kinase II Delta Inhibition and Ventricular Remodeling After Myocardial Infarction. *JAMA Cardiology*, *6*(7), 762.

Coronel, R., Wilms-Schopman, F. J. G., Opthof, T., & Janse, M. J. (2009). Dispersion of repolarization and arrhythmogenesis. *Heart Rhythm*, *6*(4), 537-543.

Cuculich, P. S., Schill, M. R., Kashani, R., Mutic, S., Lang, A., Cooper, D., Faddis, M., Gleva, M., Noheria, A., Smith, T. W., Hallahan, D., Rudy, Y., & Robinson, C. G. (2017). Noninvasive Cardiac Radiation for Ablation of Ventricular Tachycardia. *New England Journal of Medicine*, *377*(24), 2325-2336.

Gaido, O. E. R., Nkashama, L. J., Schole, K. L., Wang, Q., Umapathi, P., Mesubi, O. O., Konstantinidis, K., Luczak, E. D., & Anderson, M. E. (2022). CaMKII as a Therapeutic Target in Cardiovascular Disease. *Annual Review of Pharmacology and Toxicology*, *63*(1).

Haqqani, H. M., Kalman, J. M., Roberts-Thomson, K. C., Balasubramaniam, R. N., Rosso, R., Snowdon, R. L., Sparks, P. B., Vohra, J. K., & Morton, J. B. (2009). Fundamental Differences in Electrophysiologic and Electroanatomic Substrate Between Ischemic Cardiomyopathy Patients With and Without Clinical Ventricular Tachycardia. *Journal of the American College of Cardiology*, *54*(2), 166-173.

Irie, T., Yamakawa, K., Hamon, D., Nakamura, K., Shivkumar, K., & Vaseghi, M. (2017). Cardiac sympathetic innervation via middle cervical and stellate ganglia and antiarrhythmic mechanism of bilateral stellectomy. *American Journal of Physiology-Heart and Circulatory Physiology*, *312*(3), H392-H405.

Kelemen, K., Greener, I. D., Wan, X., Parajuli, S., & Donahue, J. K. (2022). Heterogeneous repolarization creates ventricular tachycardia circuits in healed myocardial infarction scar. *Nature Communications*, *13*(Feb 11), 830.

Kryshtal, D. O., Blackwell, D. J., Egly, C. L., Smith, A. N., Batiste, S. M., Johnston, J. N., Laver, D. R., & Knollmann, B. C. (2021). RYR2 Channel Inhibition Is the Principal Mechanism of Flecainide Action in CPVT. *Circulation Research*, *128*(3), 321-331.

Kuppe, C., Ramirez Flores, R. O., Li, Z., Hannani, M., Tanevski, J., Halder, M., Cheng, M., Ziegler, S., Zhang, X., Preisker, F., Kaesler, N., Xu, Y., Hoogenboezem, R. M., Bindels, E. M. J., Schneider, R. K., Milting, H., Costa, I. G., Saez-Rodriguez, J., & Kramann, R.

(2022). Spatial multi-omic map of human myocardial infarction. *Nature*, *608*(Aug), 766-777.
Moe, G. K. (1984). Oscillating concepts in arrhythmia research; a personal account. *International Journal of Cardiology*, *5*(1), 109-113.
Moeyersons, J., Goovaerts, G., Huijghebaert, S., Vandenberk, B., Willems, R., & Van Huffel, S. (2017). Automated T Wave End Detection Methods - Comparison of Four different methods of T wave end detection. 10th International Joint Conference on Biomedical Engineering Systems and Technologies, Porto, Portugal.
Nayyar, S., Wilson, L., Ganesan, A. N., Sullivan, T., Kuklik, P., Chapman, D., Brooks, A. G., Mahajan, R., Baumert, M., Young, G. D., Sanders, P., & Roberts-Thomson, K. C. (2014). High-Density Mapping of Ventricular Scar. *Circulation: Arrhythmia and Electrophysiology*, *7*(1), 90-98.
Njegic, A., Wilson, C., & Cartwright, E. J. (2020). Targeting Ca(2 +) Handling Proteins for the Treatment of Heart Failure and Arrhythmias. *Frontiers in Physiology*, *11*, 1068.
Nogami, A. (2015). Mapping and ablating ventricular premature contractions that trigger ventricular fibrillation: trigger elimination and substrate modification. *Journal of Cardiovascular Electrophysiology*, *26*(1), 110-115.
Pabel, S., Mustroph, J., Stehle, T., Lebek, S., Dybkova, N., Keyser, A., Rupprecht, L., Wagner, S., Neef, S., Maier, L. S., & Sossalla, S. (2020). Dantrolene reduces CaMKIIδC-mediated atrial arrhythmias. *EP Europace*, *22*(7), 1111-1118. Pinto, J. (1999). Electrical remodeling in ischemia and infarction. *Cardiovascular Research*, *42*(2), 284-297.
Pouleur, A.-C., Anker, S., Brito, D., Brosteanu, O., Hasenclever, D., Casadei, B., Edelmann, F., Filippatos, G., Gruson, D., Ikonomidis, I., Lhommel, R., Mahmod, M., Neubauer, S., Persu, A., Gerber, B. L., Piechnik, S., Pieske, B., Pieske-Kraigher, E., Pinto, F., Ponikowski, P., Senni, M., Trochu, J.-N., Van Overstraeten, N., Wachter, R., & Balligand, J.-L. (2018). Rationale and design of a multicentre, randomized, placebo-controlled trial of mirabegron, a Beta3-adrenergic receptor agonist on left ventricular mass and diastolic function in patients with structural heart disease Beta3-left ventricular hypertrophy (Be. *ESC Heart Failure*, *5*(5), 830-841. 6
Salazar, P., Beaser, A. D., Upadhyay, G. A., Aziz, Z., Besser, S., Shatz, D. Y., Nayak, H. M., & Tung, R. (2022). Empiric ablation of polymorphic ventricular tachycardia/fibrillation in the absence of a mappable trigger: Prospective feasibility and efficacy of pacemap matching to defibrillator electrograms. *Heart Rhythm*, *19*(4), 527-535.
Smoczyńska, A., Loen, V., Sprenkeler, D. J., Tuinenburg, A. E., Ritsema Van Eck, H. J., Malik, M., Schmidt, G., Meine, M., & Vos, M. A. (2020). Short-Term Variability of the QT Interval Can be Used for the Prediction of Imminent Ventricular Arrhythmias in Patients With Primary Prophylactic Implantable Cardioverter Defibrillators. *Journal of the American Heart Association*, *9*(23).
Srinivasan, N. T., Garcia, J., Schilling, R. J., Ahsan, S., Hunter, R. J., Lowe, M., Chow, A. W., & Lambiase, P. D. (2021). Dynamic spatial dispersion of repolarization is present in regions critical for ischemic ventricular tachycardia ablation. *Heart Rhythm O2*, *2*(3), 280-289.

SUMMARY

Ventricular arrhythmias leading to sudden cardiac death (SCD), are a major complication of ischemic heart disease (IHD). It is estimated that arrhythmias and SCD underlie up to 50% of overall deaths in IHD patients with the highest mortality in the first month after MI. Taking into consideration the high prevalence of IHD as leading single health problem and its increasing incidence, the prevention and treatment of SCD is an important health care priority. Over the past 2 decades, advances and developments in effective therapeutics targeting SCD in IHD have been stagnant. An important hamartia of available anti-arrhythmia agents is they were developed with a limited understanding of underlying pathophysiology of IHD and electrophysiological remodelling. Thus, insight into mechanisms and fundamental research are critical to developing effective strategies.

Under the current pathophysiology conceptual framework, arrhythmias are initiated by a triggering event, predominantly and premature ventricular complex (PVC) and maintained by a substrate of structural (fibrosis) and functional (conduction delay or repolarization dispersion) abnormalities. In **Chapter 1**, we reviewed the current understanding of mechanisms of arrhythmogenesis with a focus on *in vivo* observations from experimental studies. With this background, we undertook studies with the overall aim of gaining insights into the mechanisms of ventricular arrhythmias in IHD that could form the basis for translatable therapeutic strategies in the prevention or treatment of ventricular arrhythmia in IHD.

We formulated five research questions (**Chapter 2**) and employed the canonical framework of studying the underlying mechanisms of triggers and substrates to approach this complex problem. First, using a pig model with myocardial infarction (MI) we investigated the region and source of arrhythmia vulnerability, which identified the peri-infarct border region and adrenergic signalling (**Chapter 3**). Then, we further characterized the vulnerability with an interest in spatial vulnerability and underlying mechanisms (**Chapter 4**). In this study we characterized discrete areas of vulnerability within the MI border zone (BZ) and identified delayed afterdepolarizations (DADs) due to altered adrenergic sensitivity underly triggers post-MI. In a third study (**Chapter 5**), we developed high throughput methodologies to study the role of heterogenous cardiomyocyte repolarization in the BZ that could underlie the functional arm of the arrhythmia substrate. Finally, we performed translational studies on the value of beat-to-beat variability of repolarization, a measure of repolarization lability in predicting imminent arrhythmias in IHD. This involved an experimental study (**Chapter 6**) that used a model of acute ischemia to investigate temporal increase in BVR preceding spontaneous arrhythmias. Then, in a clinical study (**Chapter 7**), we validated that in high-risk patients a similar BVR temporal increase precedes non-sustained ventricular tachycardia.

The salient novel insights from the work are the direct demonstration of the previously postulated link between the cellular mechanisms and in vivo arrhythmia susceptibility. Novel as well is the insight into the heterogeneity that exists within the MI border zone. Towards clinical arrhythmia risk prediction we confirmed the potential for BVR as warning sign in imminent arrhythmias, and presented a novel analysis approach.

This work sets the stage for future studies to explore more in depth the molecular and cellular nature of vulnerable sites within the BZ and the potential for local targeted therapies.

ACKNOWLEDGEMENTS

1. CONFLICT OF INTEREST

Matthew Amoni (MA) and Karin Sipido (KS) report no financial or proprietary interests in any product mentioned in this thesis.

Rik Willems (RW) reports research funding from Abbott, Biotronik, Boston Scientific, Medtronic; speakers and consultancy fees from Medtronic, Boston Scientific, Biotronik, Abbott.

2. FUNDING

Matthew Amoni was the recipient of a PhD Fellowship from the Fund for Scientific Research-Flanders / Fonds voor Wetenschappelijk Onderzoek – Vlaanderen (FWO). Several project grants supported the research: FWO to KS (G.0617.09; G.0918.15 and G097021N); Bijzonder Onderzoeksfonds to RW (C14/18/079). Rik Willems holds a Senior Clinical Investigator Fellowship of the FWO.

3. PERSONAL CONTRIBUTIONS

The contribution of Matthew Amoni to this work was in the form of:

- Conception and design of experiments
- Conducting the animal experiments
- Husbandry and medical treatment of animals
- Collecting patient data
- Analysis of experimental and clinical data
- Writing and revising manuscripts and compilation of the thesis

4. SCIENTIFIC ACKNOWLEDGEMENTS

Mathhew Amoni thanks the following people and groups for their assistance in the presented body of work and for their contributions as follows:

- Karin Sipido: as promoter of this thesis, for conceptualization and study design, reviewing data, writing and revision of manuscripts.
- Rik Willems: as co-promoter of this thesis, for clinical training, conceptualization and study design, reviewing data, writing and revision of manuscripts.
- Piet Claus: for scientific support and assistance with *in vivo* experiments, magnetic resonance imaging and data analysis, writing and revision of manuscripts.
- Llewelyn Roderick, Rosa Doñate and Samaneh Ekhteraei-Tousi: for collaboration and contributions to the gene expression studies and revision of manuscripts.
- Sebastian Ingelaere: for assistance with animal experiments, clinical data collection and revision of manuscripts.
- Chandan Kadur Nagaraju: for collaboration on histology and revision of manuscripts.

- Eef Dries: for assistance with cellular electrophysiology and revision of manuscripts.
- Dylan Vermootele: for assistance with analysis of electroanatomical mapping analysis.
- Jonathan Moeyersons: for assistance with beat-to-beat variability analysis.
- Guillaume Gillbert: for assistance with immunofluorescence experiments and image analysis.
- Patricia Holemans, Roxane Menten, Annemie Biesemans and Sofie van Soest: for expert technical assistance during experiments.

5. PERSONAL ACKNOWLEDGEMENTS

This thesis is respectfully presented to Prof. Luc Sels, Rector of the KU Leuven, Professor Chris Van Geet, Vice-Rector of the Biomedical Sciences Group and, to Professor Paul Herijgers, Dean of the Faculty of Medicine.

This thesis project would not have been possible without the support and contribution of many. I mention my promotor prof.dr. Karin Sipido and co-promotor prof.dr. Rik Willems, and Prof.dr. Piet Claus and Prof.dr. Kanigula Mubagwa.

I thank the members of the jury, Prof. dr. Peter Sinnaeve, Prof. dr. Rudi Vennekens.

In Cape Town University, the late Prof.dr. Bongani Mayosi, prof.dr.Arieh Katz and Prof. Asfree Gwanyanya.

The members of the lab of Experimental Cardiology with a special thanks to my ‘technical’ promotor Patricia Holemans.

The clinical team of Electrophysiology

My family.

My friends.

Matthew, September 29, 2022.

CURRICULUM VITAE MATTHEW AMONI

September 29, 2022.

Personal Information

Name:	Matthew Amoni
Date of Birth:	13/03/1991
Nationality:	South African
Address:	231 Anne Marie street, Meyers Park, Pretoria, 0184, South Africa

Education

2009:	AS-Level Matric Certificate – Pretoria Boys High School.
2013:	Bachelor of Science in Medicine (Honours) specializing in Physiology Dissertation title: “The effects of magnesium pre-treatment on isoprenaline-induced cardiac hypertrophy, ischaemia/reperfusion-induced arrhythmias and myocardial dysfunction“ – University of Cape Town.
2016:	Bachelor of Medicine and Bachelor of Surgery (MBChB) – University of Cape Town.
2016:	Master of Science in Medicine (MSc Med) – Dissertation title: “The effects of magnesium treatment on short-term changes in heart rate variability, cardiac ventricular function and lipid profile in streptozotocin-induced diabetic rats.” – University of Cape Town.

Professional Experience

2017-present:	Doctor of Philosophy (PhD) – Provisional dissertation title: “Mechanisms of Triggers and Substrate of Ventricular Arrhythmia in Ischaemic Heart Disease” – KU Leuven.
2021-present:	Medical Internship – Tygerberg Hospital Complex

Awards

2010:	Dean's Merit List.
2013:	Vice-Chancellor' Strategic Award. Best Honours Thesis in Physiology (1st class).
2014:	Boehringer Ingelheim Award.
2016:	Best Speaker - 3rd EU/SA Cardiovascular Conference. Max & Lillie Sonnenberg Masters Award.
2018:	Gauteng Youth Excellence Award - Science
2018:	Poster Award – ESC Working group meeting – Cellular Cardiac Electrophysiology - Essen, Germany
2020:	Top Notch Presentation Award – 39th Belgian Society of Cardiology Congress

Memberships

- Health Professionals Council of South Africa (HPCSA) -Medical Doctor, active.
- European Heart Rhythm Association (EHRA), silver membership.
- European Society of Cardiology (ESC).
- Physiological Society of Southern Africa (PSSA).
- South African Heart Association (SA Heart).
- Public Health Association of South Africa (PHASA).

PUBLICATIONS

Publications marked with * are central to the PhD thesis work.

Papers in Peer-reviewed Journals

Published

1. **Amoni M**, Kelly-Laubscher R, Petersen M, Gwanyanya A. Cardioprotective and Anti-arrhythmic Effects of Magnesium Pretreatment Against Ischaemia/Reperfusion Injury in Isoprenaline-Induced Hypertrophic Rat Hearts. Cardiovasc Toxicol. 2017 Jan;17(1):49-57. doi: 10.1007/s12012-015-9355-6.

2. **Amoni M**, Kelly-Laubscher R, Blackhurst D, Gwanyanya A. Beneficial Effects of Magnesium Treatment on Heart Rate Variability and Cardiac Ventricular Function in Diabetic Rats. J Cardiovasc Pharmacol Ther. 2017 Mar;22(2):169-178. doi: 10.1177/1074248416653831. Epub 2016 Jul 8.

3. *Moeyersons J, **Amoni M**, Vandenberk B, Varon Perez C, Sipido K, Van Huffel S, Willems R. (2018). Temporal beat-to-beat variability of repolarization changes predict non-sustained ventricular tachycardia in ischemic heart disease patients. In: Proc. 45th Annual Computing in Cardiology Conference, (1-4). Presented at the 45th Annual Computing in Cardiology Conference (CinC), Maastricht, The Netherlands, 23 Sep 2018-26 Sep 2018. Computing in Cardiology 2018; Vol 45 Page 1 ISSN: 2325-887X DOI: 10.22489/CinC.2018.018.

4. Nagaraju CK, Dries E, Gilbert G, Abdesselem M, Wang N, **Amoni M**, Driesen RB, Sipido KR. Myofibroblast modulation of cardiac myocyte structure and function. Sci Rep. 2019 Jun 20;9(1):8879. doi: 10.1038/s41598-019-45078-2.

5. Burman RJ*, De Wet TJ*, **Amoni M***, Düsterwald KM*, Favara DM, Setshedi M, Rametse CL, Katz AA. Training South African clinician-scientists: Lessons from the University of Cape Town's intercalated programme. S Afr Med J. 2019 Nov 27;109(12):914-918. doi: 10.7196/SAMJ. 2019.v109i12.14175. (shared first author)

6. *Moeyersons J, **Amoni M**, Van Huffel S, Willems R, Varon C. R-DECO: an open-source Matlab based graphical user interface for the detection and correction of R-peaks. PeerJ Computer Science. 2019 5:e226 https://doi.org/10.7717/peerj-cs.226.

7. *Eef Dries*, **Matthew Amoni***, Bert Vandenberk, Daniel M Johnson, Guillaume Gilbert, Chandan K Nagaraju, Rosa Doñate Puertas, Mouna Abdesselem, Demetrio Julian

Santiago, H Llewelyn Roderick, Piet Claus, Rik Willems, and Karin R. Sipido. Altered adrenergic response in myocytes bordering a chronic myocardial infarction underlies in vivo triggered activity and repolarization instability. J Physiol. 2020 Jan 3. doi: 10.1113/JP278839. (shared first author)

8. Maarten AJ De Smet, Alessio Lissoni, Timur Nezlobinsky, Nan Wang, Eef Dries, Marta Pérez-Hernández, Xianming Lin, **Matthew Amoni**, Tim Vervliet, Katja Witschas, Eli Rothenberg, Geert Bultynck, Rainer Schulz, Alexander V Panfilov, Mario Delmar, Karin R Sipido, Luc Leybaert. Cx43 hemichannel microdomain signaling at the intercalated disc enhances cardiac excitability. J Clin Invest. 2021;131(7):e137752. https://doi.org/10.1172/JCI137752.

9. *__Matthew Amoni__, Piet Claus, Eef Dries, Chandan K. Nagaraju, Stijn De Buck, Bert Vandenberk, Sebastian Ingelaere, Dylan Vermoortele, H. Llewelyn Roderick, Karin R. Sipido, Rik Willems. Discrete sites of frequent premature ventricular complexes cluster within the infarct border zone and coincide with high frequency of delayed afterdepolarizations under adrenergic stimulation. Heart Rhythm. 2021 Aug 8;S1547-5271(21)02000-2. doi: 10.1016/j.hrthm.2021.07.067.

10. Fatma Alatrag, **Matthew Amoni**, Roisin Kelly-Laubscher and Asfree Gwanyanya. Cardioprotective effect of fingolimod against calcium paradox-induced myocardial injury in the isolated rat heart. Can J Physiol Pharmacol. 2021 Sep 24. doi: 10.1139/cjpp-2021-0381. Online ahead of print.

11. *__Matthew Amoni__, Eef Dries, Sebastian Ingelaere, Dylan Vermoortele, H. Llewelyn Roderick, Piet Claus, Rik Willems, Karin R. Sipido. Ventricular arrhythmias in ischemic cardiomyopathy – new avenues for mechanism-guided treatment. Cells. 2021; 10(10):2629. https://doi.org/10.3390/cells10102629

12. Guillaume Gilbert, Chandan Kadur Nagaraju, Robin Duelen, **Matthew Amoni**, Pierre Bobin, Thomas Eschenhagen, H Llewelyn Roderick, Maurilio Sampaolesi, Karin R Sipido. Incomplete Assembly of the Dystrophin-Associated Protein Complex in 2D and 3D-Cultured Human Induced Pluripotent Stem Cell-Derived Cardiomyocytes. Front Cell Dev Biol. 2021 Nov 4;9: 737840. doi: 10.3389/fcell.2021.737840. eCollection 2021.

13. *__Matthew Amoni__, Sebastian Ingelaere, Jonathan Moeyersons, Bert Vandenberk, Piet Claus, Robin Lemmens, Sabine Van Huffel, Karin Sipido, Carolina Varon, Rik Willems. Temporal Changes in Beat-to-Beat Variability of Repolarization Predict Imminent Nonsustained Ventricular Tachycardia in Patients With Ischemic and Nonischemic Dilated Cardiomyopathy. J Am Heart Assoc. 2022 Jul 5;11(13):e024294. doi: 10.1161/JAHA.121.024294. Epub 2022 Jun 22.

14. Stéphanie Bézy, Jürgen Duchenne, Marta Orlowska, Annette Caenen, **Matthew Amoni**, Sebastian Ingelaere, Laurine Wouters, Keir McCutcheon, Lennert Minten, Alexis Puvrez, Jan D'hooge, Jens-Uwe Voigt. Impact of Loading and Myocardial Mechanical Properties

on Natural Shear Waves: Comparison to Pressure-Volume Loops. JACC: Cardiovascular Imaging. 2022, DOI: 10.1016/j.jcmg.2022.07.011.

Added by K. Sipido on March 10th:

Accepted February 1st, 2023

Vermoortele D, **Amoni M, Ingelaere S, Sipido KR, Willems R, Claus P. Electric field-based spatial analysis of non-contact unipolar electrograms to map regional activation-repolarization intervals (JACC Clin Electrophysiol – 2023)*

Provisionally accepted (pending minor revision) February 8th, 2023

****Amoni M**, Vermoortele D, Ekhteraei-Tousi S, Doñate Puertas R, Gilbert G, Youness M, Thienpont B, Willems R, Roderick HL, Claus P, Sipido KR. Cardiomyocyte population studies reveal heterogeneous repolarization and remodeling within the myocardial infarction border zone. (Circ Arrhythm Electrophysiol)*

Revision under preparation

****Amoni M**, Ingelare S, Moeyersons J, Wets D, Tanushi A, Van Huffel S, Varon C, Sipido K, Claus P, Willems R. Regional beat-to-beat variability of repolarization increases during ischemia and predicts imminent arrhythmias in a pig model myocardial infarction (Am J Physiol: Heart & Circulation – major revision requested)*

Abstracts in peer-reviewed journals

1. **Matthew Amoni**, Roisin Kelly-Laubscher and Asfree Gwanyanya. A cardioprotective- and antiarrhythmic role of magnesium pretreatment against ischaemic injury in isoprenaline-induced hypertrophic rat hearts. SA Heart Journal, 12(4), Spring 2015. DOI: https://doi.org/10.24170/12-4-1703

2. **Matthew Amoni**, Roisin Kelly-Laubscher and Asfree Gwanyanya. Improvement of diabetes-induced cardiac autonomic dysfunction and left ventricular diastolic pressure-volume response by magnesium treatment in streptozotocin-induced diabetic rats. SA Heart Journal, 12(4), Spring 2015. DOI: https://doi.org/10.24170/12-4-1703.

3. **Matthew Amoni**, Roisin Kelly-Laubscher and Asfree Gwanyanya. Preservation of heart rate variability and improvement of cardiac ventricular distensibility by magnesium treatment in diabetic rats. Journal of African Association of Physiological Sciences. Vol 4, No 1.

4. Ofoegbu C, **Amoni M**, Brink J, Human P, Zilla P. Off-Pump Coronary Artery Bypass Grafting (OPCAB) Versus Coronary Artery Bypass Grafting (CABG) With Cardiopulmonary Bypass (CABG-CPB) In A South African Patient Population. SA Heart Journal. Volume 13, Number 3, Winter 2016. DOI: https://doi.org/10.24170/13-3-1659.

5. **Amoni M**, Bagula H, Mpakama B, Makhubele A, Colvin C. Short-term rural placements positively impacts on medical students' developments and perceptions on rural health

care. PHASA Conference 2017.

6. **Matthew Amoni**, Fatma Alatrag, Roisin Kelly-Laubscher and Asfree Gwanyanya. Differential effects of fingolimod and other transient receptor potential melastatin 7 (TRPM7) channel modulators on calcium paradox-induced myocardial injury in rat hearts. SA Heart Journal, Vol 14, No 4 (2017). ISSN: 2071-4602 (online) ISSN: 1996-6741 (print).

7. **M. Amoni**, B. Vandenberk, J. Moeyersons, S. Van Huffel, K. Sipido, R. Willems. Temporal beat-to-beat variability of repolarization (BVR) changes predict imminent non-sustained ventricular tachycardia in ischaemic heart disease patients. EP Europace, Volume 20, Issue suppl_1, March 2018, Page i41, https://doi.org/10.1093/europace/euy015.104.

8. Jonathan Moeyersons; **Matthew Amoni**; Bert Vandenberk; Carolina Varon; Karin Sipido; Sabine Van Huffel; Rik Willems. Temporal Beat-to-Beat Variability of Repolarization Changes Predict Non-Sustained Ventricular Tachycardia in Ischemic Heart Disease Patients. 2018 Computing in Cardiology Conference (CinC), 2018, pp. 1-4, doi: 10.22489/CinC.2018.018.

9. Eef Dries, Bert Vandenberk, Guillaume Gilbert, **Matthew Amoni**, Patricia Holemans, Rik Willems, Piet Claus, Karin R. Sipido. Regional heterogeneity of hyperactive non-coupled RyRs makes the peri-infarct region more prone to triggered activities after myocardial infarction. Cardiovascular Research, Volume 114, Issue suppl_1, April 2018, Pages S126–S127, https://doi.org/10.1093/cvr/cvy060.376.

10. **Matthew Amoni**, Eef Dries, Bert Vandenberk, Piet Claus, Rik Willems and Karin Sipido. Regional heterogeneity during ß-adrenergic stimulation underlies the ventricular arrhythmia triggers and substrate after myocardial infarction. SA Heart Journal, Vol 15, No 4 (2018). ISSN: 2071-4602 (online).

11. **Matthew Amoni**, Piet Claus, Eef Dries, Guillaume Gilbert, Patricia Holemans, Roxane Menten, Karin Sipido, Bert Vandenberk, Rik Willems. Enhanced adrenergic response of myocytes in the peri-infarct region underlies triggered activity arrhythmias and repolarization lability in vivo. Acta Cardiologica; 2020; Vol. 75; pp. 12. DOI: 10.1080/00015385.2020.1705029.

12. Taylor K. Pullinger, **Matthew Amoni**, Itziar Irurzun-Arana, Karin R. Sipido, Eric A. Sobie. Using a Genetic Algorithm to Parameterize a Mathematical Model of aPorcine Ventricular Cardiomyocyte. (2021). *Biophysical Journal 120(3):333a.* DOI:10.1016/j.bpj.2020.11.209

13. D Vermoortele, **M Amoni**, S Ingelaere, P Holemans, R Willems, K Sipido, P Claus. Repolarization heterogeneity within the myocardial infarction border zone correlates with variability of myocyte remodelling. European Heart Journal, Volume 42, Issue Supplement_1, October 2021, ehab724.0622, https://doi.org/10.1093/eurheartj/ehab724.0622.

14. Bezy, S., Duchenne, J., Orlowska, M., **Amoni, M**., Caenen, A., Keijzer, L.B H., McCutcheon, K., Ingelaere, S., Cvijic, M., Puvrez, A., Vos, H.J., D'hooge, J., Voigt, J-U. (2021). Natural shear wave propagation speed is influenced by changes in myocardial structural properties as well as loading conditions. In: ACTA CARDIOLOGICA: vol. 76,

(37-38).

15. S Bezy, A Caenen, J Duchenne, M Orlowska, **M Amoni**, L B H Keijzer, R Vos, J D'hooge, J U Voigt. Myocardial stiffness assessed by natural shear wave elastography is related to pressure-volume loop derived parameters. European Heart Journal, Volume 42, Issue Supplement_1, October 2021, ehab724.034, https://doi.org/10.1093/eurheartj/ehab724.034.

16. Bezy, S., J. Duchenne, M. Orlowska, **M. Amoni**, Annette Caenen, L. B. H. Keijzer, K. Mccutcheon, S. Ingelaere, M. Cvijic, A. Puvrez, H. J. Vos, J. D'hooge, and J. U. Voigt. 2021. "Natural Shear Wave Propagation Speed Is Influenced by Both Changes in Myocardial Structural Properties as Well as Loading Conditions." In European Heart Journal-Cardiovascular Imaging, 22:i167–i167. doi:10.1093/ehjci/jeaa356.146.

17. S Bezy, A Caenen, J Duchenne, M Orlowska, **M Amoni**, L B H Keijzer, R Vos, J D'hooge, J U Voigt. Myocardial stiffness assessed by natural shear wave elastography is related to pressure-volume loop derived parameters. European Heart Journal, Volume 42, Issue Supplement_1, October 2021, ehab724.034, https://doi.org/10.1093/eurheartj/ehab724.034

18. **M Amoni**, D Vermoortele, S Ekhteraeitousi, R Donate Puertas, S Ingelaere, H L Roderick, P Claus, R Willems, K R Sipido. Heterogeneous myocyte remodelling and spatial heterogeneity of repolarization within the myocardial infarction border zone. EP Europace, Volume 24, Issue Supplement_1, May 2022, euac053.596, https://doi.org/10.1093/europace/euac053.596.

19. D Vermoortele, **M Amoni**, S Ingelaere, P Holemans, R Menten, R Willems, KR Sipido, P Claus. Adrenergic stimulation amplifies the difference in beat-to-beat variability between the scar border zone and remote region. EP Europace, Volume 24, Issue Supplement_1, May 2022, euac053.330, https://doi.org/10.1093/europace/euac053.330.

POSTSCRIPTUM

We deeply mourn the passing of Matthew on October 3rd, 2022. Matthew was a brilliant young scientist, talented and hard working. He was also a very fine person, deeply committed to become a physician-scientist in cardiac electrophysiology. It has been a privilege to be his supervisors for his PhD thesis, and he is very much missed by all of us who worked and lived with him.

Karin Sipido, Rik Willems

Leuven, March 10, 2023